Model-Driven Design and Uncertainty Quantification for Cardiac Electrophysiology Experiments

Chon Lok Lei

University College

University of Oxford

A thesis submitted for the degree of

Doctor of Philosophy

Trinity 2020

Supervisors:

Prof. David J. Gavaghan
Prof. Gary R. Mirams
Dr. Michael Clerx

Industrial supervisors:

Dr. Liudmila Polonchuk
Dr. Ken Wang

Examiners:

Prof. Ruth E. Baker
Prof. Jamie I. Vandenberg

The author acknowledges support from the Clarendon Scholarship Fund, and the Engineering and Physical Sciences Research Council, the Medical Research Council and F. Hoffmann-La Roche Ltd. for studentship support.

Abstract

The goal of systems biology is to provide a predictive and quantitative understanding of complex biological systems and their experimental data using mathematical and computational models. Mathematical modelling and computational simulation has been a crucial tool for basic research in cardiac electrophysiology for decades, and has provided remarkable insights into many physiological mechanisms. More recently these quantitative cardiac models have begun to transition into safety-critical clinical and pharmaceutical development applications. Using cardiac mathematical models in such applications requires high levels of credibility as well as an accurate quantification of the uncertainty in the model predictions. In this thesis, we develop a suite of Bayesian inference and uncertainty quantification techniques and software tools to study cardiac cellular electrophysiology. We then design and perform high-throughput experiments to construct and validate cell-specific mathematical models for *human Ether-à-go-go-Related Gene* (hERG) channel dynamics, and to study its temperature dependence, which is important for cardiac safety pharmacology and cardiac action potential models. Using the Bayesian statistical framework together with the high-throughput measurements allows us to quantify the uncertainty and variability of the model parameters. We also model and analyse how experimental artefacts contribute to the observed variability of these recordings, allowing us to separate the effects of these artefacts from physiological behaviour. A similar approach for uncertainty characterisation and experimental design will have to be adapted for other ion currents to create better predictive models, as accurate ion channel models are essential for constructing trustworthy cardiac action potential models.

Contents

Publications

Publications based on thesis chapters:

1. **Lei, C. L.**, Wang, K., Clerx, M., Johnstone, R. H., Hortigon-Vinagre, M. P., Zamora, V., Allan, A., Smith, G. L., Gavaghan, D. J., Mirams, G. R., and Polonchuk, L. (2017a). Tailoring mathematical models to stem-cell derived cardiomyocyte lines can improve predictions of drug-induced changes to their electrophysiology. *Frontiers in Physiology*, 8:986

2. **Lei, C. L.**, Clerx, M., Beattie, K. A., Melgari, D., Hancox, J. C., Gavaghan, D. J., Polonchuk, L., Wang, K., and Mirams, G. R. (2019a). Rapid characterization of hERG channel kinetics II: temperature dependence. *Biophysical Journal*, 117(12):2455-2470

3. **Lei, C. L.**, Clerx, M., Gavaghan, D. J., Polonchuk, L., Mirams, G. R., and Wang, K. (2019b). Rapid characterization of hERG channel kinetics I: using an automated high-throughput system. *Biophysical Journal*, 117(12):2438-2454

4. **Lei, C. L.**, Clerx, M., Whittaker, D. G., Gavaghan, D. J., de Boer, T. P., and Mirams, G. R. (2020a). Accounting for variability in ion current recordings using a mathematical model of artefacts in voltage-clamp experiments. *Philosophical Transactions of the Royal Society A*, 378:20190348

Additional publications relating to thesis:

1. Clerx, M., Robinson, M., Lambert, B., **Lei, C. L.**, Ghosh, S., Mirams, G. R., and Gavaghan, D. J. (2019b). Probabilistic Inference on Noisy Time Series (PINTS). *Journal of Open Research Software*, 7(1):23

2. **Lei, C. L.**, Ghosh, S., Whittaker, D. G., Aboelkassem, Y., Beattie, K. A., Cantwell, C. D., Delhaas, T., Houston, C., Novaes, G. M., Panfilov, A. V., Pathmanathan, P., Riabiz, M., dos Santos, R. W., Walmsley, J., Worden, K., Mirams, G. R., and Wilkinson, R. D. (2020c). Considering discrepancy when calibrating a mechanistic electrophysiology model. *Philosophical Transactions of the Royal Society A*, 378:20190349

3. **Lei, C. L.**, Fabbri, A., Whittaker, D. G., Clerx, M., Windley, M. J., Hill, A. P., Mirams, G. R., and de Boer, T. P. (2020b). A nonlinear and time-dependent leak current in the presence of calcium fluoride patch-clamp seal enhancer. *Wellcome Open Research*, 5:152

4. Whittaker, D. G., Clerx, M., **Lei, C. L.**, Christini, D. J., and Mirams, G. R. (2020). Calibration of ionic and cellular cardiac electrophysiology models. *Wiley Interdisciplinary Reviews: Systems Biology and Medicine*, 12(4):e1482

Publications that I have contributed to while working as part of this thesis:

1. **Lei, C. L.**, Kellard, J. A., Hara, M., Johnson, J. D., Rodriguez, B., and Briant, L. J. (2018). Beta-cell hubs maintain Ca2+ oscillations in human and mouse islet simulations. *Islets*, 10(4):151-167

2. Clayton, R. H., Aboelkassem, Y., Cantwell, C. D., Corrado, C., Delhaas, T., Huberts, W., **Lei, C. L.**, Ni, H., Panfilov, A. V., Roney, C., and Dos Santos, R. W. (2020). An audit of uncertainty in multi-scale cardiac electrophysiology models. *Philosophical Transactions of the Royal Society A*, 378:20190335

3. Foster, T., **Lei, C. L.**, Robinson, M., Gavaghan, D., and Lambert, B. (2020). Model evidence with fast tree based quadrature. *arXiv*:2005.11300

4. Creswell, R., Lambert, B., **Lei, C. L.**, Robinson, M., and Gavaghan, D. (2020). Using flexible noise models to avoid noise model misspecification in inference of differential equation time series models. *arXiv*:2011.04854

Chapter 1

Introduction

The circulatory system transports blood to distribute essential substances, such as oxygen and nutrients, to tissues and to remove metabolic byproducts, for example carbon dioxide. The system is powered by a muscular organ that pumps blood around the body — the heart. Its function is critical to the health of the body.

The goal of systems biology is to integrate complex experimental data into mathematical and computational models that provide a predictive and quantitative understanding of living systems. The mathematical modelling of the electrophysiology of nerve and cardiac cells is one of the most advanced and mature areas of systems biology. These cardiac models have contributed enormously to the understanding of heart function, disease, and the origin of heart rhythm disturbances (Noble, 2008, 2011; Fink et al., 2011).

Pharmaceutical compounds can sometimes induce dangerous (side-)effects to the muscle cells in the heart, causing disturbances in cardiac rhythm. Therefore pharmaceutical companies and regulatory authorities prioritise screening for any potential side-effects the drug might induce in patients *before* it is taken by those patients — leading to the need for *cardiac safety testing* in drug development.

International pharmaceutical regulatory authorities including the U.S. Food and Drug Administration (FDA) are leading the Comprehensive *in vitro* Proarrhythmia Assay (CiPA), a process of introducing new guidelines to replace a human clinical trial (the *Thorough QT Study*) to study the proarrhythmic risk of all new drugs. The new approach will involve extensive use of *in silico* (mathematical) models of human cardiomyocytes calibrated to *in vitro* ion channel screening data, and their predictions will then be compared experimentally using human induced pluripotent stem cell-derived cardiomyocytes (hiPSC-CMs), together with a more lightweight electrocardiogram (ECG) evaluation in early clinical trials. However, there are issues that need to be addressed for the new guidelines before they can be brought into practice. For example, hiPSC-CMs provide a proxy for human adult cardiomyocytes, but they are not the same, so the hiPSC-CM experiments require interpretation and translation.

Multiple research questions arise from the proposed pharmaceutical safety guidelines. HiPSC-CM cell lines are developed from a donor with a particular genetic background, using a specific set of protocols from differentiation to maturation; how important are the differences between hiPSC-CM

cell lines, as well as cell-to-cell variability of ion current characteristics within a single line, for our understanding of cell electrophysiology and prediction of drug effects? What experimental approaches are best at characterising drug effects in ion channel screening experiments? Finally, the human cardiomyocyte model needs accurate ion channel models for predictions; how can we construct trustworthy ion channel models and assess how trustworthy they are?

The overall aim of this thesis is to establish and test a methodology to develop cell-specific mathematical electrophysiology models that in turn addresses the aforementioned scientific questions. Since *in vitro* ion channel and hiPSC-CM experiments form the backbone of the new guidelines introduced by CiPA, understanding experimental variability is crucial to such safety-critical decision-making processes. A set of robust and ready-to-apply methodologies for building cell-specific models will assist in the interpretation of these experiments. This work is not limited to drug safety testing, it can also be used for, for example, personalised medicine, disease modelling and regenerative medicine. Moreover, the techniques we develop are not limited to cardiac electrophysiology, they are broadly applicable to communities interested in general ion channel electrophysiology.

Within this broader problem statement, six different topics are addressed. We first benchmark the performance of tailoring hiPSC-CM cell-line specific models using a method based on conventional/traditional voltage-clamp protocols, and find that there is room for improvement. We then design and develop a suite of Bayesian inference and uncertainty quantification techniques and software tools to study ion channel electrophysiology. Instead of using the conventional way of characterising the ion channel models within a cardiomyocyte model, we perform *experimental design* that allows us to develop 'information-rich' protocols to obtain rapid, high-quality, high-throughput experiments that allow us to construct and to validate cell-specific models. We focus on the ionic current I_{Kr}, which is of great importance in cardiac electrophysiology and safety pharmacology. We then extend the approach to study the temperature dependence of I_{Kr} kinetics. Next, we investigate the sources of variability and uncertainty in those experiments, and pin down which uncertainties are relevant for physiological predictions, and which variabilities are likely due to experimental errors. Finally, we apply *optimal experimental design* to hiPSC-CMs and test methodologies for building cell-specific models. A schematic of the work presented in the main chapters is shown in Figure 1.1.

1.1 Thesis Outline

The next chapter, Chapter 2, introduces the necessary background information for the rest of the thesis. It explains the basic biological/physiological, experimental, mathematical, statistical, and pharmacological concepts that this thesis concerns.

Chapter 3 presents an attempt to tailor hiPSC-CM cell-line specific models with a method using conventional voltage-clamp protocols whilst assuming ideal model kinetics. Although using limited data and a relatively simple approach, we show that tailoring an hiPSC-CM model to a specific cell line leads to improved predictions of baseline behaviour and response to drugs. This chapter acts as a benchmark for the performance of hiPSC-CM cell-line specific models using the conventional

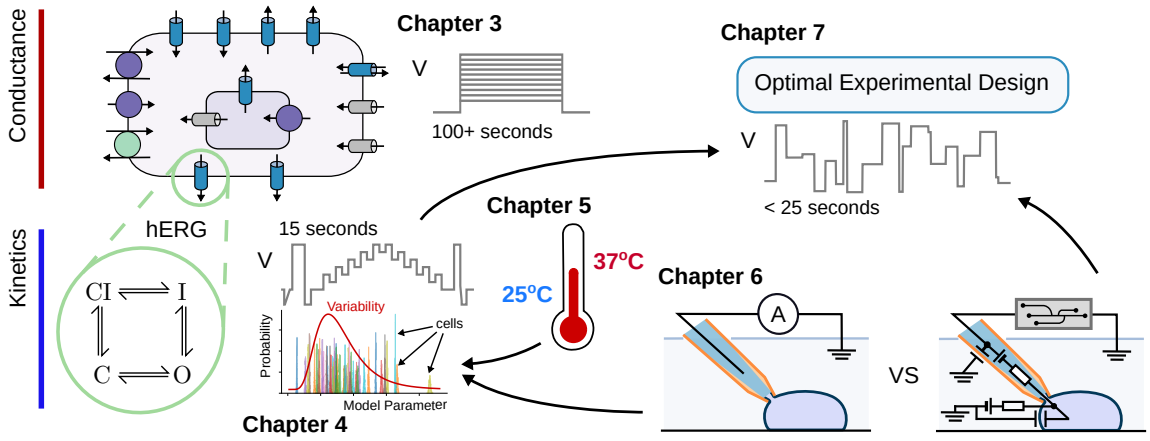

Figure 1.1: A schematic of the work presented in the thesis chapters. In Chapter 3 we tailor cell-line specific models for hiPSC-CMs using current kinetics models from the literature, suggesting the current kinetics models need to be improved. In Chapters 4–6 we then look at methods to construct better current kinetics models. Chapter 4 presents a method to rapidly characterise kinetics of the hERG channel using a high-throughput patch-clamp system, and studies the variability between experiments. In Chapter 5 we study the temperature dependence of hERG kinetics. Chapter 6 investigates the sources of experimental artefacts that may cause the observed variability of hERG kinetics. Finally, in Chapter 7 we revisit tailoring action potential models using optimal experimental design techniques to design voltage-clamp protocols while incorporating lessons learned in the previous chapters.

methods and assumptions. More importantly, it reveals the limitations of the conventional methods, which leads us to explore improvements in the following chapters.

In Chapter 4 we present a method that we have developed for high-throughput rapid characterisation of kinetics of the *human Ether-à-go-go-Related Gene* (hERG) channel, which is one of the most important ion channels in cardiomyocytes and underpins I_{Kr}. Using our novel method allows us to fit mathematical models to results of over 100 single-cell patch-clamp measurements collected simultaneously on an automated voltage-clamp platform. The automated patch-clamp data are used to parameterise a mathematical ion channel model fully, allowing automated and rapid development of mathematical models from quick, cheap, and reliable experiments. The method also allows ample data for independent validation of the models and enables us to study experimental variability and its origins in Chapter 6. We then apply our method to study the temperature dependence of hERG kinetics in the next chapter; it can also be used to study different modulating factors such as mutations or the action of pharmaceuticals, and could be adapted to study many other currents.

It is well-known that ion channel currents are highly sensitive to temperature changes. Yet, because many experiments are performed more easily at room temperature, it is common to extrapolate findings to physiological temperatures using Q_{10} coefficients or Eyring rate theory. Chapter 5 describes the use of short, information-rich protocols developed in the previous chapter to identify how kinetic parameters change with temperature. We show that the commonly used Q_{10} and Eyring formulations are incapable of describing the parameters' temperature dependence for our model. A more generalised Eyring relationship works well, but remeasuring kinetics by refitting a model is optimal. The findings have implications for the accuracy of Q_{10} coefficients in electrophysiology, and

care is needed to avoid misleading extrapolations using Q_{10} coefficients in scientific and industrial pharmaceutical applications, such as those described in Chapter 3.

Chapter 6 investigates the source of the observed experiment-to-experiment variability in Chapter 4. We derive a mathematical model that describes not just ion current dynamics, but the entire voltage-clamp experiment. The experimental artefact components of the model include: series resistance, membrane and pipette capacitances, voltage offsets, leak current, and imperfect compensations made by the amplifier for these phenomena. In this model, variability in the observations can be explained by either cell properties, measurement artefacts, or both. Remarkably, by assuming that variability arises exclusively from measurement artefacts, it is possible to explain a larger amount of the observed variability than when assuming cell-specific ion current kinetics; the first assumption also leads to a smaller number of model parameters. The result suggests that most of the observed variability in patch-clamp data measured under the same conditions is caused by experimental artefacts, and hence can be compensated for in post-processing by using our model for the patch-clamp experiment.

In Chapter 7 we revisit whole-cell modelling and hiPSC-CM models. We apply an approach similar to that of the previous chapters for studying ion channel kinetics, *optimal* experimental design for action potential models. We focus on developing a voltage-clamp experimental protocol that allows us to identify the maximum conductance values for each current type. We further consider the potential real-world challenges that one would encounter when applying to experimental recordings: first, in exploring the potential uncertainty of the ion channel kinetics, we examine the robustness of the designs using multiple existing ion channel kinetics models; secondly, we check whether it would help to consider using specific blockers to isolate each type of current, when there is discrepancy in model kinetics; finally, we consider the experimental variability that we studied in Chapter 6, and how it would affect the inferred conductance values.

In Chapter 8, we discuss how each chapter contributes to and advances the state of the art in cardiac electrophysiology. We then conclude the thesis, and finish with suggestions for future research and remaining open challenges.

Chapter 2

Background

I co-authored the following publications discussed in this chapter:

Clerx, M., Robinson, M., Lambert, B., Lei, C. L., Ghosh, S., Mirams, G. R., and Gavaghan, D. J. (2019b). Probabilistic Inference on Noisy Time Series (PINTS). *Journal of Open Research Software*, 7(1):23.

Contributions: I co-developed and maintained the open source Python package, PINTS.

Whittaker, D. G., Clerx, M., Lei, C. L., Christini, D. J., and Mirams, G. R. (2020). Calibration of ionic and cellular cardiac electrophysiology models. *Wiley Interdisciplinary Reviews: Systems Biology and Medicine*, 12(4):e1482.

Contributions: I wrote code for some examples in this review, performed data analysis, generated plots and drafted part of this review.

Overview:

This chapter provides some of the basic biological/physiological, mathematical, experimental, pharmacological, and statistical concepts and background relevant to this thesis; some of the more in-depth discussion and references to more detailed work are included in the later chapters. The human heart is critical to the health of the body, its contraction is coordinated by (bio-)electrical signals known as action potentials. We first look at cellular electrophysiology: how these electrical signals are caused by the movement of ions, i.e. electrical currents, going in and out of heart muscle cells. We then review human induced pluripotent stem cell-derived cardiomyocytes (hiPSC-CMs) which provide a new proxy to study the complex behaviour of human heart muscle cells, and their limitations. These hiPSC-CMs are proposed to be used as part of future drug testing in the Comprehensive *in vitro* Proarrhythmia Assay (CiPA) led by the U.S. Food and Drug Administration (FDA). Next we discuss the mathematical models describing the dynamics of these action potentials and currents. We then describe the modern experimental techniques for studying cellular electrophysiology and how these models are constructed. Finally we discuss how the accuracy and robustness of the models for such safety-critical decisions can be critically assessed.

2.1 Electrophysiology of the Human Heart

The human heart consists of two pumps, left and right, and each has an *atrium* and a *ventricle*. The two atria are smaller, with thinner walls than the ventricles. The right side of the heart pumps deoxygenated blood towards the lungs and oxygenated blood back to the left side of the heart. The left side of the heart then pumps the oxygenated blood around the rest of the body. The latter process is more physically-demanding and accordingly, the left ventricle has a much thicker wall than the right. A schematic of the basic anatomy of the human heart is shown in Figure 2.1 (left).

The walls of these pumps comprise layers of muscle cells, termed *cardiomyocytes*, and other cells with specialised functions. Cardiomyocytes, like neurons, are electrically *excitable*, and can be stimulated to propagate electric signals. These electric signals coordinate the pumping of the heart — a well-timed sequence of contractions of around five billion cardiomyocytes (Olivetti et al., 1995). The contraction of the cardiomyocytes is controlled by an electric signal known as the *action potential*. An action potential is the rapid rise and fall of the *transmembrane potential*, also called the *membrane potential* or *membrane voltage*, of a cell. These changes in the membrane potential trigger an influx of calcium ions into the cell (leading to a further release of calcium ions from stores within the cell); the increase of intracellular calcium ion concentration enables the formation of cross bridges between myosin and actin, which gives rise to contraction of cardiomyocytes (Bers, 2002).

In addition, the heart contains smaller numbers of cells with specialised electrical functions that help

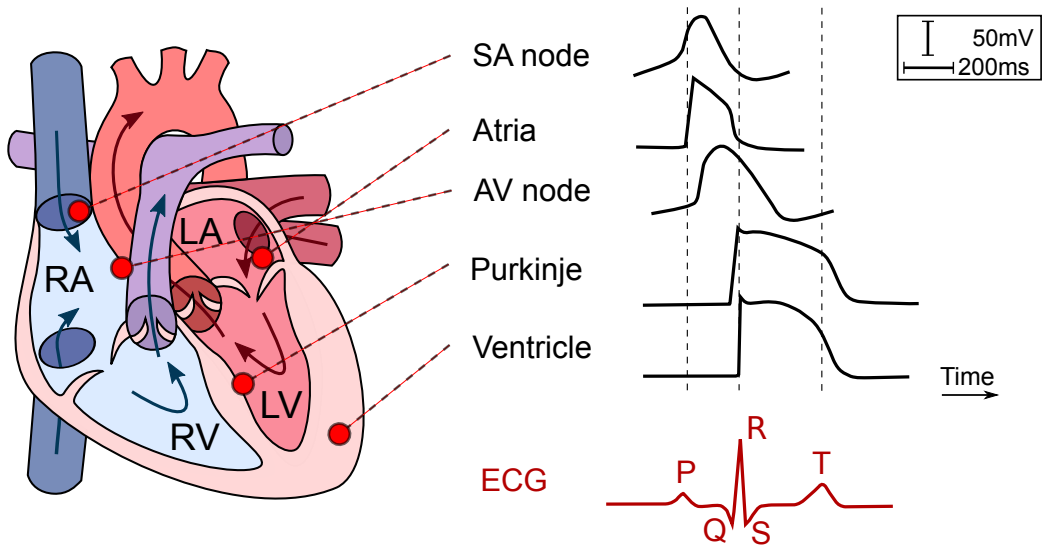

Figure 2.1: An illustration of the basic anatomy of, and action potentials across, the human heart. **(Left)** Shows the four chambers of the heart and the arrows indicate the direction of blood flow, where deoxygenated blood enters the right atrium (RA) and through the right ventricle (RV) to the lungs. Oxygenated blood from the lungs enters the left atrium (LA) and then the left ventricle (LV), which is pumped to the rest of the body. **(Right)** Shows the action potentials of different phenotypes of cardiomyocyte in the heart. These different action potentials contribute to the characteristic shape of the electrocardiogram (ECG), shown in red. Adapted from Hume and Grant (2015).

coordinating the contraction. The cells of the *sinoatrial* node exhibit spontaneous excitation, i.e. they spontaneously generate action potentials, setting the pace for the rest of the heart in healthy conditions. The electrical waves propagate from the sinoatrial node, located at the top of the right atrium, to the left and right atria triggering contraction of the atrial muscle cells. The atria are electrically shielded from the ventricles; the activation of the ventricles occurs via the cells of the *atrioventricular* node. The signals from the atrioventricular node travel down conducting *Purkinje fibres* in the septum (the muscle wall which separates the left and right ventricles) towards to the apex of the heart, which then spread over the ventricular walls causing the ventricles to contract. This completes one cycle of the pumping action of the heart.

2.1.1 Cellular electrophysiology and the action potential

Cardiomyocytes, like all cells, are surrounded by a *membrane* composed of a lipid bilayer. This membrane works as an electrical insulator: a barrier to the movement of ions, such as sodium, calcium, and potassium. *Transmembrane proteins* are embedded in the membrane of the cardiomyocytes, some of which are *ion pumps*, *ion exchangers* and *ion channels*. The ion pumps actively push ions across the membrane and maintain electrochemical gradients across the membrane, by breaking down ATP (adenosine triphosphate) into ADP (adenosine diphosphate) to obtain the required energy; the ion exchangers utilise the electrochemical gradient to move ions across against their gradient, whilst simultaneously moving a second type of ion along its gradient; and the ion channels facilitate passive diffusion and allow multiple or specific ion types to move across the membrane. The main differences between ion pumps, ion exchangers, and ion channels are reviewed by Molleman (2003).

The ion channels of interest in cardiomyocytes are mostly voltage-sensitive, and are known as *voltage-gated* ion channels. The probability of these ion channels being open, i.e. conducting current, changes as a response to the membrane voltage (Hille, 2001). There also exist other ion channels which are *ligand-gated*, *light-gated*, or controlled by *second messengers*.

To demonstrate the general idea of the formation of an action potential, we take cells from the outer layer (epicardial) of the ventricles as an example. The formation of the action potential in other types of cardiomyocytes varies slightly, see Figure 2.1 (right) which shows the differences in shape.

Under an electrical stimulus, for example an influx of positively-charged ions from the neighbouring cells which raises the intracellular potential, voltage-gated sodium ion channels open and sodium ions flow into the cell down their concentration gradient. This is known as the *fast sodium current* I_{Na}, which rapidly increases the cell membrane voltage (*depolarisation*), sometimes also called "Phase 0"[1] of the action potential (Grant, 2009).

Phase 1. A short period of *repolarisation*. The rapid inactivation of the inward sodium current I_{Na}, together with the activation of the *transient outward potassium current* I_{to}, causes a small rapid drop of the membrane voltage.

[1] Although the processes and dynamics that result in the action potential are *continuous*, by textbook convention the action potential is described as having separate "phases".

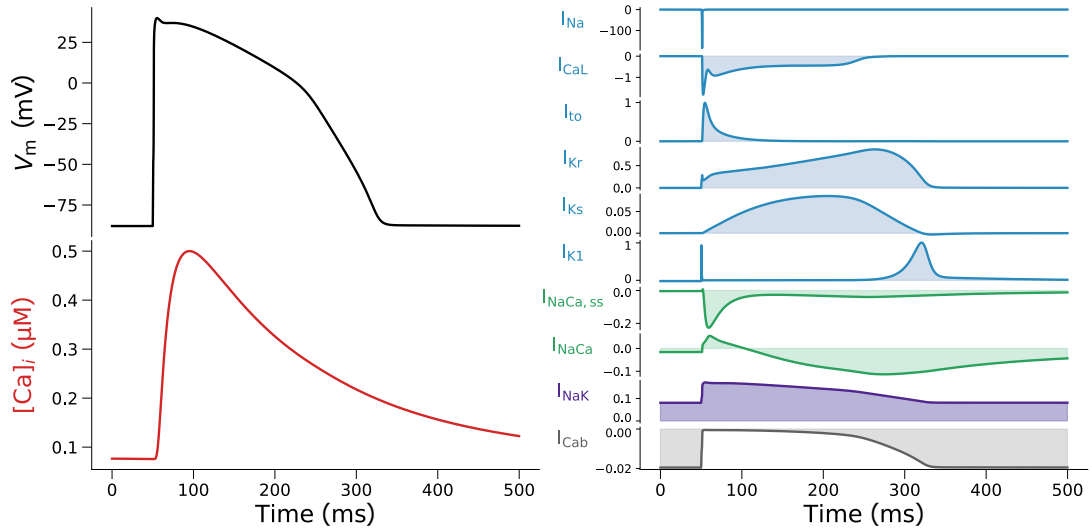

Figure 2.2: The action potential and the ionic currents simulated with the model by O'Hara et al. (2011). **(Left)** The action potential (black line) represents the transmembrane voltage dynamics of an epicardial (outer layer of) ventricular cell (top panel); shown along with the calcium transient (red line) which controls the contraction of the cell (bottom panel). **(Right)** Shows the major currents that contribute to the action potential. Each current exhibits distinctive dynamics and contributes at different stages of the action potential. Currents conducted by ion channels are shown in blue, exchangers in green, and pumps in purple. Background (or leak) currents are shown in grey.

Phase 2. A plateau phase. The entry of calcium ions, *L-type calcium current* I_{CaL}, approximately balances the outward flow of potassium ions resulting in a plateau in the action potential. This also induces a release of calcium ions from the *sarcoplasmic reticulum* (SR), known as *calcium-induced calcium release* (CICR), which triggers the contraction of the cardiomyocyte (Bers, 2002).

Phase 3. A final repolarisation. The efflux of various potassium currents, such as the *rapid delayed rectifier current* I_{Kr}, the *slow delayed rectifier current* I_{Ks} and the *inward rectifier current* I_{K1} (Nerbonne and Kass, 2005), together with the reduction of I_{CaL}, bring the membrane voltage slowly back to the resting potential.

Phase 4. An overall efflux of sodium and influx of potassium occur. This is needed to maintain homeostasis by recovering the cell to its initial state, in preparation for the next action potential.

The whole process of action potential formation is illustrated using a recent mathematical model simulation in Figure 2.2.

The transmembrane voltage dynamics depend on the phenotype of the cell, see Figure 2.1 (right). For example, atrial and ventricular myocytes maintain a stable resting potential during Phase 4 (after the repolarisation); whereas other cardiomyocytes, such as nodal type cells, possess the *pacemaker current* I_{f} which becomes active at hyperpolarised potential (DiFrancesco, 1993) , leading to spontaneous depolarisation. In all cell types, ion pumps and exchangers, such as the *sodium-potassium* (Na^+/K^+) *pump* and the *sodium-calcium* (Na^+/Ca^{2+}) *exchanger* (NCX), play an important

role in Phase 4 by restoring the concentration gradient in preparation for another action potential (Wang et al., 1996; Bers et al., 2003).

Here, only the major cardiac currents are described; for a detailed description, see for example Grant (2009).

2.1.2 Cardiac arrhythmia and disruption to the action potential

Disorders in cardiac electrical activity can induce serious and sometimes lethal disturbances in cardiac rhythm. Various factors can disrupt the action potential, for instance genetic mutations and external factors such as pharmaceutical compounds.

Genetic mutations can result in structural differences in ion channels, which alter the way that the channel conducts current and affect the action potential. For example, mutations of the fast sodium channel have been associated with Brugada syndrome (Kapplinger et al., 2010; Han et al., 2018) and type 3 Long QT[2] (LQT) syndrome (Roden et al., 1996). Similarly, mutations of the slow delayed rectifier current I_{Ks} and the rapid delayed rectifier current I_{Kr} contribute to two other major subtypes, LQT1 and LQT2, respectively (Shimizu and Antzelevitch, 1998; Curran et al., 1995).

External effects can also affect ion channel function. For example, anti-arrhythmic drugs typically bind to an ion channel, such as the fast sodium channel, the *human Ether-à-go-go-Related Gene* (hERG) channel (the alpha subunit of the ion channel that carries the current I_{Kr}), or the L-type calcium channel (Zipes and Jalife, 2009, Chapter 96). Anti-arrhythmic drugs alter the amount of current flowing through certain channels or change their opening/closing dynamics. Anti-arrhythmic drugs are intended to restore the action potential by altering the function of ion channels, but can also have unintended side-effects that cause even more severe types of arrhythmia (Nattel and Carlsson, 2006). Furthermore, non-cardiac drugs can have a similar unintended effect on ion channels, and increase the risk of arrhythmia. Therefore, it is important to find out potential side-effects any drug might induce *before* it is taken by patients — leading to the vital requirement of *cardiac safety testing* in drug development; we will shortly come back to this in Section 2.2.

2.1.3 Human stem cell-derived cardiomyocytes

For ethical reasons, human cardiomyocytes are rarely available and therefore are not routinely used in cardiac safety screening. Instead, one of the most promising alternatives is to use human stem cell-derived cardiomyocytes.

Stem cells are a type of cells that have not yet acquired a specific structure or function. Given the right stimuli, they can *differentiate*, i.e. undergo structural and functional changes to become specialised for a particular role. Human stem cells that can differentiate into cardiomyocytes are available from two sources: human embryonic stem cells (hESCs) and human induced pluripotent stem cells (hiPSCs).

[2] See Figure 2.1 that defines the QT interval of an ECG.

The first type of human stem cells, hESCs, were derived first by Thomson et al. (1998), and the first human embryonic stem cell-derived cardiomyocytes (hESC-CMs) were reported not long after by Kehat et al. (2001). However, the use of embryonic cells has raised ethical concerns (Holm, 2008). This is not the case for the other type of human stem cells, hiPSCs, which were first derived by Takahashi et al. (2007). These hiPSCs can be generated by harvesting fully differentiated and mature somatic cells from donors and reprogramming them to the pluripotent state. From this state, similarly to hESCs, hiPSCs can be differentiated into any type of cell. The first method to induce these hiPSCs into a cardiac lineage was developed by Zhang et al. (2009). The resulting cells are known as human induced pluripotent stem cell-derived cardiomyocytes (hiPSC-CMs).

Production of hiPSC-CMs has been improved to create a high yield of cardiomyocytes (Burridge et al., 2011; Mummery et al., 2012). There are well-established methodologies (Lian et al., 2013), although currently a lot of effort is dedicated to improving them. It has also been shown that hiPSC-CMs can even come from different sources of the same donor, for example dermal fibroblasts, peripheral blood mononuclear cells, etc., without their epigenetic memory resulting in a significant impact on their electrophysiology (Riedel et al., 2014). These advantages allow hiPSC-CMs to be used in many different applications, ranging from the study of human cardiac development to drug safety assays and cardiac tissue repair. Furthermore, unlike hESC-CMs, hiPSC-CMs are harvested from mature donors, which greatly increases their availability, can provide patient-specific cells, and therefore can be used in testing personalised treatments (Robinton and Daley, 2012; Shi et al., 2017).

However, these stem cell-derived cardiomyocytes usually take an "immature form of adult cardiomyocytes", both in terms of their electrophysiology and their physical structure (Synnergren et al., 2012; Lundy et al., 2013; Robertson et al., 2013; van den Heuvel et al., 2014), which has consequences for drug safety testing (Jonsson et al., 2012). Therefore we need tools to translate the measurements from these hiPSC-CMs to adult cardiomyocytes, as we discuss in the next chapter.

2.1.3.1 Electrophysiology

Human stem cell-derived cardiomyocytes share some important characteristics with adult cardiomyocytes. For example, in terms of gene expression, hiPSC-CMs show a pattern that is similar to adult cardiomyocytes (Kattman et al., 2011; Burridge et al., 2014; Bedada et al., 2016; Machiraju and Greenway, 2019). However, these stem cell-derived cardiomyocytes express different expression levels and isoforms of the ion channels, giving rise to different electrophysiological characteristics compared to adult cardiomyocytes. The differences in each ionic current between hiPSC-CMs and adult cardiomyocytes are reviewed in Chapter 3.

2.1.3.2 Physical structure and calcium handling

Adult cardiomyocytes have an elongated shape and are aligned within the cardiac muscle fibre, and are about 110–130 µm long and 30–40 µm in diameter (Ohler et al., 2009). However, not only is the average cell size of hiPSC-CMs smaller than the adult cardiomyocyte, typical diameters range from 10–50 µm, they also have a generally circular shape and a lack of aligned sarcomere structures (Gherghiceanu et al., 2011; Ma et al., 2011).

The transverse tubule (T-tubule) network in stem cell-derived cardiomyocytes is not fully developed (Lieu et al., 2009). Calcium handling in hiPSC-CMs is appreciably different to adult cardiomyocytes; the calcium subsystem in hiPSC-CMs is largely underdeveloped, and the CICR mechanism, the calcium buffering in the SR and the recycling of calcium by SERCA (sarco/endoplasmic reticulum Ca^{2+}-ATPase) are immature, as reviewed by, for example, Sedan and Binah (2011) and Blazeski et al. (2012).

2.1.3.3 Difference between cell lines

HiPSC-CMs not only differ from adult cardiomyocytes but also exhibit differences amongst themselves. Recordings of hiPSCs are usually variable across different labs (Cahan and Daley, 2013), and one major contribution to the variability in these hiPSC data is the variability *between* hiPSC lines, as reviewed by Ortmann and Vallier (2017). In the next chapter, we look at the necessity of studying the differences between cell lines for cardiac drug safety purposes.

The genetic background of the donors can be a dominant factor and result in functional differences (Rouhani et al., 2014; Choi et al., 2015; Carcamo-Orive et al., 2017; DeBoever et al., 2017). Since the genetic background of the donors is encoded in the hiPSCs, these hiPSCs have great potential to be used, for example, as a tool to investigate complex genetic mechanisms involved in disease, such as long QT syndrome (Moretti et al., 2010; Itzhaki et al., 2011a; Yazawa et al., 2011; Egashira et al., 2012; Terrenoire et al., 2013), catecholaminergic polymorphic ventricular tachycardia (CPVT) (Fatima et al., 2011; Itzhaki et al., 2012; Jung et al., 2012; Kujala et al., 2012), and arrhythmogenic right ventricular cardiomyopathy (ARVC) (Ma et al., 2013). Using hiPSC-CMs to investigate these mutations can provide crucial insights into cellular pro-arrhythmia mechanisms and the genotype-phenotype correlation of cardiovascular diseases (Moretti et al., 2010; Yazawa et al., 2011; Egashira et al., 2012; Jung et al., 2012; Kujala et al., 2012; Terrenoire et al., 2013).

2.2 Pharmaceutical Cardiac Safety Testing

Having now described the importance of cardiac drug safety testing and how hiPSC-CMs can be used for this purpose, we discuss the current and an upcoming safety guidelines for cardiac drug safety testing. This gives a strong motivation for the rest of the work presented in this thesis.

International drug safety regulations require that all newly developed compounds from any pharmaceutical company must be subjected to safety screening, a series of assays, before conducting any human trials for safety and efficacy testing of the compound. Functional assays have been developed to test whether a new compound binds to a particular ion channel. Other tests, for example *ex vivo* or *in vivo*, look at the effects of the drug on a single cardiomyocyte or cardiovascular tissue function.

2.2.1 Current safety guidelines

The International Conference on Harmonisation (ICH) agree and publish safety testing guidelines approved by all major national pharmaceutical regulators. Their S7A guidelines (ICH, 2001) established tests for adverse effects to the cardiovascular, nervous and respiratory systems. The

cardiovascular component of the ICH S7A guidelines recommended monitoring of blood pressure, heart rate and changes in the electrocardiogram. However, it has been recognised that changes in these quantities do not necessarily reflect high-risk ventricular arrhythmias. This led to the establishment of the current safety guidelines: the ICH S7B and E14 guidelines (ICH, 2005a,b).

The ICH S7B guidelines (ICH, 2005b) describe a preclinical evaluation focused on the potential for delayed ventricular repolarisation, as this is closely associated with arrhythmic risk (Yap and Camm, 2003). This includes an *in vitro* screen for block of the hERG channel which is now a standard procedure for testing each new small molecule compound. The hERG channel encodes the pore-forming alpha subunit of the ion channel $K_V11.1$ that conducts the rapid delayed rectifier potassium current, I_{Kr} (Sanguinetti et al., 1995). Reduction of I_{Kr} can prolong the ventricular action potential (Jurkiewicz and Sanguinetti, 1993), increase the QT interval on the body-surface electrocardiogram, and is associated with elevated risk of Torsade de Pointes (TdP) (Malik and Camm, 2001).

A variety of methods are used for ion channel screens. The gold standard for assessing ion channel function is the manual patch clamp technique. Automated platforms allow generation of ion channel data with high-throughput and turnover to facilitate drug development particularly in early screening phases, see a comparison in Section 2.4.1. These screens include testing on heterologous expression systems, where the hERG channel (or another) is expressed in, for example, Human Embryonic Kidney (HEK) or Chinese Hamster Ovary (CHO) cells. Following the *in vitro* I_{Kr} assay, an *in vivo* assessment of the QT interval in dogs, monkeys or guinea pigs is recommended. The QT interval is used to indicate the influence of the drug on repolarisation time (Fermini and Fossa, 2003).

The ICH E14 guidelines (ICH, 2005a), on the other hand, focus on the clinical (human) evaluation of the QT/QTc interval prolongation, in particular the "Thorough QT/QTc" study, where QTc interval is the heart-rate-corrected QT interval (Moss, 1993). Normally the trial uses randomised, placebo- and positive-controlled studies in healthy volunteers to evaluate the QT/QTc interval. One of the criteria requires that if the drug prolongs the QT interval by more than 10 ms, then further electrocardiogram studies are required in the later stages of safety testing (Shah, 2005). For further detail please refer to ICH (2005a).

Cardiac safety liability contributes to more than 25% of compound attrition at the preclinical testing stage (Laverty et al., 2011). However, these safety tests tend to give a high false positive rate, and are not rigorous enough to (a) understand fully the underlying drug mechanism and (b) provide translation of *in vivo* animal studies to human. Furthermore, the guidelines do not provide a clear route for using preclinical data to support clinical decisions. With the advent of computational modelling and novel assays using hiPSC-CMs, a new initiative for cardiac safety testing has been proposed: the Comprehensive *in vitro* Proarrhythmia Assay (CiPA) initiative.

2.2.2 The CiPA initiative

The CiPA initiative was proposed in 2013 to replace the current safety guidelines which focus on detecting delayed ventricular repolarisation. The proposed future cardiac safety tests have four components (Sager et al., 2014; Fermini et al., 2016; Gintant et al., 2016):

1. Investigate the functional effects of the compound on multiple human cardiac ion channels *in vitro*.
2. Reconstruct the action potential with the effects of the compound using an *in silico* (mathematical) model of an adult human ventricular cell.
3. Compare the expected effects of #2 using human stem cell-derived cardiomyocytes.
4. Use clinical ECG (electrocardiogram) readings with new ECG markers to check for any unexpected effects of the compound.

The first and last components revise and adapt the current safety guidelines. The proposed first component extends the current focus on the hERG channel to multiple ion channels; in addition to I_{Kr}, drug block of I_{Na}, I_{CaL}, I_{to}, I_{Ks}, and I_{K1} will be tested. The fourth component will replace the Thorough QT study in the current cardiac safety guidelines by examining any impact on the ECG in smaller-scale trials.

The third component uses the technological advantages of hiPSC-CMs, however, the experimental results from the hiPSC-CMs may not be directly comparable to that of adult cardiomyocytes nor their mathematical model in the second component, as discussed in Section 2.1.3. We therefore anticipate we would need mathematical models specifically designed for hiPSC-CMs to translate the results, though this is not a key part of CiPA. In the next section, we look at the theory of modelling for cardiac cellular electrophysiology that supports both the second component and the work presented in this thesis.

2.3 Mathematical Modelling of Cellular Electrophysiology

Mathematical modelling integrates our understanding of ion channel kinetics and cell behaviour in a quantitative fashion, and can serve as a powerful tool to predict system behaviour. The first biophysically-based mathematical description of an excitable cell was created by Hodgkin and Huxley (1952a), who modelled the action potential of squid giant axons (Hodgkin and Huxley, 1952b,c,d) as a *dynamical system*. Axons are part of neurons, which are excitable cells. Even though their structure and function are different from cardiomyocytes, the mechanisms underlying their action potential are closely related. The first mathematical model of cardiac cell electrophysiology was published by Noble (1960) and Hutter and Noble (1960).

2.3.1 The cell membrane as a circuit

The biophysical properties of the cell membrane can be expressed as an electronic circuit. The membrane of the cell separates and accumulates electrically charged particles, such as ions, on the two sides, it therefore can be described as a *capacitor* which has a capacitance $C_{\mathrm{m}} = Q_{\mathrm{m}}/V_{\mathrm{m}}$, where Q_{m} is the total charge separated by the membrane and V_{m} is the membrane potential. Ion channels, pumps, and exchangers allow ionic currents to flow across the cell membrane, and thus can be described as *variable resistors*. These variable resistors are driven by the electrochemical gradient and/or actively pump ions across the membrane, which can be described as connecting *batteries* in

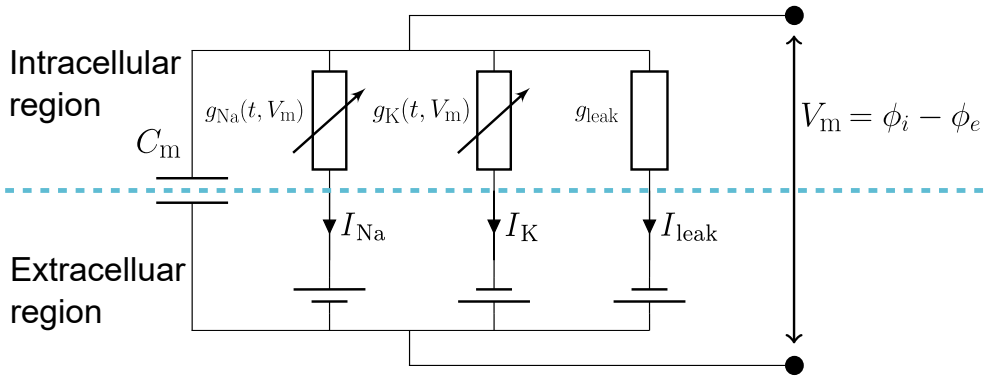

Figure 2.3: A circuit representation of the Hodgkin and Huxley (1952a) model. The cell membrane is illustrated as a cyan dashed line separating the intracellular and extracellular regions, which is represented as a capacitor with capacitance C_m. The currents carried by Na^+ and K^+ are represented as a pair of variable resistors, depending on the membrane voltage V_m, and are driven by a pair of batteries through the electrodiffusion process. Finally, a normal resistor and battery model the leak current in the cell.

series. Each pair of variable resistor and battery is then connected *in parallel* to the capacitor. In Hodgkin and Huxley (1952a), sodium and potassium currents, together with a leak current which accounted for the remaining ionic currents, were first considered. The resulting equivalent circuit is shown in Figure 2.3.

With this simplified model of the cell membrane and assuming C_m does not change over time, together with Kirchhoff's current law, it can be shown that the total current is

$$C_\mathrm{m}\frac{\mathrm{d}V_\mathrm{m}}{\mathrm{d}t} + I_{ion} = 0, \tag{2.1}$$

where I_{ion} is the total contribution of all ionic currents, $\sum_j I_j$, from each type j of the current. Therefore, we come to a dynamical description of the membrane voltage:

$$\frac{\mathrm{d}V_\mathrm{m}}{\mathrm{d}t} = -\frac{1}{C_\mathrm{m}}\sum_j I_j. \tag{2.2}$$

An external current I_stim can be added to the model to represent the stimulus current, which can be a stimulus from other cells or an artificial external stimulus, giving

$$\frac{\mathrm{d}V_\mathrm{m}}{\mathrm{d}t} = -\frac{1}{C_\mathrm{m}}\left(\sum_j I_j + I_\mathrm{stim}\right). \tag{2.3}$$

We now describe the formulation of the ionic current I_j.

2.3.2 Ion channel models

To model ionic currents I_j in Eq. (2.3), we often assume that their conduction is Ohmic (see Section 2.3.2.4 for a different assumption), that is Ohm's law $I_j = \Delta V_j / R_j$ holds, where ΔV_j is a difference in electric potential and R_j is an electrical resistance. By definition, we can equivalently use *conductance*, in units of Siemens, $G_j \equiv 1/R_j$ to describe the current. To model the voltage difference ΔV_j, we have to consider the driving force of the charge movement, which is a balance between electrical driving force and diffusion. This can be calculated by using the *Nernst equation*.

2.3.2.1 The Nernst equilibrium potential

The Nernst equation determines the induced potential difference under an ionic concentration gradient. Suppose we have a system containing two types of ion S and S'. Ion channels specific to ion S selectively allow ion S to pass across the membrane; while the other ions S' remain unchanged. At each instance, if the concentration of S on either side of the membrane is $[S]_i$ and $[S]_o$, and the electrical potential is ϕ_i and ϕ_o, then the Gibbs free energy of ion S is

$$\mathcal{G}_{S,i} = \mathcal{G}_S^0 + RT\ln([S]_i) + z_S F\phi_i, \tag{2.4}$$

$$\mathcal{G}_{S,e} = \mathcal{G}_S^0 + RT\ln([S]_o) + z_S F\phi_o, \tag{2.5}$$

for each side of the membrane: the intracellular and extracellular regions, which are denoted with subscripts i and o, respectively. The first term on the right-hand side of Eq. (2.4) and (2.5), $\mathcal{G}_S^0$, is the reference free energy, a constant, of ion S, the second term is the chemical potential, and the last term is the electrical potential of the system, where z_S denotes the valency of ion S, T the temperature, and R, F are the ideal gas constant and Faraday's constant, respectively.

The difference in free energy, $\Delta\mathcal{G}_S$, determines the preferential state of the system, driving the movement of the ion S, and is defined by

$$\Delta\mathcal{G}_S = \mathcal{G}_{S,i} - \mathcal{G}_{S,e} \tag{2.6}$$

$$= RT\ln\left(\frac{[S]_i}{[S]_o}\right) + z_S F(\phi_i - \phi_o), \tag{2.7}$$

where $(\phi_i - \phi_o)$ defines the membrane potential V_m. Therefore, by defining E_S as the membrane potential at which the net movement of ion S is zero, that is when the diffusion of S is exactly balanced by the electrical potential difference and hence $\Delta\mathcal{G} = 0$, then we arrive at the Nernst equation

$$E_S = \frac{RT}{z_S F}\ln\left(\frac{[S]_i}{[S]_o}\right). \tag{2.8}$$

E_S is known as the *Nernst potential* or *reversal potential*, as it determines the direction of the flow of ion S. Further details on the derivation can be found in, for example, Levine (1978) and Denbigh (1981).

2.3.2.2 Ionic current across the cellular membrane

If we consider a cell with only one type of ion channel which is selective for ion S, then the potential difference across the channel, i.e. the membrane voltage V_m, can be assumed to have two components: first, the potential drop due to concentration difference, given by Eq. (2.8); and, second, the potential drop due to the ion channel resistance $R_j I_j$, given the assumption of Ohmic ionic current. This gives

$$V_\mathrm{m} = R_j I_j + E_S, \tag{2.9}$$

for the ion channel that conducts current of type j and is specific to ion S. Rearranging Eq. (2.9) and replacing the reciprocal of resistance $1/R_j$ with conductance G_j, we obtain

$$I_j = G_j(V_\mathrm{m} - E_S). \tag{2.10}$$

2.3.2.3 Conductances are voltage-dependent

As described in Section 2.1.1, the ion channels of interest are mostly voltage-gated, and that means the conductance G_j is not constant but is voltage-dependent. The channel conductance can be expressed as

$$G_j = g_j f_j(V_\mathrm{m}, t \mid \boldsymbol{\theta}), \tag{2.11}$$

where g_j is the maximum possible conductance of the channels of type j. $f_j \in [0, 1]$ is the *open state occupancy* (also called *open probability*, see Section 2.3.2.5) that determines the *kinetics* (or dynamics) of the channels j. $\boldsymbol{\theta}$ is a vector of parameters that defines the function f_j.

This is a common way of expressing ion channel conductances. The form of f_j and the vector of parameters $\boldsymbol{\theta}$ vary across ion channels, and define the behaviour of the channels.

2.3.2.4 Non-Ohmic ionic current: GHK flux equation

The formulation given by Eq. (2.10) and Eq. (2.11) assumes the ionic current is Ohmic, which is a linear approximation to the transmembrane ionic currents. An alternative formulation is known as the *Goldman-Hodgkin-Katz* (GHK) equation which is a simplified solution of the *Nernst-Planck* equation (Hille, 2001).

The Nernst-Planck equation that describes the electrodiffusion process is

$$\boldsymbol{J}_j = -D_j\left(\nabla c_S + \frac{z_S F}{RT} c_S \nabla\phi\right), \tag{2.12}$$

where $\boldsymbol{J}_j$ (mol m^{-2}s^{-1}) is the flux density of the ion S through the channels of type j, D_j (m^{2}s^{-1}) the diffusion constant, c_S (mol m^{-3}) the concentration, and ϕ (V) is the electric potential. The first term on the right-hand side is *Fick's law* of diffusion; the second term is *Planck's equation* that describes the flow of ions driven by the electric field.

Suppose that the electrical field is constant throughout the membrane of thickness L (known as the *constant field approximation*) and that the flow of ions and the electric field are transverse to the membrane which reduces Eq. (2.12) to a one-dimensional problem. Also suppose that the cell membrane extends from $x = 0$ (the inside) to $x = L$ (the outside), then $\nabla\phi$ becomes $-V_\mathrm{m}/L$ with $V_\mathrm{m} = \phi(0) - \phi(L)$. The Nernst-Planck equation in Eq. (2.12) is reduced to

$$J_j = -D_j\left(\frac{\mathrm{d}c_S}{\mathrm{d}x} + \frac{z_S F}{RT} c_S \frac{V_\mathrm{m}}{L}\right). \tag{2.13}$$

Together with the boundary conditions for the concentration c_S, where $c_S(0) = [S]_i$ and $c_S(L) = [S]_o$, the solution to Eq. (2.13) becomes

$$I_j = P_j z_S^2 \frac{V_\mathrm{m} F^2}{RT} \frac{[S]_i - [S]_o e^{-z_S V_\mathrm{m} F/RT}}{1 - e^{-z_S V_\mathrm{m} F/RT}}. \tag{2.14}$$

This is known as the GHK flux equation (Goldman, 1943), where $I_j = J_j z F$ is the electrical current density through the transmembrane channel of type j, and $P_j = D_j/L$ is the *permeability* which defines the ease of crossing the membrane and is measured in moles per second. The GHK flux equation reduces to Eq. (2.8) the Nernst potential when the current is zero.

The permeability P_j can then be expressed, in a similar way to the conductance G_j in Eq. (2.11), as

$$P_j = \overline{P}_j f_j(V_\mathrm{m}, t \mid \boldsymbol{\theta}), \tag{2.15}$$

where $\overline{P}_j$ is the maximum possible permeability of the channel of type j.

Typical cardiac electrophysiology models contain a mix of GHK equation and Ohmic equation types of ionic current models. The choice of the model depends the model assumptions and the knowledge of the current: usually when there is an open pore that is selective for one kind of ion, then an Ohmic model is used; when there are multiple ions involved, for example as in an ion pump or exchanger, then a GHK formulation is used (Hille, 2001).

2.3.2.5 A note on stochasticity and single channels

In both Sections 2.3.2.3 and 2.3.2.4 the current I_j describes the current carried by *all* channels of a certain type. The current carried by an *individual* channel was first measured by Neher and Sakmann (1976), who found that single channels *open* (i.e. conduct current) and *close* stochastically. These single channels have open probabilities dictated by the energy landscape of the protein *conformations* (the spatial or structural arrangements of the protein by rotation of the atoms about single bonds). There are statistical and mathematical theories to model single ion channels, the most common models describe the process as *discrete-state continuous-time Markov process* (Gillespie, 1976).

The macroscopic current I_j with open state occupancy f_j therefore works by approximating the *proportion* of the stochastically-opening and closing single channels that are in an open state. The approximation relies on the number of single channels of type j in the cell to be large (Pullan et al., 2005); to approximate such stochastic behaviour well, Muench et al. (2020) predicted that it would require 10^3 to 10^4 channels. For example for I_Kr and hERG, the single channel conductance was estimated to be 2 pS at physiological ionic concentration (Veldkamp et al., 1995; Kiehn et al., 1996; Liu et al., 2004). The maximum conductance of I_Kr was estimated to be 7–18 nS (Ten Tusscher et al., 2004; O'Hara et al., 2011); the maximum conductance g_j of the macroscopic current is the total number of single channels of type j times the conductance of one single channel, hence the number of single channels conducting I_Kr in adult cardiomyocytes would be 4×10^3 to 9×10^3. Similarly, the maximum conductance of CHO cells over-expressing hERG was estimated to be 20–160 nS (Beattie et al., 2018; Lei et al., 2019a,b), which means the number of hERG channels would be 10^4 to 8×10^4 in the hERG-transfected CHO cells. Therefore modelling the macroscopic current using a deterministic approximation is usually sufficient.

2.3.2.6 Two common formulations of the open state occupancy

The two common formulations for the open state occupancy f_j are the *Hodgkin-Huxley model* formulation and the *Markov model* (also known as Markov states model) formulation.

The Hodgkin-Huxley model formulation uses the idea of independently varying channel '*gates*' to describe the open state occupancy f_j. These channel gates are modelled as dimensionless variables $\in [0, 1]$. Hence f_j is the product of one or more independent gating variables. For example, a

commonly used I_{Kr} model under the Hodgkin-Huxley model formulation is a combination of an 'activation' gate x_1 and an 'inactivation' gate x_2, with the open state occupancy given by

$$f_{\mathrm{Kr}} = \prod_k x_k = x_1(V_\mathrm{m})\, x_2(V_\mathrm{m}), \tag{2.16}$$

where both x_1 and x_2 are functions of V_m (see e.g. Ten Tusscher et al., 2004). Then the open state occupancy (x) and closed probability $(1-x)$ of a gate is modelled as

$$(1-x) \underset{\beta(V_\mathrm{m})}{\overset{\alpha(V_\mathrm{m})}{\rightleftharpoons}} x, \tag{2.17}$$

where α and β are the opening and closing rates (also known as the *transition rates*). This allows us to write down the rate of change of x as

$$\frac{\mathrm{d}x}{\mathrm{d}t} = \alpha(V_\mathrm{m})\,(1-x) - \beta(V_\mathrm{m})\,x. \tag{2.18}$$

This is often expressed in a slightly different form which has an explicit steady state value (x_∞) and a rate of approaching the steady state given by some time constant (τ_x):

$$\frac{\mathrm{d}x}{\mathrm{d}t} = \frac{x_\infty(V_\mathrm{m}) - x}{\tau_x(V_\mathrm{m})}, \tag{2.19}$$

where $x_\infty = \alpha/(\alpha+\beta)$ and $\tau_x = 1/(\alpha+\beta)$.

The opening and closing rates can be modelled using *transition state theory* to give

$$\alpha(V_\mathrm{m}) = A \exp\left(BV_\mathrm{m}\right), \tag{2.20}$$

$$\beta(V_\mathrm{m}) = C \exp\left(-DV_\mathrm{m}\right), \tag{2.21}$$

where A, B, C, D are constants at a given temperature. We discuss their temperature dependence form in Chapter 5.

To derive the rate of transition between two states, the occupancy of two states $p(a)$, $p(b)$ at equilibrium is assumed to follow a Maxwell-Boltzmann distribution:

$$\frac{p(a)}{p(b)} = \exp\left(-\frac{\Delta\mathcal{G}_{a,b}}{RT}\right), \tag{2.22}$$

where $\Delta\mathcal{G}_{a,b}$ is the Gibbs free energy difference between the a and b states, R the ideal gas constant, and T the absolute temperature. The Gibbs free energy $\Delta\mathcal{G}_{a,b}$ is assumed to be linearly proportional to the membrane potential V_m. Assuming a simple energy barrier model, where only one rate-limiting step is required to transition between two states, the transition rate is then directly proportional to the fraction of system in the excited state, which leads to the commonly-used exponential form in Eqs. (2.20) and (2.21), see e.g. Tsien and Noble (1969); Stevens (1978); Hille (2001).

The Markov model formulation[3], in contrast, explicitly describes the *kinetic states* of ion channels, which represent the changes in channel protein conformation as a means of predicting currents. This

[3]Note that this Markov model formulation is different from the Markov process mentioned in Section 2.3.2.5; here we are only interested in the dynamics of the probability which is deterministic.

formulation was proposed to overcome the limitation of the Hodgkin-Huxley model formulation, for example the independent gates assumption. In the Markov model formulation, Eq. (2.17) would be written as

$$\text{(closed) C} \underset{\beta(V_\text{m})}{\overset{\alpha(V_\text{m})}{\rightleftharpoons}} \text{O (open)}, \tag{2.23}$$

where the previous closed gate $(1-x)$ is now considered as one conformational state of the channel with a probability C, and the open gate is another conformational state with a probability O. Then Eq. (2.18) becomes

$$\frac{\mathrm{d}O}{\mathrm{d}t} = \alpha(V_\text{m})C - \beta(V_\text{m})O, \tag{2.24}$$

$$\frac{\mathrm{d}C}{\mathrm{d}t} = \beta(V_\text{m})O - \alpha(V_\text{m})C. \tag{2.25}$$

This can be rewritten as a general system of linear differential equations

$$\frac{\mathrm{d}\boldsymbol{u}}{\mathrm{d}t} = \mathbf{A}(V_\text{m}, t)\boldsymbol{u}, \tag{2.26}$$

where $\boldsymbol{u}$ is a vector of dynamical variables, the states, and $\mathbf{A}$ is a coefficient matrix, usually known as the *transition matrix*, defined by

$$\boldsymbol{u} = \begin{bmatrix} O \\ C \end{bmatrix}, \qquad \mathbf{A} = \begin{bmatrix} -\beta(V_\text{m}) & +\alpha(V_\text{m}) \\ +\beta(V_\text{m}) & -\alpha(V_\text{m}) \end{bmatrix}. \tag{2.27}$$

This Markov model satisfies the *state conservation law*, as the sum of all states (probabilities) is one. This implies that the columns of the transition matrix sum to zero, and that the dimensionality of the Markov model can always be reduced by one. The transition rates of the model are also required to obey the *principle of microscopic reversibility*[4], see for example Läuger et al. (1980); Läuger (1985); Rothberg and Magleby (2001); Colquhoun et al. (2004); Nagy and Tóth (2012). Finally, the open state occupancy of the channel is the sum of probabilities at open states:

$$f_i = \sum_k O_k. \tag{2.28}$$

The conversion from the Markov model to the Hodgkin-Huxley model is only possible when the Markov model has a particular symmetry, so the Hodgkin-Huxley model formulation is a special case of the Markov model. This is because the Markov model generalises by dropping the independent gate assumption.

In this thesis, we assume the model structure (the set of model equations) is known, either proposed, adapted, or taken from the literature with (theoretical) justifications. We are interested in finding the parameters of these equations that can describe experimental observations with physiologically-relevant meanings, see Section 2.6. Although we do not consider finding the 'correct' model structure in this thesis, in a publication that I led (Lei et al., 2020c), we discussed methods and considerations needed when calibrating models that are slightly wrong (known as *model misspecification* or *model discrepancy*, see also discussion in Section 2.7.2).

[4]This is also known as "detailed balance", and it requires that, in the absence of an external energy source driving the process, the rate of transition in each direction between *any* two states must be the same at thermodynamic equilibrium. This also means that time is reversible at equilibrium, and hence the name "microscopic reversibility".

2.4 Experimental Measurements of Ionic Currents

Electrophysiological models in the form of Eq. (2.3) have two observables, the voltage V and the current I. The first measurement of an action potential was in 1868, where an impulse propagation was observed in frog nerves by Julius Bernstein who invented the 'differential rheotome' (Schuetze, 1983). Later, in 1947, ionic currents were for the first time directly recorded using a feedback amplifier (a detailed explanation and mathematical model is presented in Chapter 6) which controls the membrane potential while simultaneously measuring transmembrane currents, and is now known as *voltage clamping* (Cole, 1968; Huxley, 2002; Verkhratsky et al., 2006). Such a system can also be used to observe the action potential by measuring the membrane voltage while injecting a stimulus current to the cell, known as *current clamping*, also see Hodgkin (1950).

Later, variations of the method discovered by Neher and Sakmann (1976) were developed, which are collectively known as *patch clamping*. One of these is known as the 'whole-cell patch clamp', see Figure 2.4A. During whole-cell patch clamp, a pipette is placed against the cell membrane and, by applying suction, pulls a small patch of membrane into the pipette to form a tight seal. The tight seal ensures only a very small amount of, if any, leakage current (also called the *leak current*) to flow between the pipette tip and the cell membrane. To allow electrical access to the interior of the cell, a second short burst of suction is applied to break through the membrane while having the cell remain attached. Both the extracellular and intracellular potentials can now be measured, and therefore the transmembrane voltage can be determined.

Voltage-clamp experiments are a common source of data for studying ion channels. This whole-cell voltage-clamp technique measures the overall transmembrane current. There are two main ways to distinguish and separate out individual currents. First, each individual current behaves differently,

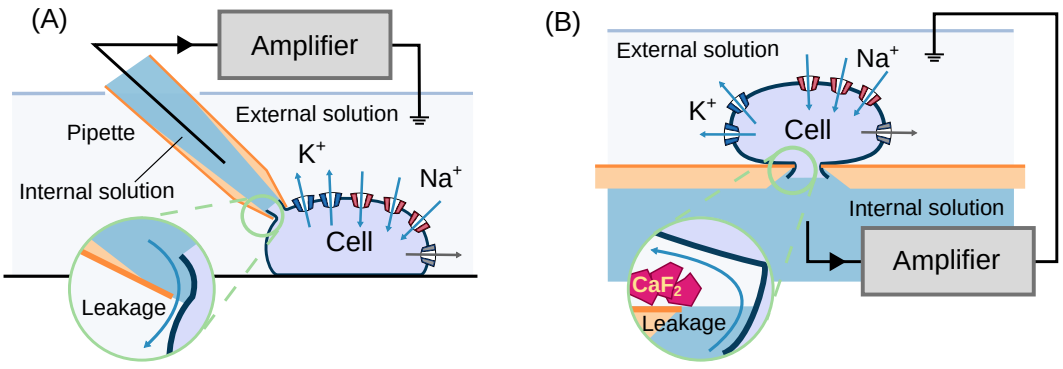

Figure 2.4: A schematic overview of the whole-cell patch-clamp experiment in a manual setup and an automated setup, adapted from a publication that I led (Lei et al., 2020b). **(A)** Shows the conventional manual patch-clamp, where a polished glass pipette is placed on the cell and suction is applied to form a tight seal. **(B)** Shows the planar design of an automated patch-clamp, where the cell is suspended on top of a micro-pore with the presence of a seal enhancer CaF_2. The grey box, amplifier, applies a command voltage to the cell through the feedback action of the input operational amplifier; a more detailed version of the setup is presented and studied in Chapter 6.

as each of them needs to take part in a different role and is hopefully uniquely identifiable during the action potential. Therefore, by varying the membrane voltage in different patterns, different and distinctive dynamics can be elicited. Second, each ion channel can be bound to different chemical compounds, known as *channel blockers*. Some of the channel blockers can be selective to a particular ion channel, which allows us to selectively inhibit one of the ion channels at a time, and hence we can deduce the dynamics of one particular type of current.

The current-clamp technique measures the membrane voltage of the cell. As described in Section 2.1.1, not all of the cells exhibit spontaneous excitation, many of the cardiac muscle cells require external stimulus (neighbouring cells in the heart) to generate action potentials. Therefore usually in a current-clamp setup, stimulus current is injected to the cell to cause excitation and generate an action potential. Unlike voltage clamping, where the dynamics of the voltage-gated ion channel currents are isolated (decoupled) by clamping the membrane voltage, in current clamping, the observed membrane voltage is the result of the complex coupling of the channel current dynamics. Therefore the current-clamp technique is usually not used as the tool for studying the dynamical behaviour of the ion channel current kinetics, but rather used to learn the missing pieces of this complex coupled system or the maximum conductances of the currents (see e.g. Johnstone et al., 2016b). However, the latter has been shown to be error prone if we do not have a complete understanding of each of the current kinetics (Lei et al., 2020c).

2.4.1 Modern experimental techniques: manual and automated setups

Whole-cell patch-clamp experiments can be performed using either manual control of a pipette's position or on automated high-throughput machines based on microfluidics. Manual patch is the conventional method, but it can be very time consuming and low-throughput; whilst automated platforms allow high-throughput recordings, which can be extremely useful for studies that require high numbers of measurements such as drug screening in the pharmaceutical industry (Elkins et al., 2013), as discussed in Section 2.2.

A schematic comparison of the two patch-clamp methods is shown in Figure 2.4. Manual patch-clamp uses a fire-polished glass pipette to form a tight electrical seal (~GΩ) between the pipette tip and the cell membrane. Although the composition of the ionic solutions in the pipette and bath depends on the type of experiments, these solutions are usually intended to be similar to the relevant physiological conditions. Automated platforms, on the other hand, usually have a very different configuration to manual patch, see Figure 2.4B; they use a design where the cells are suspended on top of a micro-pore on a planar surface. However, this planar design does not always yield as tight a seal (~ hundreds of MΩ) as the conventional manual patch-clamp. Seals can be enhanced in the presence of certain additional ions in the two solutions. For instance, a F^- containing internal solution together with a Ca^{2+} containing external solution has been used with manual patching (Tasaki and Takenaka, 1964; Kostyuk et al., 1975), and is used with many automated platforms (Kramer et al., 2020). The improvement of seal resistance with these solutions is thought to be due to the formation of CaF_2 crystals at the interface between the pipette or micro-pore and the cell, see Figure 2.4B inset; we discuss our findings of the (side-)effects due to the presence of CaF_2 in Chapter 4.

Many studies have compared manual patch clamping with automated patch clamping data, and showed that their performances are similar (Billet et al., 2017; Li et al., 2017b). In recent years many studies have begun to use automated patch-clamp systems to study ion channel electrophysiology (Li et al., 2017b; Vanoye et al., 2018; Gertler et al., 2019; Kang et al., 2019; Ng et al., 2020; Kozek et al., 2020; Toh et al., 2020), as well as the rest of this thesis.

2.5 Constructing Mathematical Models in Practice

In this section, we review the methods for constructing the mathematical models introduced in Section 2.3 using the experimental techniques described in Section 2.4.

2.5.1 A conventional approach

One typical way of studying the dynamics of the ionic current is through *summary statistics*. Hodgkin and Huxley (1952a), who proposed the first models of ionic currents, used these summary statistics to isolate and measure different aspects of ionic currents, for example time constants and voltage-dependent steady states. Following in their footsteps, many voltage-clamp protocols have been designed to highlight particular current kinetics. Typically, these protocols involve long sections during which the channels are brought into a particular steady state, before a brief interval during which a current is measured and then summarised using either a peak current or by fitting an exponential curve and deriving a time constant; we refer to these kinds of voltage protocol as the 'traditional' or 'conventional' protocols.

For example, the voltage-dependency of the inactivation steady state of an ion current is usually measured by holding a cell at a particular voltage which opens the ion channels, and then stepping the voltage up (Bendahhou et al., 1999). Then the voltage-dependency of the inactivation gating is elicited by plotting the normalised maximum current measured after each of the voltage steps against their respective voltages, known as the current-voltage (I-V) relation which is a type of summary statistic. Similarly, there are different typical voltage-clamp protocols for studying the voltage-dependency of the activation steady state, as well as for the voltage-dependency of the activation and inactivation time constants known as the τ-V relation.

Clerx et al. (2019a) summarises three different ways of using these conventional voltage-clamp measurements to characterise an ion channel kinetics model, in brief: (1) we can derive the steady state and time constant values in Eq. (2.19) by directly fitting the model equations to the I-V or τ-V relations; (2) we can simulate the model using those conventional voltage-clamp protocols to derive the I-V or τ-V relations, then we can fit these simulated relations to the experimentally derived I-V or τ-V relations; (3) we can directly use the simulated current traces from these conventional voltage-clamp protocols to fit to the raw current trace measurements. It is shown that method (3), using the raw current traces, outperforms the first two methods in terms of accuracy of predicting unseen cases and computational efficiency.

By design, these conventional protocols focus on a single aspect of an ion current so several such protocols are needed to parameterise a model fully. We revisit improvements for these conventional protocols through *experimental design* in Chapter 4.

2.5.2 A note on typical model building process

Since the first mathematical model of cardiac cell electrophysiology was published by Noble (1960), over two hundred models of cardiac electrophysiology have been published that collectively aim to capture the full complexity of cardiac cellular behaviour under a broad range of experimental conditions. Successive generations of models have often been built by partially 'tuning' parameters from the older generations to 'fit' a new experimental situation, or simply by borrowing parameters that are difficult to determine from one model to another; see for example Section 2.5.2.1. The trouble with these model building processes is that they can sometime ignore the fact that these parameters were derived under different experimental conditions or even for different species. This problem was illustrated in a meta-analysis by Niederer et al. (2009) that showed how modern human ventricular models include parameters that have been inherited from studies in at least nine different species, covering at least six different temperatures between 12–37 °C. Even more challenging is adapting a model to incorporate for example a new current, or to represent a new cell type, species or temperature; some of these issues are discussed in Section 2.7.2.

We discussed the inefficiency of the conventional voltage-clamp protocols in the previous section. Therefore, one of the obvious but important questions to address is what experiments need to be performed for updating the parameters of the models? What should be a well-recorded process has often not been recorded in the literature and is now lost. In the rest of this thesis, we address parts of these challenges, for example: in Chapter 4, we design experiments to calibrate a hERG potassium channel; in Chapter 5, we show the challenges and issues of adapting a model to represent a new temperature; in Chapter 7, we use optimal experimental design techniques to design experiments for inferring ion channel densities.

2.5.2.1 An example: the building process of hiPSC-CM models

Human stem cell-derived cardiomyocyte models were constructed by reparameterising an adult cardiomyocyte model using human stem cell-derived cardiomyocyte data. The first model of hESC-CM model was by Paci et al. (2012), which includes the early and late stages of maturation. Then, based on the experimental dataset of hiPSC-CM from Ma et al. (2011), the earlier hESC-CM model was reparameterised to the Paci et al. (2013) model. Note that the data from Ma et al. (2011), and hence the Paci et al. (2013) model, is based on *only* one of the commercially available hiPSC-CM cell lines from Cellular Dynamic International (CDI, iCell). Therefore the model does not capture the variability *between cell lines* discussed in Section 2.1.3.3.

Figure 2.5 shows a schematic overview of the Paci et al. (2013) model. It includes a fast sodium current I_{Na}, a two-part leak (or background) current $I_{\text{Na,b}}$ and $I_{\text{Ca,b}}$. The potassium current consists of four different parts, and each of them exhibits distinctive dynamics, which is a common splitting as in the adult cardiomyocyte models (for example the O'Hara et al. (2011) model). Finally, it has a

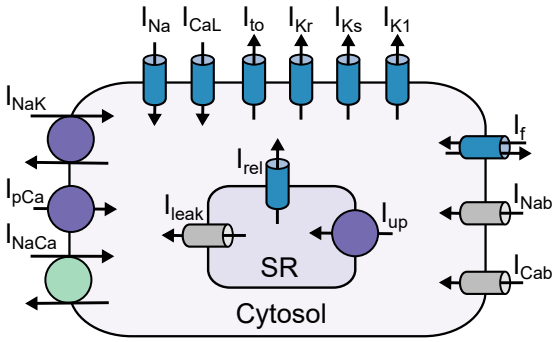

Figure 2.5: A schematic of a hiPSC-CM model (Paci et al., 2013). This model schematic reveals the structural immaturity of hiPSC-CMs, as it only has the main cytosol and the SR compartment which relates to Ca^{2+} storage and release. As in Figure 2.2, ion channels are shown in blue, pumps in purple, and exchangers in green. Background and leak currents are represented as grey channels. The arrows indicate the main direction of the current through the channels.

Ca^{2+} current I_{CaL}, together with several pumps and exchangers. The simple compartment structure shown in the schematic reflects the structural immaturity of these hiPSC-CMs.

The Paci et al. (2013) model provides both atrial-like and ventricular-like hiPSC-CMs versions (through differences in parameter values). Most of the membrane currents in the Paci et al. (2013) model are adapted from adult cardiomyocyte models such as the Ten Tusscher et al. (2004) (also known as the 'TNNP') model and the Grandi et al. (2009) model; while the calcium concentration in the SR compartment is adapted from the Paci et al. (2012) model. It has been used to investigate the electrophysiological differences between hiPSC-CMs and adult cardiomyocytes (Paci et al., 2015); it shows that the Paci et al. (2013) model (hiPSC-CMs) is more sensitive to I_{CaL} and I_{K1} than the adult cell model of O'Hara et al. (2011).

In the Paci et al. (2013) model, the spontaneous depolarisation is purely driven by the pacemaker-like current, the funny current I_f, which is thought to be unrealistic, as discussed in Section 2.1.3.1. Therefore, a recently published model by Koivumäki et al. (2018) takes the structural immaturity property of hiPSC-CMs into account and improves the calcium transient model of the Paci et al. (2013) model. Paci et al. (2018) also attempted to improve the Paci et al. (2013) model by refining the calcium transient model without the detailed spatial modelling as done in the Koivumäki et al. (2018) model. Jæger et al. (2020) attempted to 'mix-and-match' the human adult cardiomyocyte models (O'Hara et al., 2011; Grandi et al., 2010) with the Paci et al. (2013) model. Recently, Kernik et al. (2019) and Paci et al. (2020) also tried to incorporate different experimental data into the model building process.

2.5.3 Computational and numerical methods

To study the current or the membrane voltage, we need to solve the nonlinear coupled differential equations in Eq. (2.10) or Eq. (2.3). However, there is no simple general analytical solution for these differential equations unless we are at a fixed voltage. Computational modelling enables us to simulate and visualise the complex coupling and interaction between the ion currents; see e.g. Figure 2.2 showing the solutions (current and voltage) of the O'Hara et al. (2011) model.

Numerical methods for solving differential equations are rooted in the explicit forward-Euler method from 1768 (Brezinski and Wuytack, 2012). After which many different numerical schemes have been developed, such as the Runge-Kutta method. However, the system of equations in cellular electrophysiology is stiff (Cooper et al., 2015), with variables changing over very different timescales. As a result, many higher-order adaptive explicit schemes are less beneficial due to stability issues. Implicit methods offer better stability but can be computationally intensive. As discussed in Clerx and Collins (2014) and Cooper et al. (2015), one of the best approaches is to use an implicit adaptive multi-step method such as CVODE (Hindmarsh et al., 2005). In this thesis, all the simulations were performed using CVODE through Myokit, a Python interface (Clerx et al., 2016).

The error tolerance of adaptive step solvers controls the accuracy of the numerical solution; the smaller the better, but the longer it takes to solve the equations. There are two types of tolerance in adaptive step solvers: an absolute tolerance that determine the accuracy when the solution approaches zero and a relative tolerance that controls the error tolerance relative to the size of the solution when the solution is large. Johnstone (2018, Chapter 4) showed that the tolerance of the solver can introduce numerical 'noise' (on the likelihood surface, see e.g. Eq. (2.33)) when we try to find model parameters. To avoid this issue, we set tolerances within the CVODE solver to `abs_tol` $= 10^{-8}$ and `rel_tol` $= 10^{-10}$ unless otherwise specified.

2.6 Finding the Model Parameters

Once a mathematical model $f(\boldsymbol{\theta})$ with a vector of parameters $\boldsymbol{\theta}$ has been decided and some data Y have been observed, we want to match the model output to the data to learn the parameters. That is, we want to ask at what parameter set does the model give a specific output that (in some way) best matches the data — the fundamental question that we have to come across in answering the research questions set out in this thesis. This process is known as an *inverse problem*, *model calibration*, or *model training* (see a list of similar terminologies in Lei et al., 2020c). Figure 2.6 shows the parameters that we are typically interested in determining through calibration, adapted from Whittaker et al. (2020), a recent review that I co-authored which discusses some of the practical aspects in detail. In this section, we discuss some of the theories behind model calibration.

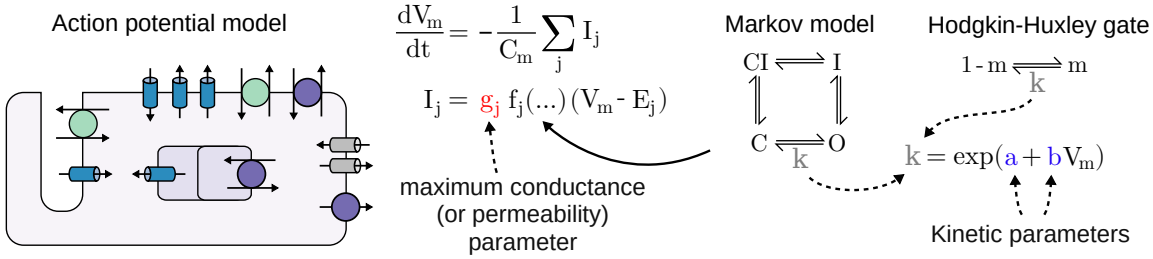

Figure 2.6: A schematic overview of cardiac electrophysiology models and parameters to calibrate. **(Left)** An action potential model contains submodels for its ion channels, pumps, and transporters. Typically the magnitude of each current type (maximum conductance or permeability) is the parameter of interest. **(Right)** Open state occupancy models determine the current kinetics as discussed in Section 2.3.2.6. Usually the parameters of these rate coefficients are the parameters of interest. Adapted from Whittaker et al. (2020).

Frequentist statistics

One way of finding the parameters is to minimise the difference between the data and the simulation using some measure g such as the sum of square differences:

$$\hat{\boldsymbol{\theta}} = \underset{\boldsymbol{\theta}\in\boldsymbol{\Theta}}{\operatorname{argmin}}\, g(\boldsymbol{\theta}) = \underset{\boldsymbol{\theta}\in\boldsymbol{\Theta}}{\operatorname{argmin}} \sum_i \left(Y_i - f_i\right)^2, \tag{2.29}$$

where $\boldsymbol{\Theta}$ is the *parameter space*, and i indicates each data point in the dataset. This is known as the *method of least squares*. Alternatively we can maximise a likelihood $\mathcal{L}$

$$\hat{\boldsymbol{\theta}} = \underset{\boldsymbol{\theta}\in\boldsymbol{\Theta}}{\operatorname{argmax}} \prod_i \mathcal{L}_i(\boldsymbol{\theta} \mid Y_i). \tag{2.30}$$

The latter method is known as *maximum likelihood estimation*.

If we assume that the data Y_i can be modelled as

$$Y_i \approx y_i = f_i(\boldsymbol{\theta}) + \epsilon_i, \qquad \text{with } \epsilon_i \sim \mathcal{N}(0, \sigma^2), \tag{2.31}$$

i.e. independent and identically distributed (i.i.d.) Gaussian noise, and that we have K datasets, then the likelihood is given by

$$\mathcal{L}(\boldsymbol{\theta} \mid Y) = p(Y \mid \boldsymbol{\theta}) \tag{2.32}$$

$$= \frac{1}{(2\pi\sigma^2)^{K/2}} \exp\left(-\frac{\sum_{i=1}^{K} \left(Y_i - f_i\right)^2}{2\sigma^2}\right). \tag{2.33}$$

The i.i.d. assumption has recently been shown in some circumstances to be oversimplified (Lei et al., 2020c; Muench et al., 2020; Creswell et al., 2020), but is used mostly throughout this thesis.

Both of these two methods give a point (single value) estimate of the parameters $\hat{\boldsymbol{\theta}}$ in the parameter space. Although this can be easily expressed, the minimisation (or maximisation) problems — generally known as optimisation problems — are by no means easy to solve. We discuss numerical methods and approximations to these problems below, Section 2.6.1.1.

Bayesian inference

One can also use the *Bayesian* approach to perform statistical inference, where we no longer consider the parameters as some fixed values to be optimised but treat them as a vector of random variables described by some joint probability distribution. Considering the parameters as random variables enables us to model or quantify the uncertainty in the parameters (see further discussion in Section 2.7). To do so, we have to realise that in the likelihood Eq. (2.32), we have presupposed a cause (the model parameters) to derive the probability of a particular effect (the data). The central idea of the Bayesian approach is that we can reverse this relationship using Bayes' theorem:

$$\underbrace{p(Y \mid \boldsymbol{\theta})}_{\text{Likelihood}} \xrightarrow{\text{Bayes' theorem}} \underbrace{p(\boldsymbol{\theta} \mid Y)}_{\text{Posterior}}. \tag{2.34}$$

As stated by Bayes' theorem, we combine prior information of the model parameters $p(\boldsymbol{\theta})$ with the likelihood of the data given each parameter $p(Y \mid \boldsymbol{\theta})$, to obtain the posterior distribution of the parameters

$$p(\boldsymbol{\theta} \mid Y) = \frac{p(Y \mid \boldsymbol{\theta})p(\boldsymbol{\theta})}{p(Y)} \tag{2.35}$$

$$\propto p(Y \mid \boldsymbol{\theta})p(\boldsymbol{\theta}). \tag{2.36}$$

The denominator of Eq. (2.35) is known as the *marginal likelihood* of the model, or *model evidence*, and can be obtained by

$$p(Y) = \int_{\Theta} p(Y \mid \boldsymbol{\theta})p(\boldsymbol{\theta}) \, \mathrm{d}\boldsymbol{\theta}, \tag{2.37}$$

which is a constant. The marginal likelihood integrates over the parameter space, also known as the *support* in statistical terms when referring to a distribution. However, the marginal likelihood is not easy to compute in high dimensions (large numbers of parameters), see also Foster et al. (2020) a preprint that I co-authored. We therefore need methods to approximate the posterior distribution; computational methods to approximate posterior distributions are discussed below, in Section 2.6.1.2.

Ideally we would always describe the parameters using the probability (posterior) distribution. Some times we quote the *moments* or the mode (known as a maximum a posteriori (MAP) estimate) of the distribution[5]. For example, we may describe a parameter with its *mean* value, which is essentially a weighted (with the probability density function) mean in the Bayesian framework. We calculate this with the following integral:

$$\mathbb{E}(\boldsymbol{\theta} \mid Y) = \int_{\Theta} p(\boldsymbol{\theta} \mid Y)\boldsymbol{\theta} \, \mathrm{d}\boldsymbol{\theta}. \tag{2.38}$$

A point estimate can be dangerous to use without some measure of our confidence in the value. A useful measure of uncertainty is the variance of the parameters:

$$\mathrm{Var}(\boldsymbol{\theta} \mid Y) = \int_{\Theta} p(\boldsymbol{\theta} \mid Y) \left(\boldsymbol{\theta} - (\mathbb{E}(\boldsymbol{\theta} \mid Y))^2\right) \mathrm{d}\boldsymbol{\theta}. \tag{2.39}$$

In terms of model prediction y_{pred}, the uncertainty in the obtained parameters can be easily forward propagated using the Bayesian framework. That is, we no longer provide a single prediction but a probability distribution:

$$p(y_{\mathrm{pred}} \mid Y) = \int_{\Theta} p(y_{\mathrm{pred}} \mid \boldsymbol{\theta}, Y)p(\boldsymbol{\theta} \mid Y) \, \mathrm{d}\boldsymbol{\theta}. \tag{2.40}$$

This is also known as the *posterior predictive distribution*. The first term of the integrand can be computed by

$$p(y_{\mathrm{pred}} \mid \boldsymbol{\theta}, Y) = p(y_{\mathrm{pred}} \mid \boldsymbol{\theta}) = \mathcal{N}(f(\boldsymbol{\theta}), \sigma). \tag{2.41}$$

The first equality is because the prediction (of the new scenario) y_{pred} is independent of the sample data Y; the second equality comes from the i.i.d. noise assumption in Eq. (2.31).

[5] Often these are called *summary statistics*, however, do not confuse these with those described in Section 2.5.1.

2.6.1 Computational methods

For the cellular electrophysiology described in this thesis, there is no simple analytical form for any of the equations above, therefore we need computational methods to solve them. A naive way of doing this is to perform a simple grid search by repeatedly evaluating all possible parameter values to find the optimum. If the model had one or two parameters, this could be a simple and intuitive approach. However, this method becomes impractical if each evaluation takes a considerable amount of time or the model is high-dimensional (e.g. number of parameters > 8). Typically, cellular electrophysiology models using the solver and setting as described above and running on a typical desktop (e.g. Ubuntu 20.04 using Intel^{R} Core^{TM} i7-6700HQ CPU running at 2.60 GHz) take $O(1)$ s[6] to complete one simulation. Even a simple ion channel kinetics model has about eight parameters (Beattie et al., 2018). All of these factors make it impractical[7] for us to perform a simple grid search for optimisation or to obtain the posterior distribution of the parameters. Therefore we need more sophisticated algorithms to solve the inverse problem, for either optimisation or sampling the posterior distribution.

In this thesis, all optimisation and sampling were performed using an open source Python package that I have co-developed, "Probabilistic Inference on Noisy Time Series" (PINTS, Clerx et al., 2019b) unless otherwise specified. PINTS is developed not only for cardiac electrophysiology, but for general statistical inference for dynamical systems and time-series problems. Unlike many other available inference software, PINTS provides many methods for optimisation and sampling, so that these can be tried easily and quickly within various statistical frameworks (likelihoods, prior distributions and measures of model fit). The design of PINTS also acknowledges the fact that dynamical systems can be difficult to solve, and that different numerical solvers can be beneficial for different problems (as discussed in Section 2.5.3), so expects users might already have spent months and years building a computational model (e.g. a simulation) of their problem. Therefore PINTS does not require users to re-implement their problems using a particular solver or software language, and all it requires is a Python wrapper for the forward simulation when given a set of model parameters to be inferred. The package provides a wealth of optimisation and sampling algorithms that are fully tested for their implementations; in the rest of this section, I will discuss some of the common algorithms for solving the inverse problem.

2.6.1.1 Searching for the optimum value

There are many optimisation algorithms that have been developed, which can be divided into sub-classes, such as linear/nonlinear programming, continuous/integer optimisations, convex/non-convex programming, etc. For the problems of interest in this thesis, we look for nonlinear, continuous, non-convex *iterative* optimisation methods; also, usually the derivative of our objective functions (either the error measure or the likelihood function) does not have a closed-form expression, although can be approximated by numerical methods such as finite differences.

[6] This is a very rough guide to the computational time needed, it heavily depends on the type of protocol, parameters, etc. that is being simulated as well as the machine being used. The bottom line is that it does not take milliseconds or hours to compute.

[7] Say if we want 10 grid per parameters for eight parameters taking 1 s per evaluation, it would take us 10^8 s, i.e. about 3.171 years to complete one search — just about the time needed to complete a D.Phil. degree at Oxford.

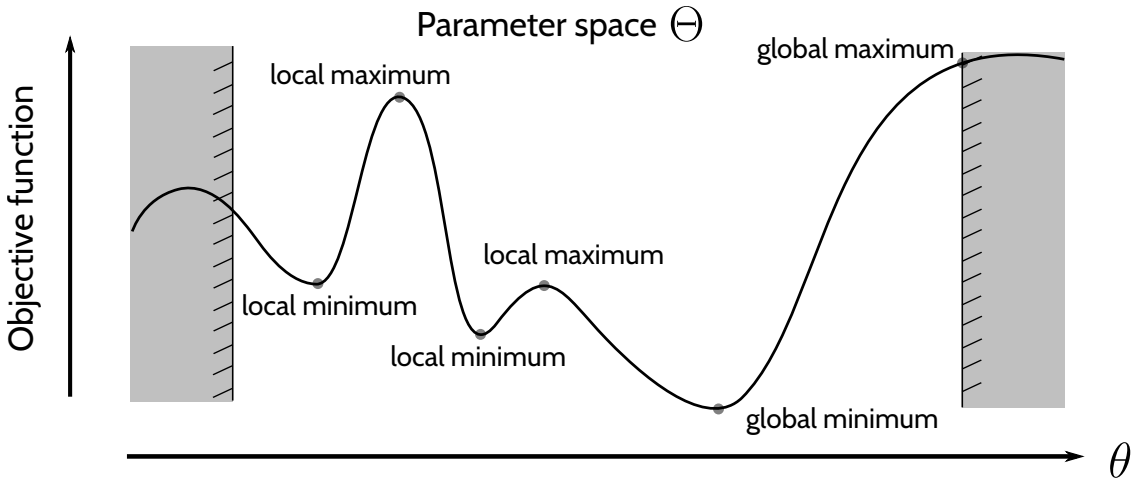

Figure 2.7: An illustration of the differences between a local optimum and a global optimum. The grey regions are outside the parameter space Θ, which are often called the boundary constraints in optimisation problems.

From a practical point of view, we divide the methods into local and global methods. A local optimisation in a minimisation problem seeks a point $\boldsymbol{\theta}^*$ such that

$$g(\boldsymbol{\theta}^*) \leq g(\boldsymbol{\theta}) \text{ for all } \boldsymbol{\theta} \in \boldsymbol{\Theta} \text{ near } \boldsymbol{\theta}^*. \tag{2.42}$$

A global minimisation searches for a point $\boldsymbol{\theta}^*$ such that

$$g(\boldsymbol{\theta}^*) \leq g(\boldsymbol{\theta}) \text{ for all } \boldsymbol{\theta} \in \boldsymbol{\Theta}. \tag{2.43}$$

Figure 2.7 illustrates the difference between the two types of optimum. Often we are interested in looking for the global optimum instead of a local one, however global optimisation is much harder and one of the challenges is determining whether the current best solution is a local or a global optimum.

One of the most simple iterative local optimisation algorithms is gradient descent invented by Augustin-Louis Cauchy in 1847 (Cauchy, 1847). This method suggests to take iterative steps proportional to the negative (or positive for maximisation) of the gradient (or derivative) of the objective function at the current point, until the next step is smaller than certain predetermined threshold. There are many other local (or convex) optimisation algorithms, such as line search algorithm, conjugate gradient methods, quasi-Newton method, etc. For further detail of the algorithms and convergence proof, see e.g. Kelley (1999); Boyd and Vandenberghe (2004); Andreasson et al. (2020). However, these traditional methods for local optimisation problems are not the best option for our problems.

In recent years, a number of nature-inspired optimisation techniques (or rather metaheuristics) have been developed to search for global optima. One example is the Genetic Algorithm which has been widely used in the field of cardiac modelling. The algorithm adapts the principle of Darwinian theory of survival of the best individual in the population through evolution operators such as selection, crossover, mutation, etc. However, Genetic Algorithms usually reach only close to the global

optimum but do not actually find the solution (Deb, 2000). Another famous example is the particle swarm algorithm first developed by Kennedy and Eberhart (1995). The algorithm is inspired by social and cooperative behaviour displayed by different species to widely explore the search space (Wang et al., 2018).

Another class of nature-inspired optimisation techniques is Evolution Strategies. Evolution Strategies are stochastic, derivative-free methods for non-linear, non-convex, continuous optimisation problems, which suits our problems of interest. A variant of Evolution Strategy that has been used extensively in the rest of the thesis is the Covariance Matrix Adaptation Evolution Strategy (CMA-ES) by Hansen (2006), as we found it to be particularly useful for our problems. In brief, the CMA-ES algorithm aims to find a multivariate Gaussian distribution $\mathcal{N}(\boldsymbol{m}, \eta^2 \boldsymbol{C})$ over the search space that is centred near an optimum. As the search proceeds, it (randomly) samples parameters from the current distribution and ranks the samples based on the objective function g, which in turn updates the multivariate Gaussian distribution (the mean $\boldsymbol{m}$, the covariance matrix $\boldsymbol{C}$ and the learning rate η) by giving higher weights to the samples with higher ranking. Akimoto et al. (2010) has shown that CMA-ES is closely related to one of the Natural Evolution Strategies (NES), the exponential (x)NES; for a review of the NES family of algorithms please refer to Wierstra et al. (2014). The theory of CMA-ES has yet to be fully understood. Akimoto et al. (2012) attempted to use an Information-Geometric Optimisation (IGO) framework (Ollivier et al., 2017) to explain the algorithm but only for a simplified version of the algorithm which does not provide the same performance as the original algorithm; for detail, please refer to Massenet (2019), a Masters thesis that I co-supervised.

2.6.1.2 Approximating the posterior distribution

As discussed in the beginning of this section, often we do not have a closed-form expression for the posterior distribution in Eq. (2.35); we therefore need methods to approximate the posterior distribution. Given the complexity of cellular electrophysiology models, no brute force method is feasible to approximate the posterior distribution (and its summaries). We therefore estimate these posterior distribution (and its summaries), indirectly, through *sampling*.

By drawing samples from the posterior distribution, we can learn many about its properties. For example, we can evaluate $\mathbb{E}(\boldsymbol{\theta} \mid Y)$ in Eq. (2.38) by drawing samples of $\boldsymbol{\theta}_i$, $i = 1, \ldots, n$, from the posterior $p(\boldsymbol{\theta} \mid Y)$ and then approximating

$$\mathbb{E}(\boldsymbol{\theta} \mid Y) = \int_{\Theta} p(\boldsymbol{\theta} \mid Y) \boldsymbol{\theta} \, \mathrm{d}\boldsymbol{\theta} \approx \frac{1}{n} \sum_{i=1}^{n} \boldsymbol{\theta}_i. \tag{2.44}$$

That is, the posterior mean of $\boldsymbol{\theta}$ is estimated by a sample mean. Ideally, we would like to draw *independent* samples from the posterior, however, this is not possible for our problems of interest. We therefore turn to *dependent* sampling methods.

One of the most widely used dependent sampling methods in computational Bayesian inference is Markov Chain Monte Carlo (MCMC)[8], first invented for use in physics in the mid twentieth century. As the name of the method family suggests, MCMC results in correlated consecutive samples, hence

[8] MCMC is named for generating a 'Markovian' (dependent) sequence of random variables.

we need more dependent samples than would be obtained independently. The difference in sampling efficiency between the two can be quantified by the *effective sample size*, see e.g. Gelman et al. (2013). We briefly introduce the concept of MCMC below that is used extensively in the rest of this thesis.

The essence of MCMC is that by starting the Markov chains at some random points $\boldsymbol{\theta}_0$ in the parameter space, and repeatedly stepping from $\boldsymbol{\theta}_i$ to $\boldsymbol{\theta}_{i+1}$ with a transition operator (also called the *transition kernel*, or *transition probability*) $T(\boldsymbol{\theta}_{i+1} \mid \boldsymbol{\theta}_i)$, the distribution of sampled values converges to a stationary distribution — in our case, the posterior distribution. The design of a MCMC algorithm is effectively to pick a transition operator that guarantees convergence of the distribution of sampled values to the stationary (target) distribution. Note that although the MCMC algorithm theoretically guarantees convergence, with a finite number of samples, the resulting distribution may not be converged (or well-mixed). One way of checking the convergence is using the Gelman-Rubin convergence statistic, often denoted as $\widehat{R}$, which compares variance in samples within and across multiple chains, for more details see Gelman et al. (2013).

A sufficient but not necessary condition for the existence of a stationary distribution is *detailed balance* (Robert and Casella, 2004), which requires that each transition $\boldsymbol{\theta}_i$ to $\boldsymbol{\theta}_{i+1}$ is reversible. The Metropolis-Hastings algorithm, one of the very well-known MCMC methods, designs the transition operator $T(\boldsymbol{\theta}_{i+1} \mid \boldsymbol{\theta}_i)$ based on detailed balance[9]. The algorithm breaks the transition into two steps: a proposing step and an accept-or-reject step. For each transition from the current sample $\boldsymbol{\theta}_i$, it first proposes the next sample $\boldsymbol{\theta}_{i+1}$ based on some proposal distribution $q(\boldsymbol{\theta}_{i+1} \mid \boldsymbol{\theta}_i)$, it then calculates the acceptance probability of the proposed sample based on

$$Pr(\text{accept} \mid \boldsymbol{\theta}_{i+1}, \boldsymbol{\theta}_i) = \min\left(1, \frac{p(\boldsymbol{\theta}_{i+1} \mid Y)}{p(\boldsymbol{\theta}_i \mid Y)} \frac{q(\boldsymbol{\theta}_i \mid \boldsymbol{\theta}_{i+1})}{q(\boldsymbol{\theta}_{i+1} \mid \boldsymbol{\theta}_i)}\right). \tag{2.45}$$

Here $p(\boldsymbol{\theta} \mid Y)$ is our posterior distribution, although the algorithm guarantees convergence for any arbitrary (stationary) distribution. Note that only the *ratio* of the posterior distribution is required (i.e. only Eq. (2.36) is needed), therefore this saves us from calculating the proportionality constant — the marginal likelihood denominator. Also, if the proposal function is symmetric, the second ratio term cancels; this is a special case known as the Metropolis algorithm. For more details, see Robert and Casella (2004).

In the rest of the thesis, we make heavy use of a variant of the Metropolis-Hastings algorithm, the Adaptive-Covariance Metropolis algorithm (Johnstone et al., 2016b; Haario et al., 2001). Here it uses a multivariate Gaussian distribution as the proposal distribution: $\boldsymbol{\theta}_{i+1} \sim \mathcal{N}(\boldsymbol{\theta}_i, \lambda\boldsymbol{\Sigma})$. One of the obvious issues with the Metropolis-Hastings algorithm is that if the proposal distribution is picked inappropriately, the chance of accepting the proposed sample will be very low, and hence the algorithm will not be able to move forward. The Adaptive-Covariance Metropolis algorithm tries to overcome this issue by self-adjusting the covariance of the proposal distribution (the rate λ and the covariance matrix $\boldsymbol{\Sigma}$) such that it can accept the proposed sample at certain prefixed rate. This

[9] Another condition that is needed is the uniqueness of stationary distribution which is guaranteed by ergodicity of the Markov process.

algorithm shows a strong link to the CMA-ES optimisation algorithm, and we found both of these algorithms are particularly useful for our problems.

For a more detailed explanation, see e.g. Robert and Casella (2004); Gelman et al. (2013); or a more accessible introduction, see e.g. Lambert (2018).

2.7 VVUQ: verification, validation, and uncertainty quantification

Since mathematical modelling and computational simulations are proposed as part of the future cardiac safety testing pipeline by the CiPA initiative (see Section 2.2.2), their accuracy and robustness must be thoroughly investigated and critically assessed. This leads to the ideas of *verification* and *validation* (VV) of computational simulations, which are generally defined in Section 2.7.1. Moreover, the current cardiac electrophysiology models produce a fixed prediction, as model parameters are generally assigned a fixed value; conversely, experimental recordings from real cardiac cells or other heterologous expression systems exhibit variability, including variability from one cell to another, known as *cell-to-cell variability* or *population variability*. The sources of uncertainty and how they are handled in the rest of this thesis are described in Section 2.7.2. Consideration of uncertainties in experimental data allows propagation of these uncertainties into model predictions, which leads to the study of uncertainty quantification (UQ). This is important for preclinical drug development, as it allows a better assessment of cardiac safety and enables a more efficient decision making process. Therefore the whole framework requires verification, validation, and uncertainty quantification (VVUQ). Finally, in Section 2.7.3, we review the current approaches and applications of VVUQ in cardiac modelling.

2.7.1 Definitions

Verification and validation together form a good basis of assessing the accuracy of the computational model. We adopt the definitions of verification and validation from Oberkampf et al. (2004):

> "*Verification: The process of determining that a model implementation accurately represents the developer's conceptual description of the model and the solution to the model.*"

> "*Validation: The process of determining the degree to which a model is an accurate representation of the real world from the perspective of the intended uses of the model.*"

The second half of this VVUQ paradigm is uncertainty quantification, which has become an indispensable part in assessing the credibility of computational models. We define it as the following:

> Uncertainty quantification: the process of determining the uncertainties and the impact of uncertainties in the model inputs (e.g. parameters and initial conditions) on the model outputs.

This definition of UQ can be divided into two stages:

1. *Uncertainty characterisation*: the concerns about the uncertainty in the model *inputs*. This process assigns probability distributions, or simple statistics such as means and variances, to input parameters, instead of single values, to characterise the uncertainty.

2. *Uncertainty propagation* (or *uncertainty analysis*): the concerns about the uncertainty in the model *outputs*. This process uses a probabilistic description to determine how uncertainty in model inputs results in uncertainty in outputs.

Note that all stages in the VVUQ process are intertwined, for example UQ improves the ability to perform validation while validation is needed after UQ. This VVUQ paradigm is widely used in many safety-critical applications, such as in the field of automotive, aerospace, nuclear, and structural engineering, as it forms a set of methodologies and frameworks for assessing the reliability and robustness of model predictions (Oberkampf and Roy, 2010; National Research Council, 2012). However, such a VVUQ framework has not been commonly employed or adapted in cardiac electrophysiology modelling, see Section 2.7.3.

2.7.2 Sources of uncertainty in cardiac modelling

The significance of UQ is clear because there are several potential sources of uncertainty in cardiac modelling. Here we discuss the sources of uncertainty described in Vernon et al. (2010) and Mirams et al. (2016) and how we handle them in this thesis:

Intrinsic variability is the temporal variability *within* the same cell that is caused by seemingly-random processes. For example, contributions from the stochastic opening of ion channels discussed in Section 2.3.2.5. In the rest of the thesis, we assume no stochastic processes in the macroscopic current.

Extrinsic variability refers to the variability across different cells of the same type. It is thought to be caused by quantities that generally vary from cell to cell, for example cell size or ion channel expression. We attempt to quantify this variability in Chapter 4 to Chapter 6. Extrinsic variability together with intrinsic variability are considered to be the *residual variability*.

Observational uncertainty addresses the uncertainty in experimental data, which includes *measurement errors* and lack of information. Measurement errors account for the errors from instrument noise or the patch clamp recordings, for example voltage artefacts or capacitance artefacts, this is investigated in detail in Chapter 6. Also, the uncertainty arising from the fact that typically only the total (or a mix of) ionic current is recorded (as mentioned in Section 2.4), represents lack of information.

Parameter uncertainty describes the uncertainty in model parameters. This can be contributed to by both the residual variability and observational uncertainty. In particular, lack of information can be one of the biggest issues, as cardiac electrophysiology models tend to combine different experimental results into one big model (Niederer et al., 2009). In this thesis,

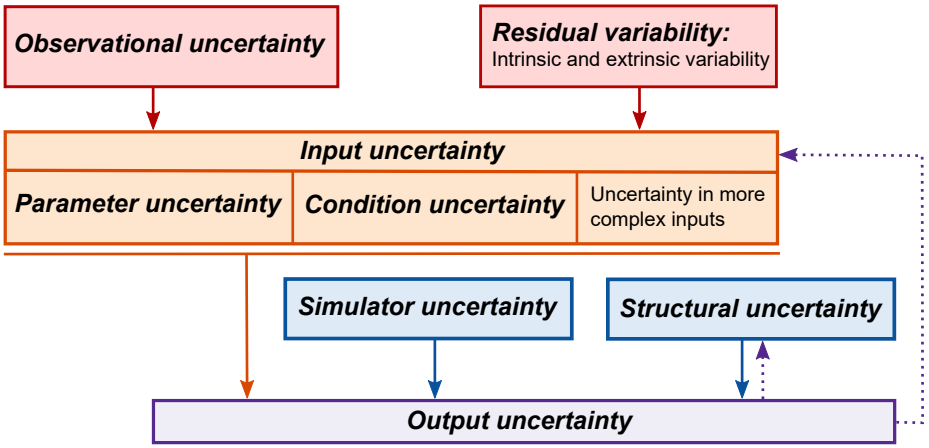

Figure 2.8: An overview of the hierarchy of the sources of uncertainty. From experiments to model input uncertainty, and how it is related to the output uncertainty. This hierarchy shows the how uncertainties propagate and where the interest of UQ lies. The dotted arrows show how the uncertainty in the model output can influence model calibration or learning of the model. Figure adapted from Mirams et al. (2016).

we therefore aim to build cell-specific models with a Bayesian approach to minimise and quantify such uncertainty.

Condition uncertainty accounts for the initial or boundary condition uncertainty. For example, in this thesis, initial conditions of the intracellular and extracellular ion concentrations and ion channel states are set by running the model into a steady state. However, we note that this might not represent the reality in the experimental setting, particularly for bigger models such as whole-cell action potential models.

Structural uncertainty (also known as *model discrepancy* or *model error*) represents the difference between a model and reality, i.e. the real physical system that it represents. An ion channel model approximates the biophysical dynamics of a population of proteins in a cell membrane, which may not be exact and the difference is accounted for by this structural uncertainty. This is studied and reviewed in Lei et al. (2020c), a recent publication that I led. We also study the consequences of this structural uncertainty in Chapter 7.

Simulator uncertainty deals with the errors associated with the approximation to the true solution of the mathematical model. This can be *numerical errors* introduced by for example discretisation in numerical methods, or errors from use of a *surrogate* model, for example an *emulator*, which approximates the outputs of a computational model that is expensive to solve. We do not use any surrogate model in this thesis, and this uncertainty has been studied in detail by for example Cooper et al. (2015) and Clerx et al. (2016), as discussed in Section 2.5.3.

Figure 2.8 shows the hierarchy of the sources of uncertainty, and how these contribute to input uncertainty and relate to output uncertainty. In practice, it can be difficult to isolate these sources of uncertainty. All of these can lead to a *parameter identifiability* issue, of which there are two types (Bellman and Åström, 1970; Raue et al., 2009; Villaverde et al., 2016), as defined below:

1. *Structural identifiability* refers to the *well-posedness* of the inverse problem for the parameters of a model, that is, whether the parameters of the model can be identified through its outputs or not. This depends on the model formulation. For example, let $y = x^{ab}$, where y is measurable (model output), x is a control variable, and a, b are parameters. The product ab can be identified but not a and b separately.

2. *Practical identifiability* refers to the possibility of determining the parameter values, with quantification of the uncertainty, when all sources of uncertainty are taken into account. This can be thought as an extension of structural identifiability, and allows consideration of the limitations caused by the quality or availability of experimental data.

2.7.3 Examples of VVUQ in cardiac electrophysiology modelling

This VVUQ approach has not been widely used in cardiac electrophysiology modelling until recently, as these models were not used in, or designed for, safety-critical applications such as cardiac safety assessment. However, since these models are now being used as part of clinical applications (Trayanova et al., 2012) and the drug safety assessment process (Mirams et al., 2014), which are safety-critical, it is important to also consider the confidence in or credibility of the model outputs (Li et al., 2020). Consequently, the application of VVUQ in cardiac electrophysiology modelling has become of interest (Geneser et al., 2007; Elkins et al., 2013; Pathmanathan and Gray, 2013, 2014; Pathmanathan et al., 2015; Johnstone et al., 2017, 2016a,b; Chang et al., 2017; Beattie et al., 2018).

Pathmanathan et al. (2015) is the first, to our knowledge, to perform formal UQ of the steady-state inactivation of the fast sodium current (I_{Na}). To study the inactivation dynamics of the I_{Na}, conventionally, the current-voltage relations are plotted (see Section 2.4) and a sigmoid function is fitted to the average of multiple recordings which then gives a set of 'best fit' parameters, termed as the 'population-averaged' approach. In Pathmanathan et al. (2015), the performance of this conventional population-averaged approach, and an 'individual-based' statistical method (*non-linear mixed effects* modelling) which also quantified the variation across cells, were compared, with a conclusion stating that the population-averaged approach "*can fail to capture the behaviour of any cell*".

Johnstone et al. (2016b) used a set of inference techniques within a Bayesian framework to quantify the ion channel maximum conductances $\{g_i\}$ in different cardiac models. This allows a quantification of uncertainties in cardiac action potential models and their conductance parameters, although residual variability, lack of information in observational uncertainty (see e.g. Chapter 6), and structural uncertainty (see e.g. Lei et al., 2020c, and Chapter 7) were not explicitly considered. Later, Johnstone et al. (2016a) and Johnstone et al. (2017) considered a part of the residual variability — extrinsic variability, where a hierarchical modelling technique was applied to synthetic action potential data and ion channel screening dose-response data.

This thesis further contributes to the methods for VVUQ as well as studying some of the major sources of uncertainty in cardiac cellular electrophysiology.

2.8 Conclusion

Having now described the background biological/physiological, mathematical, experimental, pharmacological, and statistical concepts that are concerned in the rest of this thesis, in the next chapter we look at our first attempt to tailor hiPSC-CM cell-line specific models with a method using a typical ideal kinetics assumption and conventional voltage-clamp protocols. The results of the next chapter act as a benchmark for the performance of hiPSC-CM cell-line specific models using the conventional methods; it also reveals the limitations of the methods which in turn motivates moving forward to experimental design and uncertainty quantification in the subsequent chapters.

Chapter 3

Tailoring hiPSC-CM Models: A Conventional Method

This chapter was published as: Lei, C. L., Wang, K., Clerx, M., Johnstone, R. H., Hortigon-Vinagre, M. P., Zamora, V., Allan, A., Smith, G. L., Gavaghan, D. J., Mirams, G. R., and Polonchuk, L. (2017a). Tailoring mathematical models to stem-cell derived cardiomyocyte lines can improve predictions of drug-induced changes to their electrophysiology. *Frontiers in Physiology*, 8:986.

Contributions: I performed all the mathematical modelling, data analysis, and interpretation of the results. Data were collected by the co-authors.

Overview:

This chapter presents an exploratory study of the reparameterisation of an existing cardiac action potential mathematical model from the literature to a new set of experimental data collected in an automated high-throughput system. In particular we apply this to human induced pluripotent stem cell-derived cardiomyocytes (hiPSC-CMs), as they have applications in disease modelling, cell therapy, drug screening and personalised medicine. Computational models can be used to interpret experimental findings in hiPSC-CMs, provide mechanistic insights, and translate these findings to adult cardiomyocyte electrophysiology. Different cell lines display different expression of ion channels, pumps and receptors, and show differences in electrophysiology. In this chapter, we use a mathematical model based on hiPSC-CMs from Cellular Dynamic International (CDI, iCell), and compare its predictions to novel experimental recordings made with the Axiogenesis Cor.4U line. It is shown that tailoring this model to the specific cell line, even using limited data and a relatively simple approach, leads to improved predictions of baseline behaviour and response to drugs.

Despite these improved predictions, this chapter also explores the limitations of a widely used approach and a commonly made assumption. The experimental data were obtained using what are referred to in this thesis as 'conventional'/'traditional' protocols. A detailed description and rationale of these conventional protocols is provided in Chapter 2; in brief, when designing the voltage-clamp experiments, following the

approach developed by Hodgkin and Huxley (1952a) who proposed the first models of ionic currents, often the experimental protocols involve long sections during which the ion channels are brought into a particular steady state, before a brief interval during which a current is measured. Due to the long duration of such protocols, it is impossible to apply them all in a single cell. The common assumption for re-fitting models to new experimental data, as we made in this chapter, is that the kinetics of the currents were perfectly described by a model created from previous experimental data, and only scaling the magnitudes of the currents is needed. We learn the limitations of the conventional methods and this 'perfect kinetics' assumption when applied to tailoring hiPSC-CM cell line models, which motivates us to develop novel information-rich experimental designs for studying current kinetics in the next chapter.

3.1 Introduction

In Chapter 2, we discussed the importance of human induced pluripotent stem cell-derived cardiomyocytes (hiPSC-CMs) as a promising alternative to human cardiomyocytes. Differentiation of hiPSCs into cardiomyocytes is a relatively well-established methodology (Lian et al., 2013), allowing hiPSC-CMs to be used in many different applications. In particular for drug screening and discovery, hiPSC-CMs can be used to evaluate proarrhythmic risk; hiPSC-CMs can be used as *in vitro* models that closely resemble human physiology and patient-specific conditions (Ebert et al., 2012; Mathur et al., 2015; Avior et al., 2016). Such *in vitro* studies have become more important for drug evaluation (Friedrichs et al., 2005; Pugsley, 2005; Lindgren et al., 2008; Giorgi et al., 2010) and the use of hiPSC-CMs in drug safety pipelines has been proposed as part of the U.S. Food and Drug Administration (FDA)-led Comprehensive *in vitro* Proarrhythmia Assay (CiPA) initiative (Sager et al., 2014; Ando et al., 2017).

However, as also discussed in Chapter 2, some care needs to be taken when interpreting the results of experiments on hiPSC-CMs, as many differences between hiPSC-CMs and adult cardiomyocytes still exist. For example, hiPSC-CMs have a smaller average cell size (Polak and Fijorek, 2012), lack T-tubules (Lieu et al., 2009) and have lower contractile force (Rodriguez et al., 2014). Their calcium handling machinery is underdeveloped, including changes to calcium-induced calcium release, buffering in the sarcoplasmic reticulum and recycling of calcium by SERCA (Blazeski et al., 2012; Sedan and Binah, 2011), although this is still under debate (Hwang et al., 2015). The expression levels of some ion channel genes also show some important differences. We further discuss the similarities and differences between hiPSC-CMs and adult cardiomyocytes for a few major currents in turn.

Fast inward sodium current (I_{Na}). I_{Na} and its channels in hiPSC-CMs share similar properties as those in adult cardiomyocytes (Ma et al., 2011). However, not only the expected $Na_V1.5$ ion channels that are native in cardiomyocytes but also neuronal $Na_V1.7$ channels have been detected in hiPSC-CMs (Moreau et al., 2017). Furthermore, modelling suggests that, due to the higher maximum diastolic potential and possibly the contribution of the funny current I_f to the action potential upstroke, the I_{Na} contribution to the upstroke is smaller than in adult cardiomyocytes (Jonsson et al., 2012; Goodrow et al., 2018). Although heterogeneity in the upstroke velocity of the action potential in

hiPSC-CMs has been observed (Pekkanen-Mattila et al., 2010), I_{Na} still plays a role in the conduction of the activation wave across tissue (Riedel et al., 2014).

L-type calcium current (I_{CaL}). The main properties of the I_{CaL} in hiPSC-CMs are similar to the ones in adult cardiomyocytes (Ma et al., 2011; Hwang et al., 2015). Although a degree of heterogeneity in the I_{CaL} current density has been observed: Ma et al. (2011) reported the current density to be at approximately $-17\,pA/pF$, which is slightly higher than adult cardiomyocytes; whereas a lower peak I_{CaL} values of around $-4\,pA/pF$ was observed in hESC-CMs (Sartiani et al., 2007).

Inward rectifier current (I_{K1}). I_{K1} shows noticeable differences between hiPSC-CMs and adult cardiomyocytes; unlike adult cardiomyocytes, hiPSC-CMs have little I_{K1} (Ma et al., 2011; Doss et al., 2012; van den Heuvel et al., 2014). Deficiency of I_{K1} causes a comparatively high maximum diastolic potential in hiPSC-CMs, as it is largely responsible for maintaining the resting potential in adult cardiomyocytes. Therefore, the action of other currents, for example the pacemaker current (I_f) and T-type calcium current (I_{CaT}), may result in spontaneous depolarisation in these hiPSC-CMs. The lack of I_{K1} indicates the immaturity of the hiPSC-CMs (Sartiani et al., 2007). To obtain a more adult-like electrophysiological response, attempts have been made to increase I_{K1} density by promoting the production of the $K_{ir}2.1$ ion channel protein (Lieu et al., 2013; Vaidyanathan et al., 2016), which is the I_{K1} channel protein, and by externally injecting simulated I_{K1} through the *dynamic clamp* technique (Bett et al., 2013; Verkerk et al., 2017).

Rapid activating delayed rectifier potassium current (I_{Kr}). The I_{Kr} observed in hiPSC-CMs is similar to that in adult cardiomyocytes, both in terms of the current density and activation kinetics of the channel (Ma et al., 2011). I_{Kr} has been observed in the majority of the hiPSC-CMs (Jiang et al., 2010; Honda et al., 2011; Ma et al., 2011; Doss et al., 2012). Given the low density of I_{K1}, I_{Kr} in hiPSC-CMs has been suspected to be involved in setting the maximum diastolic potential (Doss et al., 2012), which is not the case in adult cardiomyocytes.

Pacemaker (funny) current (I_f). The spontaneous depolarisation of hiPSC-CMs, and hence their spontaneous contraction (Ren et al., 2011; Elliott et al., 2011; Karakikes et al., 2014), is thought to be due to the presence of a strong I_f after repolarisation (Ma et al., 2011). Unlike adult cardiomyocytes, I_f does not appear in atrial and ventricular cardiomyocytes but only in pacemaker cells in sinoatrial and atrioventricular nodes. The activation of I_f can be affected by cyclic-AMP, by co-location of HCN4-Cav3 (Bosman et al., 2013), which is a funny current channel protein gene and Caveolin-3, and by the relative proportion of the other HCN isomers (Sartiani et al., 2007). However, the full role of I_f is still under debate in the literature, since the spontaneous activity can also be induced via the *calcium clock* (rhythmic spontaneous SR Ca^{2+} release) (Itzhaki et al., 2011b; Kim et al., 2015). The NCX exchanger, I_{CaL}, and I_{CaT} may also play an important role here (Itzhaki et al., 2011b; Kim et al., 2015).

Other currents. The remaining currents are thought to contribute less to the action potential than those described above. All of the other major types of ionic channels expressed in adult cardiomyocytes have been detected in hiPSC-CMs; this includes the slow delayed rectifier current I_{Ks}, the transient outward current I_{to}, and the T-type calcium current I_{CaT} (Jiang et al., 2010; Ma et al., 2011). These currents were found to have similar properties to those in adult cardiomyocytes, although I_{to} could not be separated into its fast and slow components (Ma et al., 2011). The pumps and exchangers, including the Na^+/K^+pump, NCX exchanger, Na^+/H^+ exchanger, and Cl^-/OH^- exchanger, have all been identified in hiPSC-CMs too, and were found to have similar kinetics as their adult counterparts (Fine et al., 2013).

The need to further understand these sub-cellular differences and to translate findings in hiPSC-CMs to adult myocytes, has driven studies to develop computational models of hiPSC-CMs as described in Chapter 2.

Each hiPSC-CM cell line is developed from a donor with a particular genetic background, using a specific set of protocols from differentiation to maturation. Besides the differences in hiPSC-CM and adult cardiomyocyte electrophysiology, differences between hiPSC-CM cell lines have also been shown (Du et al., 2015; Priori et al., 2013; Moran et al., 2014; Okano et al., 2013). Cell-to-cell variability of ion current characteristics within a single line of hiPSC-CMs was also observed (López-Redondo et al., 2016) as in adult cardiomyocytes. This property can have strong implications for our understanding of cell electrophysiology and prediction of drug effects (Mirams et al., 2016). Computational modelling can be used to understand and to quantify this intra- and inter-cell line variability, and to gain mechanistic insights into hiPSC-CM electrophysiology.

But how detailed does such modelling work need to be? Can a model based on one cell line be used to make inferences about another? How much, and what type of experimental data is needed to tailor a model to a new cell type, or even an individual cell?

In this chapter, we compare electrophysiological characteristics of the Cor.4U hiPSC-CM cell line (Axiogenesis AG, Germany) to a model by Paci et al. (2013), based on the Ma et al. (2011) studies of an hiPSC-CM cell line from CDI, iCell. First, we measured the maximum conductances of sodium, calcium and lumped outward currents in individual Cor.4U cells, and by comparing this to model predictions we attempted to infer the maximum conductances of the individual ionic currents. We focused on the maximum conductances of I_{Na}, I_{CaL}, I_{Ks}, I_{NaCa}. These maximum conductances were then used to tailor the Paci et al. (2013) model to create cell-specific models of 22 different Cor.4U cells. Using these tailored models to simulate action potentials, we found a variety of action potential waveforms exhibiting a high level of variability similar to that found in real hiPSC-CMs. We then optically measured action potential durations (APDs) in hiPSC-CM cultures under both control and drug-applied conditions, and found that – in most cases – tailored models predicted the resulting changes better than the original model. This suggests that the ion current composition differs between cell lines, and highlights the need to tailor *in silico* models to different cell lines to interpret drug-induced alterations to their electrophysiology. This chapter explores the limitations of the conventional protocols and the assumption that only maximum conductances are needed to be

fitted, and hints that more intricate methods are needed to characterise the current kinetics as we do in the next few chapters.

3.2 Methods

3.2.1 Current measurements in Cor.4U cells

Sodium, calcium, and lumped outward currents were measured in Cor.4U cells in the whole-cell patch clamp configuration using the Nanion SyncroPatch 96 platform (Nanion Technologies GmbH, Germany). The configuration of the automated patch-clamp setup is very similar to the one shown in Figure 2.4B. Sodium and lumped outward currents were measured using an intracellular solution containing (in mM) 50 KCl, 60 KF, 10 NaCl, 10 HEPES, and 20 EGTA (pH: 7.2), and a bath solution containing (in mM) 150 NaCl, 4 KCl, 1 $MgCl_2$, 1.2 $CaCl_2$, 10 HEPES, and 5 glucose (pH: 7.4). Calcium current recordings were made using an intracellular solution containing (in mM) 50 CsCl, 60 CsF, 10 TEA-Cl (a potassium current blocker), 5 HEPES, 10 EGTA, 4 Na2-ATP, 0.1 Na-GTP, and 0.1 cAMP (pH: 7.2) and a bath solution containing (in mM) 130 NMDG, 10 $BaCl_2$, 4 $CsCl_2$, 1 $MgCl_2$, 2 $CaCl_2$, 10 HEPES, and 5 glucose (pH: 7.4). All currents were recorded at room temperature.

For the sodium current measurements, cells were held at −80 mV and then stepped to potentials ranging from −60 mV to 60 mV with 10 mV increments, before returning to the holding potential. The step duration was 20 ms and the interval between steps was 5 s. The calcium current experiments used a similar protocol, but with 200 ms steps from −40 mV to 40 mV. The outward current was measured with 500 ms steps from −40 mV to 50 mV, with a 10 s interval between steps. All three protocols are illustrated in Figure 3.1.

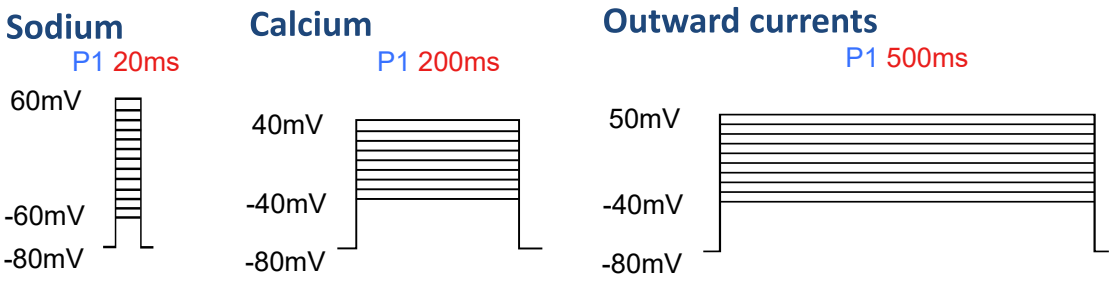

Figure 3.1: Voltage protocols used for sodium, calcium and lumped outward current measurements (not to scale). A 5 s waiting interval between pulses for sodium and calcium voltage protocols was used; with a 10 s waiting interval between pulses for outward current voltage protocol.

For the outward current experiments, we fitted directly to the experimental current traces (see Section 3.2.5). As discussed in Chapter 2, often during whole-cell patch clamp experiments, a leak current to ground occurs, which is introduced to the measured current, whenever the seal between a pipette and cell (or internal solution and cell in high-throughput machines) is not perfectly insulated from the bath (extracellular) solution. Therefore a leak current correction at voltage V was applied using $I_{\text{leak}} = V/R_{\text{leak}}$ where R_{leak} was the leak resistance estimated at the holding potential. Capacitance artefacts were filtered out by omitting the first 10 ms after each change in potential (see e.g. Ogden and Stanfield, 1994).

3.2.2 Patch clamp action potential measurements in hiPSC-CMs

Action potentials in iCell hiPSC-CMs (CDI, USA) plated on coverslips were measured in whole-cell patch-clamp configuration using a HEKA amplifier (EPC 10 USB Triple, HEKA Elektronik, Germany). Recordings were made using a pipette solution containing (in mM) 10 NaCl, 125 KCl, 1 $MgCl_2$, 10 HEPES, 0.1 Na_3GTP, 5 Mg-ATP, 5 EGTA (pH 7.2) and a bath solution containing (in mM) 150 NaCl, 4 KCl, 1.2 $CaCl_2$, 1 $MgCl_2$, 10 HEPES (pH 7.4). Cells were stimulated at a frequency of 1 Hz, for at least 50 cycles before recording.

3.2.3 Optical mapping action potential measurements in Cor.4U cultures

Action potentials were recorded from Cor.4U cultures with optical mapping using the CellOPTIQ electrophysiology platform (Clyde Biosciences Ltd). Cells were incubated in serum-free media at (30 ± 2) °C, and transiently loaded with voltage sensitive fluorescent dye di-4-ANEPPS (20 µL of stock solution 27 mM in ethanol; University of Connecticut Health Center). The loaded dye was then excited with a peak wavelength 470 nm LED, and the emitted fluorescence from the Cor.4U hiPSC-CMs was recorded at a sample frequency of 10 kHz. Measurements were performed before and after addition of Dofetilide, Quinidine, Sotalol and Verapamil at the concentrations shown in Table 3.1. Paracetamol was applied as a negative control.

A semi-automatic data analysis method based on the work of Wang et al. (2015) was employed to normalise the data. In short, heuristics were used to form an initial estimate of the start and end time of the action potential. The region just before the estimated upstroke was used to determine $V_{\text{normalised}} = 0$, while the 95$^{\text{th}}$ percentile of the data during the (estimated) action potential was used as $V_{\text{normalised}} = 1$. We then calculated the final APD_{90} and APD_{50} from this normalised signal, which were defined as APDs at 90 % and 50 % repolarisation, respectively.

3.2.4 Simulated experiments

Simulations of the patch clamp protocols were carried out using the model by Paci et al. (2013) that was described in Section 2.5.2.1. Initial intracellular and extracellular ion concentrations were set to the values used in the experiments. For the I_{Na}, I_{CaL}, and I_{outward} voltage clamp experiments,

IC50 [µM]	Dofetilide	Quinidine	Sotalol	Verapamil
I_{Kr}	0.0052 [a]	0.3 [b]	111.4 [d]	0.25 [d]
I_{Na}	147.9 [a]	16.6 [c]	7013.9 [d]	32.5 [d]
I_{CaL}	26.7 [a]	15.6 [c]	193.3 [d]	0.2 [d]
I_{Ks}	415.8 [a]	no significant effect	no significant effect	no significant effect
x [µM]	0.03, 0.1, 0.3, 1.0	0.01, 0.1, 1.0, 10	0.3, 3.0, 30, 300	0.01, 0.1, 1.0, 10

Table 3.1: Summary of the applied reference drugs which are a variety of multi-channel blockers, including the IC50 values for the corresponding ion channels, and the applied drug concentration (x). The IC50 data are from (*a*) Obejero-Paz et al. (2015), (*b*) Po et al. (1999), (*c*) Mirams et al. (2011), and (*d*) Kramer et al. (2013).

concentrations were clamped (corresponding to the buffering effects of the pipette), but for action potential simulations concentrations were allowed to vary following model equations. The temperature parameter in the model, which affects reversal potentials as well as I_{CaL} permeability and I_{Kr}, I_{NaK}, and I_{NaCa} kinetics, was set to 25 °C (298 K) to match the experimental temperature. Simulations were performed as described in Chapter 2. All codes and data are freely available online, see Data and Software Availability at the end of the chapter.

3.2.5 Estimating maximum conductances of individual ion currents

The maximum conductance of I_{Na} was estimated by scaling the I_{Na} conductance in the (Paci et al., 2013) model to match the peak current recorded experimentally with the sodium protocol ($n = 35$ cells), based on the assumption that the peak current is composed of I_{Na} alone. We tested this assumption by running a simulated experiment, where we observed that I_{Na} alone would reach 1.01× the initial inward deflection after each voltage step. So the peak is almost entirely due to sodium and only decreased slightly by the presence of other currents. Similarly, the recordings made with the calcium protocol ($n = 25$ cells) were used to directly infer the maximum conductance of I_{CaL}.

To estimate the conductances of the remaining major currents, we used the recordings made with the outward-current protocol ($n = 22$ cells). Using the hiPSC-CM model by Paci et al. (2013), we simulated the response to this protocol of I_{Na}, I_{CaL}, I_{K1}, I_{Kr}, I_{Ks}, I_{to}, I_f, and I_{NaCa}; see Figure 3.2. We then tried to find a weighted sum of these simulated currents that could replicate the measured signal. This was done by minimising the sum of square errors between measured and simulated current during the voltage steps, using the global optimisation method Covariance Matrix Adaptation Evolution Strategy (CMA-ES) as described in Chapter 2. The procedure was repeated for each of the 22 measured cells, resulting in a unique set of scaling factors per cell.

While this protocol was intended to find values for only the outward currents (such as I_{Kr}, I_{Ks}, and I_{to}) we chose to vary the inward currents I_{Na} and I_{CaL} in the optimisation to reduce the risk that

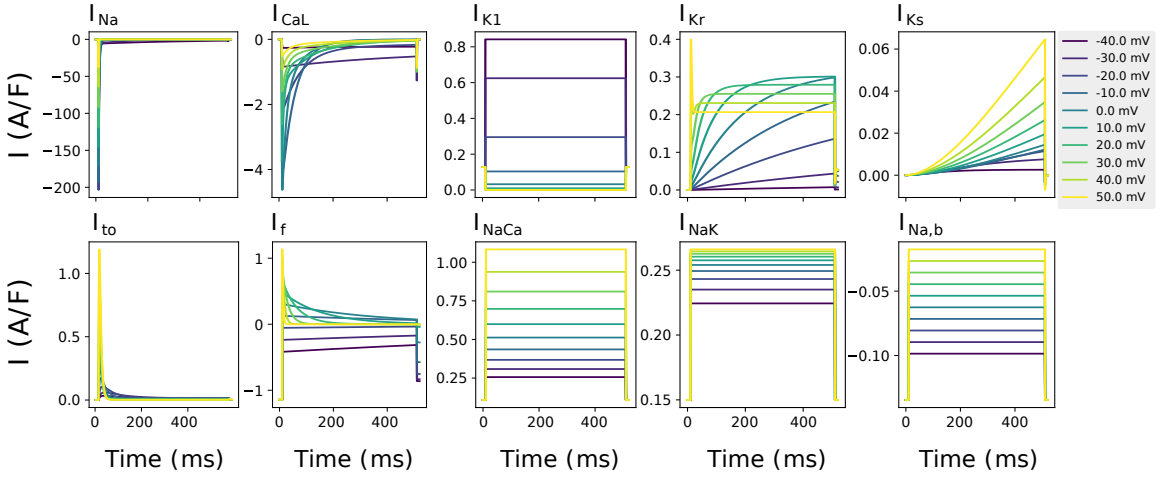

Figure 3.2: The major ionic currents in the (unaltered) Paci et al. (2013) model. All currents were elicited by 500 ms steps from a holding potential of −80 mV to step potentials of −40 mV to 50 mV with 10 mV increments (see Figure 3.1). Note that, because internal and external concentrations were held constant, I_{NaCa}, I_{NaK} and $I_{Na,b}$ show constant current at a given voltage.

any inward currents in the signal would erroneously be attributed to the outward currents (see e.g. Sarkar and Sobie, 2010). Note that we do not use these fitted I_{Na} and I_{CaL} conductances because we fit these from other dedicated experiments; they were included here just to yield more accurate outward current fits. After finding that the most prominent outward currents were I_{Ks} and I_{NaCa} (see Section 3.3.2), we ran a second optimisation with only I_{Ks} and I_{NaCa}: little change was observed, but we expect that fitting outward currents together with I_{Na} and I_{CaL} is likely to yield slightly more accurate results.

Convergence of the optimisation results was verified by repeating the process ten times, using different random seeds for each run. We found that the L^2 norm of the difference between the first and repeated scaling factor vectors was smaller than 10^{-5} for all 10 random starting points. To further verify the identifiability of the problem, we performed the same analysis on synthetic data (with synthetic noise), and were able to successfully infer the conductance scaling factors (see Figure 3.3 and Table 3.2). We note that this analysis assumes the kinetics of the currents have low model discrepancy, i.e. reflect the kinetics of the real currents well; this assumption has been commonly used, see e.g. Britton et al. (2013), Groenendaal et al. (2015), and Johnstone et al. (2016b). We further discuss this limitation in Section 3.4.4 and revisit this assumption later in this thesis, in Chapter 7.

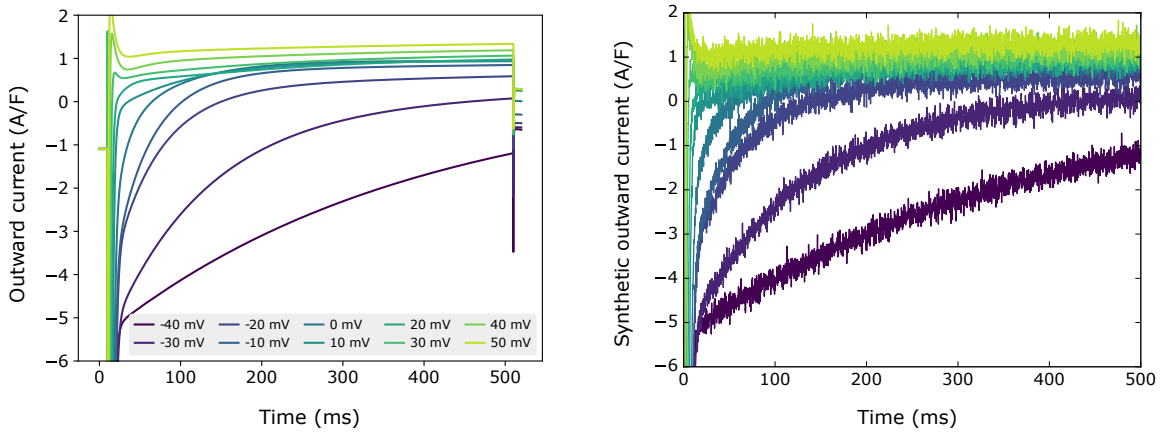

Figure 3.3: Simulated transmembrane current during the outward protocol (see Figure 3.1), calculated from the original (untailored) model. **(Left)** Without noise. **(Right)** With Gaussian noise of $\sigma = 0.15\,\mathrm{A/F}$.

Finally, to quantify the contribution of each current to the total outward current, we defined a contribution score c_i for each current I_i as

$$c_i = \frac{|I_{\text{final},i}|}{\sum_j |I_{\text{final},j}|}, \tag{3.1}$$

where $I_{\text{final},i}$ was defined as the current measured at the end of the final step of the outward-current protocol. This measure simply gives us a sense of the proportion of outward current that is contributed by each individual component during the end of the 50 mV step, but it is not used in tailoring the models.

3.2.6 Predicting the shape of the action potential

Next, the estimated maximum conductances were used to tailor the Paci et al. (2013) model to individual cells from the Cor.4U cell line. A total of 22 model variants were parameterised, corresponding

	Without noise		With Gaussian noise $\sigma = 0.15$ A/F	
Currents	scaling	contribution	scaling	contribution
I_{Na}	1.00	0.00	1.00	0.00
I_{CaL}	1.00	1.30	1.00	1.30
I_{K1}	1.00	0.00	1.01	0.00
I_{Kr}	1.00	15.05	1.01	15.18
I_{Ks}	1.00	4.70	1.21	5.68
I_{to}	1.00	0.09	1.06	0.09
I_{f}	1.00	0.00	1.01	0.00
I_{NaCa}	1.00	78.86	0.99	77.74

Table 3.2: Synthetic data study. We tested whether our outward current experiment theoretically contains enough information to retrieve the conductances that produced synthetic data from the original Paci et al. (2013) model under our outward protocol (see Figure 3.1), with and without noise (also see Figure 3.3). The scaling factors are taken with respect to the maximum conductance found in the original Paci et al. (2013) model.

to the 22 cells for which the outward current was measured. Since we found many currents were not discernible in the recorded outward current (see Table 3.3), we only applied the cell-specific scaling factors for I_{Ks} and I_{NaCa}. All tailored models used the same I_{Na} and I_{CaL} scaling factors, found in the inward current experiments which were measured in different cells and hence any covariance could not be accounted for. The remaining currents were left unchanged, as they are necessary for other cellular behaviour, such as homeostasis, even though they might not contribute strongly to the recorded outward current. Finally, Na^+, K^+, and Ca^{2+} evolve in time according to the Paci et al. (2013) model, to mimic the intact cell conditions of our optical mapping experiments.

These tailored models were then used to simulate baseline action potentials, as well as action potentials with drug perturbation. The effects of drugs on ion current maximum conductances were modelled using the Hill equation (Hill, 1910; Weiss, 1997)

$$f(x) = \frac{1}{1 + (x/\text{IC50})^h}, \tag{3.2}$$

where x denotes the concentration of the applied drug, IC50 is the inhibitory concentration 50 % value, h is the Hill coefficient, and $f(x)$ is a scaling factor for the maximum conductance that varies from 0 (full block) to 1 (no block).

For each cell and each drug, a model was created where the maximum conductances of the ion currents were scaled according to Eq. (3.2) using the IC50 values from Table 3.1 and a Hill coefficient of 1.0. For comparison, the same scaling factors were applied to an original model with the untailored conductance values from Paci et al. (2013).

In our optical mapping experiments, cells formed a spontaneously-beating and electrotonically-coupled monolayer. However, in this preparation not all cells beat at their spontaneous rates. Most cells will fire an action potential when triggered by an activation wave from their neighbours rather than spontaneously, and a relatively small region of (by definition) faster spontaneously-beating cells sets the pacing rate for the entire monolayer. Therefore, to mimic this effect, we paced the cells by

injecting a current of 5.6 A/F for 5 ms (I_{stim} in Eq. (2.3)) at the mean rates observed in the optical mapping experiments, for a given compound, to account for any action potential rate dependency. We used the cycle lengths of 1.375 s for Dofetilide, 1.176 s for Quinidine, 0.933 s for Sotalol, 0.905 s for Verapamil and 1.0 s for Paracetamol and all other experiments. To allow direct comparison with the optical mapping data, the simulated action potential was normalised using the same algorithm (see Section 3.2.3).

3.3 Results

3.3.1 I_{Na} and I_{CaL} in Cor.4U cells

Figure 3.4 shows the peak current-voltage (I-V) relationships for I_{Na} and I_{CaL}, measured in Cor.4U cells. The mean peak current in 35 cells (I_{Na}) and 25 cells (I_{CaL}) is plotted, as are the 25th and 75th percentiles. Compared to the prediction of the original Paci et al. (2013) model (created from iCell hiPSC-CM data), the experimental data show a lower amplitude of both currents in Cor.4U cells. We had to scale by a factor 0.69 to match the mean peak I_{Na}, and 0.80 to match the mean peak I_{CaL} recordings. The simulated I_{Na} peaked at the same potential as the experimental data, suggesting the activation kinetics of I_{Na} in iCell and Cor.4U cell lines are similar. The simulated I_{CaL} kinetics followed the Paci et al. (2013) model, and were left-shifted relative to experimental data. Further experiments established that this shift was due to a right-shift in the experimental I-V curve due to Ba^{2+} being present in the I_{CaL} voltage clamp experiment bath solution as shown in Figure 3.5, hence we do not adjust the kinetic terms and tailor only the maximum conductance.

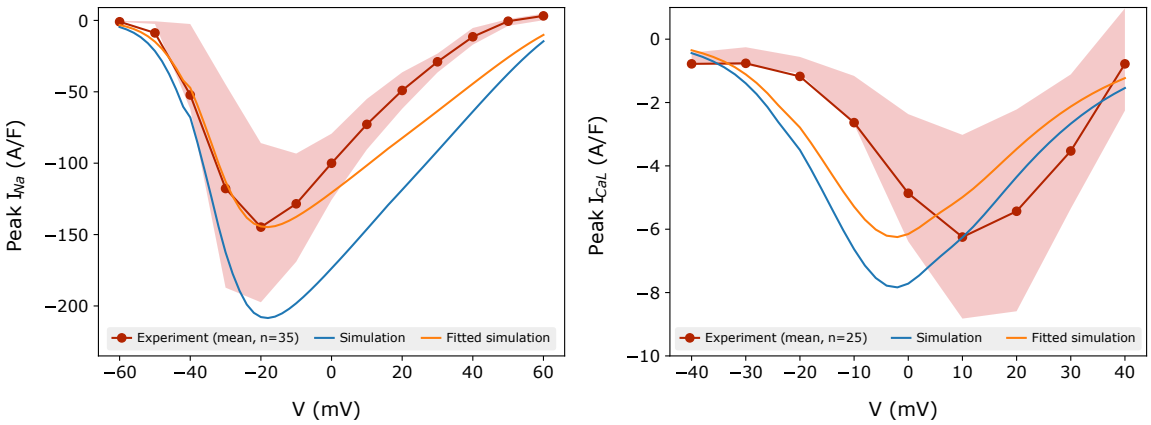

Figure 3.4: Current-voltage (I-V) relationship for I_{Na} (**left**) and I_{CaL} (**right**). The red lines represent the mean peak current measured experimentally in 35 (I_{Na}) and 25 cells (I_{CaL}), and the shaded areas show the 25th and 75th percentiles of the experimental data. The peak-current voltage relation simulated with the unaltered Paci et al. (2013) model for the same protocol is shown in blue. The orange lines show the simulated results after scaling to match the maximum current.

3.3.2 The outward protocol strongly elicits I_{Ks}

Figure 3.6 (left panel) shows the current measured with the outward-current protocol in a single Cor.4U cell. To analyse the composition of this current, we simulated the same protocol, and looked

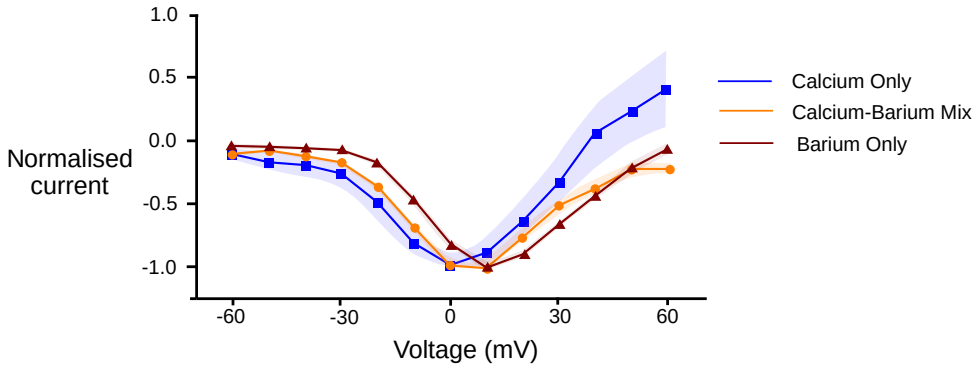

Figure 3.5: Normalised I_{CaL} I-V relationship, measured with Ca^{2+}, Ba^{2+}, and Ca^{2+}/Ba^{2+} solutions. Mean peak currents were $-3.1\,A/F$ (Ca^{2+} only, $n = 8$), $-2.7\,A/F$ (Ca^{2+}/Ba^{2+}, $n = 3$), and $-4.5\,A/F$ (Ba^{2+}, $n = 3$). The main experiments used in the this chapter were performed using a Ca^{2+}/Ba^{2+} mix, which can cause a shift in the kinetics towards more positive potentials. Since we used this data only to capture a scaling coefficient, this shift was not included in our tailored models. However, due to potential between-batch variability in hiPSC-CM, it was crucial that we performed all experiments in the same batch of cells, and so calcium-only data here (recorded later in a different batch of cells) could not be used.

for a sum of scaled transmembrane currents from the Paci et al. (2013) model that gave a similar result (see Section 3.2.5). We repeated this process for each of the 22 cells with measured outward current, and obtained the scaling factors s for each cell and current shown in Table 3.3. Note that the scaling factors s are *relative* to the original Paci et al. (2013) model. In many cases, the optimisation routine indicated that the kinetic profile of certain currents was not discernible in the measured outward current. This is indicated in the table with a dash (—) for any scaling factor smaller than than 10^{-10}. After seeing these results, as a comparison, we also tried fitting by varying only I_{Ks} and I_{NaCa} (and using the scaling factors for I_{Na} and I_{CaL} determined previously), and the results are similar as shown in Table 3.4.

For most cells, we found that the measured responses differed greatly, in both the shape and size of the currents, from the original model predictions (see Figure 3.3), leading to a poor quality of fit (see Figure 3.6 bottom). As a result, the best reconstructions of the simulated current relied almost entirely on a greatly amplified I_{Ks} current, along with a strong I_{NaCa}current, while other currents such as I_{Kr} and I_f were notably absent. Based on this, we might assume that I_{Ks} and I_{NaCa} are more strongly expressed in Cor.4U cells than in the iCell cells the Paci et al. (2013) model was based on. As an initial verification of these findings, we repeated some outward current measurements in the presence of Chromanol (an I_{Ks} blocker), see Figure 3.7 for an example where I_{Ks} is indeed significant. The near-zero contributions of other currents (e.g., I_{Kr}) does not imply that these currents are completely absent in Cor.4U cells, but instead suggests that the currents *as simulated from the model* could not be found in our recordings using the specified patch clamp protocol. This is a strong hint that changes to the kinetics of the currents will be required to accurately simulate the ion currents in Cor.4U cells at this temperature using the model by Paci et al. (2013). Such a mismatch in kinetics would also explain the large remaining errors between measurements and fit seen in Figure 3.6 (bottom), causing other currents, such as I_{Kr}, to be fitted as absent. This is discussed further in Section 3.4.4.

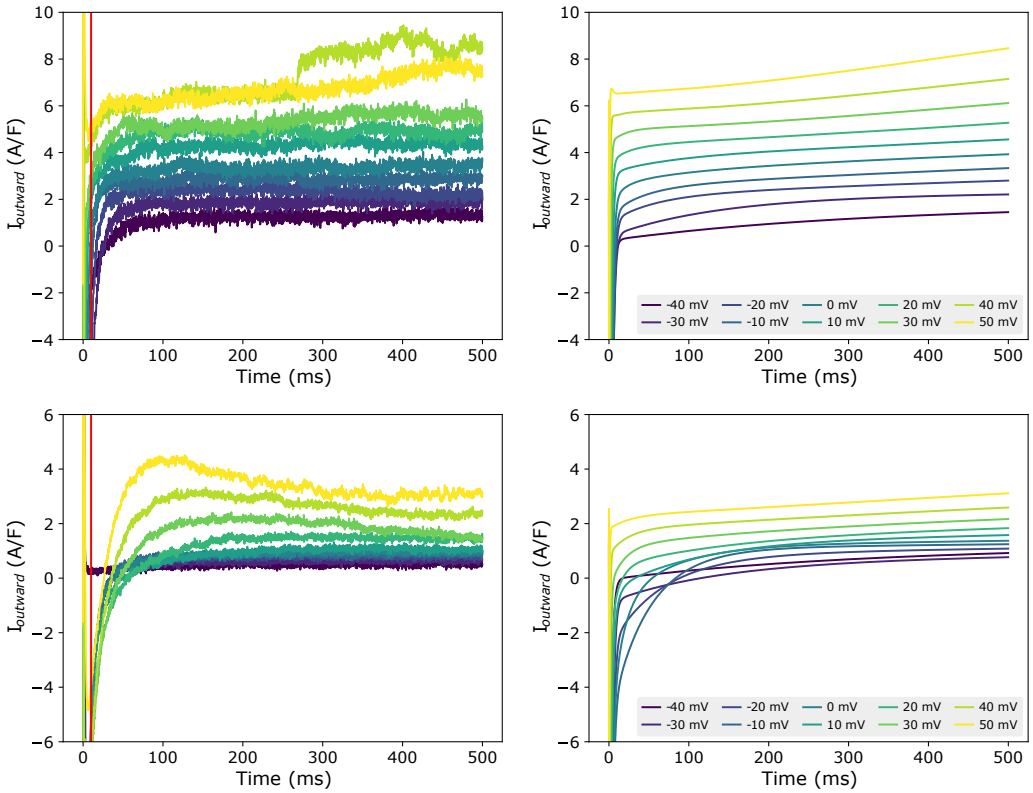

Figure 3.6: **(Left)** Experimentally measured outward current in cells #19 (top) and #20 (bottom) during the outward protocol. Data to the left of the vertical red (10 ms) was omitted to remove capacitance artefacts. **(Right)** Simulated transmembrane current during the same protocol, as set during the optimisation process for cells #19 and #20. Note that this figure includes *all* scaling factors set by the optimisation routine (see Section 3.2.5), including ones not included in the final tailored models (such as I_{Na} and I_{Kr}).

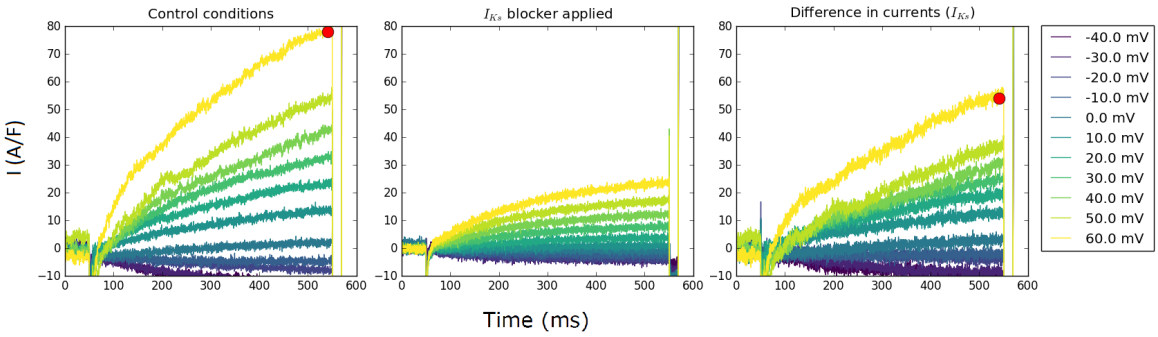

Figure 3.7: Recording of the transmembrane current of Cor.4U cell using the outward current protocol (see Figure 3.1). **(Left)** control conditions. **(Middle)** after drug application of 100 µM Chromanol (an I_{Ks} blocker). **(Right)** the difference in the traces which represents the Chromanol-sensitive current (predominantly I_{Ks}). The contribution score c for the measured I_{Ks}, calculated using Eq. (3.1) (i.e. ratio of the indicated red markers), is 69.2, which is indeed comparable to the averaged contribution score of the 22 tailored models 56.3 ± 20.8 (mean and standard deviation of the column c under I_{Ks} in Table 3.3).

3.3.3 Tailored models

We then created tailored models by modifying the original Paci et al. (2013) model in two ways: First, we scaled the maximum conductances of I_{Na} and I_{CaL} by a factor 0.69 and 0.8, respectively, to

	I_{NaCa}		I_{Ks}		I_{Kr}		I_{K1}		I_f	
Cell	*s*	*c*	*s*	*c*	*s*	*c*	*s*	*c*	*s*	*c*
1	3.32	28.5	139	71.2	—	—	—	—	—	—
2	2.08	21.2	129	78.5	—	—	—	—	—	—
3	7.55	50.3	125	49.5	—	—	—	—	—	—
4	21.1	43	467	56.8	—	—	—	—	—	—
5	6.89	29.9	270	70	—	—	—	—	1.18	—
6	9.3	42.4	211	57.4	—	—	—	—	—	—
7	0.951	29.6	37.6	69.9	—	—	—	—	—	—
8	1.54	56.7	19.5	42.8	—	—	0.118	0.000258	—	—
9	1.7	35.2	52	64.3	—	—	—	—	—	—
10	1.67	98.6	—	—	—	—	0.104	0.000362	—	—
11	0.38	16.7	31.5	82.5	—	—	—	—	—	—
12	0.696	38.2	18.6	60.9	—	—	—	—	—	—
13	3.05	25	153	74.7	—	—	—	—	—	—
14	1.28	14.7	125	84.9	—	—	—	—	—	—
15	1.19	34.1	38.3	65.3	—	—	—	—	—	—
16	3.02	51.4	47.3	48	—	—	—	—	—	—
17	2.35	59	27	40.4	—	—	—	—	—	—
18	4.03	32.7	138	66.9	—	—	—	—	—	—
19	5.74	73.4	28.9	22	1.84	4.5	0.513	0.000388	—	—
20	2.35	80.5	9.18	18.8	—	—	1.18	0.0024	—	—
21	3.77	40.2	93.7	59.6	—	—	—	—	—	—
22	13.9	44.6	288	55.1	—	—	—	—	—	—

Table 3.3: The scaling factors (s) and the relative contribution (c) of individual ion currents to the measured outward current in Cor.4U cells ($n = 22$). Values lower than 10^{-10} are shown as dashes (—). The scaling factors are taken with respect to the maximum conductance found in the original Paci et al. (2013) model. I_{to} values were lower than 10^{-10} for all cells. Because of the many low values for I_{to}, I_{Kr}, I_{K1}, and I_f, only the values for I_{NaCa} and I_{Ks} were used to create the tailored models.

match the averaged data from the inward current experiments. We then further modified this model to create 22 tailored models based on the 22 cells in which outward current was measured, by applying the I_{Ks} and I_{NaCa} scaling factors from Table 3.3.

3.3.4 Variability in $I_{outward}$ predicts variability in action potential

Significant variability in the outward currents was observed among the Cor.4U cells. This can be seen from the scaling factors in Table 3.3, but it is also evident when inspecting peak $I_{outward}$ in Figure 3.8.

Figure 3.9 (left panel) shows action potentials simulated with the tailored models. A wide variety of action potentials could be seen, with some models showing a spike-and-dome waveform, some showing a more triangular waveform, and with a varying slope in resting potential (leading to different degrees of auto-excitation). Some models also show beat-to-beat alternans, or fail to completely depolarise. The corresponding contribution of the major currents throughout the action potentials are also shown in Figure 3.10.

Recordings of action potentials in single hiPSC-CMs show a similar variety of action potential

	I_{NaCa}		I_{Ks}			I_{NaCa}		I_{Ks}	
Cell	s	s_{fix}	s	s_{fix}	Cell	s	s_{fix}	s	s_{fix}
1	3.32	2.08	139	163	12	0.696	0.338	18.6	19.6
2	2.08	1.19	129	144	13	3.05	1.93	153	174
3	7.55	6.04	125	156	14	1.28	—	125	150
4	21.1	16.8	467	571	15	1.19	0.621	38.3	44.9
5	6.89	6.15	270	281	16	3.02	1.68	47.3	74.2
6	9.3	7.3	211	255	17	2.35	1.73	27	35
7	0.951	0.58	37.6	38.9	18	4.03	1.86	138	187
8	1.54	1.28	19.5	18	19	5.74	6.44	28.9	16.2
9	1.7	0.958	52	63	20	2.35	1.93	9.18	13.3
10	1.67	1.06	—	6.89	21	3.77	3.12	93.7	102
11	0.38	0.0124	31.5	32.7	22	13.9	10.3	288	375

Table 3.4: The scaling factors (s) in Table 3.3 compared with the scaling factors (s_{fix}) which we only varied I_{Ks} and I_{NaCa} (and using the scaling factors for I_{Na} and I_{CaL} determined in previously), for I_{Ks} and I_{NaCa}. The scaling factors are taken with respect to the maximum conductance found in the original Paci et al. (2013) model. As shown, the scaling factors when varying only I_{Ks} and I_{NaCa} conductance are similar to those found when varying multiple currents.

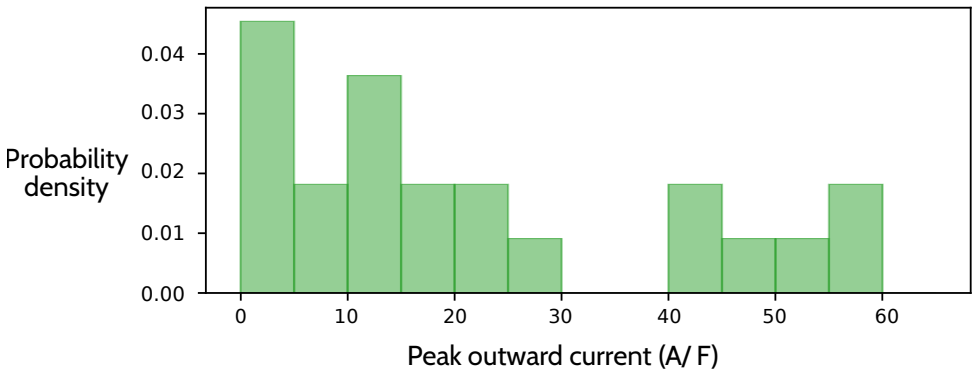

Figure 3.8: The distribution of peak outward currents in 22 cells. The current values are in A/F, showing the variability of the outward currents in terms of the current density.

waveforms. Figure 3.9 (right panel) shows action potentials measured in seven different iCell hiPSC-CMs. Again, various waveform morphologies (roughly corresponding to atrial, ventricular and sinoatrial node action potentials) and differing levels of auto-excitability can be distinguished. Whilst these recordings are for a different cell line than our tailored models, the inter-cell variability in channel expression within a batch of hiPSC-CMs has not been observed to be markedly different between cell lines (see e.g. the relative size of the 'error bars' in Figure 2 of Blinova et al., 2017).

3.3.5 Tailored models improve predictions of APD

Figure 3.11 (left panel) shows the median of all simulated traces as shown in Figure 3.9, along with the 25$^{\text{th}}$ and 75$^{\text{th}}$ percentiles. The optically recorded action potentials from the Cor.4U cells were plotted on the same graph (the median shown as black line and the 25$^{\text{th}}$ and 75$^{\text{th}}$ percentiles shown as grey shading). Due to the increased outward current, the tailored models exhibit a shorter APD than

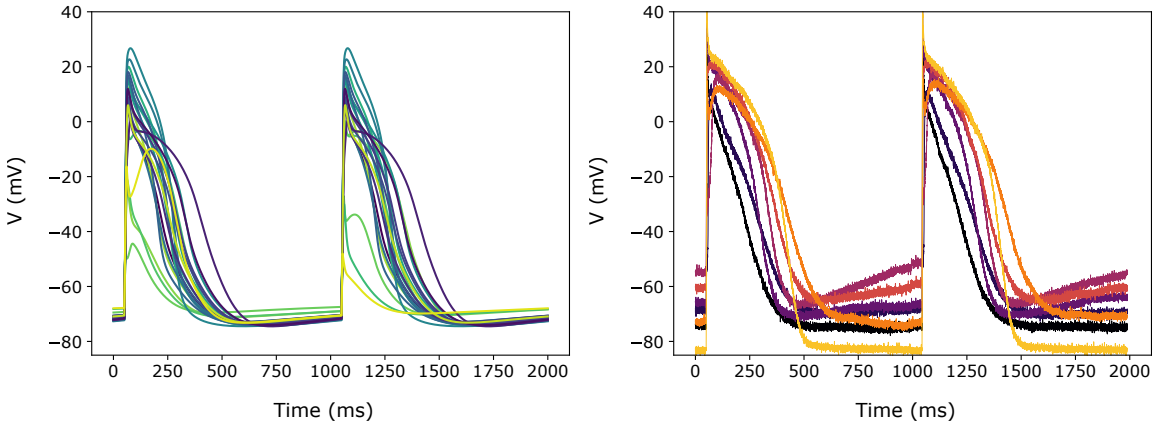

Figure 3.9: Predicted variability in the tailored action potential models is similar to inter-cell variability in a batch of hiPSC-CMs. **(Left)** Simulated action potentials from the 22 tailored cell-specific Cor.4U models exhibit a variety of action potential waveforms. **(Right)** Experimentally measured action potentials in seven individual iCell hiPSC-CMs also show significant variability.

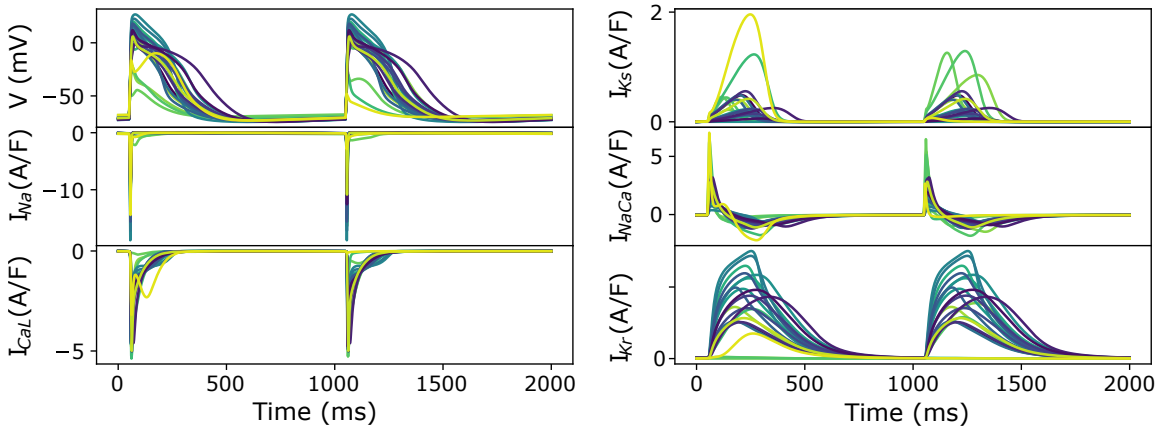

Figure 3.10: The corresponding contribution of the modified currents I_{Na}, I_{CaL}, I_{Ks} and I_{NaCa}, along with I_{Kr}, throughout the simulated action potentials for the 22 cells. Note that even I_{Kr} was not modified, because of the feedback of the membrane potential and ionic concentrations, it exhibits variability throughout the 22 cells.

the original model, that matches the measured APDs more closely in the early and late repolarisation phase. A histogram of APDs in measured and simulated cells is shown in Figure 3.11 (right panel), with the blue line representing the result from the original model.

3.3.6 Tailored models can give better prediction of drug block effects

Figure 3.12 shows the dose-response curves of the APD_{90} of four drugs, measured experimentally and simulated using the original and tailored models. Results for the control drug paracetamol show that the APD_{90} remains unchanged in the dose-response curves. For all four drugs tested, although not fitting the experimental data exactly, the tailored models match the measured data more closely than the original model. For Dofetilide in particular, the tailored models show a realistically smaller increase in APD than the original model, which shows alternans and then repolarisation failure at higher drug concentrations. For Quinidine, although the tailored models do not fit better at the highest concentration, we improve the predictions at lower concentrations.

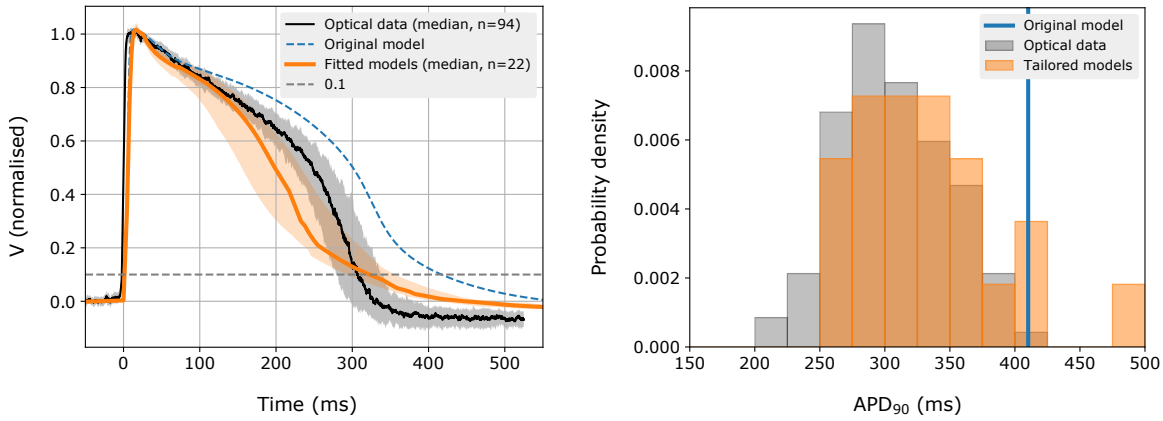

Figure 3.11: **(Left)** The predicted 1 Hz steady pacing action potentials from the individual cell optimised models (orange), the original Paci et al. (2013) model (dashed blue), and optical mapping measurements (black) in the control conditions. We show the median and 25th and 75th percentiles of the optical mapping (grey) and action potential models (orange). All data shown are normalised (see Section 3.2.3). For models that exhibited strong alternans (i.e. where only every second action potential showed a spike-and-dome morphology) the longer of the two action potentials was used. **(Right)** A histogram of APD_{90} in the fitted models and optical mapping control (drug free) experiments. As we might expect, there is more variation in APD in the individual-cell tailored action potential models than the electrotonically-coupled tissue measurements, but the distribution is centred appropriately.

Predictions made with the adult cardiomyocyte model by O'Hara et al. (2011) are shown for comparison. Note how the adult cardiomyocyte model predicts APD prolongation with Verapamil, whereas both the tailored and original hiPSC-CM models accurately predict the shortening that is observed in hiPSC-CM optical mapping. Such qualitative differences highlight the need for models specific to hiPSC-CMs to interpret experimental findings in these cells.

3.4 Discussion

In this chapter, we reparameterised a mathematical model of hiPSC-CMs based on the iCell cells to a new set of Cor.4U hiPSC-CM experiments measured using conventional methods. Using the simple method of scaling maximum conductances — without altering ion current *kinetics* — we created models tailored to individual hiPSC-CMs. The obtained fits had a high root-mean-square error (RMSE), which suggests that the ion current kinetics in the iCell-based model by Paci et al. (2013) do not closely match those in Cor.4U cells, as further discussed in Section 3.4.4.

However, like real hiPSC-CMs, these tailored models show differences in action potential from cell to cell, with action potential waveforms broadly similar to ventricular, atrial and sinoatrial-node action potentials. The predicted single-cell APD_{90} was shorter in tailored models than in the original model, and showed a better match with optical mapping measurements in electrotonically-coupled hiPSC-CM cultures. The effects of Dofetilide, Quinidine, Sotalol and Verapamil on the APD were simulated, and again the tailored models provided a closer fit. These results show that there are electrophysiological differences between hiPSC-CM cell lines, and that simple adjustments to computational hiPSC-CM models can already partially accommodate them.

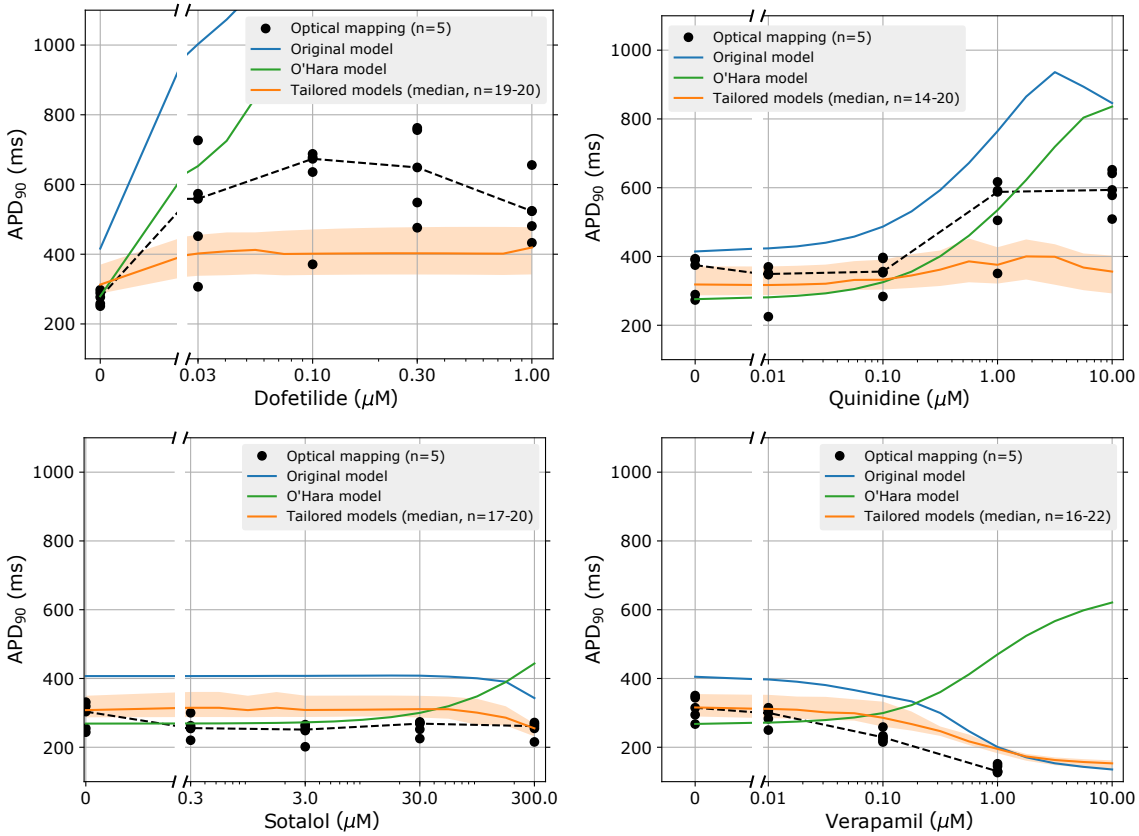

Figure 3.12: Dose-response curves of the APD_{90} for four drugs: Dofetilide, Quinidine, Sotalol, and Verapamil. The individual optical mapping measurements are shown as black dots, with the median shown as a dotted black line. Predicted responses from the original model are shown in blue, and the tailored model predictions are shown in orange (solid line is median and shaded region indicates 25^{th}–75^{th} percentiles. Models (tailored or original) that exhibited strong alternans (i.e. where only every second action potential showed a spike-and-dome morphology) were omitted from the figure. Because this caused the number of predictions in the tailored model distribution to vary, the minimum and maximum number of predictions per drug is shown as n = minimum – maximum. At higher concentrations, Dofetilide block causes repolarisation failure in both the original model and the O'Hara model.

In this section we first discuss the implications of this exploratory study in turn. Then we discuss the limitations and lessons learnt at the end of this section, to accentuate the drawback of using conventional methods, and to motivate the rest of the studies in this thesis.

3.4.1 Cell-line differences in ion current densities

We obtained maximum conductance values for the inward currents I_{Na} and I_{CaL} that are lower than suggested by the Paci et al. (2013) model based on iCell cells, while I_{Ks} and I_{NaCa} were increased in most Cor.4U cells. The slight reduction in I_{CaL} and increase in I_{Ks} suggests a decrease in APD. This was borne out by the action potential simulations, and was consistent with our optical mapping measurements which showed shorter APDs compared to the action potential simulated by the original Paci et al. (2013) model. Our simulations displayed a similar degree of action potential variability to the experimental hiPSC-CM recordings, but larger variability than the optical mapping measurements.

Both findings are consistent given that electrotonic coupling of cells (present in the optical mapping experiments) reduces variability.

A potential explanation of the large I_{Ks} current is suggested by Lei et al. (2017b). It shows that both the KCNQ1 and KCNE1 (subunits of the channel carrying I_{Ks}) were present in the Cor.4U cells, however, KCNE1 was not as well expressed in iCells. The difference in KCNE1 expression could lead to the observed larger I_{Ks} currents in the Cor.4U cells compared to iCells, and hence a shorter APD and less prolongation under I_{Kr} blockers, which is in agreement with Blinova et al. (2017). Our observation is supported by Silva and Rudy (2005) who found that native I_{Ks} (from channels comprised of both KCNQ1 and KCNE1) activates more than with KCNQ1 only.

3.4.2 Cell-to-cell differences in hiPSC-CMs

HiPSC-CMs, from the same donor and differentiated/matured in the same way, can display vastly different action potential waveforms, reminiscent of those of ventricular, atrial, and sinoatrial-node cells. Our tailored models, created by varying the maximum conductances of I_{NaCa} and I_{Ks}, showed a similar model-to-model (cell-to-cell) variety in style of generated action potentials. This shows that variation in genetic expression, which correlates directly with maximum conductance (Schulz et al., 2006), could be enough to explain the different action potential waveforms observed in hiPSC-CMs. However, it does not preclude other explanations, and it is possible the action potentials could take on a more distinct shape if differences in ion channel kinetics were also included, see discussion in Section 3.4.4.

3.4.3 Predictions of drug action

The sharp increase in I_{Ks} seen in the Cor.4U tailored models suggests Cor.4U cells have a stronger reliance on I_{Ks} as a repolarising force, and will therefore be less likely to show action potential prolongation when treated with I_{Kr} blocking drugs (see, e.g. the Figure 5 of Blinova et al., 2017, which shows, for eight out of 12 drugs with comparable concentrations and prolongation in iCells, the Cor.4U cells have a smaller APD prolongation than the iCells). Consistent with this suggestion, simulations of treatment with the potent I_{Kr} blocker Dofetilide showed only a modest increase in APD at concentrations that caused the iCell-cell based model to display excessive action potential prolongation resulting in alternans. Treatment with Quinidine, a less potent I_{Kr} blocker, showed similar results.

The modest APD increase predicted by the tailored models underestimated the APD prolongation observed in the data, suggesting the role of I_{Kr} as a repolarising force was underestimated in these models. Application of Verapamil, which blocks I_{CaL} as well as I_{Kr}, had a smaller effect in our tailored models than in the original model, which is again consistent with the lowered levels of I_{Kr} and I_{CaL}. The strong I_{Ks}-reliance we observed may be problematic when using these hiPSC-CMs as models for ventricular myocytes, where I_{Ks} only plays a major part when other repolarising currents are blocked or in the presence of sympathetic stimulation (Jost et al., 2005).

We expect more refined experiments, as outlined in the rest of this thesis, will be able to better separate the ionic currents and to better estimate I_{Kr} conductance.

3.4.4 Limitations and lessons learnt

In this chapter, we used a set of conventional protocols together with a simple method of scaling maximum conductances to create models tailored to individual hiPSC-CMs. The obtained fits were clearly not optimal, and the ion current profiles during voltage steps could not be recreated well. It is likely that the model we used does not accurately capture the kinetics of ion currents in the experiments, for example due to differences in subunit expression (Lei et al., 2017b), the difference of temperature (see e.g. Chapter 5), or the measurement difficulties inherent in experiments (Chapter 6) and modelling (Lei et al., 2020c). A channel's kinetics play an important role in its contribution of a current to the different phases of the action potential. Modifying the kinetic parameters which characterise the I-V relationship for the activation, inactivation, deactivation, etc. of a channel could change both the current and the action potential, and would influence responses to drugs. Varying the kinetic parameters would also alter the conductances we estimated. Since models of ion channel kinetics contain many parameters, specifically designed experiments (e.g. with channel blockers and/or specialised voltage protocols) will be required to refine these kinetic models (Clerx et al., 2019a; Whittaker et al., 2020). However, it typically takes too long to apply an array of conventional protocols to fully characterise a current's kinetics in a single cell, before considering characterising multiple ion currents. In the next chapter, Chapter 4, we therefore redesign the voltage-clamp protocols to rapidly characterise the kinetic models using a high-throughput system.

The method of fitting multiple currents to a single experimental recording is a highly useful approach, as it reduces the number of experiments needed to tailor a model. However, due to the limitation of experiments being performed in different cells, we were not able to examine the covariance between the inward and outward currents. Also, since the fitting depends on the number of current conductances to be fitted and the experimental data (e.g. the quality of the data and the actual current shape), one may run into problems of practical identifiability if one tries to refit kinetic parameters here (e.g. multiple combinations of conductance and kinetic parameters that can provide an equally good fit, as in Fink and Noble, 2009). Additional experiments with refined experimental designs will therefore be needed to identify all parameters. We use the idea of optimal experimental design (OED) to account for such limitations in Chapter 7.

There are further limitations that are not addressed in this thesis but are worth pointing out. First, variability/uncertainty in drug-ion channel interaction parameters (IC50s) from different labs or repeats of experiments will also impact our simulation predictions. A probabilistic uncertainty quantification framework using the techniques proposed by Elkins et al. (2013) and Johnstone et al. (2017) could be used to address this. Second, the Cor.4U-tailored predictions of both baseline action potential and drug responses matched the optical mapping data more closely than the un-tailored model. However, these optical mapping data were gathered from cultures of spontaneously beating electrotonically coupled cells, while our simulations are of paced single hiPSC-CMs. Another avenue for future work would be to combine (a representative distribution of) tailored cell-specific models into heterogeneous tissue models (Bowler et al., 2019).

To conclude, the conventional approach and the perfect-kinetics assumption that we have taken in this chapter shows multiple drawbacks. It clearly demonstrates that more intricate methods are needed to

characterise the currents and to refine the kinetics of the currents. In the next few chapters, we address these limitations through experimental design; we first focus on improving ion channel kinetics modelling before coming back to hiPSC-CMs later in Chapter 7. In the next chapter, we look at the *human Ether-à-go-go-Related Gene* (hERG) potassium channels encoding the pore-forming alpha subunit of the ion channel $K_V11.1$ that conducts I_{Kr}, and develop methods to rapidly characterise its kinetics.

3.5 Data and Software Availability

Data and software (GitHub repository):
https://github.com/CardiacModelling/tailored-ipsc-models

Chapter 4

High-Throughput Rapid Characterisation of hERG Kinetics

This chapter was published as: Lei, C. L., Clerx, M., Gavaghan, D. J., Polonchuk, L., Mirams, G. R., and Wang, K. (2019b). Rapid characterization of hERG channel kinetics I: using an automated high-throughput system. *Biophysical Journal*, 117(12):2438–2454.

Contributions: I assisted in designing the study, carried out the experiments, designed the computational analysis, wrote the simulation codes, and performed all the analysis.

This chapter also led to: Lei, C. L., Fabbri, A., Whittaker, D. G., Clerx, M., Windley, M. J., Hill, A. P., Mirams, G. R., and de Boer, T. P. (2020b). A nonlinear and time-dependent leak current in the presence of calcium fluoride patch-clamp seal enhancer. *Wellcome Open Research*, 5:152. This publication investigated the origin of the leftover current described in Section 4.5.3 below.

Overview:

In the previous chapter, we created cell-specific models by fitting the maximum conductances in an action potential model to hiPSC-CM data, under the assumption of perfect current model kinetics. However, we saw that the fitted models were not optimal under this assumption, as the ion current profiles during voltage steps could not be recreated well. The perfect kinetics assumption becomes inevitable when tailoring whole-cell models as in Chapter 3, mostly because the conventional voltage-clamp protocols require a long duration to measure each specific gating processes. An array of these conventional protocols would be needed to fully characterise a current; such a protocol would typically be too long to be applied in a single cell, and characterising multiple ion current kinetics would be even more difficult. We therefore need a different design of experiments to characterise cell-specific models of ion channel kinetics.

In this chapter, we consider the *human Ether-à-go-go-Related Gene* (hERG) channel when developing a new approach to experimental design, allowing rapid characterisation of its kinetics. hERG is a good choice for our new approach because of its great importance in cardiac electrophysiology and safety pharmacology. We develop a new 15 second protocol to characterise hERG ($K_V11.1$) kinetics, suitable for both manual and

high-throughput systems. We apply the protocol to Chinese Hamster Ovary (CHO) cells stably expressing hERG1a on the Nanion SyncroPatch 384PE, a 384-well, automated patch-clamp platform. We define and apply quality control criteria, selecting 124 cell measurements from the full dataset. From these recordings we construct 124 cell-specific variants/parameterisations of a hERG model at 25 °C. We then validate these models by comparing their predictions to measurements of eight further (validation) protocols, run on the same cells in the same experiment. We combine the experimental recordings using a hierarchical Bayesian model, which we use to quantify the uncertainty in the model parameters, and their variability from experiment to experiment.

This chapter provides the foundation for the next two chapters, and it demonstrates the feasibility of designing experiments to high-throughput characterise ion channel kinetics. Moreover, the results of the experiment-to-experiment variability here allows us to suggest reasons for the observed variability, which we investigate further in Chapter 6.

4.1 Introduction

As described in Chapter 2, voltage-clamp experiments are a common source of data for calibrating ion channel models, and are typically time consuming to perform. For example for the *human Ether-à-go-go-Related Gene* (hERG) channel, in Vandenberg et al. (2006), examining voltage dependence of activation using the conventional protocols lasted at least 10 minutes before examining deactivation, inactivation and recovery from inactivation. Hence these protocols are typically too long for a single cell recording, as discussed in the previous chapter.

Chapter 2 also discussed the importance of understanding and quantifying variability between experiments when establishing the credibility and applicability of model predictions, whether it be due to cell-to-cell variability (also known as *extrinsic variability* or *population variability*) or to observational errors/uncertainties. Quantifying the variability in ion channel kinetics requires a large number of high-quality patch-clamp measurements, and ideally all recorded cell-specifically to include any correlation effect. However, the duration of a standard combination of protocols makes it difficult to use them to fully characterise the current in a single cell, so that reaching the required number of cells even on automated high-throughput systems for a thorough statistical analysis would be a very difficult and time consuming task.

In order to address the above two challenges, this chapter demonstrates the feasibility of designing and applying high-throughput experiments to accurately and rapidly characterise cell-specific ion channel kinetics. In particular, we design experiments to characterise the kinetics of hERG on a high-throughput system.

Previous efforts have been made to address the variability observed in drug block measurements on the hERG channel (Kirsch et al., 2004). More recently, simulation experiments have shown that condensed voltage-clamp protocols can be used to provide the required information to characterise channel kinetics in a much shorter time (Hobbs and Hooper, 2008; Fink and Noble, 2009). A study by Beattie et al. (2018) demonstrated *in vitro* that sinusoidal protocols can be used to rapidly

(8 seconds) characterise hERG kinetics on a manual patch-clamp setup. This study addressed part of the challenges, as it demonstrated that it is possible to design experiments to characterise cell-specific hERG kinetics models on a manual patch-clamp system for nine cells. However, due to hardware limitations, some automated high-throughput systems can only perform square wave or ramp voltage-clamp protocols, so the sinusoidal protocols are not applicable in these systems. Therefore, the variability of baseline hERG characteristics remains incompletely understood, due to an insufficient number of recordings available from a manual patch-clamp setup.

This chapter presents a new approach to overcome these problems by using a novel protocol and a high-throughput system to rapidly record many cells' kinetics in parallel. Using these methods, we construct 124 cell-specific parameterisations of a hERG model, and validate all of our model predictions against a set of independent protocols that have not been used in training/fitting the model. To ensure the stability and reproducibility of our results *within the same cells*, we repeat all of our measurements twice. We employ a hierarchical Bayesian framework (a multi-level statistical modelling technique) to describe the variability of hERG channel conductance and kinetics between cells, and to infer the covariance between the model parameters across different cells. A schematic of this approach is shown in Figure 4.1.

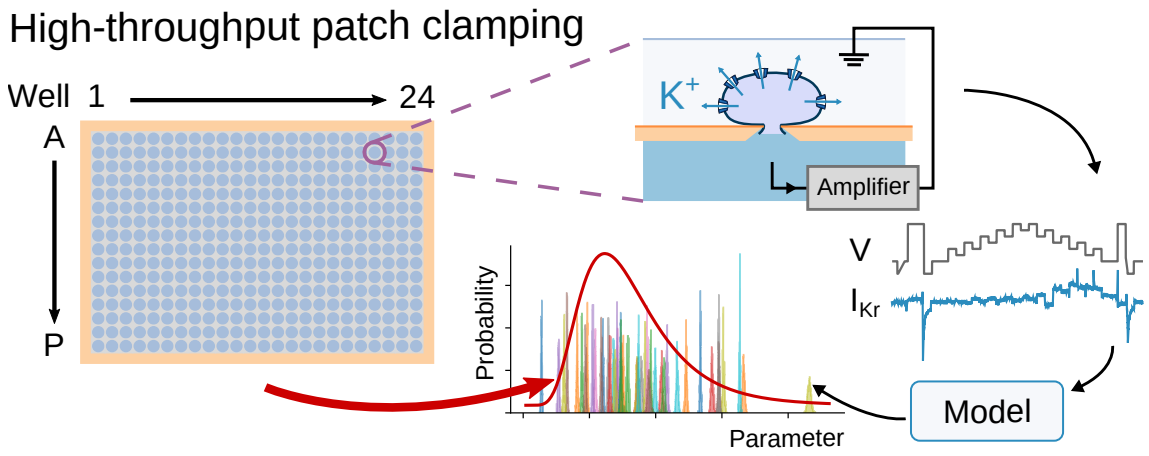

Figure 4.1: A schematic of the high-throughput characterisation experiments. On the left, we show a 384 well high-throughput patch-clamp platform. In each well, automated patch-clamp experiments (see also Figure 2.4B) are performed using the new voltage-clamp protocol (V) to elicit information-rich I_{Kr} signals (see Figure 4.2). Probability distributions of the model parameters can be inferred for each well's experiments (see Section 4.3.1). With the large number of repeats, the variability of hERG kinetics parameters can also be studied (shown by the red curve, see also Section 4.3.2).

This chapter presents a first step in moving away from the approach used in Chapter 3. We not only develop a novel method to construct validated trustworthy models of ion channel kinetics to overcome the limitations set out by the previous chapter, but also begin to consider cell-to-cell variability in ion channel models by performing rapid characterisation experiments on a high-throughput system, allowing us to investigate the sources of this variability further in Chapter 6.

In the next section, I first describe the novel protocol design. Then I describe methods to analyse data collected using the new protocol. We then test the robustness of the protocol with synthetic data

studies. Finally, I provide the experimental methods and present the experiments and subsequent models using this new protocol on the Nanion SyncroPatch 384PE, a 384 well automated patch-clamp platform (Figure 4.1).

4.2 Protocol Design for Rapid Characterisation of Current Kinetics

I first describe the mathematical model of hERG that we use in this chapter, as it motivates the design. Then I introduce the novel protocol and discuss the rationale underlying the design.

4.2.1 Mathematical model

The model structure that we use is a Hodgkin and Huxley-style (see also Chapter 2) hERG model by Beattie et al. (2018), and this model structure has been widely used in many studies with slight

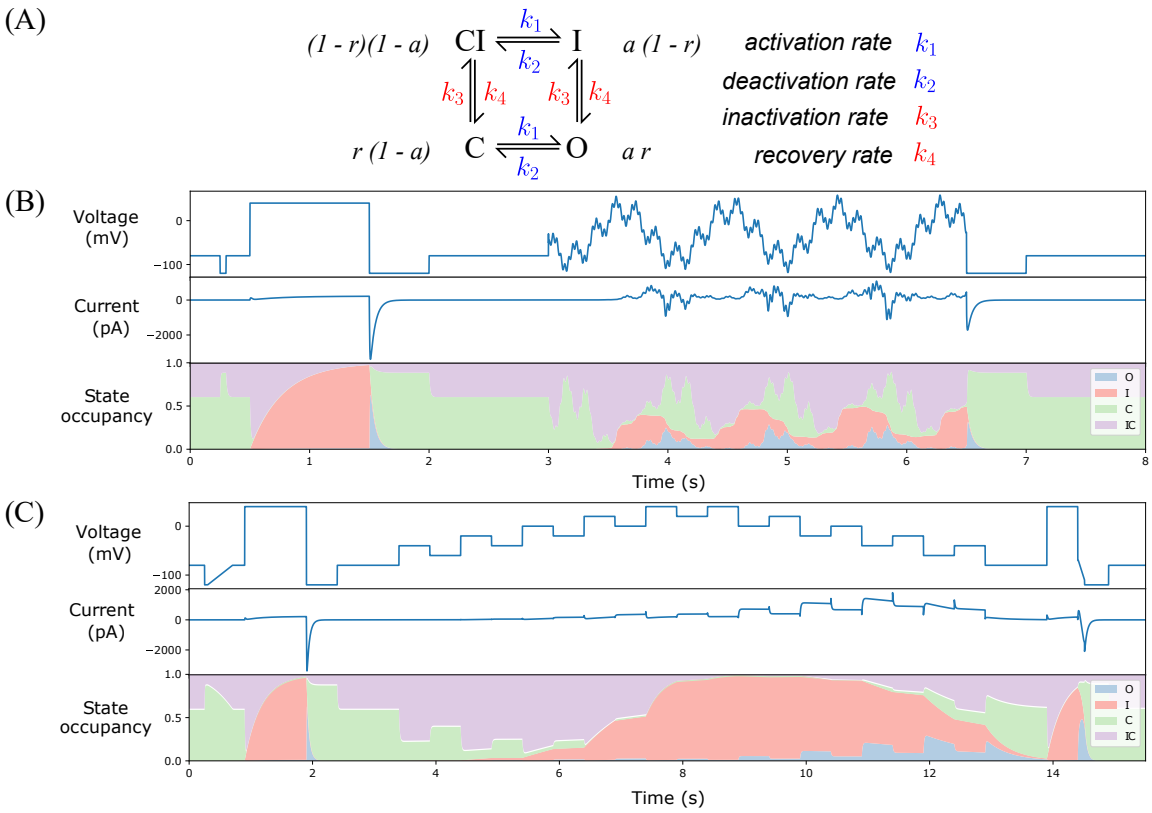

Figure 4.2: **(A)** The Hodgkin-Huxley model structure shown in equivalent Markov state diagram format. Four states are linked with arrows with rate transitions described on the right. The probabilities of each state are given next to them in terms of the Hodgkin-Huxley gates *a* and *r*. **(B)** A manual patch-clamp protocol comprised of an 8-second voltage-clamp protocol designed for rapid characterisation of ion channel kinetics by Beattie et al. (2018). **(C)** Our novel 15-second protocol, which we term the '*staircase protocol*', designed for any patch-clamp set-up including high-throughput automated systems, that is similarly able to characterise the full kinetics of the hERG channel model. Both (B) and (C) show the voltage protocol (top panel), an example of the simulated current using the room temperature parameters from Beattie et al. (2018, Cell #5) (middle panel), and the corresponding state occupancy (bottom panel).

modifications: the root of the model traces back to Zeng et al. (1995), where the same model structure is used but with the inactivation gate modelled as an instantaneous steady-state response. Later in the Ten Tusscher et al. (2004) model, the same model structure was used, but extra parameters were introduced to make the time constant independent of the steady state. In this chapter, we refer the current conducted by the hERG1a ($K_V11.1$) channel as I_{Kr} for convenience. The current is modelled as a function of the voltage V, with a standard Ohmic expression,

$$I_{Kr} = g_{Kr} \cdot a \cdot r \cdot (V - E_K), \tag{4.1}$$

where g_{Kr} is the maximal conductance, a is a Hodgkin and Huxley (1952a) activation gate, and r is an inactivation gate. E_K is the reversal potential, as defined in Chapter 2; and here E_K was calculated directly using Eq. (2.8), where the valency of K^+ (z_K) is 1. The extracellular and intracellular concentrations of K^+, $[K^+]_o$ and $[K^+]_i$, respectively, were determined by the experimental solutions as 4 mM and 110 mM, respectively. The equivalent Markov model structure is shown in Figure 4.2, where

$$\frac{da}{dt} = \frac{a_\infty - a}{\tau_a}, \qquad \frac{dr}{dt} = \frac{r_\infty - r}{\tau_r}, \tag{4.2}$$

$$a_\infty = \frac{k_1}{k_1 + k_2}, \qquad r_\infty = \frac{k_4}{k_3 + k_4}, \tag{4.3}$$

$$\tau_a = \frac{1}{k_1 + k_2}, \qquad \tau_r = \frac{1}{k_3 + k_4}, \tag{4.4}$$

and

$$k_1 = p_1 \exp(p_2 V), \qquad k_3 = p_5 \exp(p_6 V), \tag{4.5}$$

$$k_2 = p_3 \exp(-p_4 V), \qquad k_4 = p_7 \exp(-p_8 V). \tag{4.6}$$

Our model consists of nine positive parameters $\boldsymbol{\theta} = \{g_{Kr}, p_1, \ldots, p_8\}$, where the units of the parameters in this chapter are $\{\text{pS}, \text{s}^{-1}, \text{V}^{-1}, \text{s}^{-1}, \ldots\}$. All of model parameters must be inferred from the experimental data.

As discussed in Chapter 2, we expect a leak current to ground to occur in the experiments. We use the common assumption that the leak current is linear in the voltage to model

$$I_{leak} = g_{leak} \cdot (V - E_{leak}), \tag{4.7}$$

where g_{leak} is the leak current conductance and E_{leak} is the leak current reversal potential.

In this chapter and the next, we assume the voltage V in the model takes the exact form of the voltage-clamp protocols (denoted as V_{cmd} in Chapter 6), which is a typical assumption frequently used when analysing experimental data. We criticise this assumption in the Discussion and thoroughly assess in Chapter 6.

4.2.2 Staircase protocol

Our novel 15 second protocol designed for characterising hERG kinetics is termed the '*staircase protocol*'. A comparison between the staircase protocol and a previously developed sinusoidal protocol (Beattie et al., 2018) is shown in Figure 4.2B and C. Due to hardware limitations, the sinusoidal protocol does not work on many high-throughput automated systems as they cannot perform clamps to arbitrary time-varying functions and are limited to linear ramps and steps. Hence the idea from Beattie et al. (2018) — using an 'information-rich' protocol — was adapted, and the rationale of our staircase protocol is discussed below. We designed the staircase protocol with only voltage steps and ramps, such that it is applicable to any patch-clamp machine. This staircase protocol is shown in Figure 4.2C. A time series version of the full protocol is available online, see Data and Software Availability at the end of the chapter.

The underlying rationale of the *staircase protocol* shown in Figure 4.2C is to force the system to reveal its full dynamics by exploring different transitions of the voltage, over a physiologically relevant voltage range. By observing the changes in the current before and after each step, the voltage dependency of the channel at that particular voltage transition can be deduced. Each voltage step is held for 500 ms, which is long enough to observe the characteristic decay of I_{Kr}. Therefore, by going through different step-ups and -downs, the protocol explores the dynamics at different voltage values, and hence our statistical inference method is able to infer the underlying model parameters.

Two ramps are implemented before and after the main staircase. The ramp at $t = 0.3$ s, termed the '*leak ramp*', is used to estimate the leak current. We assumed that at -80 mV, I_{Kr} is fully closed and will not be opened by going to a voltage below -80 mV. We therefore implemented a linear ramp from -120 mV to -80 mV over 400 ms. All non-zero current measured during the leak ramp was assumed to be leak current in the form of Eq. (4.7), and a linear regression can then be used to fit its current-voltage (I-V) relation and to obtain the leak model parameters. This leak ramp can be used to check the linearity of the leak current, that is the linearity in its I-V relation (see Figure 4.3), which cannot be achieved using the standard single voltage step method for leak estimation (see Section 4.5.3.2).

The second ramp at $t = 14.41$ s, termed the '*reversal ramp*', is intended to estimate experimentally the reversal potential E_{K} by having a ramp over 100 ms that quickly crosses the expected E_{K}, which we expect to be in the range of -70 mV to -100 mV. At these voltages no current can be measured as the channel is nearly closed. We therefore implemented a large step up to 40 mV to open the channel followed by a 10 ms step to -70 mV to remove capacitive effects before the reversal ramp, so that we can record a high signal-to-noise ratio (SNR) I_{Kr} trace that goes from positive to negative before the channel closes. Examples of experimentally recorded currents (see Section 4.5) during the two ramps are shown in Figure 4.3.

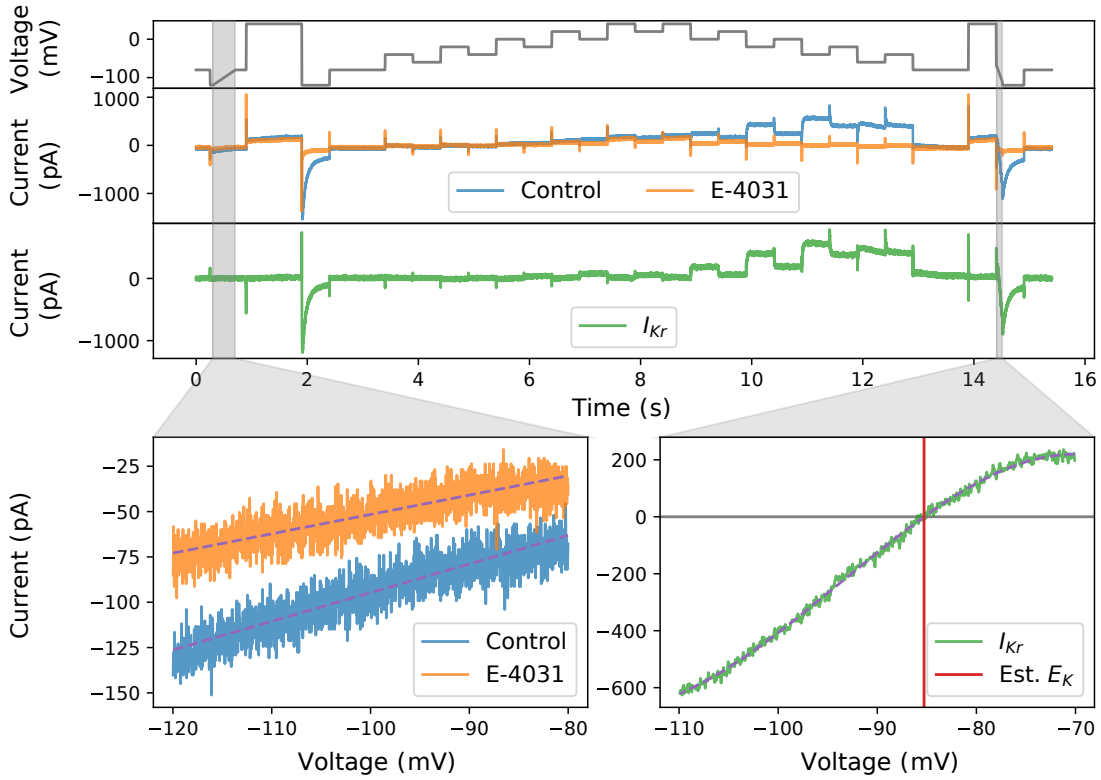

Figure 4.3: Example of an experimental recording (see Section 4.5) using the two ramps (greyed out sections) implemented in the staircase protocols. The first ramp is designed to estimate the leak current; the second ramp is designed to experimentally estimate the E_{K} value. Top three panels show the staircase voltage-clamp protocol (grey), the raw currents before (blue) and after (orange) E-4031 application, and the estimated I_{Kr} (green; the subtraction between the blue and orange traces), respectively. Below shows the I-V curves measured during the two ramps. Linear regressions were applied to each of the I-V relation in the first ramp, shown as dashed lines. Third order polynomial regression was applied to the I-V curve in the second ramp, shown as dashed lines (see also Figure 4.23). Both of them show a good fit to the data.

4.3 Analysis Methods

4.3.1 Statistical model and parameter inference

To infer model parameters from experimentally observed data under a probabilistic and Bayesian framework, we specified a statistical model to relate the mathematical model and the observed experimental data:

$$I_{\mathrm{Kr}}^{\mathrm{data}} = I_{\mathrm{Kr}}^{\mathrm{model}} + \epsilon. \tag{4.8}$$

We assumed that noise arises from a normal distribution $\epsilon \sim \mathcal{N}(0, \sigma^2)$. As described in Chapter 2, this is equivalent to writing $I_{\mathrm{Kr}}^{\mathrm{data}} \sim \mathcal{N}(I_{\mathrm{Kr}}^{\mathrm{model}}, \sigma^2)$, which allows us to formulate the likelihood of observing the data $\mathbf{y} = \{y_k\}$ given parameters $\boldsymbol{\phi}$ as

$$p(\mathbf{y} \mid \boldsymbol{\phi}, \sigma) = \frac{1}{\sqrt{2\pi\sigma^2}} \exp\left(- \sum_k \frac{\left(z_k(\boldsymbol{\phi}) - y_k\right)^2}{2\sigma^2} \right), \tag{4.9}$$

where $\mathbf{z} = \{z_k\}$ is the model simulation of the $I_{\text{Kr}}^{\text{model}}$. We transformed our positively constrained physical model parameters $\boldsymbol{\theta}$ to unconstrained optimisation variables $\boldsymbol{\phi}$ using a log-transformation:

$$\boldsymbol{\phi} = \ln(\boldsymbol{\theta}). \tag{4.10}$$

Using Bayes' theorem (see Chapter 2), we can now write an equation for the likelihood of a parameter set given the observed data (the posterior) as

$$p(\boldsymbol{\phi}, \sigma \mid \mathbf{y}) = \frac{p(\boldsymbol{\phi})p(\mathbf{y} \mid \boldsymbol{\phi}, \sigma)}{p(\mathbf{y})} \propto p(\boldsymbol{\phi})p(\mathbf{y} \mid \boldsymbol{\phi}, \sigma), \tag{4.11}$$

with the prior

$$p(\boldsymbol{\phi}) = \mathcal{U}(\boldsymbol{\phi}^{\min}, \boldsymbol{\phi}^{\max}), \tag{4.12}$$

where $\mathcal{U}(\cdot)$ represents a uniform distribution.

Here $\mathbf{y}$ was assumed to be the $I_{\text{Kr}}^{\text{data}}$ in Eq. (4.8), after leak correction and E-4031 subtraction have been applied as part of the data processing (see Section 4.5.3). For the prior, we assumed a uniform distribution, using bounds adapted from the physical constraints for the rate constants in the kinetics parameters introduced in Beattie et al. (2018), which has the form $k = A\exp(BV)$, viz., Eqs. (4.5) and (4.6). For parameters of the form A, $[\theta_i^{\min}, \theta_i^{\max}]$ is chosen to be $[10^{-7}, 10^{3}]\,\text{ms}^{-1}$; and for parameters of the form B, $[\theta_i^{\min}, \theta_i^{\max}]$ is chosen to be $[10^{-7}, 0.4]\,\text{mV}^{-1}$. Such a formulation extends our model parameters to $\{\boldsymbol{\theta}, \sigma\}$, to fully describe both the biophysical and statistical models.

We used a two-step approach to infer the model parameters. Firstly, we used a global optimisation algorithm, Covariance Matrix Adaptation Evolution Strategy (CMA-ES), as described in Chapter 2, to identify the parameters. Secondly, we used a Monte-Carlo based sampling scheme to obtain the posterior distribution, using a population Markov Chain Monte Carlo (MCMC) algorithm (Jasra et al., 2007) with adaptive Metropolis (see Chapter 2) as the base sampler. The benefits of this approach are twofold. First, using a Bayesian framework allows us to incorporate prior knowledge. Second, we construct a probability (posterior) distribution to quantify uncertainty in the parameter set due to noise in the data.

4.3.2 Hierarchical Bayesian model

As we collect hundreds of measurements from the automated high-throughput system, we would like to also capture how the measurements vary between experiments (see Figure 4.1). This information not only can be used to predict how the system might behave in the future, but can also be used to find correlations between the parameters if formulated appropriately. One way of doing this is to consider the I_{Kr} model parameters as random variables that are drawn from some unknown distribution. This distribution has parameters of its own, which we are interested in. This gives rise to a hierarchical problem: The model parameters for each cell are drawn from the 'top-level' distribution, and the data generated from each cell is drawn from a statistical distribution based on those model parameters. We applied a multi-level modelling technique known as a hierarchical Bayesian model to combined multiple experimental recordings. We first introduce the hierarchical Bayesian model framework, then we describe how it was applied to the data and the hERG model.

4.3.2.1 An introduction to hierarchical Bayesian modelling

The basic idea of the framework follows from the Bayesian approach discussed in Chapter 2. Let us suppose we have some observed data y_i and a dataset-specific model with parameter θ_i governing the data generating process for y_i, with N observed data, i.e. $i = 1, 2, \ldots, N$. If we assume that the parameters $\theta_1, \theta_2, \ldots, \theta_N$ are generated[1] from some 'top-level' process governed by some parameter ζ. The 'top-level' parameters, ζ in this case, are known as the *hyperparameters*, and the prior distributions of these hyperparameters are called the *hyperpriors*. The statistical model for the data i can be summarised as

$$\begin{aligned} &\text{Data} && y_i \sim p(y_i \mid \theta_i, \zeta), \\ &\text{Parameter} && \theta_i \sim p(\theta_i \mid \zeta), \\ &\text{Hyperparameter} && \zeta \sim p(\zeta). \end{aligned}$$

Applying Bayes' theorem, with the likelihood $p(y_i \mid \theta_i, \zeta)$ and its prior $p(\theta_i, \zeta)$, the posterior distribution for this hierarchical Bayesian model becomes

$$p(\zeta, \theta_i \mid y_i) = \frac{p(y_i \mid \theta_i, \zeta) p(\theta_i, \zeta)}{p(y_i)} \tag{4.13}$$

$$= \frac{p(y_i \mid \theta_i, \zeta) p(\theta_i \mid \zeta) p(\zeta)}{p(y_i)} \tag{4.14}$$

$$\propto p(y_i \mid \theta_i, \zeta) p(\theta_i \mid \zeta) p(\zeta). \tag{4.15}$$

4.3.2.2 Applying hierarchical Bayesian modelling

Under the hierarchical Bayesian model framework, we assume that the vector of the (transformed) parameters $\boldsymbol{\phi}$ for a particular cell j is a sample from a multivariate normal distribution which describes how these parameters are distributed between all cells, namely $\boldsymbol{\phi}_j \sim \mathcal{N}(\boldsymbol{\mu}, \boldsymbol{\Sigma})$. Given our choice of parameter transformation, this is equivalent to writing $\boldsymbol{\theta}_j \sim \text{LogNormal}(\boldsymbol{\mu}, \boldsymbol{\Sigma})$, that is, the vector of parameters $\boldsymbol{\theta}$ for a particular cell j is a sample from a multivariate log-normal distribution. Then we used the hierarchical Bayesian model to infer the hyperparameter set $\boldsymbol{\zeta} = \{\boldsymbol{\mu}, \boldsymbol{\Sigma}\}$, a concatenation of all the individual hyperparameters within the mean vector $\boldsymbol{\mu}$ and covariance matrix $\boldsymbol{\Sigma}$ across cells, and hence determined any correlation in model parameter sets between cells. Later we tested the validity of this log-normal distribution assumption in Section 4.6.3.

The hierarchical Bayesian posterior was specified as the product of: (a) the probability of producing data $\mathbf{y}_j$ on each cell given the model parameter vector for each cell $\boldsymbol{\theta}_j$ and noise σ_j,

$$p_{\text{low-level}} = \prod_{j=1}^{N_e} p\left(\mathbf{y}_j \middle| \boldsymbol{\theta}_j, \sigma_j\right); \tag{4.16}$$

(b) the probability of obtaining each individual well parameter set $\boldsymbol{\theta}_j$ from the 'top-level' log-normal distribution across wells defined by the hyperparameters $\boldsymbol{\mu}$ and $\boldsymbol{\Sigma}$,

$$p_{\text{top-level}} = p\left(\boldsymbol{\theta}_1, \ldots, \boldsymbol{\theta}_{N_e} \middle| \boldsymbol{\mu}, \boldsymbol{\Sigma}\right); \tag{4.17}$$

[1] These parameters must be generated exchangeably, i.e. they do not follow some specific order.

and (c) the priors — the hyperprior and the prior of σ_j,

$$p_{\text{priors}} = p\left(\boldsymbol{\mu}, \boldsymbol{\Sigma}\right) \times \prod_{j=1}^{N_e} p\left(\sigma_j\right). \tag{4.18}$$

That is,

$$p\left(\boldsymbol{\mu}, \boldsymbol{\Sigma}, \boldsymbol{\theta}_1, \ldots, \boldsymbol{\theta}_{N_e}, \sigma_1, \ldots, \sigma_{N_e} \,\middle|\, \mathbf{y}_1, \ldots, \mathbf{y}_{N_e}\right) \propto p_{\text{low-level}} \times p_{\text{top-level}} \times p_{\text{priors}}, \tag{4.19}$$

where $\boldsymbol{\mu}, \boldsymbol{\Sigma}$ are the hyperparameters representing the mean vector and covariance matrix of the individual 'low-level' parameters, and $\boldsymbol{\theta}_1, \sigma_1, \boldsymbol{\theta}_2, \sigma_2, \ldots, \boldsymbol{\theta}_{N_e}, \sigma_{N_e}$ are the set of individual 'low-level' parameters for each of the N_e repeats of the experimental recordings $\mathbf{y}_1, \mathbf{y}_2, \ldots, \mathbf{y}_{N_e}$. The parameter dependency for this hierarchical Bayesian model is shown in Figure 4.4.

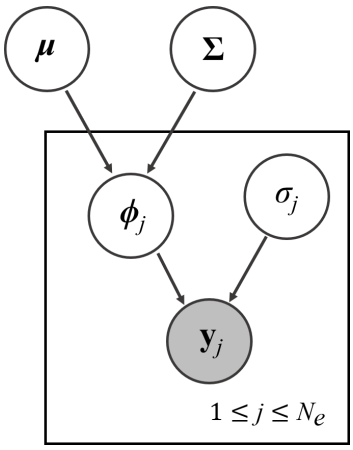

Figure 4.4: Hierarchical Bayesian model showing parameter dependency for combining multiple experiments. $\boldsymbol{\mu}, \boldsymbol{\Sigma}$ are the hyperparameters of the hierarchical model which represent the mean and covariance matrix, respectively, of the parameters across wells. $\boldsymbol{\theta}_1, \sigma_1, \ldots, \boldsymbol{\theta}_{N_e}, \sigma_{N_e}$ are the set of individual 'low-level' parameters for each of the N_e wells in the high-throughput experimental recordings $\mathbf{y}_1, \ldots, \mathbf{y}_{N_e}$. The parameters in the box are different for each well and are indexed as the j^{th} well. All parameters, and their probability distributions, are inferred from the shaded variable $\mathbf{y}_j$, the experimental data. Prior distributions are required for parameters with no inward-pointing arrows.

4.3.2.3 Choice of hyperparameter priors

Here we define our choice of hyperparameter priors, which is required for our hierarchical Bayesian model, see Figure 4.4. For computational ease, we chose the priors of the hyperparameters to be conjugate priors. A conjugate prior is the prior that makes the posterior distribution follows the same parametric form as the prior distribution, and it is useful because we can directly perform Bayesian updating by modifying the parameters of the prior distribution rather than computing integrals, see for example Gelman et al. (2013).

Since we assumed the (transformed) model parameters follow a multivariate normal distribution

$$p(\boldsymbol{\phi}_j \mid \boldsymbol{\mu}, \boldsymbol{\Sigma}) = \mathcal{N}\left(\boldsymbol{\mu}, \boldsymbol{\Sigma}\right), \tag{4.20}$$

the prior of $\boldsymbol{\mu}$ was chosen to be a multivariate normal distribution, and the prior of $\boldsymbol{\Sigma}$ was chosen to be an inverse-Wishart distribution $\mathcal{W}^{-1}$, see for example Gelman et al. (2013) for the derivation of these conjugate priors. That is, we specified

$$p(\boldsymbol{\mu}, \boldsymbol{\Sigma}) = p(\boldsymbol{\mu} \mid \boldsymbol{\Sigma}) p(\boldsymbol{\Sigma}), \tag{4.21}$$

where

$$p(\boldsymbol{\mu} \mid \boldsymbol{\Sigma}) = \mathcal{N}\left(\boldsymbol{\mu}_0, \frac{1}{m}\boldsymbol{\Sigma}\right) \quad \text{and} \quad p(\boldsymbol{\Sigma}) = \mathcal{W}^{-1}(\boldsymbol{\Psi}, \nu). \tag{4.22}$$

$\boldsymbol{\mu}_0, m, \boldsymbol{\Psi}, \nu$ are the prior parameters, where m controls our confidence in the prior mean $\boldsymbol{\mu}_0$, and ν for the prior covariance $\boldsymbol{\Psi}$. Then the posterior distribution of the hyperparameters, which is required as part of the hierarchical Bayesian model (Eq. (4.19)), becomes

$$p\left(\boldsymbol{\mu} \,\middle|\, \boldsymbol{\Sigma}, \boldsymbol{\phi}_1, \ldots, \boldsymbol{\phi}_{N_e}\right) = \mathcal{N}\left(\frac{N_e \overline{\boldsymbol{\phi}} + m\boldsymbol{\mu}_0}{N_e + m}, \frac{1}{N_e + m}\boldsymbol{\Sigma}\right), \tag{4.23}$$

and

$$p\left(\boldsymbol{\Sigma} \,\middle|\, \boldsymbol{\phi}_1, \ldots, \boldsymbol{\phi}_{N_e}\right) = \mathcal{W}^{-1}\left(\boldsymbol{\Psi} + N_e \boldsymbol{S} + \frac{N_e m}{N_e + m}(\overline{\boldsymbol{\phi}} - \boldsymbol{\mu}_0)(\overline{\boldsymbol{\phi}} - \boldsymbol{\mu}_0)^T, N_e + \nu\right), \tag{4.24}$$

where

$$\overline{\boldsymbol{\phi}} = \frac{1}{N_e} \sum_{j=1}^{N_e} \boldsymbol{\phi}_j, \tag{4.25}$$

and

$$\boldsymbol{S} = \frac{1}{N_e} \sum_{j=1}^{N_e} (\overline{\boldsymbol{\phi}} - \boldsymbol{\phi}_j)(\overline{\boldsymbol{\phi}} - \boldsymbol{\phi}_j)^T. \tag{4.26}$$

We have now defined all the necessary components for the hierarchical Bayesian model.

4.3.2.4 Correlation and posterior predictive distribution

Here we describe the benefits of using the hierarchical Bayesian model defined in Eq. (4.19). First, we can use the inferred covariance matrix $\boldsymbol{\Sigma}$ in Eq. (4.19) to study the correlation ($\text{corr}(\boldsymbol{\theta})$) between the model parameters. The covariance matrix $\boldsymbol{\Sigma}$ and the correlation matrix $\text{corr}(\boldsymbol{\theta})$ are related by

$$\text{corr}(\boldsymbol{\theta}) = \text{diag}(\boldsymbol{\Sigma})^{-1/2}\, \boldsymbol{\Sigma}\, \text{diag}(\boldsymbol{\Sigma})^{-1/2}, \tag{4.27}$$

where $\text{diag}(\cdot)$ denotes the diagonal entries of the matrix.

Second, we can compute the posterior predictive distribution $p(\boldsymbol{\theta} \mid \cdots)$ using the hierarchical Bayesian model, where $(\cdots)$ indicates all other variables appearing in Eq. (4.19). The posterior predictive distribution allows us to make predictions about how future experiments will behave. It can be computed using

$$p(\boldsymbol{\theta} \mid \cdots) = \int_{\boldsymbol{\zeta}} p(\boldsymbol{\theta} \mid \boldsymbol{\zeta}) p(\boldsymbol{\zeta} \mid \cdots)\, \mathrm{d}\boldsymbol{\zeta}, \tag{4.28}$$

where $\boldsymbol{\zeta} = \{\boldsymbol{\mu}, \boldsymbol{\Sigma}\}$, a concatenation of all the individual hyperparameters within $\boldsymbol{\mu}$ and $\boldsymbol{\Sigma}$. The integration was approximated by summing over the probability density functions which are defined by the samples of $\boldsymbol{\zeta}$.

4.3.3 Sampling the hierarchical distribution

We are not able to write down an analytical form of the posterior distribution, thus we approximate the posterior through sampling from the distribution, as discussed in Chapter 2. However, the number of parameters in the hierarchical Bayesian model is very large. For Eq. (4.19), it works out as $N(N+1)/2 + (N_e+1)N + N_e$, for an N parameter I_{Kr} model. With our choice of I_{Kr} model and the size of the dataset, we expect $N = 9$ and $N_e > 100$, giving us more than 1000 model parameters and hyperparameters for which to infer probability distributions. This high dimensional problem can be computationally intractable using algorithms such as the Adaptive-Covariance Metropolis algorithm described in Chapter 2. Instead, Metropolis within Gibbs (MwG) (Gilks et al., 1995) sampling is a very powerful method to explore high dimensional probability distributions, such as our hierarchical Bayesian model, but even MwG can be very time consuming. We therefore tested a further simplification of the MwG to approximate the sampling algorithm, which we have termed '*pseudo-Metropolis within Gibbs (pseudo-MwG)*'.

With our pseudo-MwG, we assumed that the likelihoods of our individual experiment parameters are unlikely to be affected by the top-level distribution. This is because the sampled data using the information-rich staircase protocol have thousands of data points whilst we have only ~ 100 individual experiments. We therefore separated the sampling steps between the likelihood of all the individual experiments and the likelihood of the hyperparameters. That is, we first *independently* sample the likelihood of each individual experiment, using the population MCMC algorithm. Then we sample the hyperparameters using Eqs. (4.20)–(4.26) while replacing $\boldsymbol{\phi}_j$ with $\boldsymbol{\phi}_{j,l}$ which are the independently obtained l^{th} samples of the individual experiments j.

We tested the validity of this simplification in Section 4.4.4 (Figure 4.8) by comparing the hierarchical Bayesian model parameter inference on synthetic data using the pseudo-MwG and the MwG, and found that the pseudo-MwG can approximate the MwG very well. Note that this simplification is only applicable for our particular setting — where the number of data points in the time traces vastly outweighs the number of cells, and in fact effectively we conclude the hierarchical model is not needed — the top level parameters do not significantly influence the inference of the lower level ones.

We note that we can further simplify our pseudo-MwG, which we call a '*simplified pseudo-MwG*', given our information-rich staircase protocol. Later we see that the MCMC marginal distributions in Figure 4.8 are very narrow relative to the spread of each of the experiment parameters. By approximating these narrow distributions as single points (i.e. the Dirac delta functions at their maximum a posteriori (MAP) estimates), we then estimate the posterior distribution by simply sampling the hyperparameters. We use Eqs. (4.20)–(4.26) to sample the hyperparameters while replacing $\boldsymbol{\phi}_j$ with point-estimates of the parameters of the individual experiments j. This simplification is checked against the MwG using synthetic data in Section 4.4.5.

4.3.4 Numerical implementation

Model simulations, inference, and sampling were performed as described in Chapter 2. All codes and data are freely available online, see Data and Software Availability at the end of the chapter.

4.4 Synthetic Data Studies

Before implementing experiments, we confirmed the identifiability of model parameters using our protocols and parameter inference algorithms through a synthetic data study. First, we used the synthetic data to design our protocols and to ensure that the protocols give access to sufficient information for parameter characterisation. Second, we assessed our inference methods, described in Section 4.3.1, by asking how confident we are in our inferred parameters. Finally, we tested our hierarchical Bayesian model, to ensure that it is possible to infer the underlying distribution of the parameters.

4.4.1 Generating synthetic data

We generate synthetic data by simulating the I_{Kr} model in Eq. (4.1), with some fixed known parameter sets $\boldsymbol{\theta}^{\text{true},j}$ and $j = 1, 2, \ldots, N_e$, voltage protocol, initial values, and sampling time (time-step).

First, we based our choice of $\boldsymbol{\theta}^{\text{true},j}$ on the parameters identified from a previous study (Beattie et al., 2018, Table F11 Cell #5), $\boldsymbol{\theta}^{\text{lit}}$. We then generated a set of parameters $\{\boldsymbol{\theta}^{\text{true},1}, \boldsymbol{\theta}^{\text{true},2}, \cdots, \boldsymbol{\theta}^{\text{true},N_e}\}$. We assumed there exists an underlying correlation *between* each model parameter, which can be described by a covariance matrix $\boldsymbol{\Sigma}^{\text{true}}$. Therefore we sampled the parameters from a (covarying) multivariate normal distribution, that is

$$\boldsymbol{\theta}^{\text{true},j} \sim \text{LogNormal}(\boldsymbol{\theta}^{\text{lit}}, \boldsymbol{\Sigma}^{\text{true}}). \tag{4.29}$$

To generate the covariance matrix $\boldsymbol{\Sigma}^{\text{true}}$, we first randomly generated a correlation matrix $\text{corr}(\boldsymbol{\theta}^{\text{true}})$ for this synthetic data study, which was a sparse symmetric definite positive matrix. Then the covariance matrix $\boldsymbol{\Sigma}^{\text{true}}$ was computed by inverting Eq. (4.27) and setting its (i,i) entry to be the variance ρ_i^2 (which we set $\rho_i = 0.2 \times \left|\theta_i^{\text{lit}}\right|$). In other words, we considered that we performed N_e experiments (recordings), and there was cell-cell variability between experiments.

Second, we fixed the voltage V of the model as the calibration voltage-clamp protocol — the staircase protocol (see Figure 4.2C) that we developed for the high-throughput systems. Third, for the initial values, we ran the model at $V = -80\,\text{mV}$ for a long period (100 s), to allow the model to settle at its steady state at $V = -80\,\text{mV}$. Since we are able to mimic this in the actual experiments, we assume the model does not depend on the choice of the initial values.

Finally, we add synthetic noise which follows an independent and identically distributed (i.i.d.) normal distribution with a mean of zero and standard deviation σ (i.e. $\sim \mathcal{N}(0, \sigma^2)$) to the simulated traces with time step 0.5 ms, as we specified in our statistical model in Section 4.3.1. We chose σ at a reasonable scale, $\sigma = 11\,\text{pA}$, to mimic the white noise observed from some of our pilot experiments using the high-throughput system.

4.4.2 Single synthetic experiment

We start by showing the staircase protocol is information-rich for our model, in that we are able to fully recover the 'true' parameters in a synthetic data study using our protocol. Figure 4.5 shows the

inferred model parameters in a synthetic experiment, where $\boldsymbol{\theta}^{\text{true}} = \boldsymbol{\theta}^{\text{lit}}$. It shows three[2] independently sampled marginal posterior distributions of each parameter (first and third columns), with indications of the 'true' parameters $\boldsymbol{\theta}^{\text{true}}$ (black dashed lines) which we used to generate the synthetic data, and the CMA-ES inferred parameters (red lines). Both the traces (second and fourth columns) and the three independently run posterior distributions show a good indication of the convergence of the MCMC chains, and the Gelman-Rubin convergence statistic, $\widehat{R}$, was less than 1.1 for all parameters (Gelman et al., 2013). We are able to recover the 'true' parameters $\boldsymbol{\theta}^{\text{true}}$ with high accuracy and a narrow credible interval[3] using our inference techniques together with our developed staircase protocol. Therefore we are confident that, with both the high information-content protocol and the inference techniques, it is theoretically possible to infer all parameters of the model.

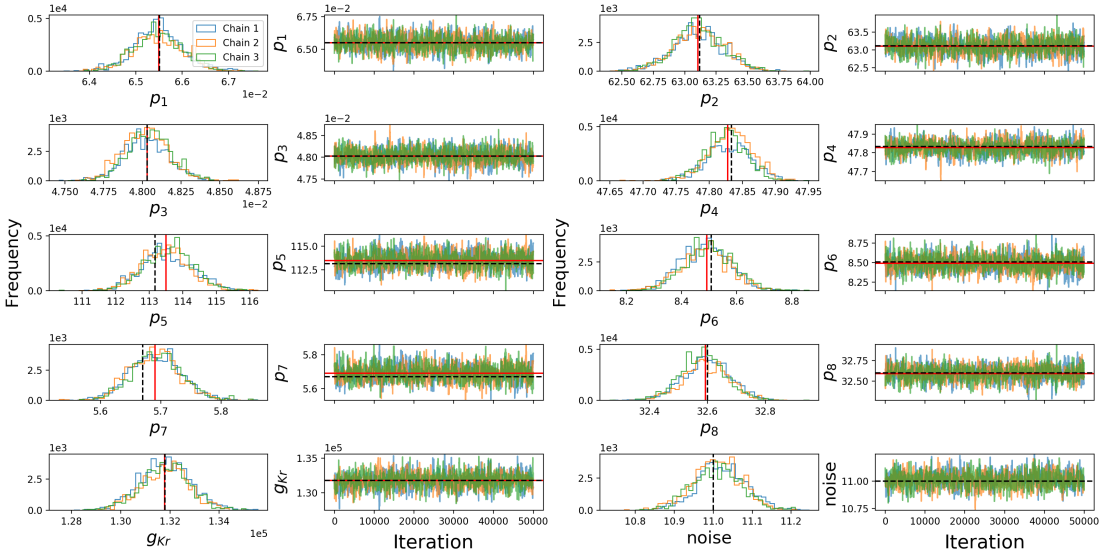

Figure 4.5: Parameter inference of single synthetic experiment, $N_e = 1$. **First, Third columns:** Show the marginal histograms of the posterior distribution of each parameter. **Second, Fourth columns:** The trace plots for our MCMC chains indicating that our MCMC chains have converged and are well mixed. Each panel shows the posterior distribution of three independently run MCMC with good agreement. The true (synthetic) parameters are indicated as black dashed lines and the CMA-ES inferred parameters are shown as red lines.

4.4.3 Hierarchical synthetic experiments

Figure 4.6 shows the results of the hierarchical Bayesian model applied in the synthetic data study with $N_e = 120$. It shows the marginal histograms of the model parameters for each individual experiment (left y-axis) and the marginal posterior predictive distribution (right y-axis, red lines). This synthetic data study is equivalent to having N_e repeats of the same experiment. Unlike the single experiment study in Section 4.4.2, the implications of the obtained posterior predictive distribution $p(\boldsymbol{\theta} \mid \cdots)$ are much more powerful.

First, we can view this posterior predictive distribution as the underlying distribution that governs the parameters. The marginal posterior predictive distributions closely resemble the true distribution (black dashed lines, the multivariate normal distribution in Eq. (4.29)). This indicates that we are able

[2]Typically we used three to four independent chains starting with random starting points sampled from the priors.
[3]Non-strictly speaking, a credible interval is the Bayesian version of the confidence interval.

to recover the underlying distribution of the parameters, and therefore we can rely on the methods to be applied in real experiments.

Second, as the name implies, this is a *predictive* distribution. Given the observed individual experiments, we can infer a distribution which allows us to predict what might happen in a future experiment. To demonstrate this, we can consider the posterior predictive distribution in Eq. (4.28) as $p(\boldsymbol{\theta}_{N_e+1} \mid \cdots)$, where $\boldsymbol{\theta}_{N_e+1}$ is our 'future' $(N_e+1)^{\text{th}}$ experiment that we perform. Therefore the distribution that we construct is able to tell us what is likely to happen in the future experiments — based on the observations from previous experiments.

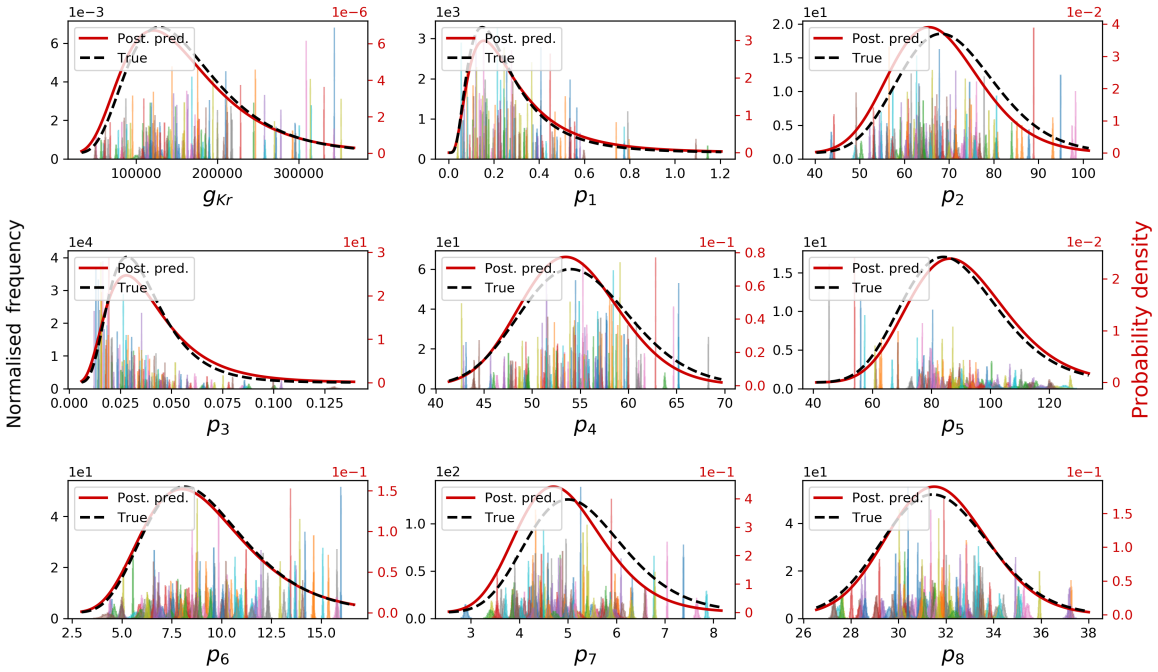

Figure 4.6: Parameter inference using the hierarchical Bayesian model in the synthetic data study, with $N_e = 120$. **Left *y*-axis**: the marginal histograms of the model parameters for each individual experiment. The histograms are normalised such that the area under each histogram equals to unity, to represent the marginal distributions. **Right *y*-axis**: the marginal posterior predictive distributions and the true probability density function that generates the parameters.

With a prior that had no assumptions about the underlying covariance between parameters, we were able to reconstruct the correlation matrix $\text{corr}(\boldsymbol{\theta})$ in Eq. (4.27) of our predefined distribution. The posterior marginal histograms for each entry of the correlation matrix are shown in Figure 4.7 (upper triangle). The diagonals are by definition equal to one, so they are not shown. All the inferred marginal posterior distributions for each entry cover the true underlying correlation value (dashed black vertical lines). Therefore we have confidence that our method is able to correctly infer the underlying correlation between parameters.

Figure 4.7 (lower triangle) shows the correlation between each pair of parameters. Each contour ring represents the 95% credible intervals of the joint distribution of the two parameters, for both the recovered (blue) and the true (black-dashed) covariance matrices. As long as the main axis of the ellipse is not parallel to the x- or y-axis, it indicates the two parameters are not pairwise-independent.

The diagonal shows the sampled predictive posterior distributions; the mean of these samples gives $p(\boldsymbol{\theta} \mid \cdots)$ shown in Figure 4.6. Again, it shows that we are able to recover the general shape of the underlying correlation with high accuracy.

Note that, in this synthetic study, the correlation matrix that we recovered may not make any physical

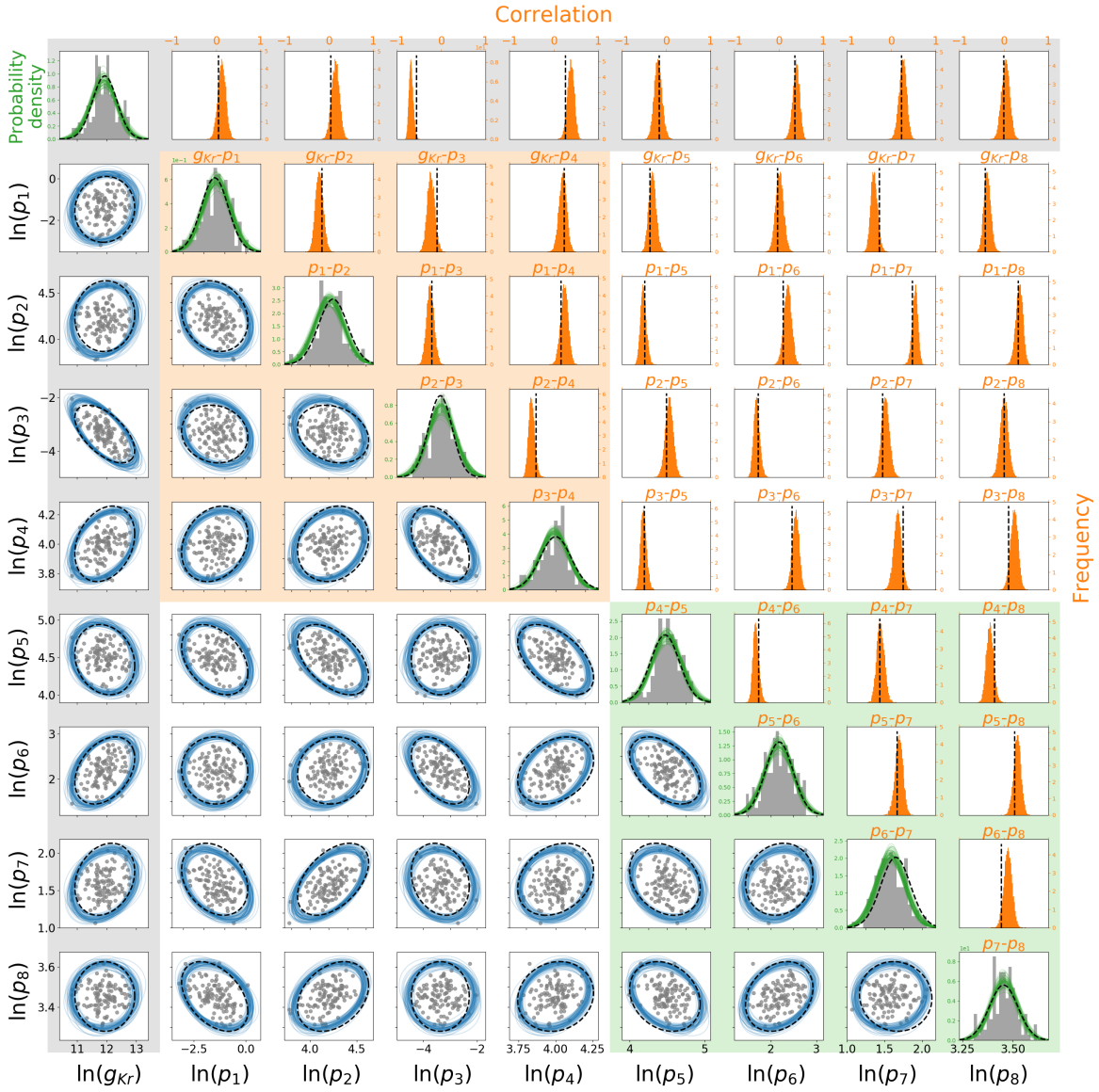

Figure 4.7: The inferred correlation in model parameters across experimental wells using the hierarchical Bayesian model on the synthetic data, with $N_e = 120$. All parameter values shown here are natural log-transformed. The 120 parameter samples $\{\boldsymbol{\theta}^{\text{true},j}\}_j$ (experiments) are shown in grey (dots and histograms), which were generated with the distribution shown in black. **Lower triangle (blue):** The 95% credible region boundary for the reconstructed distribution of parameters across experiments. Each credible region ellipse is reconstructed from one sample of the $\boldsymbol{\mu}, \boldsymbol{\Sigma}$ across-experiment distribution parameters from the MCMC chain of size 10^5, for clarity only 200 samples are shown here. **Diagonal (green):** The sampled posterior probability density functions before integration to give $p(\boldsymbol{\theta} \mid \cdots)$, shown in detail in Figure 4.6. **Upper triangle (orange):** The marginal histograms for each entry of the correlation matrix defined by Eq. (4.27). The shadings in the background indicate how these parameters relate to the model structure: the orange box contains the gates a in model, green box contains gate r, and grey relates to the conductance.

sense — as we randomly generated it. However, in real experiments, this correlation matrix tells us which parameters are correlated. That is, if it contains any non-zero values in the off-diagonal with a small credible interval in the orange distributions, then this informs us how the parameters of the model are related.

4.4.4 Validation for the pseudo-Metropolis within Gibbs

The analyses of the experimental results shown in this chapter use the pseudo-MwG method. Here we provide a brief comparison between our pseudo-MwG method and the MwG for approximating the posterior predictive distribution. We use $N_e = 30$ to demonstrate their similarity. The value was chosen as it is similar to the minimum cell yield we found in Chapter 5 and is computationally tractable.

Figure 4.8 shows the posterior predictive distribution and the histograms of the individual experiments constructed from the pseudo-MwG method (solid lines) and the MwG method (dashed lines). It has the same style of plot as in Figure 4.6, where the left-axes show the marginal histograms and the right-axes show the marginal posterior predictive distributions. The posterior predictive distributions constructed from the pseudo-MwG and MwG look very similar. Therefore, with our staircase protocol as the likelihood of the low-level experiments, we are able to simplify our procedure to the pseudo-MwG without losing much accuracy comparing to the MwG algorithm. We expect the agreement to hold for larger N_e as well.

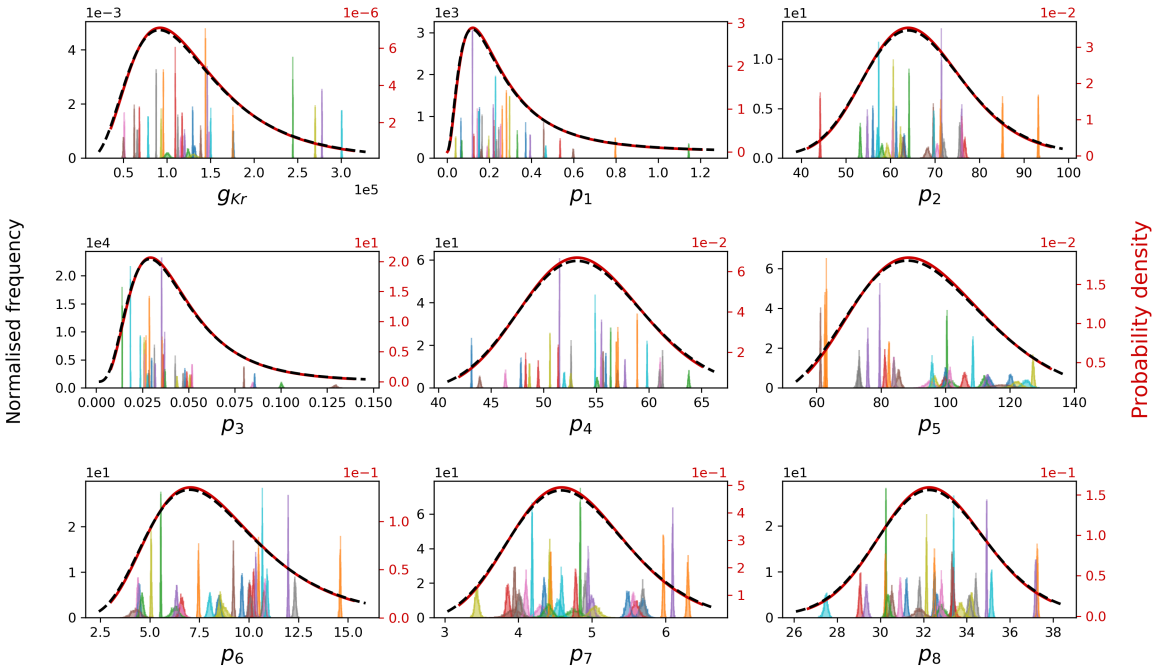

Figure 4.8: Comparing the hierarchical Bayesian model parameter inference on synthetic data using the pseudo-MwG (solid lines) and the MwG (dashed lines) methods, with $N_e = 30$. **Left *y*-axis**: the marginal histograms of the model parameters for each individual experiment. **Right *y*-axis**: the marginal posterior predictive distributions.

4.4.5 Validation for a further simplified Metropolis within Gibbs

Figure 4.9 shows the posterior predictive distribution constructed from the *simplified* pseudo-MwG method (solid lines) and the MwG method (dashed lines). Again, the posterior predictive distributions constructed from the simplified pseudo-MwG and MwG look very similar. Therefore, we can further simplify our pseudo-MwG sampling scheme to estimate the posterior-predictive distribution.

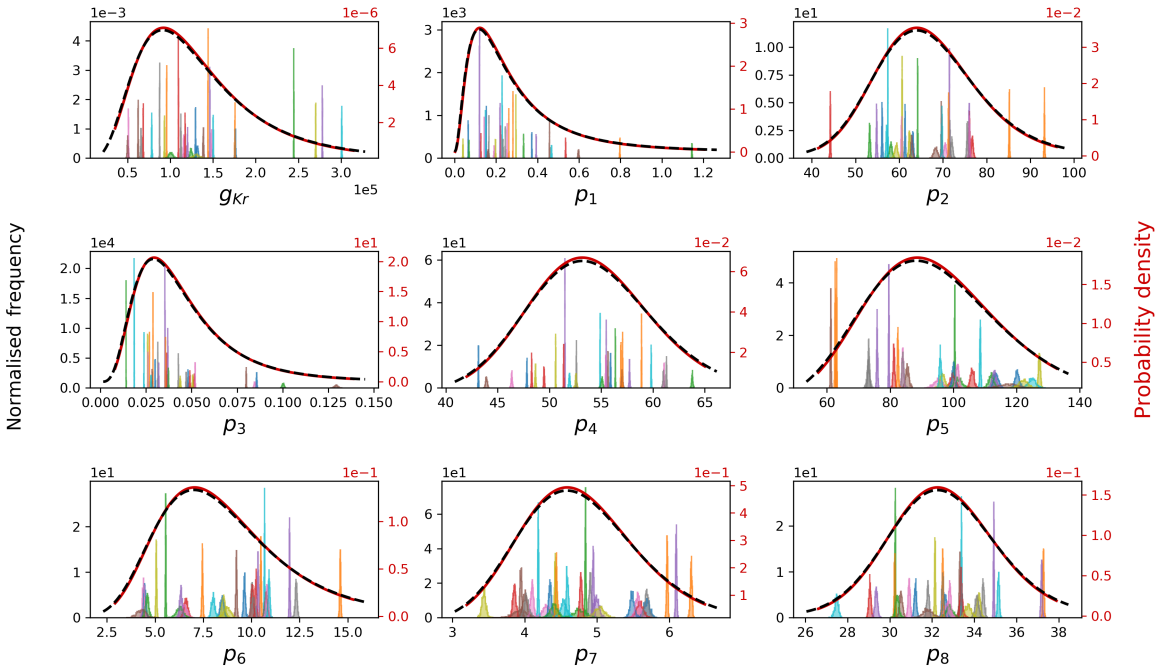

Figure 4.9: Comparing the hierarchical Bayesian model parameter inference on synthetic data using the *simplified* pseudo-MwG (solid lines) and the MwG (dashed lines) methods, with $N_e = 30$. **Left *y*-axis**: the marginal histograms of the model parameters for each individual experiment for the MwG method. **Right *y*-axis**: the marginal posterior predictive distributions.

4.4.6 Convergence to the true distribution

We then check the performance of our method with different numbers of experiments/cells N_e, and confirm that the result converges to the correct answer as N_e increases. We calculate the score with root-mean-square error (RMSE) for the correlation matrix, where

$$\text{RMSE}(\text{corr}) = \frac{1}{N_e}\sqrt{\sum_{i}^{N_e}\sum_{j}^{N_e}\left(\text{corr} - \text{corr}_{\text{true}}\right)^2_{i,j}}, \tag{4.30}$$

and its slight variant root-mean-square percentage error (RMSPE) for standard deviation (std), where

$$\text{RMSPE}(\text{std}) = \sqrt{\frac{1}{N_e}\sum_{i}^{N_e}\left(\frac{\text{std}^i - \text{std}^i_{\text{true}}}{\text{std}^i_{\text{true}}}\right)^2} \times 100\%. \tag{4.31}$$

We used RMSPE, instead of RMSE, for the standard deviation to avoid different parameter magnitudes from dominating the calculation.

Figure 4.10 shows the RMSPE of the standard deviation (left) and RMSE of the correlation (right) as function of the numbers of experiments/cells N_e. For the RMSPE of the standard deviation,

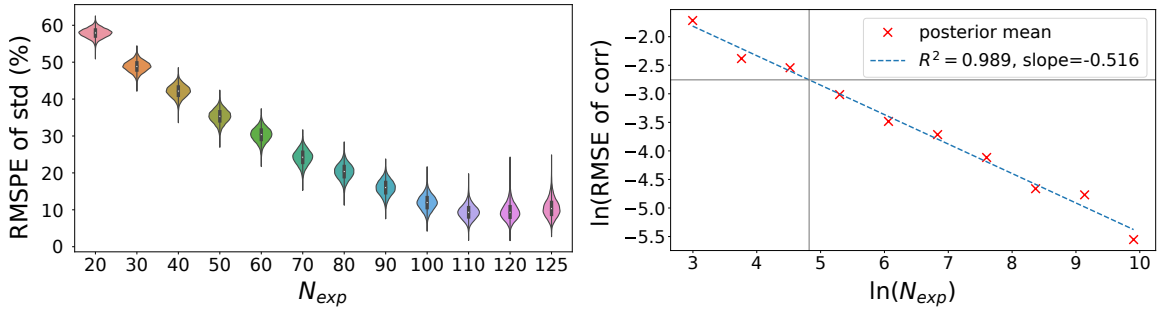

Figure 4.10: The RMSPE of standard deviation (left) and RMSE of correlation (right) as function of the numbers of experiments/cells N_e. Each violin plot and posterior mean is constructed using 10^4 samples. Grey lines show where $N_e = 124$, with an RMSE value of 0.064.

Figure 4.10 (left), we repeated the above analysis with $N_e = 20, 30, ..., 120$ and 125. We can clearly see that the RMSPE of the standard deviation decreases as N_e increases. Hence it is convincing that our method is converging to the true answer in the synthetic data studies.

For the RMSE of the correlation, Figure 4.10 (right), we further test the convergence rate of the RMSE value. To run with sufficiently large N_e, we used the *simplified* pseudo-MwG. With this, we ran N_e up to 2×10^4. We plotted both axes in natural-log scale. We then applied a linear regression, in which a slope of -0.516 is obtained. Therefore, we conclude that convergence rate of the RMSE of the correlation is roughly consistent with $\propto 1/\sqrt{N_e}$. We also expect the likely errors in our experiments in the next sections, with $N_e = 124$, to be about 6.4%, shown as grey lines.

4.5 Experimental Methods

Whole-cell patch-clamp voltage-clamp experiments were performed on Chinese Hamster Ovary (CHO) cells stably transfected with hERG1a (K_V11.1), at 25 °C, using the Nanion SyncroPatch 384PE platform (Nanion Technologies GmbH, Germany), see Figure 4.1. The configuration of the automated patch-clamp setup is very similar to the one shown in Figure 2.4B. I performed all experiments in this chapter at F. Hoffmann-La Roche in Basel. The temperature of the system's 'cell hotel' was set to ~15 °C. The machine is an automated high-throughput platform, in which each run (or chip) is able to measure up to 384 wells (with one cell per well) simultaneously. Single hole chips with medium resistance (Nanion order number #221102) were used.

A schematic of the experimental procedure is shown in Figure 4.11, which also shows the voltage-clamp protocols used in the experiments. A total of nine voltage-clamp protocols were used, including our newly developed staircase protocol (in green), and a sequence of validation protocols (in blue), consisting of an activation I-V protocol, a steady-state inactivation I-V protocol, a hERG screening protocol, a delayed afterdepolarization (DAD)-like protocol, an early afterdepolarization (EAD)-like protocol, and action potential-like protocols with beating frequency 0.5 Hz, 1 Hz and 2 Hz, as shown in Figure 4.11. Note that, due to the automated platform, the action potential-like protocols have to be comprised of a series of linear ramps and steps rather than curves. Details of the protocols are given in Section 4.5.1. Every protocol (the entire procedure in Figure 4.11) was applied to every well.

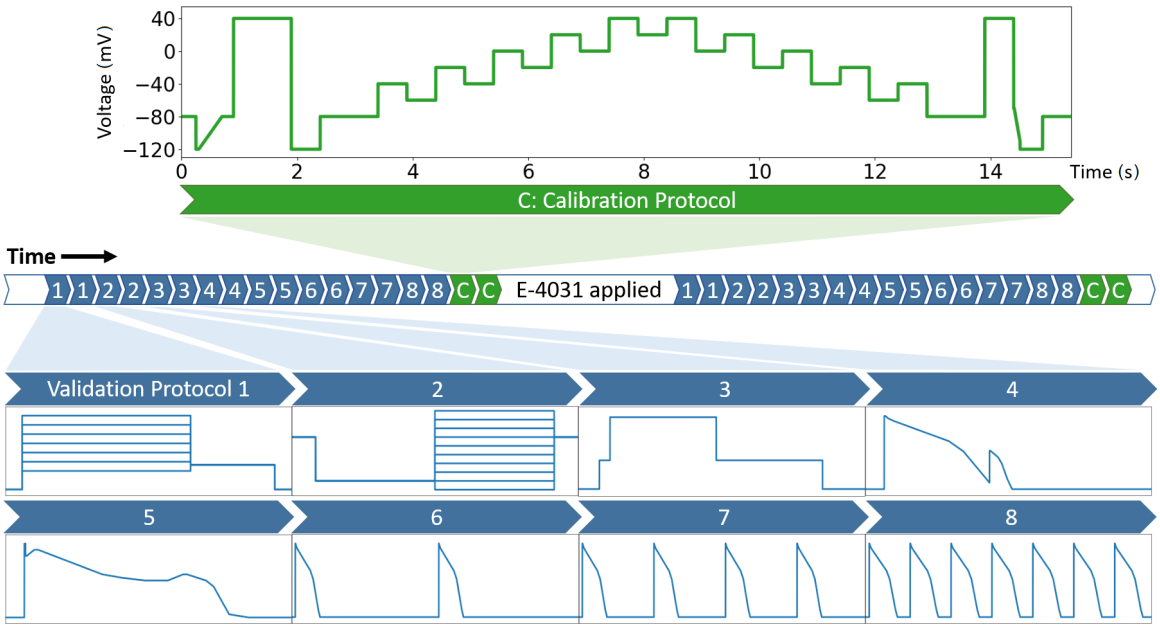

Figure 4.11: A schematic of the experimental procedure showing the sequence of voltage-clamp protocols used. A total of nine voltage-clamp protocols were used, each of them was performed four times: twice before E-4031 addition, and twice after, to ensure stability and reliability of the recordings. Only the staircase protocol (green, 15 seconds) was used for fitting (or calibrating) the mathematical model. All of the other eight protocols (blue) were used for validation only. White sections indicate a non-measurement region, where cells were held at −80 mV to allow the cells to settle to steady state between protocols (>5 s), or were continuously stimulated by the hERG screening protocol to allow the drug to wash in (>5 min). For details of the protocols please refer to Section 4.5.1.

Since our quality control (see Section 4.5.3.3) is primarily based on the calibration recording, we decided to apply the calibration protocol at the end such that we could check the cell is stable for the entire experiment, including the validation protocols.

Only the staircase protocol (green) was used in fitting (or *calibrating*) the mathematical model. We show that we can fully characterise I_{Kr} for each cell using just this one protocol. A demonstration that a mathematical model is able to reproduce the experimental training data is not sufficient to conclude that it is a good representation of ion channel kinetics — in particular, we may be uncertain how well the model performs under physiological conditions. The fitted models for each cell were therefore validated by comparing with experimental data from each of the other eight protocols (blue in Figure 4.11). Our validation set consists of (a) two conventional I-V protocols together with a simple hERG activation step and (b) five physiologically-inspired protocols that mimic cardiac action potentials. The first set allows us to compare with the conventional approach. More importantly, the action potential clamps in the second set allow us to have confidence in predictions of I_{Kr} responses, which is particularly useful when an ion channel model is embedded in a cardiac action potential model. This series of validations aims to demonstrate that the models fitted using this new protocol yield trustworthy cell-specific predictions.

4.5.1 Details of the validation voltage-clamp protocol

4.5.1.1 Validation #1: Activation I-V protocol

From the initial period 100 ms at holding potential of −80 mV, a step to V_{step} for 1 s, followed by a 500 ms step to −40 mV, before a 100 ms step back to holding potential; this was repeated seven times with a different V_{step} on each repeat. V_{step} ranged from −50 mV to 40 mV in 15 mV increments. This protocol is shown in Figure 4.12B.

4.5.1.2 Validation #2: Steady-state inactivation I-V protocol

From the initial period 100 ms at holding potential of −80 mV, a step to 20 mV for 500 ms, followed by a step to V_{step} for 500 ms, before a 100 ms step back to holding potential; this was repeated 10 times with a different V_{step} on each repeat. V_{step} ranged from −140 mV to 40 mV in 20 mV increments. This protocol is depicted in Figure 4.12C.

4.5.1.3 Validation #3: hERG screening protocol

From the initial period 100 ms at holding potential of −80 mV, a step to −40 mV for 50 ms, and a step to 20 mV for 500 ms, followed by a step to −40 mV for 500 ms, before a 200 ms step back to holding potential. This protocol is shown in Figure 4.12D.

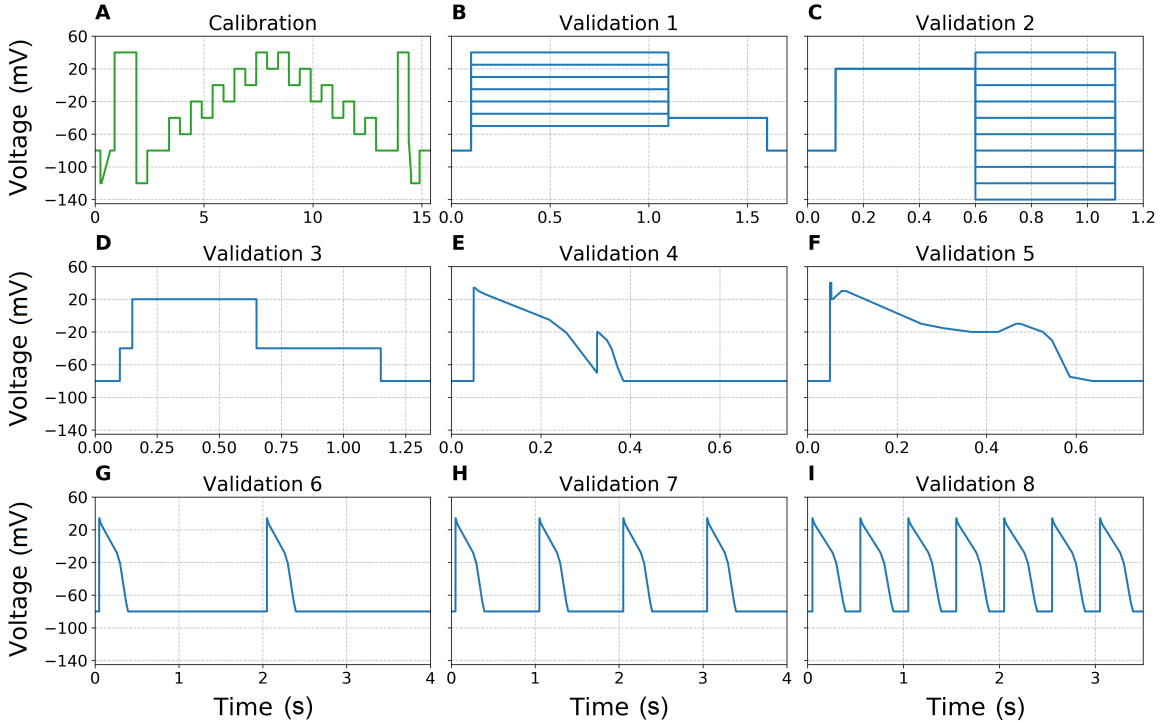

Figure 4.12: All voltage-clamp protocols used in this chapter, from **A** to **I** are (green) our newly developed staircase protocol described in Section 4.2.2, (blue) the activation I-V protocol, the steady-state inactivation I-V protocol, the hERG screening protocol, the DAD-like protocol, the EAD-like protocol, and the action potential-like protocol with beating frequency 0.5 Hz, 1 Hz and 2 Hz. All protocols are shown with the same voltage axes for comparison; however due to the different time scales, each of them has its own time axis.

4.5.1.4 Validations #4-8: DAD-like, EAD-like, action potential-like protocols

Details are described in Table 4.1, and each protocol is shown in Figure 4.12E-I, respectively.

DAD-like protocol

Type	V (mV)	**Duration** (ms)
Step	-80	50
Step	34	3
Ramp	30	8
Ramp	26	15.2
Ramp	-5	142.6
Ramp	-21	38.4
Ramp	-70	68.6
Step	-20	2
Ramp	-30	20
Ramp	-40	10
Ramp	-65	15
Ramp	-80	12
Step	-80	15.2
Step	-80	350

DAD-like protocol

Type	V (mV)	**Duration** (ms)
Step	-80	50
Step	40	3
Step	20	3
Ramp	30	20
Step	30	10
Ramp	-10	168
Ramp	-15.5	50.6
Ramp	-20	61.2
Step	-20	60
Ramp	-10	40
Step	-10	10
Ramp	-20	50
Ramp	-30	20
Ramp	-75	40.5
Ramp	-80	50
Step	-80	13.7
Step	-80	100

Single action potential-like protocol

Type	V (mV)	**Duration** (ms)
Step	-80	50
Step	34	3
Ramp	30	8
Ramp	26	15.2
Ramp	-8	183.6
Ramp	-21	39
Ramp	-68	70.5
Ramp	-80	25.2
Step	-80	—

Table 4.1: Details of the DAD-like (Validation #4), EAD-like (Validation #5), action potential-like (Validations #6-8) protocols. It shows as a sequence of steps and ramps that approximates different types of action potential shapes, as these are the only available settings in the automated machine used. The voltage (V) in the type Ramp represents the final targeted voltage that the ramp finishes, starting from the previous voltage within the given duration; for example, the first ramp in the EAD-like protocol means it starts from 34 mV and ramps to 30 mV in 8 ms. The single action potential-like protocol shows the protocol for one unit action potential-like protocol that repeats in 0.5 Hz, 1 Hz, and 2 Hz.

4.5.2 Electrophysiology solutions

The compositions of all the electrophysiology solutions, including both the external solutions (bath solutions) and the internal solution (equivalent to the pipette solution in manual patch clamp), are shown in Table 4.2. External solutions were added in the following order: first 'fill chip' solution to the measurement chip, and the suspended hERG CHO cells, then the 'seal enhancer' solution for enhancing the seal by forming CaF_2 crystal around the cells (note they have extra high concentration of Ca^{2+}, so we need to reduce/dilute it later), followed by adding the extracellular 'reference' solution for Ca^{2+} dilution. All the voltage-clamp measurements were performed after adding all these external solutions.

The solutions were added sequentially to the wells, by removing half of the previous solutions from the wells each time. Therefore, the final ratios of the external (extracellular) solution are 1:1:2 — proportions of 0.25 of the 'Fill Chip' concentrations, 0.25 of the 'Seal Enhancer' concentrations, and 0.5 of the 'Reference' concentrations, as shown in the 'Extracellular' solution in Table 4.2. For each well, the volume of the final solution during recording is 80 μL.

4.5.3 Post-processing experimental data

We assumed that our observed current from hERG CHO cells under control conditions is

$$I_{\text{observed}}^{\text{control}} = I_{\text{Kr}} + I_{\text{contaminating}} + I_{\text{leak}}^{\text{a}}. \tag{4.32}$$

Solution		Intracellular	Fill Chip	Seal Enhancer	Reference	Extracellular
pH value (titrated with)		7.2 (KOH)	7.4 (NaOH)	7.4 (HCl)	7.4 (HCl)	—
Osmolarity (mOsm)		260-300	300-330	290-330	290-330	—
Chemicals	**Source / Cat#**	**[ ] in** mM	**[ ] in** mM	**[ ] in** mM	**[ ] in** mM	**[ ] in** mM
NaCl	Merck / K38447104807	10	150	80	80	97.5
KCl	Merck / K36782536	10	4	4	4	4
KF	Acros Organics / 201352500	100	—	—	—	—
$MgCl_2$	Merck / A914133908	—	1	1	1	1
$CaCl_2$	Acros Organics/ 349615000	—	1.2	5	1	2.05
HEPES	Applichem A1069	10	10	10	10	10
Glucose	Fluka / 49159	—	5	5	5	5
NMDG	Fluka 66930	—	—	60	40	35
EGTA	Fluka / 03778	20	—	—	—	—
Sorbitol	Sigma / S1876	—	—	—	40	20

Table 4.2: Electrophysiology solutions for hERG CHO cell experiments on the Nanion SyncroPatch 384PE machine, all solutions are sterile filtered. All hERG CHO cells were suspended in $1/3$ extracellular 'fill chip' solution $+$ $2/3$ Hanks' Balanced Salt Solution (HBSS).

To ensure the currents we analyse are predominantly I_{Kr}, we performed a series of offline post-processing corrections to remove the leak current $I^{\text{a}}_{\text{leak}}$ and any other currents contaminating the recording $I_{\text{contaminating}}$. First, linear leak corrections were applied to all measurements to eliminate the leak current $I^{\text{a}}_{\text{leak}}$. Second, E-4031 subtraction was applied to remove the contaminating background currents $I_{\text{contaminating}}$. These corrections are described in detail in the rest of this section, as well as our partially-automated quality control criteria.

4.5.3.1 hERG-specific block subtraction

To eliminate any contaminating voltage-dependent background currents in the measurements, $I_{\text{contaminating}}$ in Eq (4.32), we measured the full set of nine voltage protocols twice, see Figure 4.11; once with dimethyl sulfoxide (DMSO) vehicle conditions in which $I^{\text{control}}_{\text{observed}}$ in Eq. (4.32) was measured, and once under the addition of 0.5 μM E-4031, a hERG channel selective blocker with IC_{50} value $\lesssim$10 nM, so that the leftover current

$$I^{\text{E-4031}}_{\text{observed}} = I_{\text{contaminating}} + I^{\text{b}}_{\text{leak}}. \tag{4.33}$$

$I_{\text{contaminating}}$ was thought to be endogenous current, i.e. the sum of any native voltage-dependent ion currents that were present in CHO cells alongside the overexpressed hERG, however we later found that it was mostly another form of leak current, see the note discussed below. We denoted the new leak current as $I^{\text{b}}_{\text{leak}}$, and we assumed the leak current changed over time, hence in general $I^{\text{b}}_{\text{leak}} \neq I^{\text{a}}_{\text{leak}}$.

As shown in Figure 4.11, a period of $\sim$5 min was allowed for the E-4031 block to reach equilibrium, and multiple hERG screening protocols were applied to allow opening of the hERG channel (Ishii et al., 2003). All currents shown or used in this chapter are the leak corrected currents measured in control conditions minus the leak corrected currents that remained after E-4031 addition, which we assume yields uncontaminated I_{Kr}.

Note: later in Lei et al. (2020b), a publication that I led, we discovered that the leftover current in Eq. (4.33) was due to the presence of the CaF_2 crystal for seal enhancement (see Chapter 2), giving

rise to another form of non-biological leak current. We have shown that most of this leftover current can be reproduced on a manual patch clamping setup using the same F^- containing internal and Ca^{2+} containing external solutions without any biological cell, and can be eliminated by simply removing the F^- containing solution. This current is what we termed the nonlinear time-dependent leak current in Lei et al. (2020b). Nevertheless, the post-processing procedure described in this section can still be used to eliminate most of the unmodelled currents as discussed in Lei et al. (2020b).

4.5.3.2 Leak correction

We use the model in Eq. (4.7) to estimate the leak current $I_{\text{leak}}^{\text{est.}}$. If we subtract an estimated leak off both $I_{\text{observed}}^{\text{control}}$ and $I_{\text{observed}}^{\text{E-4031}}$ then our final I_{Kr} is given by

$$I_{\text{Kr}} \approx \underbrace{\overbrace{\left(I_{\text{observed}}^{\text{control}} - I_{\text{leak}}^{\text{est. a}}\right)}^{\text{Leak correction}} - \overbrace{\left(I_{\text{observed}}^{\text{E-4031}} - I_{\text{leak}}^{\text{est. b}}\right)}^{\text{Leak correction}}}_{\text{E-4031 subtraction}}, \tag{4.34}$$

where $I_{\text{leak}}^{\text{est. a}}$, $I_{\text{leak}}^{\text{est. b}}$ are leak currents estimated using Eq. (4.7). Depending on the protocol, we estimate the parameters $g_{\text{leak}}, E_{\text{leak}}$ in one of two ways; either by using a step between two voltages or by using a linear ramp, as discussed below.

For the staircase protocol, which was used for model calibration, we used the leak ramp implemented at the first second of the staircase protocol to estimate the leak current. Figure 4.3 shows the use of the leak ramp for inferring the leak model parameters; the recorded current during the ramp shows a reliably good linear relation.

In a similar fashion, for *all* validation protocols, instead of a linear ramp, a conventional step method was used. A 20 ms leak-step from −80 mV to −100 mV was used to leak-correct the experimental data. This method was implemented and performed automatically by the platform we used before every protocol to correct the recording that followed. However, we noticed that some of these leak corrections can 'over-correct' or 'under-correct' the current. For example, I_{Kr} should only be negative when the voltage is below its reversal potential, approximately −85.2 mV, if the leak-corrected current showed a negative current at voltages substantially larger than the reversal potential, then we conclude that the automated system had overestimated the leak current. Such over-correction or under-correction was most noticeable during the highest voltage step during the protocol, where I_{leak} was at its maximum. For each validation protocol, we then specified a time-window where we believe I_{Kr} should be almost zero (please refer to the GitHub repository provided at the end of this chapter for the specified time-window values). To rectify the over- or under-correction, we re-estimated the leak correction by adding an extra linear leak current of the form $g_{\text{leak}}^{*}(V + 80\,\text{mV})$, where g_{leak}^{*} was chosen such that the average of the final leak-corrected current during the specified time-window was zero. Due to the linearity, the final leak correction remains the same form as Eq. (4.7) but with different parameter values.

QC name	Criterion description
QC1.rseal	Check R_{seal} within [0.1, 1000] GΩ.
QC1.cm	Check C_{m} within [1, 100] pF.
QC1.rseries	Check R_{series} within [1, 25] MΩ.
QC2.raw	Check raw trace recording SNR is over 25 (SNR defined as var(trace) / var(noise)).
QC2.subtracted	Check subtracted trace SNR > 25.
QC3.raw	Check 2 sweeps of raw trace recording are similar by comparing the RMSD of the two sweeps < mean(RMSD to zero of the two sweeps) × 0.2.
QC3.E4031	Check 2 sweeps of E-4031 trace recording are similar (same comparison as QC3.raw).
QC3.subtracted	Check 2 sweeps of subtracted trace recording are similar (same comparison as QC3.raw).
QC4.(...)	Check R_{seal}, C_{m}, R_{series}, respectively, before and after E-4031 change (defined as std / mean) < 0.5.
QC5.staircase	Check the maximum current during the second half of the staircase changes by at least 75% of the raw trace after E-4031 addition.
QC5.1.staircase	Check RMSD to zero of staircase protocol changes by at least 50% of the raw trace after E-4031 addition.
QC6.subtracted	Check the first step up to +40 mV, before the staircase, in the subtracted trace is bigger than −2 × estimated noise level.
QC6.1.subtracted	Check the first +40 mV during the staircase, with the same criterion as QC6.subtracted.
QC6.2.subtracted	Check the second +40 mV during the staircase, with the same criterion as QC6.subtracted.

Table 4.3: A summary of the fully automated quality control criteria for the staircase protocol, QC1–QC6. RMSD, root-mean-square distance; SNR, signal-to-noise ratio; std, standard deviation; var, variance.

4.5.3.3 Partially automated quality control

After the experiments, we applied a set of criteria as an automated selection process for quality control of our experimental data. The details of our six criteria are summarised in Table 4.3. As the first quality control criterion, QC1, we applied a cut-off for seal resistance (R_{seal}), cell capacitance (C_{m}), and series resistance (R_{series}) through the whole set of measurements. QC2 required a high SNR recording, such that our measurements contained enough useful information for model inference. We also compared the stability of the recordings in QC3, where each protocol consisted of two measurements recorded in the same cell that must be similar and stable. QC4 required R_{seal}, C_{m}, and R_{series} to be stable before and after E-4031 addition. QC5 required that the addition of hERG blocker E-4031 must reduce a certain amount of the recorded current, to ensure that our recordings consisted mainly of I_{Kr} even before adding the blocker. Finally, over-correction of leak can occur during high voltage steps, as discussed in Section 4.5.3.2, QC6 ensured that no negative current occurred at voltages substantially larger than the reversal potential. Note that, QC1 to QC4 are general criteria that are advocated to be used in all whole cell patch-clamp voltage-clamp experiments, whereas QC5 and QC6 contain prior knowledge of I_{Kr} and are tailored to hERG measurements.

Using our automated high-throughput system, we recorded a total of 384 well recordings. Our automated quality control removed 173 wells, leaving 211 well recordings. We then manually checked all the recordings, and subsequently removed a further 28 wells that were not similar to the rest of the 183 cells, six examples are shown in Figure 4.13. We found our manually removed recordings fall into two main categories, as shown in orange and red; the good recordings (green) are shown for comparison. For the first category (orange), although they seem to contain I_{Kr}, they were heavily 'contaminated' by other signals which were most probably a combination of leak and endogenous (or nonlinear time-dependent leak) currents. For the second category (red), the recordings lacked any characteristic dynamics of I_{Kr}; for example during the first big repolarising step from 40 mV to −120 mV, the recordings do not show any negative spikes that we would associate with

hERG opening. None of these were considered to be good recordings of I_{Kr}. Therefore our automated quality control has achieved >86% positive predictive value for selecting the bad recordings. The machine's 'standard' quality control selects wells mainly based on the R_{seal}, C_m, and R_{series} values, which were set to the same values we used in our automated QC1 in Table 4.3, and removed only 46 wells (which were all within our 173 discarded wells), i.e. with a <23% positive predictive value. Our automated quality control software is available online, see Data and Software Availability at the end of this chapter.

Our mostly-automated quality control was applied only to the staircase calibration protocol. Here, we further require our validation data to contain high quality validation recordings. We therefore manually selected 124 cells within our 183 cells that passed our quality control and hence have good recordings for both calibration and validation protocols; this ensures the quality of the experimental data used in this chapter. The overall success rate of recording our staircase protocol is 183 of 384 wells and for the full set of protocols is 124 of 384 wells, which can be performed within one hour.

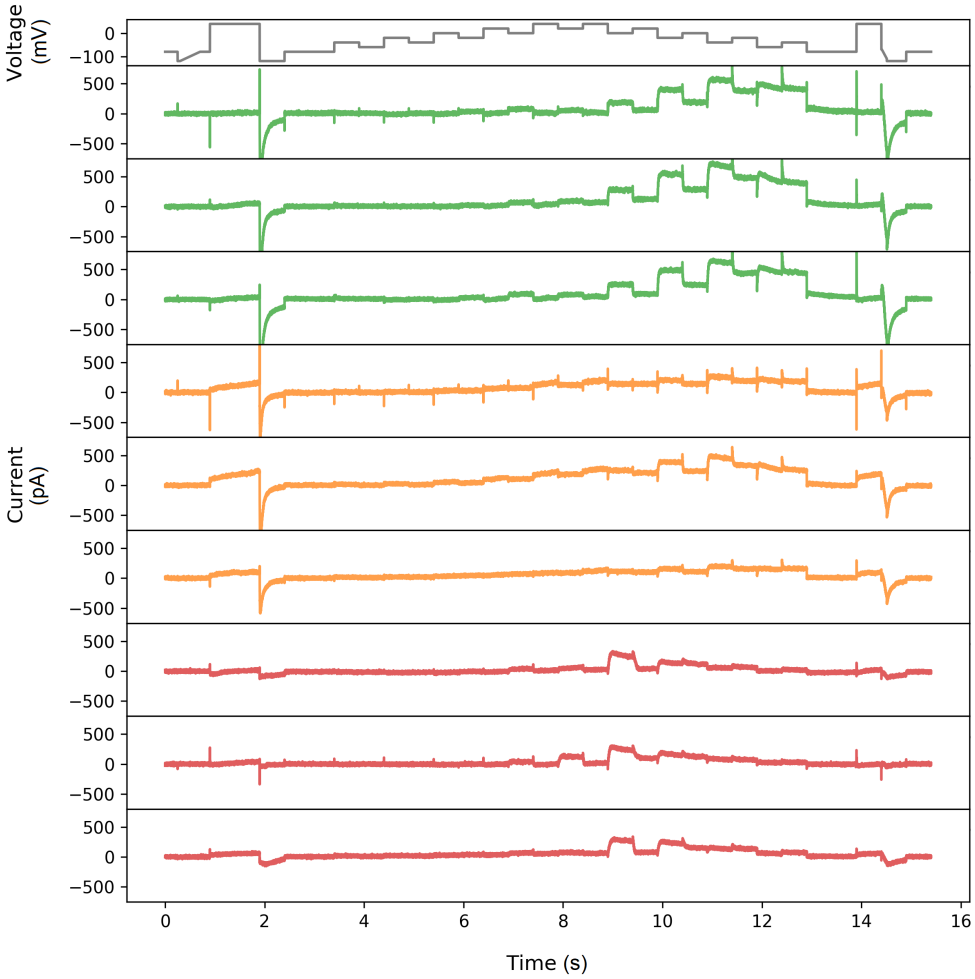

Figure 4.13: A comparison of the recordings that pass the automated quality control and those that we manually removed. Top panel shows our staircase protocol. Following are three good recordings (green) and six manually removed recordings (orange/red). We found our manually removed recordings fall into two main categories, which are the recordings that were heavily 'contaminated' by other signals (orange) and the recordings that lacked any characteristic dynamics of I_{Kr} (red).

4.6 Results of High-Throughput Experiments

4.6.1 High-throughput experimental recordings

Figure 4.14 shows the voltage-clamp recordings measured with the nine different protocols, and the corresponding voltage protocols. All results shown are the first of the two repeats of our recordings. Our analysis was repeated for the second of the two repeats to ensure the reproducibility of our results in the same cells: the intrinsic (within-cell) variability is sufficiently small to be negligible, see Figure 4.18.

Figure 4.14A shows the staircase protocol (black) and the corresponding experimental recordings (blue). The middle panel shows the raw current recording of a single cell; the bottom panel shows the normalised current recordings from all 124 wells that passed quality control. Normalisation is applied for visual comparison only, as each hERG-transfected CHO cell is expected to have a different total conductance hence giving a different magnitude of the current recorded. Currents are normalised by scaling them to minimise the absolute difference between each trace and a reference trace (middle panel). Since the reference trace is used only to normalise other traces for visualisation, and is not used in model fitting, we simply picked a representative trace from our data that had reasonably low noise. Our recordings show a very similar result to the I_{Kr} simulation shown in Figure 4.2, and the simulated result used parameters calculated/fitted completely independently by Beattie et al. (2018).

Figure 4.14B–I show the recordings of the other eight validation protocols from the *same cells*. The activation step in Figure 4.14D recorded a typical I_{Kr} response, where the step down of voltage to −40 mV largely opens the channels. Figure 4.14G–I also shows typical I_{Kr} responses to the action-potential clamp at different pacing frequencies, where I_{Kr} is active during repolarisation of the action potential. Also note the sharp opening of I_{Kr} at the upstroke which changes with pacing frequencies and increases dramatically but very consistently across all the recorded cells.

4.6.2 Individual cell fitting and validation

Figure 4.15 shows the same voltage-clamp recordings (blue) in Figure 4.14, measured under the nine different protocols (black), together with model fitting and validation results. All recordings shown were performed on a *single cell*. The mathematical model, shown as red lines, is fitted *only* to the data recorded under the staircase protocol that is shown in Figure 4.15A. The result of the fitting for a single cell is shown in the middle panel of Figure 4.15A, demonstrating an excellent fit between experimental measurement and simulated current. The inferred parameters are shown and studied in detail in the next three sections.

In Figure 4.15B–I, we show the results of the validation predictions under eight other protocols. We validated our trained model by testing its ability to predict independent experimental outcomes under different protocols, which were measured *in the same cell*. All validation predictions were performed by using the inferred parameters in the fit to the staircase protocol (Figure 4.15A) to simulate the other eight protocols (Figure 4.15B–I). The predictions of all the protocols match very well to the experimental data, with the simulated currents giving a close match to the experimental recordings.

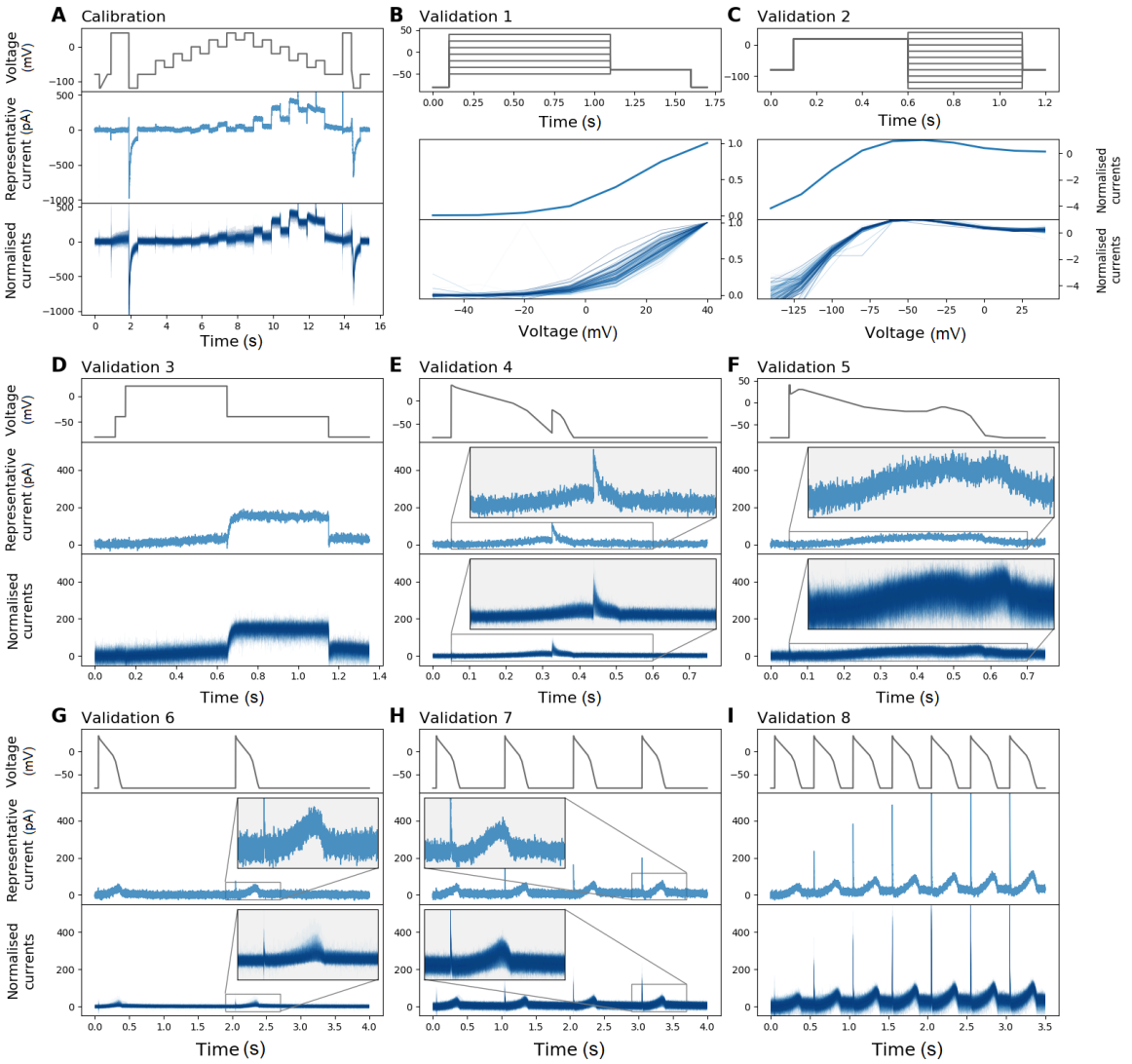

Figure 4.14: Whole-cell patch-clamp voltage-clamp recordings under nine different protocols which were all measured in each cell. **(A)** Shows the staircase protocol (top panel) in black and the corresponding recording on a single cell (middle panel) and normalised recordings from all 124/384 wells that passed quality control (bottom panel) in blue. Conductance normalisation was done by multiplying each current by a scaling factor to minimise the absolute difference between each trace and a reference trace (middle panel). **(B)**–**(I)** The eight different protocols used as validation of the model calibration. All experimental recordings, both the single cell (middle) and 124 cells (bottom), are shown in blue, which were measured under the protocol (black) shown in the panels immediately above. In **(B)** and **(C)**, Validation #1 and #2 show the I-V relations extracted from the currents.

The physiologically-inspired voltage-clamp protocols (Figure 4.15E–I) mimic the membrane voltage of the cardiac action potential at normal conditions at different beating rate and EAD/DAD-like conditions. The ability to predict the current response under these physiologically-inspired voltage-clamp protocols is particularly important for use in physiological or pharmacological studies. This shows the reliability of the hERG ion-channel model predictions at different physiological conditions, for example, when it is embedded in a whole-cell cardiac model for further predictions.

In Figure 4.16 we present our model fitting and validation results for all 124 cells, compared against

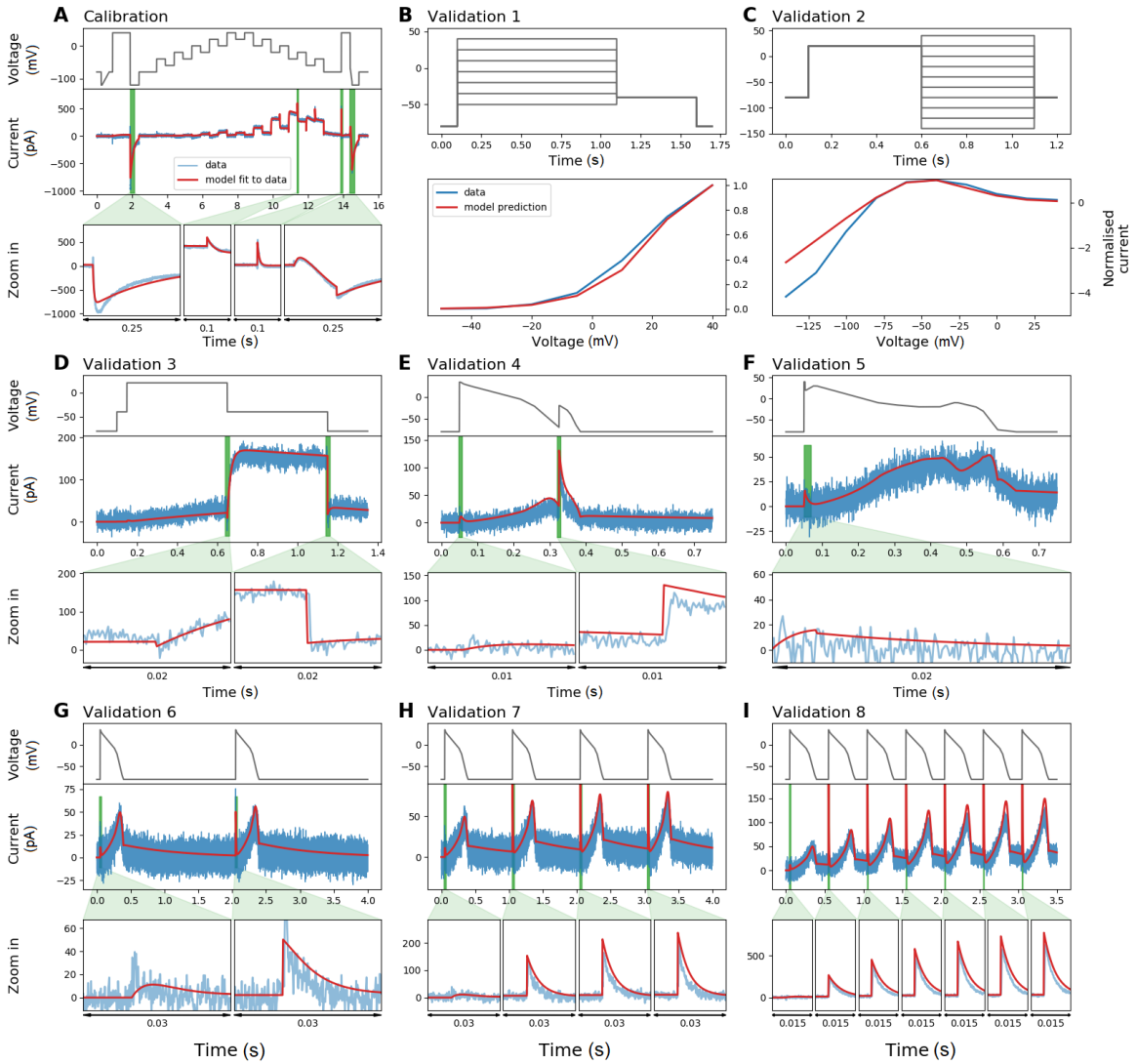

Figure 4.15: Whole-cell patch-clamp voltage-clamp recordings under nine different protocols which were measured on a single cell, and the model fitting and validation results. **(A)** Shows the staircase protocol (black) and the corresponding recording (blue). The mathematical model is calibrated using this recorded data, and shown as a red line. **(B)**–**(I)** The eight different protocols used as validation of the calibrated model. All experimental recordings are shown in blue, which were measured under the protocol (black) shown in the panels immediately above, and the validation predictions of the model are shown in red. Zoomed-in image of the green shaded regions are shown underneath each panel to reveal the details of the spikes, in which our model also shows excellent predictions of the faster timescale behaviour. In **(B)** and **(C)**, Validation #1 and #2 show the I-V relations extracted from the currents.

the experimental recordings measured under the nine different protocols. We applied the same fitting and validation procedure, as used for the single cell discussed above, to all 124 cell measurements. To visualise the variability in only hERG kinetics (and not maximum conductance), we plotted all currents normalised as described in the previous section.

We quantified the fits and predictions using RRMSE defined as the root-mean-square error between the model simulation and the experimental data, divided by the root-mean-square distance of the data

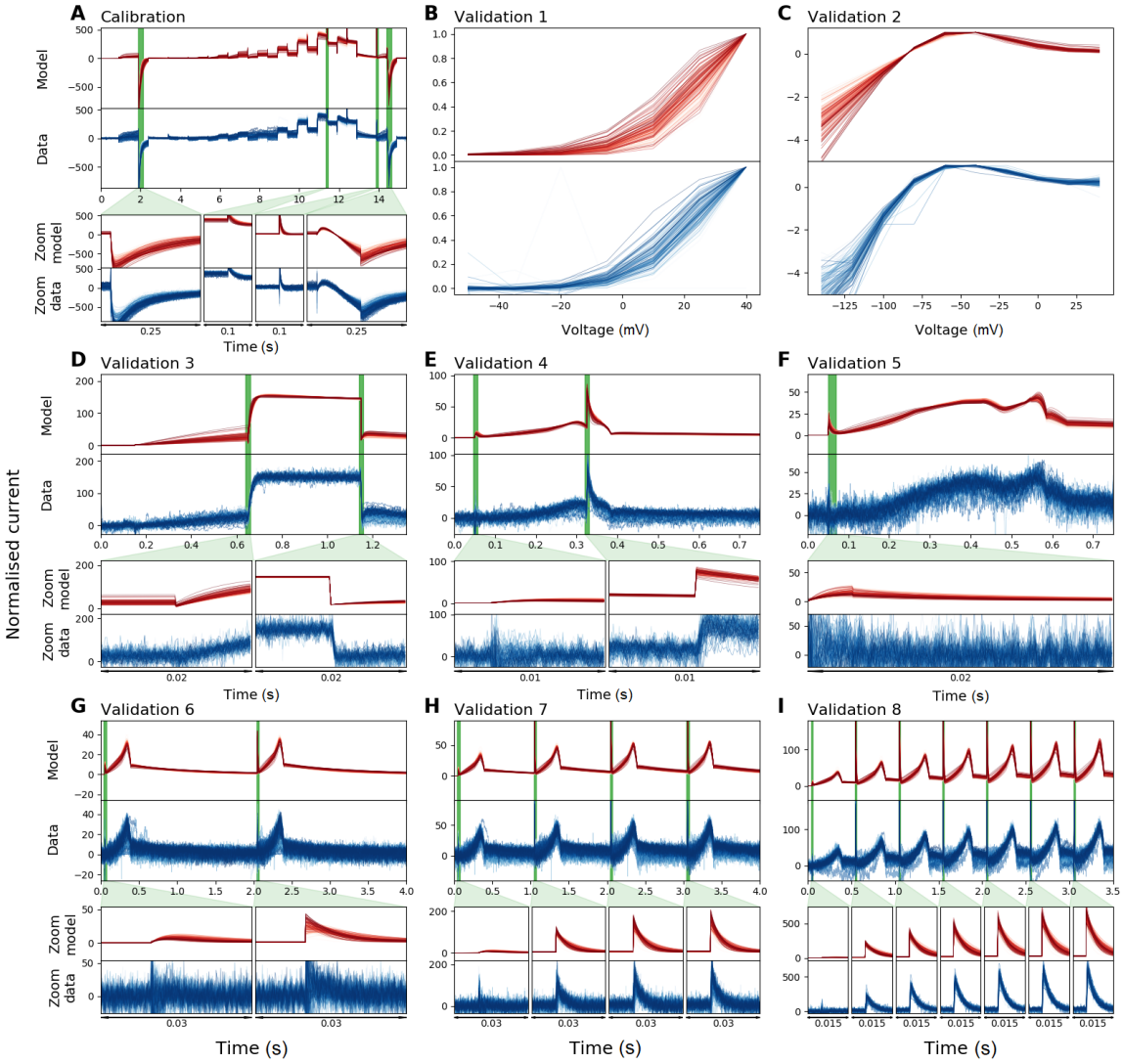

Figure 4.16: Normalised whole-cell patch-clamp voltage-clamp recordings for 124 cells under nine different protocols, and the model fitting and validation results. All currents are normalised by scaling them to minimise the absolute difference between each trace and a reference trace. **(A)–(I)** The staircase protocol which is used as the calibration protocol, and a sequence of validation protocols. All the model calibration results and validation predictions are shown in the top panels (red), and are compared against the experimental recordings shown in the bottom panels (blue). Magnifications of the green shaded regions are shown underneath each panel to reveal the details of the spikes, in which our models show extraordinarily good predictions to the details. The normalised current for all protocols are shown except for the activation I-V protocol and the steady-state inactivation I-V protocol where the summary statistic I-V relationships are shown.

to a zero current trace:

$$\text{RRMSE} = \sqrt{\sum \left(I_{\text{Kr}}^{\text{model}} - I_{\text{Kr}}^{\text{data}}\right)^2 \Big/ \sum \left(I_{\text{Kr}}^{\text{data}}\right)^2}. \tag{4.35}$$

Using this RRMSE quantification, the difference in the absolute size of the current across cells due to varying conductance is eliminated, and RRMSE scores are comparable between cells. Figure 4.17 shows the RRMSE histograms for all cells and for all of the protocols. Markers indicate the best ($*$), median (‡) and 90$^{\text{th}}$ percentile (#) RRMSE values, and corresponding raw traces are shown in the three panels above. The diamond marker ♦ indicates the reference cell shown in Figures 4.14 and 4.15.

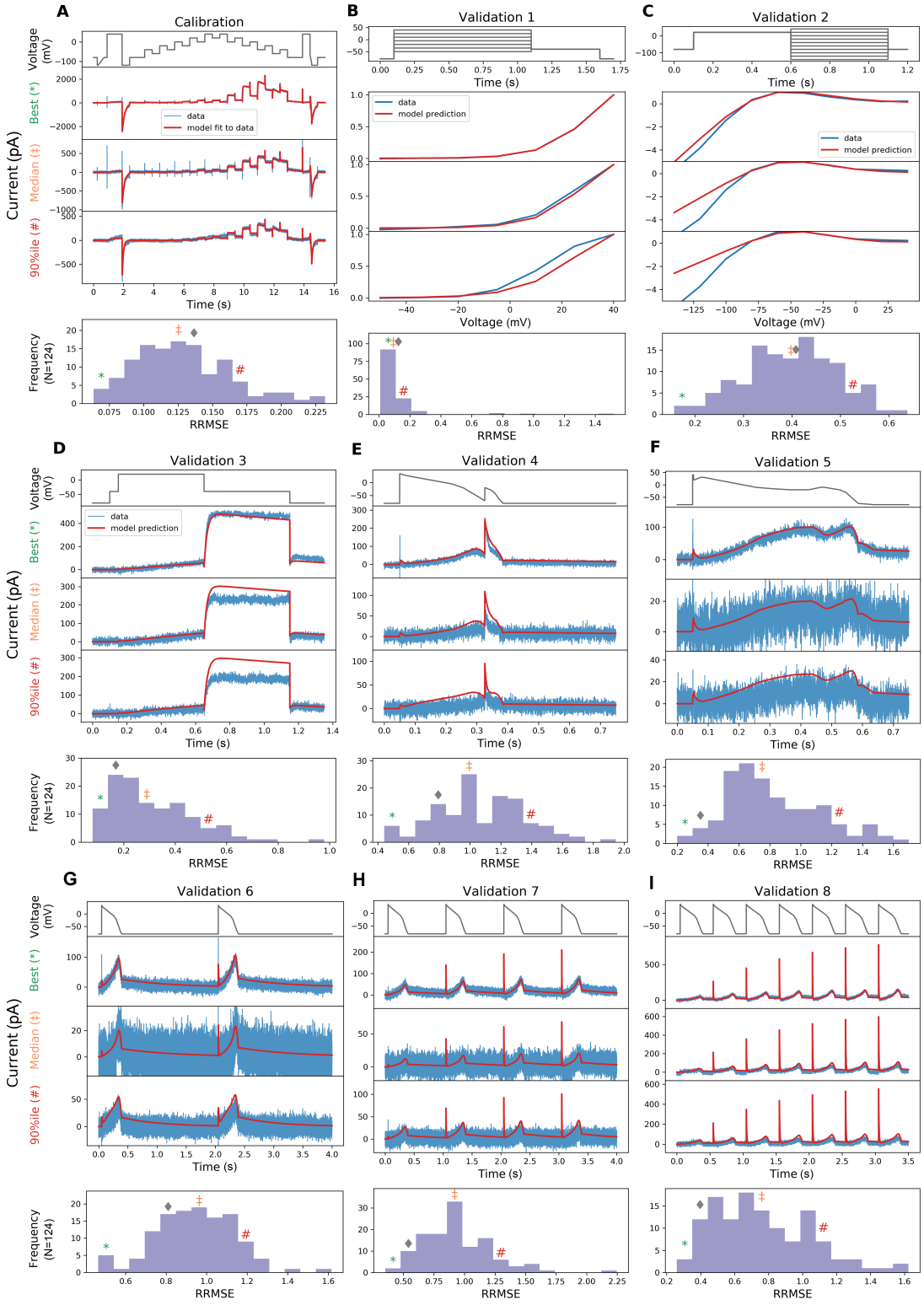

Figure 4.17: The relative root-mean-square error (RRMSE, given by Eq. (4.35)) histograms for all protocols. Each histogram represents the same 124 cells with a different protocol and relative root-mean-square error (RRMSE) each time. Markers indicate the best (∗), median (‡) and 90$^{\text{th}}$ percentile (#) RRMSE values, and diamond marker (♦) indicates the error for the reference traces shown in Figures 4.14 and 4.15. **(A)–(I)** Show the staircase protocol, and a sequence of validation protocols. For each protocol, the raw traces with the best, median and 90$^{\text{th}}$ percentile RRMSE values, for both the model (red) and data (blue) are shown, with the voltage clamp above. Note that the currents are shown on different scales, to reveal the details of the traces.

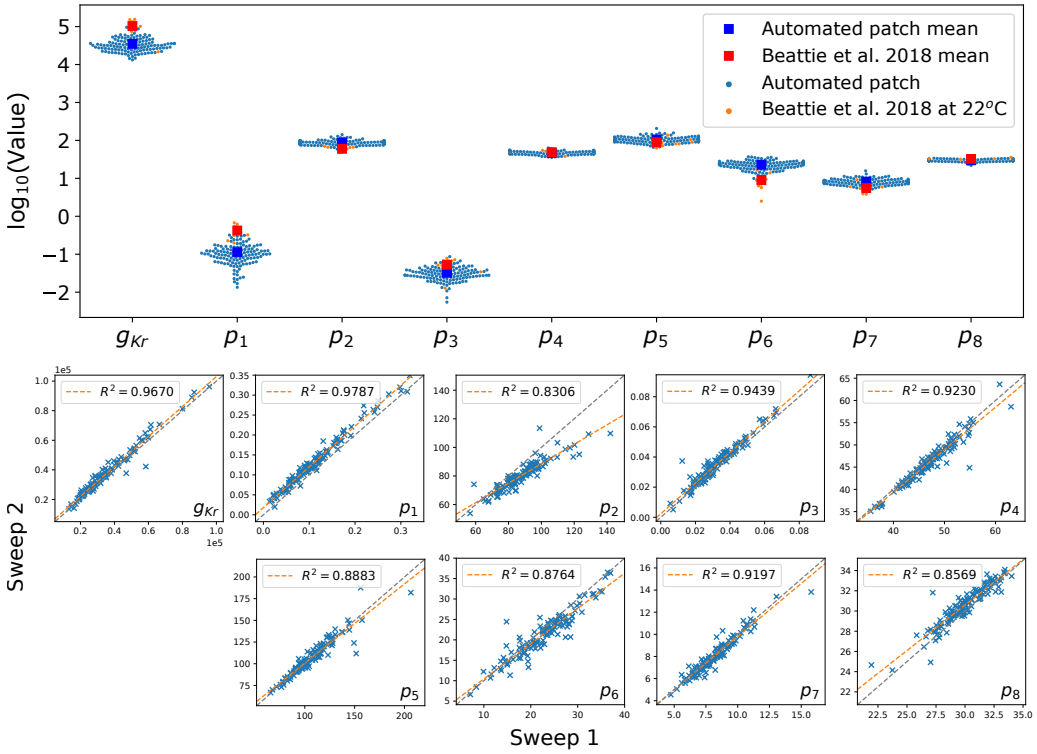

Figure 4.18: Cell-specific model parameters at around 25 °C. **(Top)** The inferred parameter values shown here are obtained from the staircase protocol calibration and are also the parameters used in the model predictions in Figure 4.16. It also shows the manual patch obtained parameters (orange), measured at around 22 °C, from Beattie et al. (2018). The inferred kinetic parameter values from the automated high-throughput system are broadly consistent with the manual patch measurements. **(Bottom)** A comparison of the two repeats of the measurements, using the same analysing method. It shows that our results are reproducible in the same cells, and the intrinsic (within-cell) variability is relatively small compared to extrinsic (between-cell) variability.

There are some small discrepancies in the predictions, for example in Figure 4.17B in the 90$^{\text{th}}$ percentile predictions. But overall these results demonstrate that all our 124 models make very good predictions for the recorded current kinetics.

Next, we qualitatively inspect the variability in the hERG kinetics measurements. Since we measured the I_{Kr} using exactly the same experimental set-up for each cell, we can clearly see the variability *between measurements* in all of the recordings, as illustrated in Figure 4.16. Different protocols demonstrate different levels of variation. It is clear that, amongst the six protocols, the staircase protocol and the two I-V protocols show the strongest variation between measurements.

To investigate this further, we have used our mathematical model to study the variability in the parameter values that could drive the observed variability in the outputs. Figure 4.18 shows the inferred parameter values which are used in the model predictions in Figure 4.16. Since we assume all cells share the same mechanistic model underlying the hERG currents our inferred cell-specific model parameters capture the cell-to-cell variability, or rather experiment-to-experiment variability. In Figure 4.18, our inferred parameters are plotted against manual patch parameters (shown as orange dots/red squares), measured at a slightly lower (room) temperature, from Beattie et al. (2018); our identified parameters are broadly in alignment with manual patch results. This agreement gives us

further confidence that our high-throughput method is reproducible, and results are meaningful. We can also see that there is more variability in some parameters than others, also seen in the previous study (Beattie et al., 2018). In particular, p_1, p_3, and p_6 show stronger variability, which vary over an order of magnitude while the others vary only within an order of magnitude. Conductance g_{Kr} also varies significantly, but this might be expected given different expression levels for individual cells.

4.6.3 Well-to-well variability characterisation

We applied the hierarchical Bayesian model to analyse the variability within the experimental recordings and correlations between inferred well-to-well parameter sets. The result of applying our hierarchical model is shown in Figure 4.19. The measurement uncertainty for the parameters of *each individual well* is shown with a marginal posterior distribution — the coloured histograms. Most of the parameters give a narrow credible interval, which reinforces our certainty in the information content of the calibration protocol. Many of the distributions of the individual wells overlap — that is, we cannot distinguish between the two sets of parameters given our uncertainty in them. However, some of the individual distributions are distinct from each other, demonstrating considerable variability *between wells*.

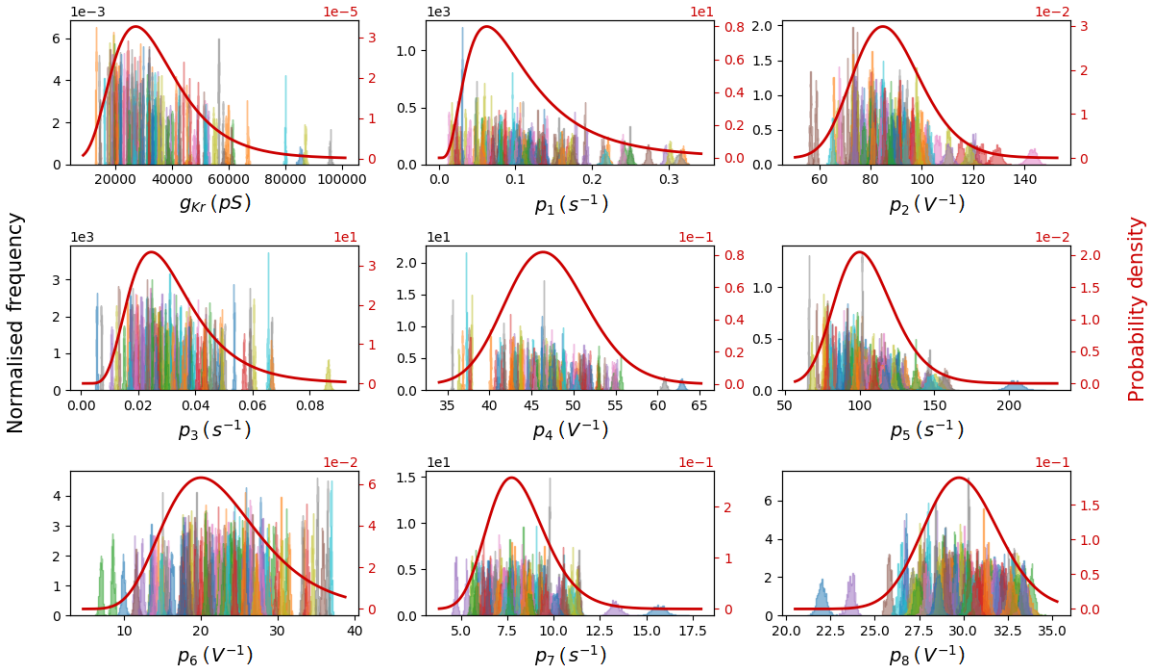

Figure 4.19: The marginal distributions from the hierarchical Bayesian model for all model parameters. **Left *y*-axis:** Individual histograms — the normalised marginals (probability densities) for each parameter in each well, with different colours representing the 124 individual wells. Each of them show a narrow distribution which implies good confidence in our inferred parameters for the individual well. **Right *y*-axis:** Red distribution — the marginal posterior predictive distributions across-cells $p(\boldsymbol{\theta} \mid \ldots)$, which are assumed to follow a multivariate log-normal distribution for each parameter are shown as red curves. They are the inferred underlying distribution between cells for each of the parameters.

The power of the hierarchical Bayesian model can then be used to summarise and capture the experiment-to-experiment variability. The hyperparameters of the model describe both the mean $\boldsymbol{\mu}$

	g_{Kr} (pS)	p_1 (s^{-1})	p_2 (V^{-1})	p_3 (s^{-1})	p_4 (V^{-1})	p_5 (s^{-1})	p_6 (V^{-1})	p_7 (s^{-1})	p_8 (V^{-1})
Mean	3.23×10^4	0.0948	86.9	0.0298	46.9	104	21.9	8.05	29.9
95th %ile (mean)	3.00×10^4 3.48×10^4	0.0843 0.106	84.5 89.3	0.0276 0.0323	46.0 47.8	100 107	20.8 23.1	7.77 8.34	29.5 30.3
95th %ile (exp)	1.42×10^4 7.36×10^4	0.0259 0.346	63.6 119	0.0124 0.0718	38.0 57.8	70.6 152	12.0 40.1	5.43 11.9	25.9 34.5

Table 4.4: The mean values of the model parameters model parameters $\boldsymbol{\mu}$ in Eq. (4.19). The two set of 95th percentiles are the 95% credible intervals of (mean) the uncertainty of the mean parameter vector $\boldsymbol{\mu}$; and (exp) the posterior predictive distribution.

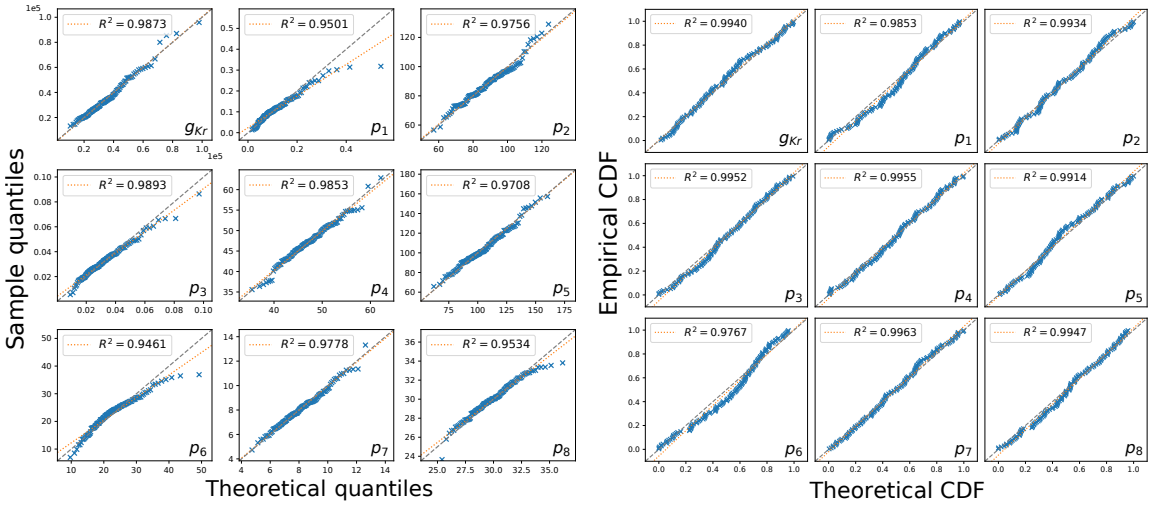

Figure 4.20: Quantile-quantile (Q-Q; **left**) and probability-probability (P-P; **right**) plots of the 124 individual experiments and our posterior predictive distribution. For each parameter, (**left**) the quantiles of the marginal posterior predictive distribution (theoretical quantiles) are plotted against the quantiles of the posterior mean of the 124 cells (sample quantiles); (**right**) the cumulative distribution of the marginal posterior predictive distribution (theoretical CDF) are plotted against the cumulative distribution of the posterior mean of the 124 cells (empirical CDF). It shows that the posterior predictive distribution is an appropriate distribution for the data.

and (co-)variance $\boldsymbol{\Sigma}$ of parameter sets across wells, with experimental uncertainty taken into account. We estimated this posterior predictive distribution in Eq. (4.28) using the samples of hyperparameters (the mean and covariance matrix of the individual cell's parameters), and its marginal distributions are shown for each parameter as the red curves in Figure 4.19. This distribution can be used to *predict* the likelihood and variability of parameter sets from further wells in future experiments. The mean values of the samples of $\boldsymbol{\mu}$ (which is equivalent to the mean of the posterior predictive distribution) and its 95% credible intervals are provided in Table 4.4.

We quantify the goodness of the posterior predictive distribution from our hierarchical Bayesian model, compared to the 124 individual experiments, by means of a quantile-quantile (Q-Q) plot and a probability-probability (P-P) plot. The Q-Q (or P-P) plot is a graphical method for comparing two probability distributions, in our case the 124 individual experiments and our posterior predictive distribution $p(\boldsymbol{\theta} \mid \cdots)$, by plotting their quantiles (or cumulative distributions) against each other. Figure 4.20 shows the Q-Q (left) and P-P (right) plots. For each parameter, the marginal posterior

predictive distributions are plotted against the posterior mean of the 124 cells. We applied linear regression, shown as orange lines, and they all lie very close to the line of identity (grey dashed lines). These analyses support our results and suggest that our posterior predictive distribution, together with the log-normal distribution assumption, is an appropriate distribution for the data.

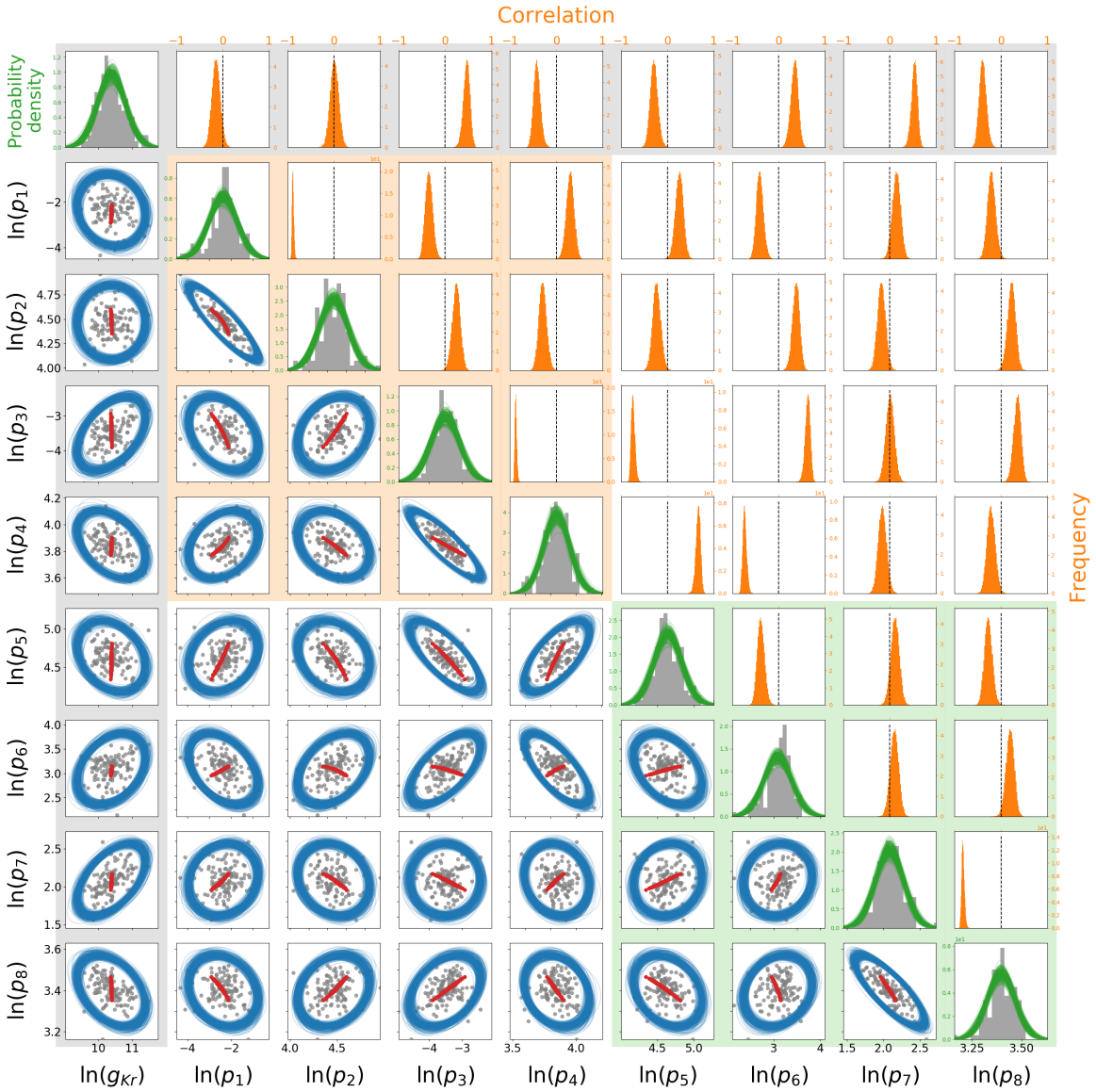

Figure 4.21: The inferred correlation in model parameters across experimental wells. All parameters shown here are natural log-transformed. The posterior mean parameters ($\boldsymbol{\theta}$) of each of the 124 individual wells are shown in grey (dots and histograms). **Lower triangle (blue):** The 95% credible region boundary for the distribution of parameters across wells. Each credible region ellipse is reconstructed from one sample of the $\boldsymbol{\mu}, \boldsymbol{\Sigma}$ across-cell distribution parameters from the MCMC chain of size 10^5, for clarity only 200 samples are shown here. Simulated voltage error offset (described in the Discussion) is shown as red dots. **Diagonal (green):** The sampled posterior probability density functions before integration to give $p(\boldsymbol{\theta} \mid \cdots)$, shown in detail in Figure 4.19. **Upper triangle (orange):** The marginal histograms for each entry of the correlation matrix defined by Eq. (4.27). The common assumption of independence (correlation of zero) is shown as black vertical lines for comparison. The shadings in the background indicate how these parameters relate to the model structure: the orange box contains the gates a in model, green box contains gate r, and grey relates to the conductance.

Finally, we used the hierarchical Bayesian model to investigate the correlation *between model parameters across different wells*. In the sampled hyperparameters, the covariance matrix $\boldsymbol{\Sigma}$ reveals any correlation between our model parameters. The typical assumption concerning the variability of parameters is that they are independent, i.e. in the covariance matrix all entries except the diagonal are zero. In the upper triangle (orange) of Figure 4.21, we compare our inferred correlation between parameters (calculated using Eq. (4.27)) with this common assumption (black vertical dashed lines). It is obvious that there are many entries where zero is outside our credible interval, which implies that the model parameters are correlated. Therefore the independence assumption is not supported by our findings, and we take a closer look at the results below.

To visualise the correlation between parameters better, the 95% credible regions for each pair of parameters are shown in the lower triangle (blue) of Figure 4.21; plotted against the scatter plot of the 124 cells individual posterior mean parameters (shown on a log-scale). Each blue ellipse is reconstructed from a sample of hyperparameters, where the contour of the 95% credible region of the two-variate marginal distribution defined by the hyperparameter sample is shown; capturing most of our individual posterior mean parameters appropriately. In this plot, a perfect circle implies there is no correlation between the pair of parameters. However, we can clearly see that most of our pairwise parameters show an elliptical shape, which means some degree of correlation between the pairwise parameters exists. This strongly suggests that correlations between parameters are embedded in the experiment-to-experiment variability. Finally to ensure our observed correlations are biophysically relevant, rather than a sign of identifiability problems, Figure 4.22 shows how cell-specific parameters make accurate cell-specific predictions. We further discuss explanations and hypotheses for such observed correlations in the next section.

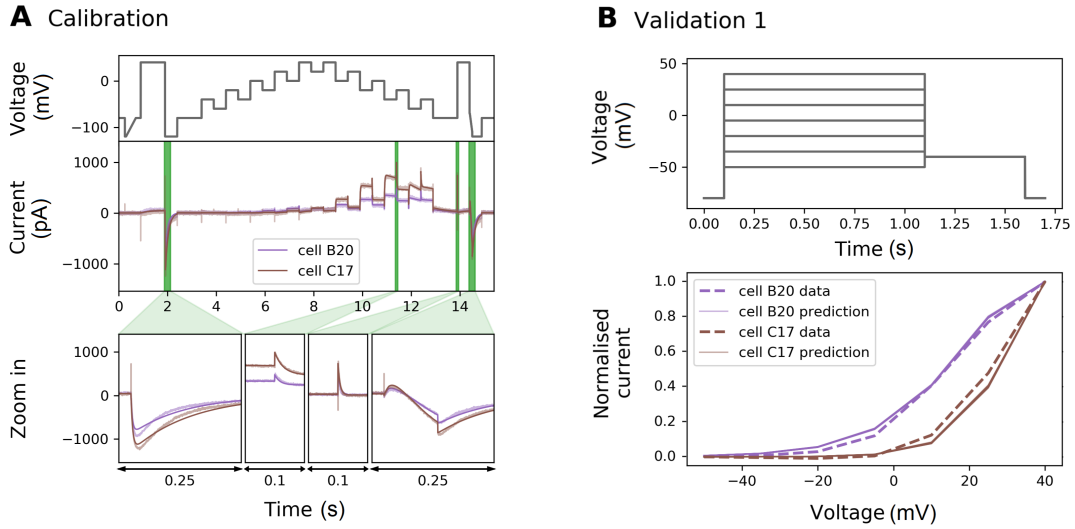

Figure 4.22: A comparison of fits and predictions for cells B20 (purple) and C17 (brown). **(A)** Fits from the posterior (50 samples) from the two cells and corresponding experimental data under the staircase calibration protocol, with corresponding cell-specific data shown in the background. Note that although there are 50 fits plotted, these appear to be a single line for each cell as the parameter samples are so close that the forward simulations are indistinguishable at this scale. **(B)** Predictions based on 50 samples of the cell-specific posteriors under the activation I-V protocol (Validation #1).

4.7 Discussion

In this chapter, we have developed a short, high information-content staircase voltage-clamp protocol for I_{Kr} that can be applied in automated high-throughput patch-clamp systems. We then used a mathematical model to characterise channel kinetics by fitting its parameters to recordings made under this new protocol. In this section we first discuss the benefits of using this novel approach to construct trustworthy models of ion channel kinetics as compared to the conventional methods. The novel approach developed in this chapter also enables us to study the ion channel kinetics under different conditions, such as mutations, pharmaceutical compounds, and different temperatures (as we demonstrate in the next chapter). Second, we discuss how these high-throughput rapid characterisation experiments allow us to suggest reasons for the observed variability, and lead us to investigate the origin of the observed variability in Chapter 6.

4.7.1 High-throughput rapid characterisation of ion channel currents

Here, we no longer use I-V or τ-V relations to characterise hERG kinetics, but rather we use a mechanistic model and its parameterisation to capture our knowledge of channel kinetics. A different design of voltage-clamp protocol, which is short and able to elicit a high information-content signal of hERG current, was used to calibrate the hERG kinetics model. The benefits of this approach are threefold. First, current 'rundown' during the protocol has less of an effect over shorter experiments (10s seconds), as compared to conventional I-V and τ-V protocols (10s minutes), hence it is much easier to obtain a measurement that remains stable. Second, given its short duration, it is easy to repeat the measurement, to examine within-cell reproducibility/variability. Third, our staircase protocol can be used to rapidly create *cell-specific models of kinetics* (which is much harder to do using the more time-consuming conventional I-V and τ-V protocols).

We have shown that our 15-second staircase protocol can be performed in an automated high-throughput system. We have found that each of the resulting 124 models is consistent with previous manual patch clamp results (Beattie et al., 2018, limited to nine cells), implying that these methods are reproducible. We can now easily produce large data sets for further analysis, which is usually difficult, if not impossible, to achieve with manual patch clamp. The predictions of the cell-specific models are not perfect, as we examined in Figure 4.17, and there may be room for improvement in terms of the model structure and further optimisation of the calibration protocol. But we are able to calibrate our model to the extent that it can replicate both experimental training data *and* predict validation data very well (Figure 4.15). Our models can predict the current response to the physiologically-relevant action potential protocols, demonstrating that our I_{Kr} models could be useful in predicting cardiac electrical activity in both healthy and arrhythmic situations (Beattie et al., 2018). This provides assurance that our *cell-specific models*, which are constructed in a *high-throughput* manner, have great potential for future uses.

With our 124 *cell-specific* hERG models, we are able to study experiment-to-experiment variability in the hERG channel. Such experiment-to-experiment variability is captured using our hierarchical

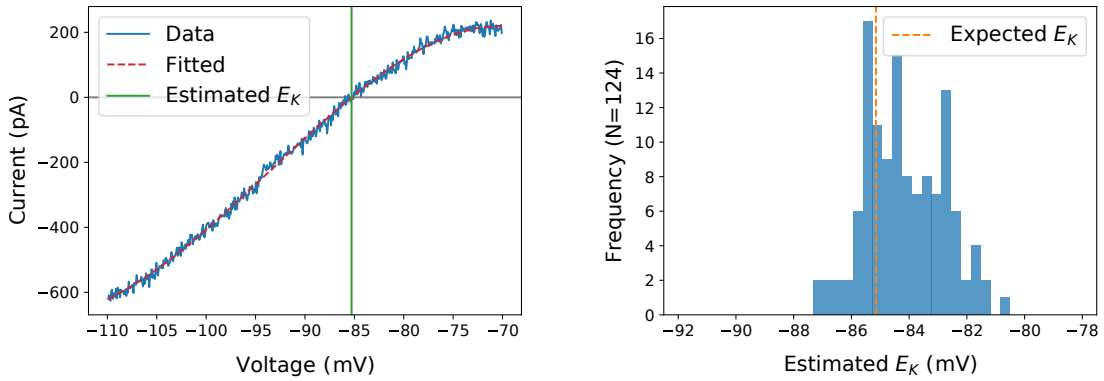

Figure 4.23: **(Left)** An example of the current-voltage relationship plotted for the last ramp in the staircase protocol, and how it is used to estimate the E_{K} reversal potential value for I_{Kr} in one well. **(Right)** Histogram of E_{K} values estimated using the reversal ramp technique. The E_{K} values here were estimated from the same 124 wells used in the main results. The dashed orange vertical line shows the expected E_{K} calculated directly from temperature and concentrations using the Nernst equation (Eq. (2.8)).

Bayesian model, where the posterior predictive distribution is constructed and describes the underlying variability of the parameters (Figure 4.19). Instead of using a series of I-V and τ-V curves, here we evaluate the variability of the observed hERG channel kinetics using mathematical model parameters. The variability in the parameter values predicts the observed differences in the channel kinetics, see also Figure 4.22. In addition, we can use our posterior predictive distribution to predict what might happen in future experiments, based on the observed experiments.

4.7.2 Sources of variability

We have successfully quantified the variability *between wells* via our inferred model parameters. However, the underlying cause of this variability is an open question. There are possibilities at two extremes. One is that the variability is truly cell to cell, and ion channel kinetics do vary because of different intracellular conditions, one may speculate in terms of gene expression, the presence of subunits, phosphorylation states, or suchlike. The other possibility is that ion channel kinetics are precisely identical in each cell, but there are some experimental artefacts, varying between wells, that are causing the observed variability in parameters from each well. Below we discuss hints in our results as to which of these extremes is the leading cause of variability, and we investigate this in detail in Chapter 6.

As shown in Figure 4.3, the 100 ms reversal ramp at 14.41 s was introduced to estimate experimentally the hERG reversal potential E_{K}^{j} in each of the j wells, for details see the rationale of the staircase protocol in Section 4.5. In Figure 4.23, we show an example E_{K}^{j} derivation using the reversal ramp and a histogram of E_{K}^{j} values estimated from the 124 wells.

Our obtained histogram of E_{K}^{j} values is distributed close to our theoretical E_{K} from the Nernst equation (Eq. (2.8)), with a standard deviation of 1.36 mV. Since all of our measurements were performed on one 384 well plate, they shared the same extra- and intra-cellular solutions and were recorded at (almost) the same temperature. We would therefore expect the real variability in reversal potential to be much smaller than this observed variability.

A hypothesis then, is that the reversal potential E_{K} really occurs at the Nernst calculated value, and observed deviations from this inferred from the reversal ramp provide an estimate for a 'voltage error' in the applied voltage clamp: $\Delta V^j = E_{\mathrm{K}}^j - E_{\mathrm{K}}$, perhaps due to an imperfect compensations of other external effects, such as junction potentials and electrode offsets (see details in Chapter 6). We test this hypothesis via the model before we further investigate this in detail in Chapter 6: by applying a staircase protocol with voltage error offsets of ΔV^j estimated from each of the 124 cells, generating synthetic data from these voltage clamps, and then re-fitting parameters.

Figure 4.21 (lower triangle) shows the results of our voltage error offset simulations in red dots. If there was an error in the applied voltage clamp in each well, then we would expect to see parameters appearing to co-vary along the red lines (made up of individual dots/fits) in Figure 4.21. The observed primary parameter covariance directions and magnitudes from this procedure (red lines) align suspiciously well with much of the observed variability in the experiments (blue ellipses inferred from grey dots).

This simple test suggests that the observed variability in parameters may be due to well-well variability in patch-clamp artefacts rather than cell-cell variability in ion channel kinetics. In Chapter 6, we build a more complete mathematical model of such patch-clamp artefacts to investigate in detail the causes of the observed variability. We should also note that despite patch-clamp artefacts being an apparent cause of parameter variability, there are not necessarily larger artefacts in this automated system than might be expected in manual patch clamp.

4.8 Conclusion

In this chapter, we have taken a first step in moving away from the conventional approaches and designed a 15-second staircase protocol to study and characterise hERG channel kinetics. We first tested the experimental design through synthetic data studies. We then demonstrated the feasibility and practicality of applying the design on an automated high-throughput system. We defined and applied quality control criteria, and selected 124 cell measurements for constructing hERG models. Our 124 cell-specific variants of the hERG model that are calibrated using the staircase protocol are able to predict eight other validation protocols with a high accuracy, including physiologically-inspired action potential-like voltage clamps. Using a hierarchical Bayesian modelling approach, we provide a quantitative description of the variability and uncertainty within our 124 cell-specific models.

With our rapid characterisation techniques and the hierarchical Bayesian modelling approach, we have opened a new gateway to study parameter correlations between cells and investigate experimental variability. We have found that some model parameters are strongly cross-correlated, but not all. This result may hint at the origin of the variability, which we investigate in detail in Chapter 6.

In the next chapter, Chapter 5, we directly apply our methods developed in this chapter to study the temperature dependence of the hERG kinetics which are commonly represented with either Q_{10} coefficients or an Eyring relationship. However, a detailed comparison and assessment of the applicability of these representations has not yet been undertaken.

4.9 Data and Software Availability

Data and software (GitHub repository):
https://github.com/CardiacModelling/hERGRapidCharacterisation

Staircase protocol in time series format:
https://github.com/CardiacModelling/hERGRapidCharacterisation/blob/master/protocol-time-series/protocol-staircaseramp.csv

Automated quality control software:
https://github.com/CardiacModelling/hERGRapidCharacterisation/blob/master/lib/hergqc.py

Chapter 5

Temperature Dependence of hERG Kinetics

This chapter was published as: Lei, C. L., Clerx, M., Beattie, K. A., Melgari, D., Hancox, J. C., Gavaghan, D. J., Polonchuk, L., Wang, K., and Mirams, G. R. (2019a). Rapid characterization of hERG channel kinetics II: temperature dependence. *Biophysical Journal*, 117(12):2455–2470.

Contributions: I assisted in designing the study, carried out the experiments, designed the computational analysis, wrote the simulation codes, and performed all the analysis.

Overview:

In the previous two chapters, we looked at reparameterising an action potential model with a conventional approach and constructing a mathematical model of an ion channel using experiments recorded at room temperature. However, we are mostly interested in responses at physiological temperature, and ion channel behaviour can depend strongly on temperature generally, with faster kinetics at physiological temperatures leading to considerable changes in currents relative to room temperature. Commonly, these temperature-dependent changes in voltage-dependent ion channel kinetics (rates of opening, closing, inactivating and recovery) are commonly represented with Q_{10} coefficients or an Eyring relationship. In this chapter we assess the validity of these representations by characterising channel kinetics at multiple temperatures. Following on from Chapter 4, we focus on the *human Ether-à-go-go-Related Gene* (hERG) channel, which is important in drug safety assessment and commonly screened at room temperature, so that results require extrapolation to physiological temperature. In Chapter 4 we established a reliable method for high-throughput characterisation of hERG1a ($K_V11.1$) kinetics, using a 15-second information-rich protocol. In this chapter, we use this protocol to study the temperature dependence of hERG kinetics in the same cells, Chinese Hamster Ovary (CHO) cells over-expressing hERG1a, on the Nanion SyncroPatch 384PE. We characterise the temperature dependence of hERG gating by fitting the parameters of a mathematical model of hERG kinetics to data obtained at five distinct temperatures between 25 and 37 °C, and validate the models using different protocols. Our models reveal that activation is far more temperature sensitive than inactivation. We show that the

temperature dependence of the kinetic parameters is not represented well by Q_{10} coefficients: it broadly follows a generalised, but not the standardly-used, Eyring relationship. We also demonstrate that experimental estimates of Q_{10} coefficients are protocol-dependent, which can be error-prone and misleading if they are used without extra care. Our results show that a direct fit using our 15-second protocol best represents hERG kinetics at any given temperature, whilst the Generalised Eyring theory is the best alternative if no such data are available.

5.1 Introduction

In the previous chapter, we used experimental data recorded at room temperature to construct a model of an ion channel, as often room temperature experiments are easier to perform and have higher success rates. However, ion channel behaviour can depend strongly on temperature (Dhaka et al., 2006; Yang and Zheng, 2014), with physiological temperatures typically leading to faster kinetics and different magnitudes of current than at room temperature, see for example (Vandenberg et al., 2006, Figure 1). These temperature-dependent changes in voltage-dependent ion channel kinetics, e.g. rates of activation, deactivation, inactivation and recovery, are commonly represented with either Q_{10} coefficients (Hodgkin et al., 1952; Collins and Rojas, 1982; Zhou et al., 1998; Vandenberg et al., 2006; Li et al., 2016; Mauerhöfer and Bauer, 2016) or an Eyring relationship (Tsien and Noble, 1969; Hille, 2001; Irvine et al., 1999; Fink et al., 2008).

In this chapter, we characterise channel kinetics at multiple temperatures, and test the validity of Q_{10} and Eyring rate theories by testing whether the kinetic parameters follow the trends that these theories assume. We study the temperature dependence of the *human Ether-à-go-go-Related Gene* (hERG) channel which is important in drug safety assessment (Friedrichs et al., 2005) and has been shown to have temperature-dependent kinetics (Zhou et al., 1998; Vandenberg et al., 2006; Mauerhöfer and Bauer, 2016).

Previous studies, Zhou et al. (1998) and Vandenberg et al. (2006) measured hERG1a temperature dependence, and compared room and physiological temperature kinetics under typical activation and inactivation current-voltage (I-V) protocols. A similar study with hERG1a/1b was performed more recently by Mauerhöfer and Bauer (2016). Unless otherwise specified, we refer to hERG1a simply as 'hERG' in the remainder of this chapter. Previous studies have consistently reported that hERG kinetics are highly temperature-sensitive, something that is perhaps a property of potassium channels more widely (Yang and Zheng, 2014).

Furthermore, drug screening data is often collected at room temperature, and requires extrapolation to physiological temperature. Temperature extrapolation relies heavily on the accuracy of models of temperature-dependence. Some effort has been made to model temperature effects on hERG kinetics based upon literature data (Zhou et al., 1998; Vandenberg et al., 2006); for example Fink et al. (2008) attempted to use an Eyring relationship and Li et al. (2016) used Q_{10} coefficients. However, a detailed comparison and assessment of the applicability of these representations has not yet been reported.

In this chapter, we study and model the temperature dependence of hERG kinetics using a cell-specific fitting technique, for a range of room-to-physiological temperatures. We employ the staircase protocol

developed in Chapter 4. We use the same mechanistic model and parameterise it to characterise hERG kinetics at multiple temperatures. We then compare whether the estimated parameters as a function of temperature follow the temperature dependence of rate theories.

5.2 Commonly-used temperature adjustments for kinetic rates

In this section we discuss commonly-used temperature adjustments/models for kinetic rates in voltage-gated ion channels — the Eyring relationship and the Q_{10} coefficient — and the consequences of these theories for the temperature-dependence of parameters within an ion channel model.

5.2.1 Models of transition rates and their temperature dependence

Mathematical ion channel models are often expressed as a Hodgkin-Huxley model (Hodgkin and Huxley, 1952a) or a Markov state model (Fink and Noble, 2009), and both have transition rates (which we will call k) between the channel gates/states, as introduced in Chapter 2 and used in Chapter 4. From the derivation in Section 2.3.2.6, we expect the rate of transition between any two states to follow

$$k = A \cdot \exp\left(BV\right), \tag{5.1}$$

where A, B are model parameters (constants). In this chapter, we use the terms 'Parameter A' and 'Parameter B' to refer to A and B in Eq. (5.1).

5.2.1.1 Eyring formulations

The temperature dependence of channel transitions is embodied in the Eyring equation. The original Eyring equation was derived from basic thermodynamics and statistical mechanics, following from the concepts of Gibbs free energy, entropy and enthalpy (Eyring, 1935). The typical form used to model voltage-dependent transition rates previously (Tsien and Noble, 1969; Hille, 2001; Irvine et al., 1999; Fink et al., 2008) is

$$k_{\text{TypicalEyring}} = \frac{k_B}{h} \cdot T \cdot \exp\left(\frac{\Delta S}{R} - \frac{\Delta H}{R}\frac{1}{T} + \frac{z_e F}{R}\frac{1}{T}V\right), \tag{5.2}$$

with physical constants: k_B the Boltzmann constant, R the ideal gas constant, h the Planck constant, F the Faraday constant, T the absolute temperature, and V the transmembrane voltage. The following are unknowns (or 'kinetic parameters') to be determined: ΔS the entropy difference, ΔH the enthalpy difference, z_e the effective valency of the structure undergoing conformational change. A more generalised Eyring relationship can be given by

$$k_{\text{GeneralisedEyring}} = \frac{k_B}{h} \cdot T \cdot \exp\left(\frac{\Delta S}{R} - \frac{\Delta H}{R}\frac{1}{T} + \frac{z_e F}{R}\frac{1}{T}V + DV\right), \tag{5.3}$$

where D is a coefficient that describes a temperature-independent effect of voltage on the transition rate. The Generalised Eyring relationship is commonly used in the field of manufacturing engineering and battery engineering (for example Bhattacharyya and Soejoeti, 1981; Escobar and Meeker, 2006;

Redondo-Iglesias et al., 2017, 2018), although to the best of our knowledge it has not been directly applied to ion channel modelling.

Without loss of generality, we can rewrite (reparameterise) Eq. (5.3), using unknowns a_{GE}, b_{GE}, c_{GE} and d_{GE}, absorbing all other constants into these four new parameters, as

$$k_{\mathrm{GeneralisedEyring}} = a_{\mathrm{GE}} \cdot T \cdot \exp\left(-b_{\mathrm{GE}} \cdot T^{-1}\right) \cdot \exp\left(\left(c_{\mathrm{GE}} \cdot T^{-1} + d_{\mathrm{GE}}\right) V\right), \tag{5.4}$$

where $a_{\mathrm{GE}} = (k_B/h)\exp(\Delta S/R)$, $b_{\mathrm{GE}} = \Delta H/R$, $c_{\mathrm{GE}} = (z_e F)/R$, and $d_{\mathrm{GE}} = D$. By comparing Eq. (5.1) and Eq. (5.4), then we have

$$A = a_{\mathrm{GE}} \cdot T \cdot \exp\left(-b_{\mathrm{GE}} \cdot T^{-1}\right), \tag{5.5}$$

$$\ln(A/T) = \ln(a_{\mathrm{GE}}) - b_{\mathrm{GE}} \cdot T^{-1}, \tag{5.6}$$

and

$$B = c_{\mathrm{GE}} \cdot T^{-1} + d_{\mathrm{GE}}. \tag{5.7}$$

Therefore, plotting $\ln(A/T)$ against T^{-1} should yield a linear relationship if the Generalised Eyring relationship holds. Similarly, from Eq. (5.7), we see that plotting B against T^{-1} yields a linear relationship for the Generalised Eyring relationship; or a proportional relationship for the Typical Eyring relationship ($d_{\mathrm{GE}} = 0$). We refer to a plot of $\ln(A/T)$ or B as a function of T^{-1} as an '*Eyring plot*'.

5.2.1.2 Q_{10} coefficients

Another approach that is commonly used to describe temperature dependence in biological and chemical processes is the use of Q_{10} coefficients. The Q_{10} relationship is an empirical expression (Běhrádek, 1930), which assumes reaction rates increase exponentially with temperature, and has been applied extensively to ion channel kinetics from Hodgkin and Huxley's work to the present day (Hodgkin et al., 1952; Collins and Rojas, 1982; Zhou et al., 1998; Vandenberg et al., 2006; Li et al., 2016; Mauerhöfer and Bauer, 2016). Using Q_{10} coefficients, we can express the transition rates as

$$k_{\mathrm{Q10}} = Q_{10}^{(T-T_{\mathrm{ref}})/(10^{\circ}\mathrm{C})} \cdot \alpha \cdot \exp\left(\beta V\right). \tag{5.8}$$

Here, α and β are parameters for the rates, and T_{ref} is the reference temperature for the extrapolation. A Q_{10} coefficient is, by definition, calculated using the ratio of the rates at $T_{\mathrm{ref}} + 10^{\circ}\mathrm{C}$ and T_{ref}. Comparing Eq. (5.1) and Eq. (5.8), we have

$$\ln A = a_{\mathrm{Q10}} T + c_{\mathrm{Q10}}, \tag{5.9}$$

$$\ln(A/T) = \frac{a_{\mathrm{Q10}}}{T^{-1}} + \ln(T^{-1}) + c_{\mathrm{Q10}}, \tag{5.10}$$

and

$$B = \beta, \tag{5.11}$$

where $a_{\mathrm{Q10}} = (\ln Q_{10})/10^{\circ}\mathrm{C}$, $c_{\mathrm{Q10}} = \ln\alpha - (T_{\mathrm{ref}} \ln Q_{10})/10^{\circ}\mathrm{C}$. Therefore, if the Q_{10} formulation is accurate, then plotting $\ln(A/T)$ against T^{-1} should yield a nonlinear relationship, and B against T^{-1} is a horizontal line.

5.2.2 A theoretical comparison of the Eyring formulation and Q_{10} coefficient

We now compare the Generalised Eyring relationship (Eq. (5.3)), the Typical Eyring relationship (Eq. (5.2)) and the Q_{10} expression (Eq. (5.8)). Note that the Eyring relationships have been related to the Q_{10} expression (Tsien and Noble, 1969; Ito et al., 2015) to interpret the Q_{10} coefficient as the change of entropy and enthalpy. However, in this chapter, we treat the two formulations independently.

For parameter A in Eq. (5.1), under the Eyring plot where we plot $\ln(A/T)$ (on the y-axis) against $1/T$ (x-axis), both the Generalised Eyring and Typical Eyring relationships (Eq. (5.6)) give a straight line, $y = mx + c$; while the Q_{10} expression (Eq. (5.10)) becomes $y = a/x + \ln(x) + b$ which is not. This difference could be used to tell which theory is correct, but within our temperature regime the Q_{10} expression on the Eyring plot gives a curve that is indistinguishable, in practical terms, from a linear Eyring relationship, as shown in the top of Figure 5.1.

Therefore the only practically measurable difference between the proposed temperature relationships is in the B parameters (which set the voltage dependence of the transition rate) in Eq. (5.1). The Generalised Eyring relationship implies that B has a *linear relationship* with T^{-1}; the Typical Eyring relationship restricts B to be *directly proportional* to T^{-1}; and under the Q_{10} coefficient formulation,

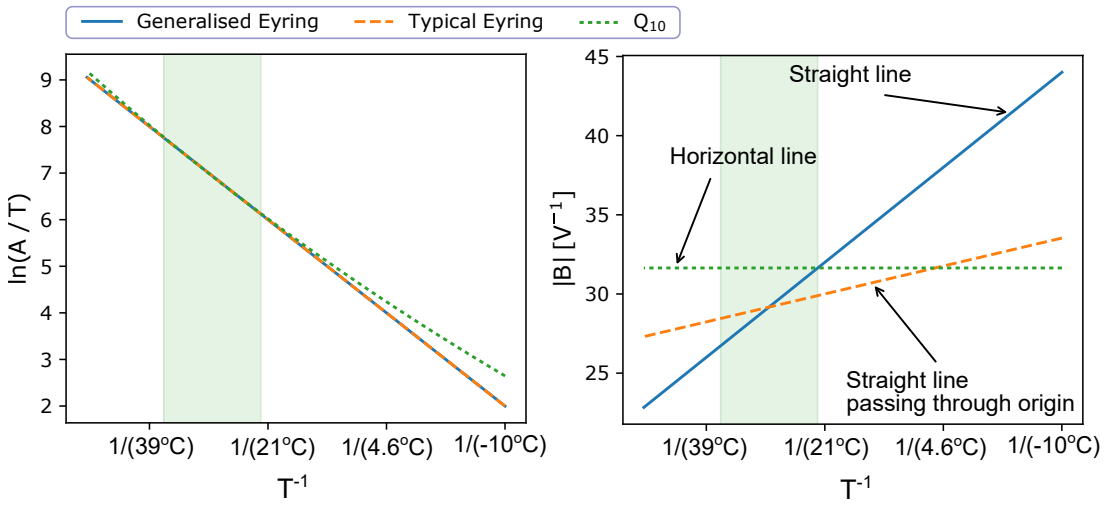

Figure 5.1: An Eyring plot illustrating the difference between a Generalised Eyring equation (Eq. (5.3)), a Typical Eyring equation (Eq. (5.2)), and a Q_{10} formulation (Eq. (5.8)). This plot extends from $-10\,^{\circ}\mathrm{C}$ to $50\,^{\circ}\mathrm{C}$ to highlight the differences between the three formulations. The green shaded region marks the temperature range of interest, from 22–37 °C. The Generalised Eyring relationship shown has $[\ln a_{\mathrm{GE}}, b_{\mathrm{GE}}, c_{\mathrm{GE}}, d_{\mathrm{GE}}] = [40, 1000, 3000, -70]$, and the Typical Eyring and Q_{10} relationships are the best fits to the generated Generalised Eyring relationship. Both Eyring formulations give the same straight line dependence for $\ln(A/T)$ and even the nonlinear Q_{10} formulation is indistinguishable (for practical purposes) within the relevant temperature range. However, the three formulations can display very different behaviour when examining the temperature dependence of the voltage-dependence parameter B: the Generalised Eyring relationship leads to any straight line; the Typical Eyring relationship gives straight lines passing through the origin; and the Q_{10} formulation can be only horizontal lines in the Eyring plot.

B is a *constant* that does not depend on temperature. These differences are illustrated in the right hand panel of Figure 5.1.

The Typical Eyring relationship is a special case of the Generalised Eyring relationship, and therefore the Typical Eyring relationship would hold if $D = 0$ were obtained when fitting the Generalised Eyring relationship: it will become clear that this is not the case for our data. We hence compare the Generalised Eyring relationship and the Q_{10} formulation in the rest of this chapter.

There have been previous temperature-dependent hERG modelling studies. Fink et al. (2008) expressed hERG kinetics using the Typical Eyring relationship (Eq. (5.2)), but its parameters were derived from experimentally estimated Q_{10} values in Vandenberg et al. (2006) yielding an incomplete form of the Eyring relationship based on Q_{10} values. Li et al. (2016) used a Q_{10} formulation (Eq. (5.8)) to model temperature dependence of hERG kinetics for simplicity, but did not investigate to what extent this captured temperature-dependent changes in the kinetics.

Modelling temperature effects in ion channel kinetics not only has applications in cardiac safety pharmacology, it is also commonly used in action potential modelling more generally. Many cardiac action potential models (Greenstein and Winslow, 2002; Iyer et al., 2004; Tanskanen et al., 2005; Sampson et al., 2010) adapted the Mazhari et al. (2001) hERG model which used Q_{10} values from Zhou et al. (1998) to extrapolate room temperature recordings to physiological temperature. These extrapolations cause considerable changes to rates, often exceeding changes introduced when modelling diseases or other conditions (Clerx, 2018). Similarly, the Christé et al. (2008) hERG model was based on measurements at room temperature and extrapolated to 37 °C using Q_{10} values from Vandenberg et al. (2006). Within action potential models, many other ion current models (such as I_{Na}, I_{CaL}, etc.) are also based on experiments performed at different temperatures (Niederer et al., 2009), most of which are then corrected via Q_{10} extrapolations (Courtemanche et al., 1998; Ten Tusscher et al., 2004; O'Hara et al., 2011; Paci et al., 2013; Lei et al., 2017a).

5.3 Methods

The experimental methods, mathematical model of I_{Kr}, and the I_{Kr} model parameter inference methods used in this chapter are identical to the methods detailed in Chapter 4. Here we focus on the methods used specifically for studying the temperature dependence of the channel.

5.3.1 Experimental methods

Whole-cell patch-clamp voltage clamp experiments were performed on Chinese Hamster Ovary (CHO) cells stably transfected with hERG1a ($K_V11.1$). Measurements were performed using the Nanion SyncroPatch 384PE (Nanion Technologies GmbH, Germany), an automated high-throughput platform in which each run (or chip) is able to measure 384 wells (with one cell per well) simultaneously. For details, see Experimental Methods in Chapter 4.

5.3.1.1 Temperature control

The SyncroPatch platform has a temperature control unit with software PE384TemperatureControl, which consists of a temperature controller and several temperature monitors placed around the machine compartment. The machine compartment contains all the solutions on stand-by and is where the measurements occurred. Since the temperature controller consists of a heater with a fan, the platform can only maintain temperatures higher than room temperature. The lowest temperature we could maintain indefinitely was 25 °C, which is determined by room temperature (≈ 22 °C) plus heat generated by the machine's operation (≈ 3 °C), even if the heat controller itself was set to a lower temperature.

To ensure that we recorded the temperature correctly, an external K-Type thermometer was used to ensure the temperature difference between the measuring stage and the machine in-built temperature monitors was $\lesssim 0.5$ °C. Note that the temperature readouts could differ from the temperature set on the controller even after equilibrium, particularly close to room temperature, so we used the thermometer and temperature monitors' readouts as the true temperature of the experiments. The temperatures of the five experiments were 25, 27, 30, 33, and 37 °C, and the uncertainty of our temperature measurements was estimated to be ±1 °C by comparing the temperature differences at various locations of the compartment. Due to the machine taking a substantial amount of time to change temperature, distinct experiments were performed at different temperatures using different cells (the same cell line but different individual cells in each well on sometimes different days).

5.3.1.2 Post-processing experimental data

We performed a series of quality control checks and corrections (in post-processing) to ensure the currents recorded represent only I_{Kr}; for details, see Post-processing experimental data in Chapter 4. Cells were then selected based on partially automated quality control described in Section 4.5.3.3, resulting in $N_e = 124, 91, 85, 84, 45$ cells being selected for measurements at 25, 27, 30, 33, and 37 °C, respectively; and the 25 °C data were examined in Chapter 4. The lower yield of cells at higher temperatures was mostly due to: reduced success in the cell capture step, before any recording started; and also, to a lesser extent, deterioration of the patch clamp.

5.3.1.3 Data visualisation

Each hERG-transfected CHO cell was expected to have a different total conductance, hence giving a different magnitude for the current recording. Therefore normalisation was applied for visual comparison. Note that the validation of model predictions was performed *without* normalisation (a conductance was fitted for each cell individually). To avoid any circular reasoning involved in normalising based on the g_{Kr} parameter fit within the models (which, at this point, may or may not vary with temperature), we used an experimental maximum conductance estimate. The experimental estimate is approximated by extrapolating the negative tail current, after the first 40 mV to −120 mV step, back to the time the voltage step occurred, as shown in Figure 5.2. Note that this normalisation method is imperfect as it relies on a particular gating process (activation gate $a \approx 1$ at the end of the 40 mV step) which has some dependence on the kinetics we aim to compare, but the 22 °C parameterisation of the model (Beattie et al., 2018) suggests $a \approx 1$ is a reasonable approximation

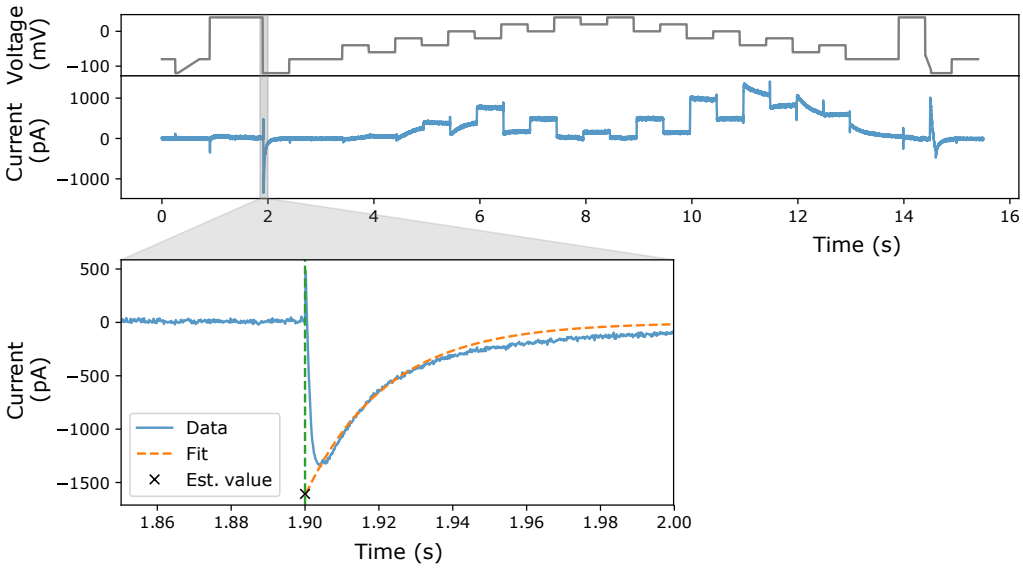

Figure 5.2: An illustration of the estimation of the maximum conductance value (black cross). In the magnified plot, the negative tail current (blue) after the first 40 mV to −120 mV step is extrapolated back to the time the voltage step occurred (indicated by the green vertical dashed line). The extrapolation is done by fitting a single exponential function (orange dashed line) to the tail current.

(even for lower temperatures) at this point in the protocol. However, since this method removes the conductance dependency, it has a benefit over the normalisation-to-a-reference-trace method used in Chapter 4 by preserving the different magnitudes of currents from *different temperatures*.

5.3.2 Mathematical model

We used the same Hodgkin and Huxley-style structure hERG model described in Chapter 4; see Section 4.2.1 for detail. Model simulations were performed as described in Chapter 2. All codes and data are freely available online, see Data and Software Availability at the end of the chapter.

5.3.3 Independent parameter fits at each temperature

The fitting procedure used in this chapter follows exactly that laid out in Chapter 4, but is repeated for each of the five temperatures. For details, see Sections 4.3.1 and 4.3.2.

For each temperature T, we combined multiple experimental recordings using a hierarchical Bayesian model, as in Chapter 4: The hierarchical Bayesian likelihood is given by

$$\begin{aligned}\mathcal{L}\left(\boldsymbol{\mu}, \boldsymbol{\Sigma}, \left\{\boldsymbol{\theta}_j, \sigma_j\right\}_{j=1}^{N_e} \middle| \left\{\mathbf{y}_j\right\}_{j=1}^{N_e}\right) \propto & \prod_{j=1}^{N_e} p\left(\mathbf{y}_j \middle| \boldsymbol{\theta}_j, \sigma_j\right) \\ & \times p\left(\left\{\boldsymbol{\theta}_j\right\}_{j=1}^{N_e} \middle| \boldsymbol{\mu}, \boldsymbol{\Sigma}\right) \\ & \times p\left(\boldsymbol{\mu}, \boldsymbol{\Sigma}\right) \times \prod_{j=1}^{N_e} p\left(\sigma_j\right), \end{aligned} \tag{5.12}$$

where $\boldsymbol{\mu}, \boldsymbol{\Sigma}$ are the hyperparameters of the hierarchical model representing the mean vector and covariance matrix from which the individual 'low-level' (well-specific) parameters are drawn. $\{\boldsymbol{\theta}_j, \sigma_j\}_{j=1}^{N_e}$

are the set of individual 'low-level' parameters for each of the N_e repeats of the experimental recordings $\{\mathbf{y}_j\}_{j=1}^{N_e}$. The three terms on the right hand side of Eq. (5.12) correspond to: (a) the likelihood of *all* the individual (low-level) experiments; (b) the likelihood of the hyperparameters (top-level); and (c) the prior of the hyperparameters and the prior of σ_j.

We assumed $\boldsymbol{\phi}_j$ for a particular cell (experiment) j follows a multivariate normal distribution, namely $\boldsymbol{\phi}_j \sim \mathcal{N}(\boldsymbol{\mu}, \boldsymbol{\Sigma})$. There are two distributions describing the well-well variability in this hierarchical Bayesian model, one is the variability of the samples of the mean parameter vector $\boldsymbol{\mu}$, and the other is the covariance matrix $\boldsymbol{\Sigma}$. As discussed in Chapter 4 Discussion, we investigate in detail in the next chapter how patch-clamp artefacts in each well might cause the well-well variability represented by $\boldsymbol{\Sigma}$. In Chapter 6 we conclude that the uncertainty in $\boldsymbol{\mu}$ represents our uncertainty in the underlying *physiology*, and we believe it corresponds to our uncertainty in the physiological hERG temperature response, rather than our expected variability in the results of future experiments which would require $\boldsymbol{\Sigma}$ too. Therefore in the rest of the chapter, we use the uncertainty in $\boldsymbol{\mu}$ to quantify our uncertainty in the model parameters.

For the choice of likelihoods and priors and sampling algorithms we used the *simplified* pseudo-Metropolis within Gibbs (pseudo-MwG) algorithm introduced in Chapter 4. All inference and sampling was done via an open source Python package that I co-developed, PINTS (Clerx et al., 2019b) as described in Chapter 2; code is available online, see Data and Software Availability at the end of the chapter.

5.3.4 Fitting Eyring and Q_{10} relationships

To investigate how well the two temperature models, the Generalised Eyring and the Q_{10} relationships, can explain the temperature dependency of hERG kinetics, we fitted the two temperature models to the inferred distribution of the mean parameter vector $\boldsymbol{\mu}(T)$ for all temperatures T. To do so, first we transformed both the temperature models and $\boldsymbol{\mu}(T)$ to the Eyring plot form (see Figure 5.1). Second, we modelled the marginal distribution of $\boldsymbol{\mu}(T)$ of p_i at each T in the Eyring plot using a normal distribution with mean $\overline{\mu}_i(T^{-1})$ and standard deviation $\sigma_{\mu,i}(T^{-1})$. We further assumed both $\overline{\mu}_i(T^{-1})$ and $\sigma_{\mu,i}(T^{-1})$ follow the temperature models, given by Eq. (5.6), (5.7) for the Generalised Eyring relationship and Eq. (5.10), (5.11) for the Q_{10} formulation.

Finally, given $\overline{\mu}_i(T^{-1})$ and $\sigma_{\mu,i}(T^{-1})$, we applied linear regression for parameters A, B in the Generalised Eyring model (Eq. (5.6), (5.7) to infer $a_{\text{GE}}, b_{\text{GE}}, c_{\text{GE}}, d_{\text{GE}}$) and a least squares method for only parameters A in the Q_{10} relationship (Eq. (5.10) to infer $a_{\text{Q10}}, c_{\text{Q10}}$) with the Levenberg-Marquardt algorithm provided in SciPy (Jones et al., 2001); once to fit the mean and once to fit the standard deviation of each parameter as a function of temperature. Due to the simplicity of the problem after our transformation, a relatively simple optimisation algorithm was sufficient. For the constant B parameter in the Q_{10} relationship (Eq. (5.11)), we followed the standard way of using a Q_{10} relationship where rates are extrapolated from room temperature. Therefore we extrapolated to other temperatures using $\overline{\mu}_i(T^{-1})$ and $\sigma_{\mu,i}(T^{-1})$ at $T = 25\,^{\circ}\text{C}$.

The estimated mean as a function of temperature was used to perform predictions for each temperature model; the estimated standard deviation as a function of temperature allowed us to compute the uncertainty bounds for the I_{Kr} model parameters for each temperature model.

5.4 Results

5.4.1 Temperature dependence of recordings

Figure 5.3 shows the normalised voltage clamp recordings measured with the nine different protocols, and the corresponding voltage protocols, at the five temperatures. Each panel, from top to bottom, shows the voltage clamp protocol (black), normalised recordings (blue) that passed quality control at 25, 27, 30, 33, and 37 °C, respectively. All results shown are the first of the two repeats of our recordings.

Figure 5.3A shows the staircase calibration protocol (in black) and the corresponding experimental recordings (in blue). The change in the recorded current as temperature increased was prominent, it increased the size of the current but also highlighted alterations to the kinetics: during the first half (3–8 s) of the staircase protocol, at low temperature, there was almost no current recorded; however, at physiological temperature, the current was almost as big as the current recorded during the second half (8–13 s) of the staircase protocol. Furthermore, the shape of the current during the second half (8–13 s) of the staircase protocol also changed as temperature increased. This demonstrates that the staircase protocol contains some useful information on how kinetics change with temperature.

Figure 5.3B–I shows experimental recordings for the other eight validation protocols from the same cells. In Validation #1 (Figure 5.3B) we saw the activation I-V curve shifting to a lower voltage at higher temperatures. In Validation #3 (Figure 5.3D) and Validation #6–9 (Figure 5.3G-I) larger hERG currents were observed at higher temperatures. Both these responses for hERG have been reported previously (Vandenberg et al., 2006).

5.4.2 Temperature-dependent fits and predictions

In Chapter 4, we showed exclusively the quality of fits and predictions for the hERG models at 25 °C, as this could be most easily compared with previous manual patch results (Beattie et al., 2018); the models replicated both the experimental training *and* validation data very well.

Figure 5.4 shows the model fitting and validation results for all recorded cells at 37 °C alongside the experimental recordings measured under the nine different protocols. We fitted the model to the staircase protocol (Figure 5.4A) and validated against the other eight protocols (Figure 5.4B–I). To visually compare the variability in hERG kinetics (and not conductance), currents are normalised by scaling them to minimise the absolute difference between each trace and a reference trace (as in Chapter 4).

We applied the same error measure as in Chapter 4, the relative root-mean-square error (RRMSE) defined in Eq. (4.35), to quantify the fits and predictions. Figure 5.5 shows the RRMSE histograms

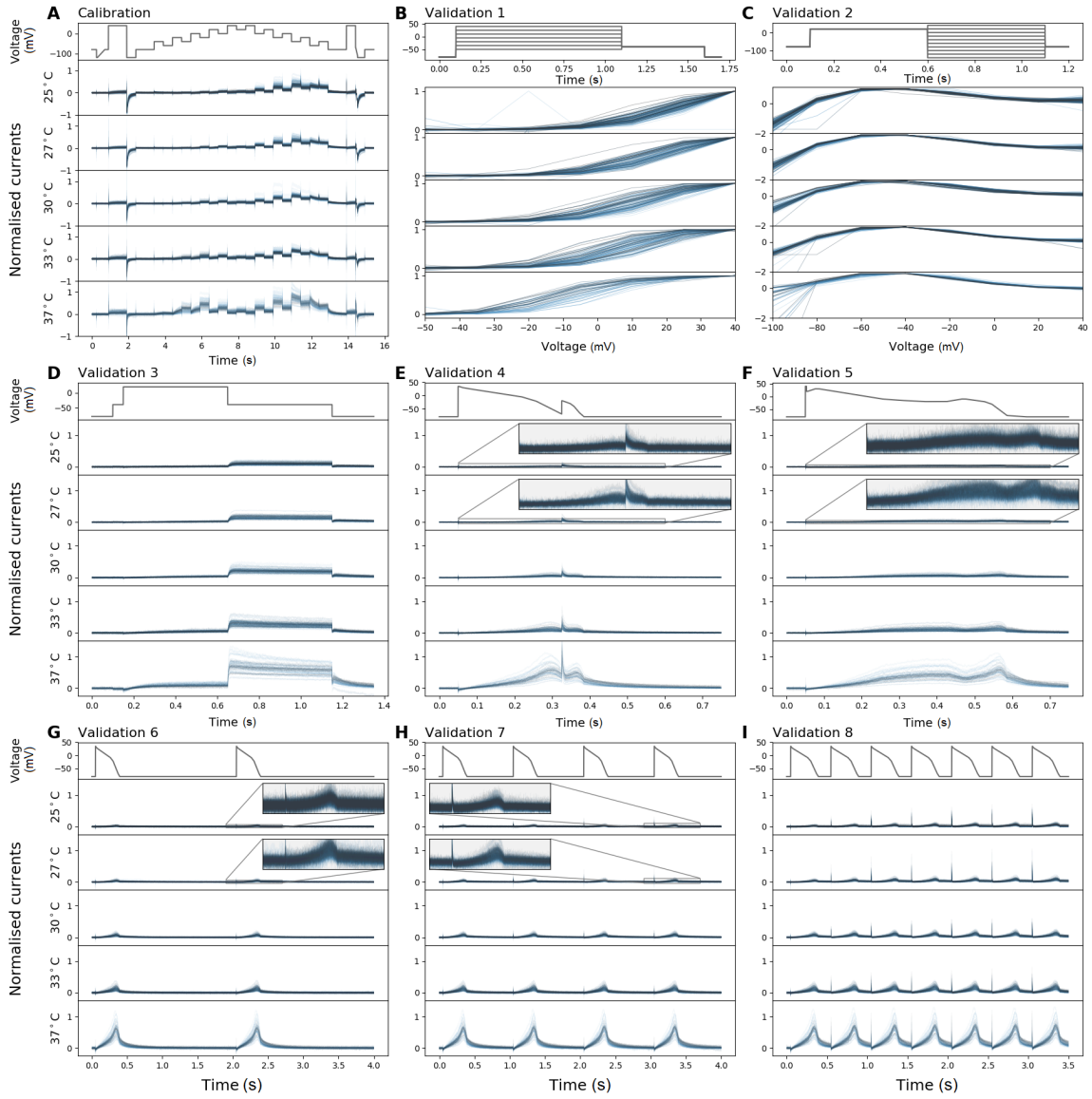

Figure 5.3: Whole-cell patch-clamp voltage clamp recordings (normalised) under nine different protocols, which were all measured in each cell, at five temperatures. For each panel, from top to bottom shows the voltage clamp protocol (black), normalised current recordings (blue) that passed quality control at 25, 27, 30, 33, and 37 °C respectively. **(A)** The calibration protocol, the staircase protocol. **(B)–(I)** The eight different protocols used as validation of the model calibration, which are the activation I-V protocol, the steady-state inactivation I-V protocol, the hERG screening protocol, the delayed afterdepolarization (DAD)-like protocol, the early afterdepolarization (EAD)-like protocol, and the cardiac action potential-like protocol at 0.5 Hz, 1 Hz and 2 Hz, respectively. In **(B)** and **(C)**, Validation #1 and #2 show the I-V relations extracted from the currents.

for all cells and for all protocols at 37 °C. Markers indicate the best (∗), median (‡) and 90$^{\text{th}}$ percentile (#) RRMSE values, and corresponding raw traces and predictions are shown in the three panels above. We note that the models only show single exponential decays due to the limitations of the model structure whilst the data seem to show double exponential decays. These results demonstrate that the hERG model remains a very good representation of the current kinetics, even at 37 °C, the highest temperature.

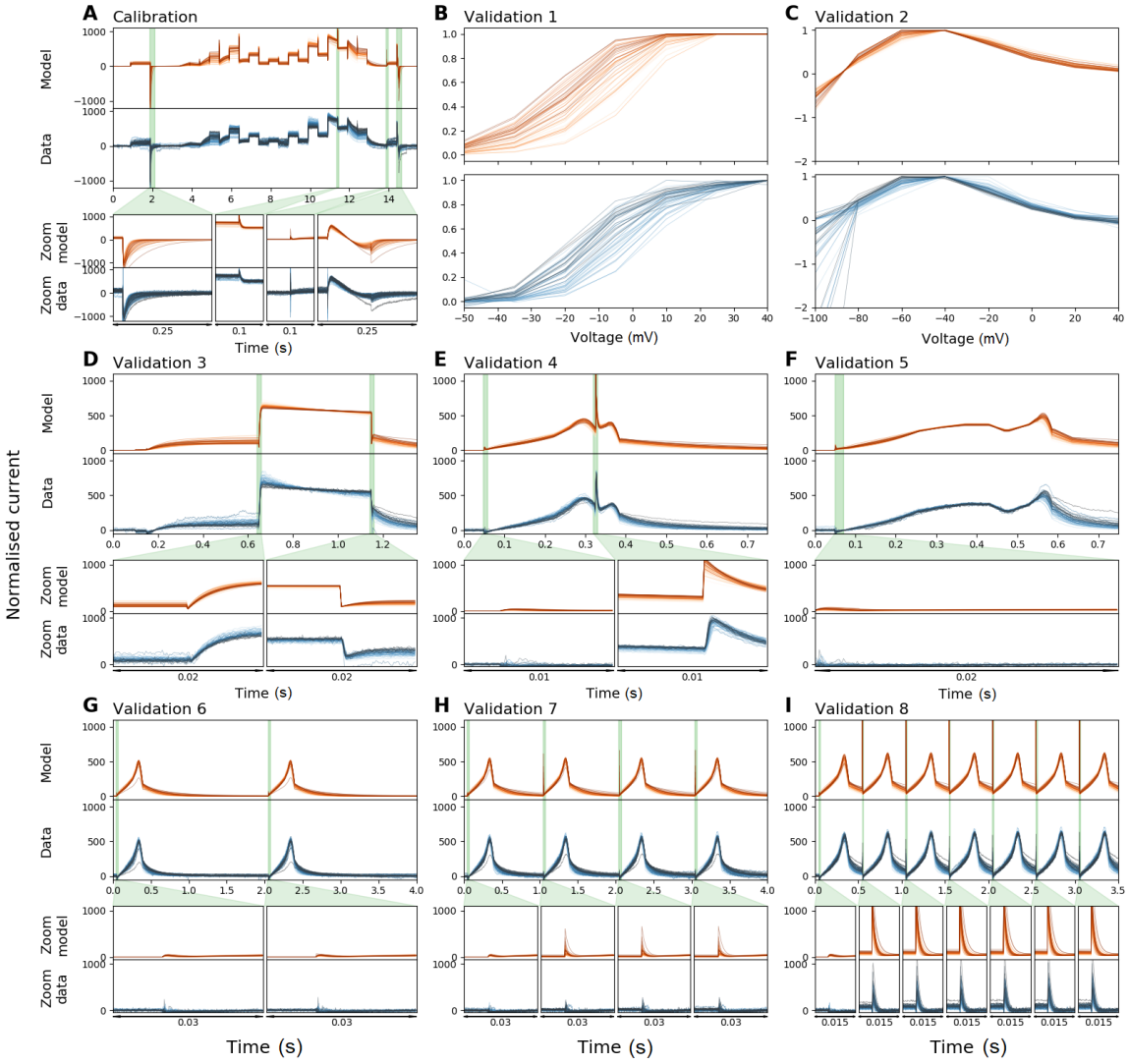

Figure 5.4: Whole-cell patch-clamp voltage clamp recordings under night different protocols, and the model fitting and validation results, at 37 °C. All currents are normalised by scaling them to minimise the absolute difference between each trace and a reference trace. From **(A)** to **(I)**: The results of the staircase protocol which is used as the calibration protocol, the activation I-V protocol, the steady-state inactivation I-V protocol, the hERG screening protocol, the DAD-like protocol, the EAD-like protocol, and the cardiac action potential-like protocol at 0.5 Hz, 1 Hz and 2 Hz, respectively. All the model calibration results and validation predictions are shown in the top panels (orange), and are compared against the experimental recordings shown in the bottom panels (blue). Zoomed-in of the green shaded regions are shown underneath each panel to reveal the details of the spikes, in which our models show extraordinarily good predictions to the details. The normalised current for all protocols are shown except for the activation I-V protocol and the steady-state inactivation I-V protocol where the summary statistic I-V relationships are shown. Each cell is shown with a unique colour.

5.4.3 Temperature dependence of inferred model parameters

Figure 5.6 shows the inferred parameter values, which are used in the model predictions in Figure 5.4 and the intermediate temperatures, as a function of temperature. The figure shows the inferred distribution of the hyperparameter mean vector $\boldsymbol{\mu}$ (Eq. (5.12)) using the simplified pseudo-MwG at each temperature in a violin plot. The mean values and 95% credible intervals of the hyperparameter

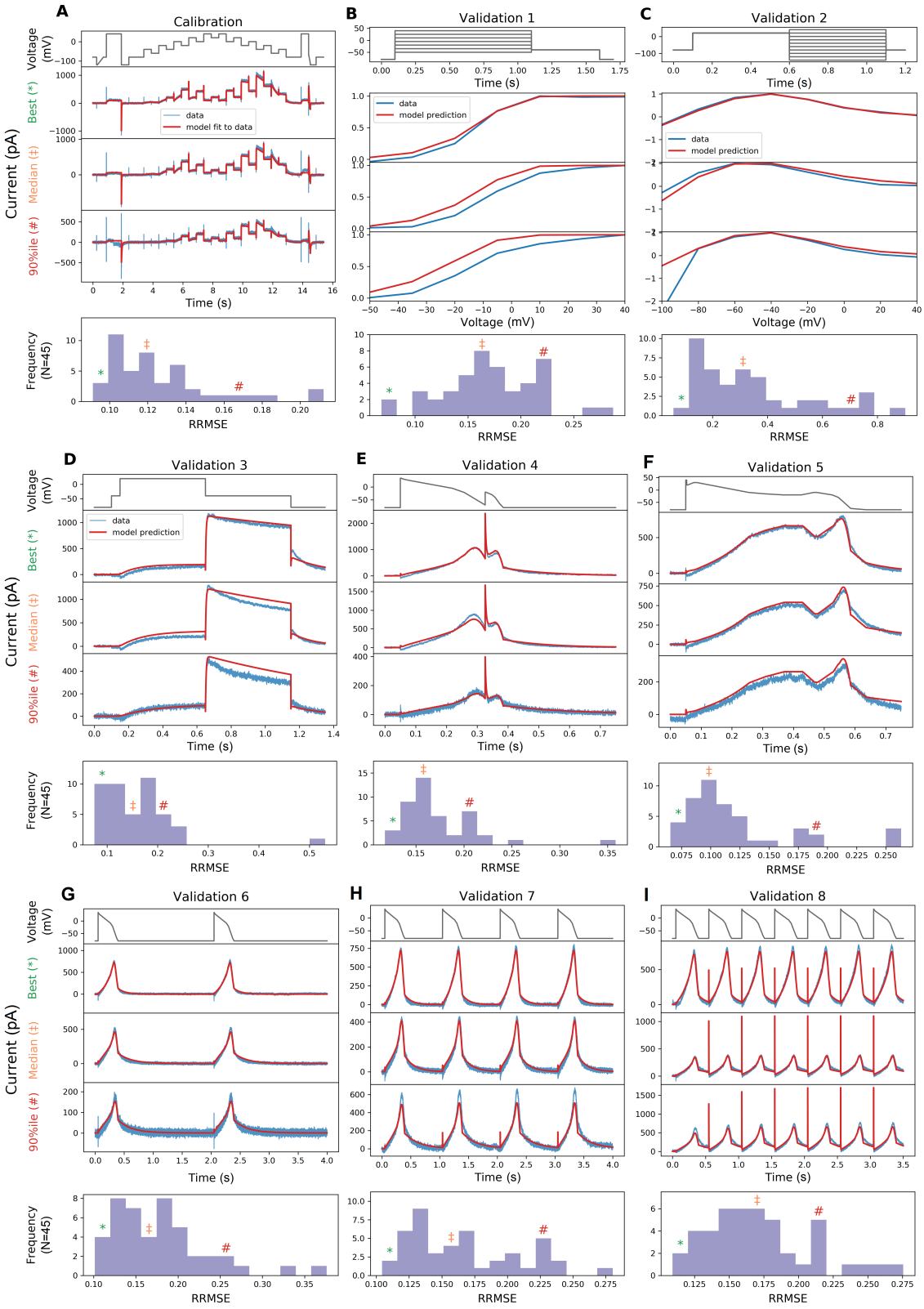

Figure 5.5: The RRMSE (given by Eq. (4.35)) histograms for all cells and for all protocols at 37 °C. Markers indicate the best (∗), median (‡) and 90$^{\text{th}}$ percentile (#) RRMSE values. The raw traces with the best, median and 90$^{\text{th}}$ percentile RRMSE values, for both the model (red) and data (blue), are shown in the panels above, together with the voltage protocol shown on top. **(A)–(I)** Show the staircase protocol, and a sequence of validation protocols. Note that the currents are shown on different y-axis limits, to reveal the details of the traces.

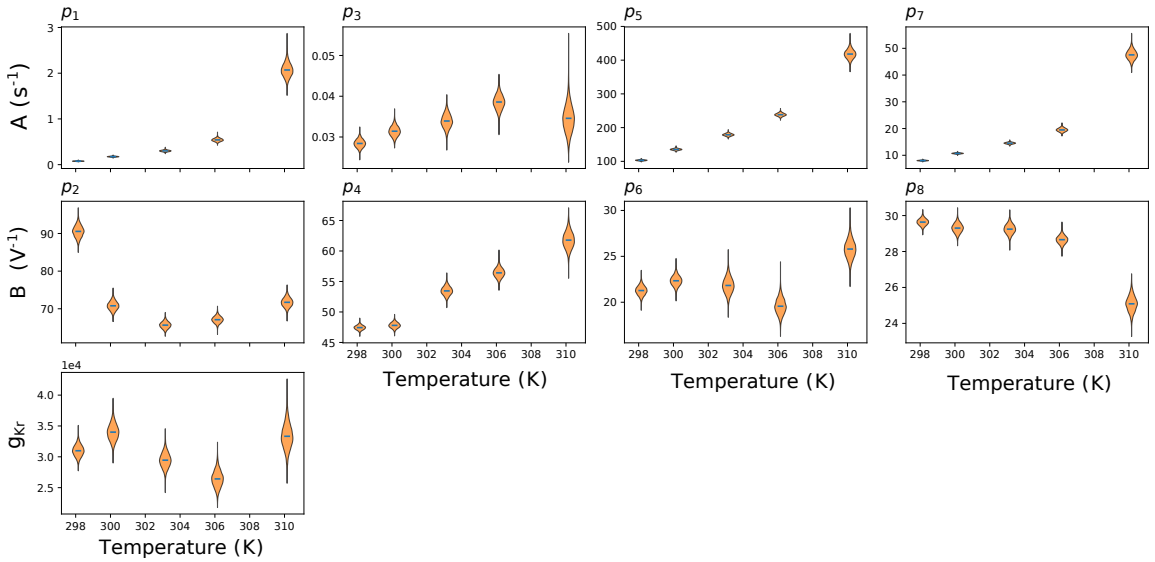

Figure 5.6: Model parameters plotted as a function of temperature. Here only the inferred distribution of the hyperparameter mean vector $\boldsymbol{\mu}$ (Eq. (5.12)) using the simplified pseudo-MwG at each temperature is shown. Parameters A, B refer to Eq. (5.1). Model parameters show different degrees of temperature dependency. The conductance g_{Kr} does not show a prominent change as temperature increases.

	g_{Kr} (pS)	p_1 (s^{-1})	p_2 (V^{-1})	p_3 (s^{-1})	p_4 (V^{-1})	p_5 (s^{-1})	p_6 (V^{-1})	p_7 (s^{-1})	p_8 (V^{-1})
$T = 25°C$	3.10×10^4	0.0765	90.5	0.0284	47.4	103	21.3	8.01	29.6
$T = 27°C$	3.40×10^4	0.175	70.8	0.0314	47.8	135	22.3	10.7	29.3
$T = 30°C$	2.94×10^4	0.300	65.7	0.0339	53.5	179	21.8	14.5	29.2
$T = 33°C$	2.64×10^4	0.540	67.1	0.0385	56.4	238	19.6	19.5	28.7
$T = 37°C$	3.33×10^4	2.07	71.7	0.0344	61.8	418	25.8	47.5	25.1

Table 5.1: The mean values of the model parameters $\boldsymbol{\mu}$ (in Eq. (5.12)) for all temperatures, corresponding to the mean values shown in Figure 5.6.

mean vector $\boldsymbol{\mu}$ for all temperatures are provided in Tables 5.1 and 5.2.

If the model kinetics were exhibiting temperature dependence following Q_{10} or Eyring rate theory, then lines whose function is specified by these principles would fit the inferred parameters in Figure 5.6.

In Figure 5.6, most parameters show an obvious monotonic trend as temperature increases; although a handful take a slightly more complicated form. It is obvious that the B parameters we inferred (p_2, p_4, p_6, and p_8 in the second row) are *not* constant over temperatures as would be expected using a Q_{10} relationship. We will compare these inferred parameters with the theoretical relationships in detail in the next section.

We then applied Eqs. (4.3) and (4.4) to calculate the steady-states a_∞, r_∞ and time constants τ_a, τ_r at the five temperatures, using the mean of the inferred distribution of $\boldsymbol{\mu}$ at each temperature. Figure 5.7 shows the resulting voltage dependency of the steady-states and time constants of the model gates a and r, where each temperature is indicated by a different colour (25 °C blue to 37 °C red).

	g_{Kr} (pS)	p_1 (s^{-1})	p_2 (V^{-1})	p_3 (s^{-1})	p_4 (V^{-1})	p_5 (s^{-1})	p_6 (V^{-1})	p_7 (s^{-1})	p_8 (V^{-1})
$T = 25°C$	2.91×10^4	0.0656	87.4	0.0265	46.7	100	20.3	7.73	29.3
	3.29×10^4	0.0892	93.7	0.0305	48.2	106	22.3	8.29	30.0
$T = 27°C$	3.13×10^4	0.158	68.4	0.0290	46.9	130	21.2	10.3	28.8
	3.68×10^4	0.193	73.3	0.0340	48.7	140	23.5	11.1	29.8
$T = 30°C$	2.71×10^4	0.268	63.9	0.0305	52.0	171	20.1	13.9	28.7
	3.20×10^4	0.336	67.5	0.0376	54.9	186	23.6	15.2	29.8
$T = 33°C$	2.38×10^4	0.477	65.3	0.0350	54.9	229	17.9	18.1	28.2
	2.92×10^4	0.612	68.9	0.0424	58.0	248	21.4	20.9	29.1
$T = 37°C$	2.94×10^4	1.78	69.3	0.0284	59.0	391	23.8	4.4e+1	24.2
	3.77×10^4	2.39	74.2	0.0418	64.6	446	27.9	51.3	26.0

Table 5.2: The 95th percentile of the samples (95% credible intervals) of the model parameters $\boldsymbol{\mu}$ (in Eq. (5.12)) for all temperatures. The top row for each temperature shows the lower bound; the bottom row shows the upper bound.

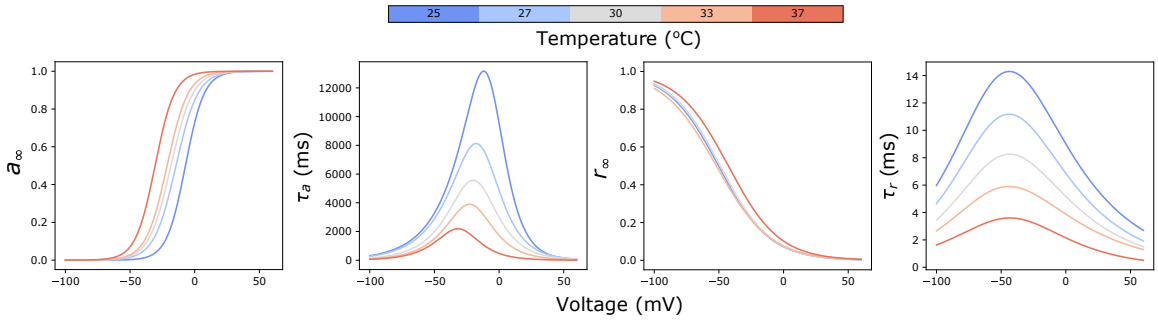

Figure 5.7: Predicted voltage dependency of steady-states and time constants of the model gates a and r at different temperatures. These lines are calculated directly from inferred parameters using Eqs. (4.3) and (4.4) with the independently-fitted hierarchical Bayesian model mean values.

Figure 5.7 shows that as the temperature increases, the steady-state of the activation gate a shifts in a negative voltage direction, a prediction from the fitted model that is in agreement with the experimental observations in Validation #1: the voltage of half-maximal activation ($V_{1/2}$) of a_∞ shifts from -7.5 mV at 25 °C to -30.9 mV at 37 °C, without a noticeable change in the slope factor. However, the steady-state of the inactivation gate r does not show a prominent change over temperatures.

The time constants of both gates τ_a, τ_r show a similar effect as temperature increases; the maximum τ_a drops from 13.2 s at 25 °C to 2.2 s at 37 °C, and the maximum τ_r drops from 14.3 ms at 25 °C to 3.6 ms at 37 °C. Note that τ_a is on the order of seconds while τ_r is in milliseconds. The voltage which maximises the time constant shifts from -11.6 mV at 25 °C to -31.7 mV at 37 °C for the activation gate, although it does not show a noticeable change for the inactivation gate.

5.4.4 Comparing models of temperature dependence

Figure 5.8 shows the Generalised Eyring relationship and the Q_{10} equation fitted to the inferred parameters shown in Figure 5.6 (orange violin plot). The results are shown in the Eyring plot form: $\ln(A/T)$ and $|B|$ as functions of T^{-1}. The Generalised Eyring fits are shown as green fan charts with

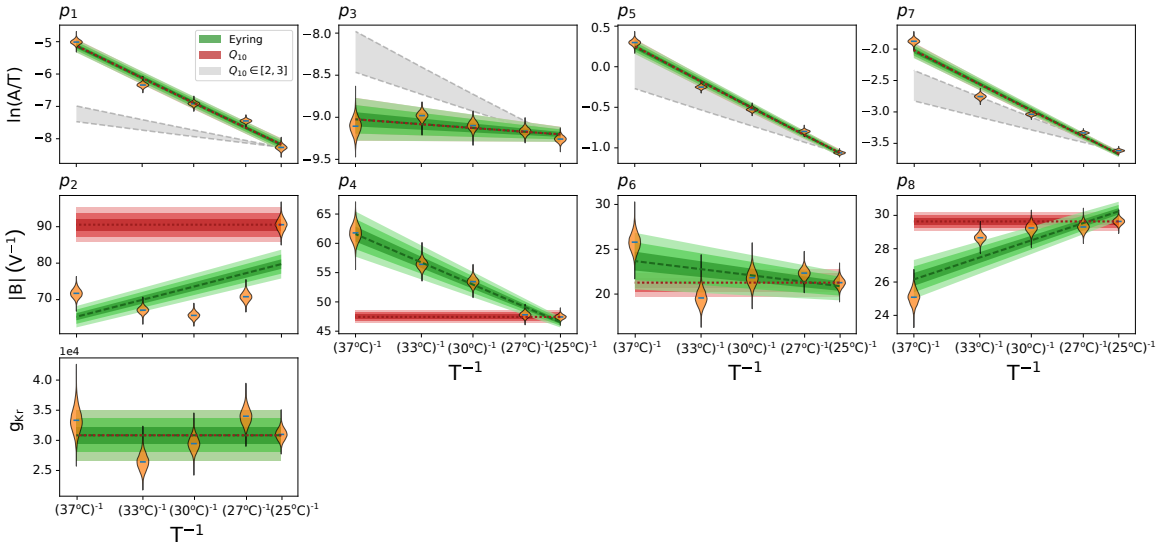

	ΔS ($JK^{-1}mol^{-1}$)	ΔH ($Jmol^{-1}$)	z_e	D (V^{-1})
k_1	389.543	195330.0	9.59193	-293.601
k_2	-235.457	11514.1	9.98987	-435.358
k_3	75.3932	84017.4	-1.85611	93.1319
k_4	125.715	105487.0	-2.71481	75.4196

	Q_{10}	α (s^{-1})	β (V^{-1})
k_1	13.1283	0.0843731	90.5512
k_2	1.19849	0.030066	-47.4353
k_3	3.0847	103.436	21.2742
k_4	4.08594	7.62406	-29.6366

Figure 5.8: Fitting of Generalised Eyring equation and Q_{10} equation to the distribution of the mean parameter values (mean over all wells, $\boldsymbol{\mu}$, shown with an orange violin plot) on the Eyring axes. The obtained Generalised Eyring fits are shown as green fan charts with the first three standard deviations; the obtained Q_{10} fits are shown in red. The fitted parameters for the Generalised Eyring and Q_{10} equations are shown in the bottom right tables, one set for each k_i, $i = 1, 2, 3, 4$. For Q_{10} equations, $T_{\text{ref}} = 298.15\,\text{K}$ was used. Note that the non-zero estimations of D in the Generalised Eyring relationship indicate that the Typical Eyring cannot fit to all B parameters, as it is required to go through the origin. For comparison to typical Q_{10} values in literature, where Q_{10} values are commonly assumed to be around 2 to 3, we show a $Q_{10} \in [2, 3]$ relationship with the grey shaded region.

the first three standard deviations; the Q_{10} fits are shown similarly in red. The obtained parameters for the Generalised Eyring equation (Eq. (5.3)) and the Q_{10} equation (Eq. (5.8)) are given in the bottom right tables, one set for each rate k_i, $i = 1, 2, 3, 4$. Reassuringly, the values in the tables are comparable to (the same orders of magnitude as) typical literature values for ion channel models (Tsien and Noble, 1969; Irvine et al., 1999; Zhou et al., 1998; Dhaka et al., 2006; Vandenberg et al., 2006; Fink et al., 2008).

From the illustration in Figure 5.1, we expect the Generalised Eyring and Q_{10} formulations to be indistinguishable for the A parameters, and indeed in Figure 5.8, the green fan charts (Generalised Eyring) are on top of the red fan charts (Q_{10}) in the first row: both formulations are able to fit to the inferred model's A parameters.

Figure 5.8 shows that the Generalised Eyring equations fit the inferred B parameters better than the Q_{10} equations. The Generalised Eyring equations are able to fit the inferred model parameters to a large extent except for p_2; whereas the B parameters in the Q_{10} equations are not temperature dependent (by definition), which is contradicted by our observations.

Furthermore, it is evident that for parameters p_4, p_6 the two lines cannot intercept the y-axis close to the origin, as they are decreasing rather than increasing on these plots. Parameters p_2 and p_8 also have non-zero estimates of D in the Generalised Eyring relationship, indicating that the Typical Eyring relationship cannot be fit to any of our B parameters. The closest Typical Eyring relationship for p_8 is actually the example shown earlier in the bottom panel of Figure 5.1. The gradient of the Generalised Eyring fit is approximately twice as steep as the Typical Eyring fit would require for this parameter.

In the literature, Q_{10} coefficients for biological processes such as channel gating are commonly thought to take values from around two to three (Ranjan et al., 2011). To investigate this assumption, we projected our 25 °C model parameters directly using Eq. (5.8) with $Q_{10} \in [2, 3]$ and shown as the grey shaded region in Figure 5.8. Parameter p_5 in the inactivation rate (k_3) gives a Q_{10} just above three, but none of our other inferred relationships for parameter A is close to the range $Q_{10} \in [2, 3]$.

We further assess the performance of the temperature dependence models by comparing their mean model predictions against the data and the temperature-specific models. Figure 5.9 shows the mean model predictions from the temperature-specific parameters (orange), the Generalised Eyring formulation (dotted green), and the Q_{10} coefficient (dashed red) for the staircase protocol. All predictions are generated with the same mathematical model, Eq. (4.1), where the rate constants in Eq. (4.3) and Eq. (4.4) are replaced by Eq. (5.4) (for the Generalised Eyring formulation) and Eq. (5.8) (for the Q_{10} coefficient) computed with the inferred parameters shown in the tables of Figure 5.8, with Q_{10}-based predictions based on extrapolation from 25 °C. The top panel shows the staircase protocol, followed by the normalised current at five different temperatures. Data (in Figure 5.3A) are shown in fan charts style with the 30^{th}, 60^{th} and 90^{th} percentiles in blue. At low temperatures, all three models agree with the data. At higher temperatures, particularly at 37 °C, the predictions from the Generalised Eyring formulation (dotted green) still agree reasonably with the temperature-specific independently fitted parameters (orange) and both fit the data (blue) well. However, the prediction using Q_{10} coefficients deviates from the data during the spikes (see zoomed-in images on the right) and does not predict the time-course accurately during 4–7 s and 12–13 s of the staircase protocol (see insets in Figure 5.9).

Figure 5.10 shows a 2 Hz action potential-like protocol prediction version of Figure 5.9. All the three mean models are able to predict the current during the repolarisation of the action potential clamp very well. The spikes during the upstrokes are however badly predicted by the Q_{10} coefficient mean model; while the Generalised Eyring formulation, similar to the temperature-specific parameters, gives a prediction closer to the data.

5.5 Discussion

This chapter addresses one of the questions set out in Chapter 3: whether a (simple) scaling of rates in ion channel models is enough to capture the temperature dependence of the channel kinetics. A short answer to that is “possibly not”. In this chapter we have examined the temperature dependence of hERG kinetics, at five temperatures ranging from room to body temperature, with 45 to 124

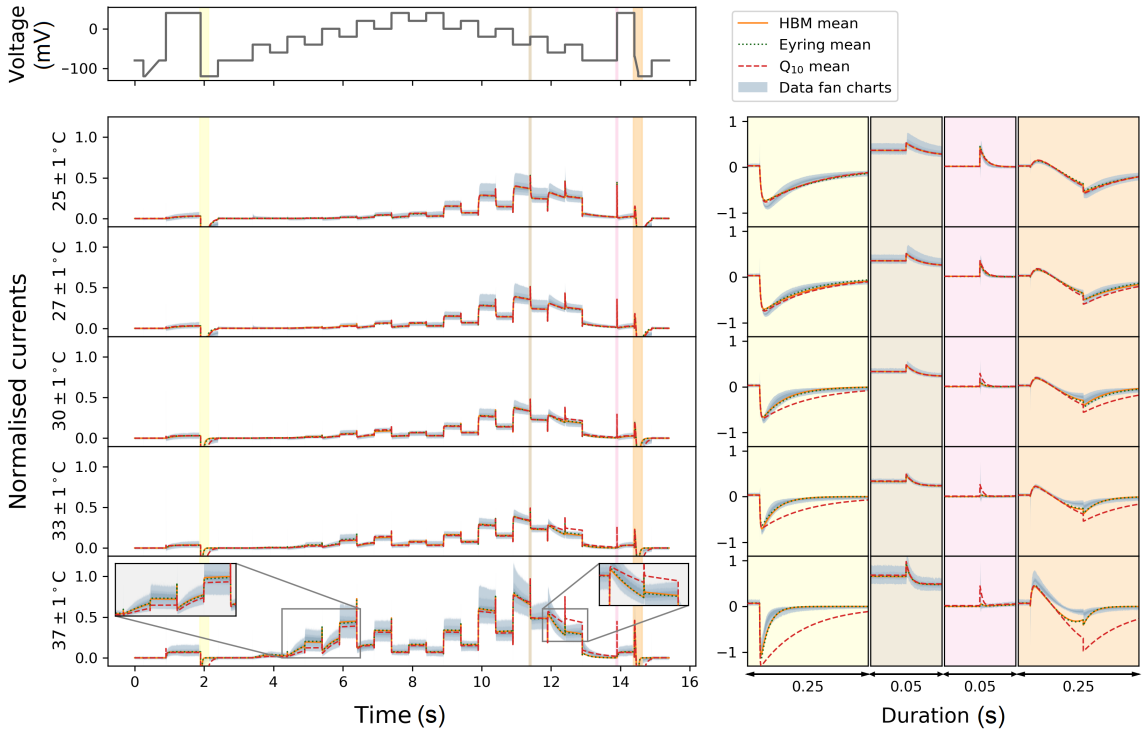

Figure 5.9: Comparison of the Generalised Eyring formulation (dotted green) and Q_{10} coefficient (dashed red) mean predictions for the staircase protocol. Top figure shows the staircase protocol, followed by the normalised current at five different temperatures. Data (in Figure 5.3A) are shown in fan charts style with the 90^{th}, 60^{th} and 30^{th} percentiles in blue. The mean prediction from the hierarchical Bayesian model (HBM) is shown in orange. Zoomed-in regions are shown on the right with colours matching the highlighted regions of the main plots on the left.

cells per temperature. We have used a mechanistic model and its parameterisation to capture our knowledge of the hERG kinetics. By assuming that all cells share the same mechanism underlying hERG kinetics we have used the inferred model parameters at different temperatures to reveal the temperature dependence of hERG gating kinetic parameters. This is, to our knowledge, the first systematic effort to have taken this approach.

5.5.1 Temperature dependence of hERG kinetics

Using the staircase protocol, we were able to characterise hERG kinetics to the extent that our model can replicate both the experimental training *and* validation data very well, for *all* of the measured temperatures. Our models can predict the current response to the physiologically-relevant action potential protocols with a very high accuracy, demonstrating that our I_{Kr} models are robust in predicting hERG current, in both healthy and arrhythmic situations. This gives us confidence that the *cell-specific model* parameters do represent and capture hERG kinetics at the given temperatures.

The directly fitted models reveal that the activation gate has a much higher temperature sensitivity than the inactivation gate. This effect is shown in both the comparison of steady-states and time constants (Figure 5.7) and the inferred Q_{10} coefficients (Figure 5.8) where the Q_{10} values for the activation gate (k_1, k_2) are overall higher than the inactivation gate (k_3, k_4). Our results suggest that

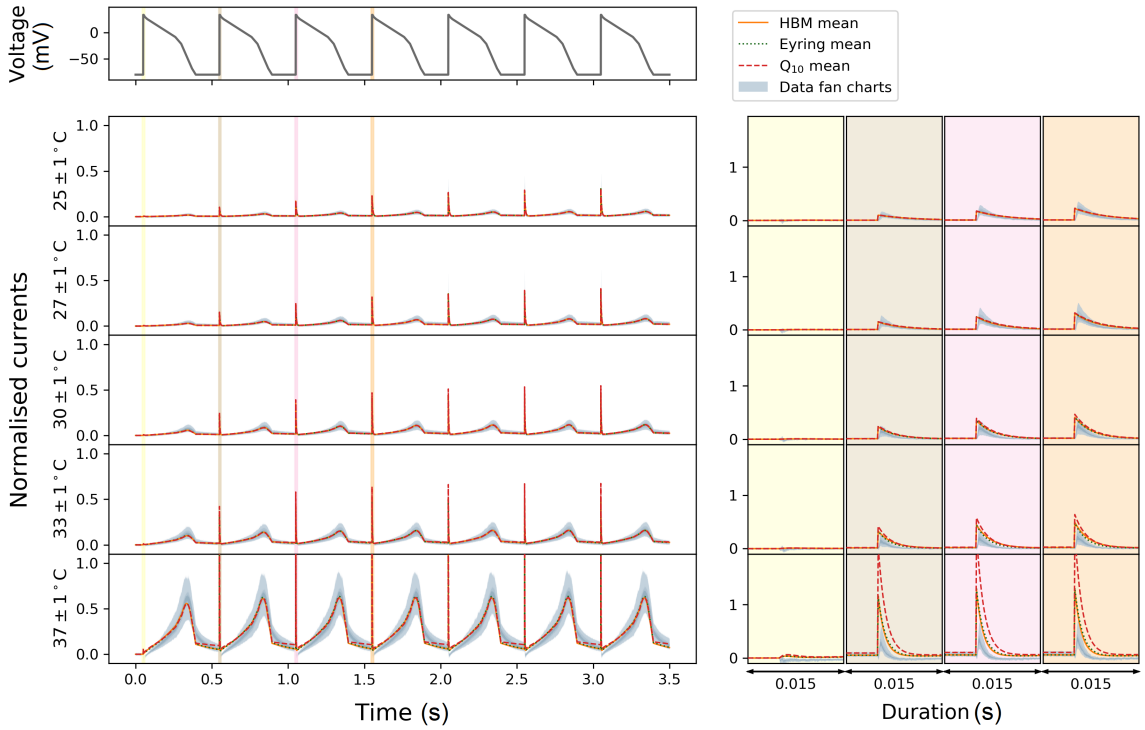

Figure 5.10: Comparison of the Generalised Eyring formulation (dotted green) and Q_{10} coefficient (dashed red) mean predictions for the 2 Hz action potential-like protocol. Top figure shows the staircase protocol, followed by the normalised current at five different temperatures. Data (Figure 5.3A) are shown in fan charts style with the 90$^{\text{th}}$, 60$^{\text{th}}$ and 30$^{\text{th}}$ percentiles in blue. The mean prediction from the hierarchical Bayesian model (HBM) is shown in orange. Zoomed-in regions are shown on the right with colours matching the highlighted regions of the main plots on the left.

there is no common Q_{10} value for different transition rates. In fact, the model equations (a gate x has $x_\infty = k_i/(k_i + k_j)$ and $\tau_x = 1/(k_i + k_j)$) suggest that if either the steady state changes or the τ-V curve shifts as function of temperature, then the transition rates k_i and k_j should have different Q_{10} values.

Our inferred Q_{10} coefficient for the rate of activation (k_1) is relatively high compared to literature results (Zhou et al., 1998; Vandenberg et al., 2006). However, our findings are not implausible, when compared to other potassium channels, such as $K_V2.1$ and $K_V4.3$, which can have maximum Q_{10} values in the 20–30 range (Yang and Zheng, 2014). Other ion channels can also exhibit a very high temperature sensitivity, such as transient receptor potential (TRP) ion channels which were reported to have Q_{10} values ranging from 2–15 (Dhaka et al., 2006). We now compare our model predictions with earlier literature results.

5.5.2 A comparison to literature results

Our hierarchical Bayesian models at different temperatures are not only able to predict our validation data but also able to reproduce the temperature dependence seen in previous studies (Vandenberg et al., 2006), where the increase of temperature caused a large increase in the overall ‘steady state open probability’. Figure 5.11 shows that our simulations (right panel) are broadly consistent with

the temperature effect observed by Vandenberg et al. (2006) (left panel). The fan charts show the 30th, 60th and 90th percentiles of the simulations, representing the *inter-experiment* (well-well) variability. There are differences between our simulations and their experimental results, with a smaller open probability at low temperatures in our simulations and a slight shift of the curves to the right. Nevertheless, our results are broadly consistent with the temperature effect observed by Vandenberg et al. (2006) and predict a very similar 'width' for this steady state window of open probability and also agree with the absolute values of the probabilities at the higher temperature very well.

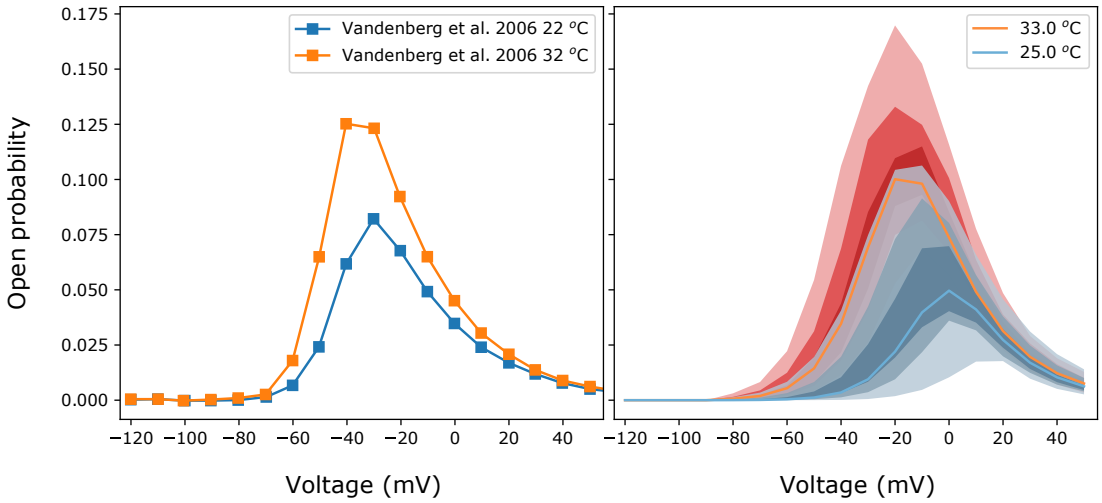

Figure 5.11: Voltage dependence of steady state 'open probability' as defined by Vandenberg et al. (2006, Figure 6) using a multiplication of experimental approximations for the product $a_\infty r_\infty$. **(Left)** Data extracted from Vandenberg et al. (2006, Figure 6). **(Right)** The fan charts show the 90th, 60th and 30th percentiles of the hierarchical Bayesian model simulations, representing the *experiment-experiment* variability. Orange/red represents 32–33 °C, and blue represents 22–25 °C.

We also compared the model given by the mean of the posterior for $\boldsymbol{\mu}$ at 37 °C (Table 5.1) with existing I_{Kr} models from within action potential models by using the Cardiac Electrophysiology Web Lab (Cooper et al., 2016; Daly et al., 2018). The CellML description (Garny et al., 2008) is available online, see Data and Software Availability at the end of the chapter. Interestingly, the new model shows a striking concordance for predicted current under action potential clamps with the Markov model by Fink et al. (2008), as shown in Figure 5.12.

5.5.3 Experimental protocol dependence of Q_{10}

Q_{10} formulations have often been estimated in the past with different protocols, even for the same gating process (e.g. activation). For example, two well-known experimental studies of temperature dependence of hERG kinetics, by Zhou et al. (1998) and Vandenberg et al. (2006), estimated the Q_{10} coefficients using different protocols and analyses, and reported two different sets of Q_{10} coefficients (see Table 5.3) for various gating processes. We asked, if the two experiments were to be repeated with the *same underlying kinetics*, would they agree with one another? Using our directly-fitted models at 25 °C and 37 °C, we simulated the two different sets of experiments described in (Zhou et al., 1998; Vandenberg et al., 2006). We then estimated two sets of Q_{10} coefficients following the

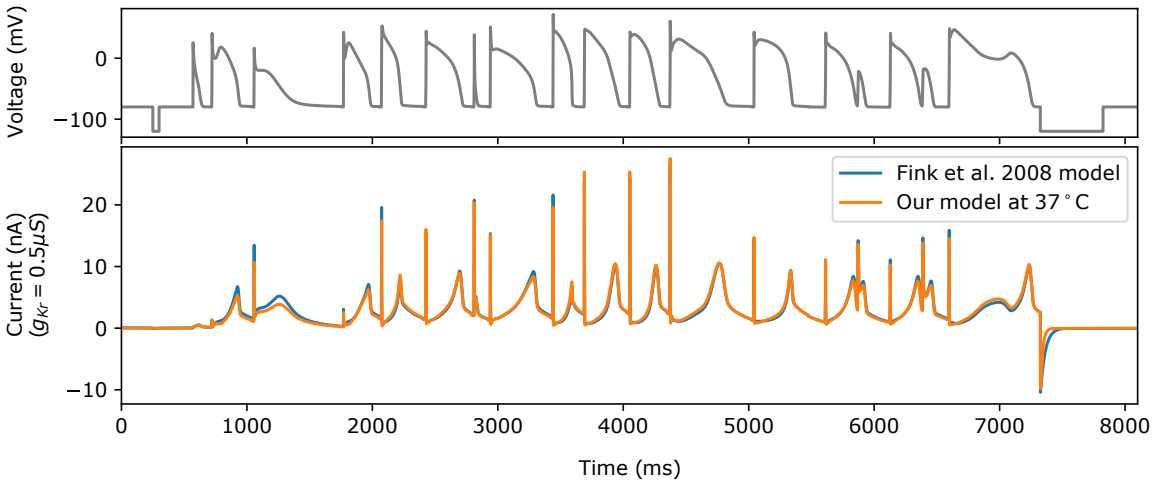

Figure 5.12: A comparison of predictions of the Fink et al. (2008) I_{Kr} model and our mean model using the posterior for $\boldsymbol{\mu}$ at 37 °C, under a series of action potential clamps. Both models have the same fixed $g_{\text{Kr}} = 0.5$ µS to compare the differences in kinetics.

protocols and analysis in each of the papers, and the obtained values are shown in Table 5.3. The findings in Table 5.3 show that due to *different protocols* the estimated Q_{10} coefficients can disagree. Furthermore, neither of the protocols reproduces the direct estimate of Q_{10} coefficients from the model parameter temperature relationships (shown in the bottom right of Figure 5.8). We conclude that extreme caution should be used when directly modifying rates in models with experimental estimations of Q_{10} coefficients.

5.5.4 Implication for ion channel temperature dependence

Fitting directly to the staircase protocol at different temperatures does not require any assumption about the underlying temperature dependence of the kinetic parameters, except that the model structure does not change. The existing well-known models/approximations for temperature dependence of ion channel transition rates are the Q_{10} and Typical Eyring formulations. This chapter has raised concerns about how accurate these relationships are. In terms of parameter values (Figure 5.8) neither of these methods is able to capture the full temperature dependence of the directly-fitted parameters, $\boldsymbol{\mu}(T)$, and predictably this impairs their ability to fit and predict currents (Figure 5.9). However,

	Zhou et al. (1998)		Vandenberg et al. (2006)	
	Reported values	Model estimation	Reported values	Model estimation
Activation	6.25 ± 2.55	10.67 ± 7.482	2.1 ± 0.30	7.400 ± 4.111
Deactivation	1.36 ± 0.40	2.016 ± 0.764	1.7 ± 0.30	3.692 ± 1.224
Inactivation	3.55 ± 0.87	3.421 ± 1.028	2.5 ± 0.53	2.750 ± 0.900
Recovery	3.65 ± 0.73	2.991 ± 0.730	2.6 ± 0.26	4.436 ± 2.763

Table 5.3: Q_{10} coefficients for each gating process, estimated using the protocols specified in Zhou et al. (1998) and Vandenberg et al. (2006). The values were derived from simulations performed using the temperature-specific hierarchical Bayesian model fits at 25 °C and 37 °C.

using a Generalised Eyring relationship (not commonly used in ion channel modelling) can closely mimic our full direct fitting approach. Whilst the model predictions using the Q_{10} formulation can generally predict overall trends in temperature effects, the predictions cannot capture the details of the current, compared to the Generalised Eyring relationship or the full direct fitting approach (see Figures 5.9 and 5.10). We therefore suggest neither Q_{10} formulations nor the Typical Eyring relationship should be used: the Generalised Eyring relationship is much better for temperature predictions. But for the best results the model should be refitted at any temperature of interest using an information-rich protocol, such as our staircase protocol.

The nonlinearity of some kinetic parameters on the Eyring plots implies the Generalised Eyring relationship is a reasonable but imperfect temperature model. Under the assumption that the model structure is correct, we accurately captured the kinetics at each temperature, and the model structure stays the same for all temperatures. However, we could challenge these assumptions, and suppose that the Generalised, or even Typical, Eyring relationship is true for any transition of ion channel from one conformational state to another. In this case, the Eyring formulation not matching the individual temperature parameter sets could imply that, either: (a) the hERG model structure that we have assumed is incorrect, i.e. the relationship not holding is a consequence of discrepancy between the model and reality; or, (b) our procedure did not accurately capture the kinetic parameters at each temperature, but the fact that the parameters give excellent fits and predictions (and many parameters do follow expected trends) perhaps alleviates this concern; or, (c) in reality, the energy landscape of ion channel conformations changes with temperature, and a given transition in the model represents a different jump in conformational state, i.e. the model structure should change with temperature (which has been modelled previously for hERG by Di Veroli et al. (2013)).

In any case, applying a simple treatment such as the Q_{10} coefficient to an imperfect model that violates the assumptions above would not automatically alleviate any mismatch. Since our temperature-specific fits can replicate both the experimental training data *and* the validation data very well at all temperatures, the model is a good *representation* of hERG kinetics. Hence it is better to apply a rapid and reproducible procedure, as illustrated here, for generating all the parameters within a model at a new temperature, whenever possible. However, if necessary, then the Generalised Eyring relationship would be a preferable choice for predicting kinetics at a new temperature where measurements cannot be, or have not been, taken. While further work might show our results are more generally applicable to other channels, for now they should be interpreted as being specific to hERG1a.

5.6 Conclusion

In this chapter, we have studied the temperature dependence of hERG kinetics using a 15-second high-information content protocol developed in Chapter 4. We characterised the temperature dependence by fitting a mathematical model of hERG channel kinetics to data obtained at five distinct temperatures between 25 and 37 °C. We constructed between 45 and 124 cell-specific hERG models at each temperature using the 15-second calibration protocol, and our cell-specific variants of the hERG model were able to predict currents under eight independent validation protocols with high accuracy. We represented the variability in parameters using a hierarchical Bayesian model, and were able to

reproduce the temperature dependence observed in previous literature studies. Our models reveal that the hERG activation process has a higher temperature sensitivity than the inactivation process. The Q_{10} coefficients that we obtained range from 1.2 to 13.1 for different processes, falling outside the commonly assumed range of around 2 to 3. Moreover, the temperature dependence of the kinetic parameters we obtained takes a more complicated form than that predicted by Q_{10} coefficients. Although the temperature dependence cannot be described by a Typical Eyring approach, it broadly follows a Generalised Eyring relationship. Our results show that a direct fit to the 15-second protocol is the best representation of hERG kinetics at a given temperature, whilst the Generalised Eyring theory is the best alternative if no such data are available.

After applying the methods developed in Chapter 4 to study the temperature dependence of ion channel kinetics, again, we see strong experiment-to-experiment variability in measurements at different temperatures, similar to the previous chapter. It is worth noting that the variability that we discuss in Chapters 4–6 is fundamentally different from that has been discussed in Chapter 3. Here, we refer to the variability of the *kinetics* rather than the *maximum conductance* between measurements, as further discussed in the next chapter. However, since the cells expressed the same genes and were measured at the same time under highly similar conditions, the resulting current *kinetics* were expected to be more similar across cells. In the next chapter, we look for the origin of the observed variability in these measurements. That is, we address the question that arises in these two chapters: Does the observed variability result from biological or physiological variability, or could it rather be caused simply (or mostly) by measurement artefacts?

5.7 Data and Software Availability

Data and software (GitHub repository):
https://github.com/CardiacModelling/hERGRapidCharacterisation

CellML version of the mean 37 °C model:
https://github.com/CardiacModelling/hERGRapidCharacterisation/blob/master/lei_2019_37C.cellml

Chapter 6

A Mathematical Model of Artefacts in Patch-Clamp Experiments

This chapter was published as: Lei, C. L., Clerx, M., Whittaker, D. G., Gavaghan, D. J., de Boer, T. P., and Mirams, G. R. (2020a). Accounting for variability in ion current recordings using a mathematical model of artefacts in voltage-clamp experiments. *Philosophical Transactions of the Royal Society A*, 378:20190348.

Contributions: I assisted in designing the study, derived the mathematical models, built the model cells, carried out the experiments, and wrote code for and performed all the simulations and data analysis.

Overview:

In the previous chapters we fitted cell-specific models to information rich recordings of *human Ether-à-go-go-Related Gene* (hERG)1a ($K_V11.1$) measured simultaneously using an automated high-throughput system. In those chapters, we assumed our recordings were measured with only Gaussian noise and studied the observed cell-cell variability by considering the variability in the resulting cell-specific model parameters. In this chapter we revisit this ideal measurement assumption to consider instead whether the source of the variability might be measurement artefacts. We do this by constructing a model that describes not just ion current dynamics, but the entire voltage-clamp experiment. The experimental artefact components of the model include: series resistance, membrane and pipette capacitance, voltage offsets, leak current, and imperfect compensations made by the amplifier for these phenomena. In this model, variability in the observations can be explained by either cell properties, measurement artefacts, or both. Remarkably, by assuming that variability arises exclusively from measurement artefacts, it is possible to explain a larger amount of the observed variability than when assuming cell-specific ion current kinetics. This assumption also leads to a smaller number of model parameters. This chapter suggests that most of the observed variability in patch-clamp data measured under the same conditions is caused by experimental artefacts, and hence can be compensated for in post-processing by using this new model for the patch-clamp experiment.

6.1 Introduction

High levels of variability in ion channel kinetics have been observed in many studies (Bekkers et al., 1990; Finkel et al., 2006; Feigenspan et al., 2010; Golowasch, 2014; Santillo et al., 2014; Altomare et al., 2015; Annecchino and Schultz, 2018). In Chapter 4 we analysed *human Ether-à-go-go-Related Gene* (hERG) current kinetics recorded simultaneously in 124 cells using an automated high-throughput patch-clamp machine (see Figure 4.1). The experiments used Chinese Hamster Ovary (CHO) cells stably expressing hERG1a. Since the cells over-expressed the same gene and were measured at the same time under highly similar conditions, one might expect the resulting current *kinetics* to be very similar across different cells. However, a high level of variability was seen, similar to that in previous studies using manual patch-clamp experiments conducted one cell at a time over several days (Beattie et al., 2018). This raises a question — what is the origin of the observed variability?

All of these voltage-clamp measurements for studying the ion channel kinetics were done under a whole-cell patch-clamp configuration (see Chapter 2) using a patch-clamp amplifier. In voltage-clamp mode, the patch-clamp amplifier is a sensitive feedback amplifier that rapidly calculates, applies and reports the small currents necessary to maintain a given voltage across a cell's membrane (and vice versa for current-clamp mode) (Sigworth, 1995b). Typical peak current magnitudes are on the order of pA to μA, depending on the size and type of cell; the voltage across the cell membrane (potential inside minus outside) typically is within the range -140 to $+60$ mV.

Figure 6.1 (left) shows an idealised voltage-clamp experiment, where the cell is connected directly to an ammeter which records the current of interest, I_{ion}, while clamping the membrane to the command voltage, V_{cmd}. In other words, a perfect patch-clamp experiment can be represented with the following simple equations/assumptions:

$$\boxed{\begin{aligned} \text{(command voltage) } V_{\text{cmd}} &= V_{\text{m}} \text{ (membrane voltage),} \\ \text{(measured current) } I_{\text{out}} &= I_{\text{ion}} \text{ (current of interest).} \end{aligned}} \qquad \begin{aligned} &(6.1) \\ &(6.2) \end{aligned}$$

This is the first of three ways of modelling the patch-clamp system that will be discussed in this chapter (each enclosed in boxes as above).

In realistic voltage-clamp experiments, as illustrated in Figure 6.1 (right), the cell membrane acts as a capacitor in parallel to the ion currents. Between the pipette electrode and the cell, there is a *series resistance*, which induces a mismatch between the membrane voltage V_{m} and the command voltage V_{cmd}, causing a shift in measured current-voltage relationships (Marty and Neher, 1995; Sherman et al., 1999). Furthermore, there is a voltage offset introduced between the pipette electrode and the cell (Neher, 1995); and the wall of the pipette (or the well plate in an automatic system) behaves as a capacitor. Finally, a finite seal resistance can cause a substantial leak current that contaminates the recording of the current of interest. All of these can be *partially* compensated by the patch-clamp amplifier using real-time hardware adjustments, or addressed in post-processing, and the remainder are what we term '*experimental artefacts*'. Often the existence of a leak current is acknowledged and an estimate for it is subtracted in a post-processing step to modify the I_{out} in Eq. (6.2) as we will

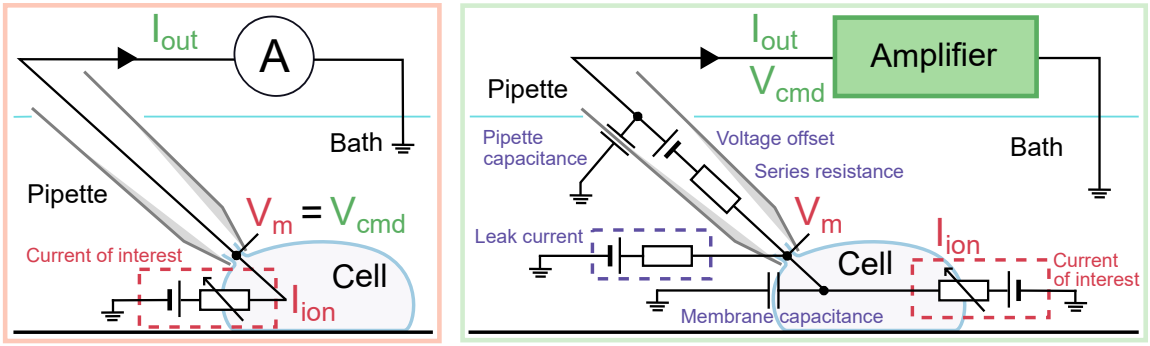

Figure 6.1: Schematics of the voltage-clamp experiment: **(left)** idealised and **(right)** more realistic. **(Left)** Only the current of interest (red) is modelled. The membrane voltage, V_{m} (red), is assumed to be the same as the command voltage, V_{cmd} (green), set by the amplifier, and the observed current, I_{out} (green), is assumed to be equal to the ion channel current, I_{ion} (red). **(Right)** Here, not only the current of interest (red) is modelled, but the patch-clamp amplifier process (green) and all of the experimental artefacts (purple) are included in the model. The differences between V_{m} (red) and V_{cmd} (green), and between I_{ion} (red) and I_{out} (green) are explicitly modelled in this framework.

discuss later. Although real-world experiments suffer from the other remaining artefacts, most studies assume the experimental apparatus perfectly compensates for any discrepancies, so the idealised assumptions (Eqs. (6.1)–(6.2)) are frequently used when analysing experimental data.

In this chapter, we relax the typical, ideal voltage-clamp assumptions by introducing a mathematical model that accounts for artefacts, imperfect amplifier compensations for artefacts, together with any residual uncompensated leak current. We then validate the mathematical model experimentally using electrical model cells, for which we designed a new type of electrical model cell which exhibits simple dynamic behaviour. Using this new mathematical model, variability in observations can be attributed to measurement artefacts as well as current properties. We develop a method to optimise the following quantities at the same time: ion current maximal conductance for each cell; a set of current kinetic parameters common to all cells; and measurement artefact parameters for each cell. Finally, we compare fits and assess the predictions of models calibrated with either the ideal voltage-clamp assumptions (used in Chapter 4) or realistic voltage-clamp assumptions we develop in this chapter.

This chapter quantifies one of the important sources of uncertainty, the observational uncertainty discussed in Chapter 2. Artefacts also become an important aspect to be considered as we design further experiments in the next chapter.

6.2 A detailed mathematical model of a voltage-clamp experiment

Figure 6.2 presents an expanded circuit for the more realistic voltage-clamp experiment shown in Figure 6.1 (right), including the amplifier components that compensate for the additional artefacts in the realistic experiment. Our goal is to observe the ion current across the cell membrane, I_{ion}. This

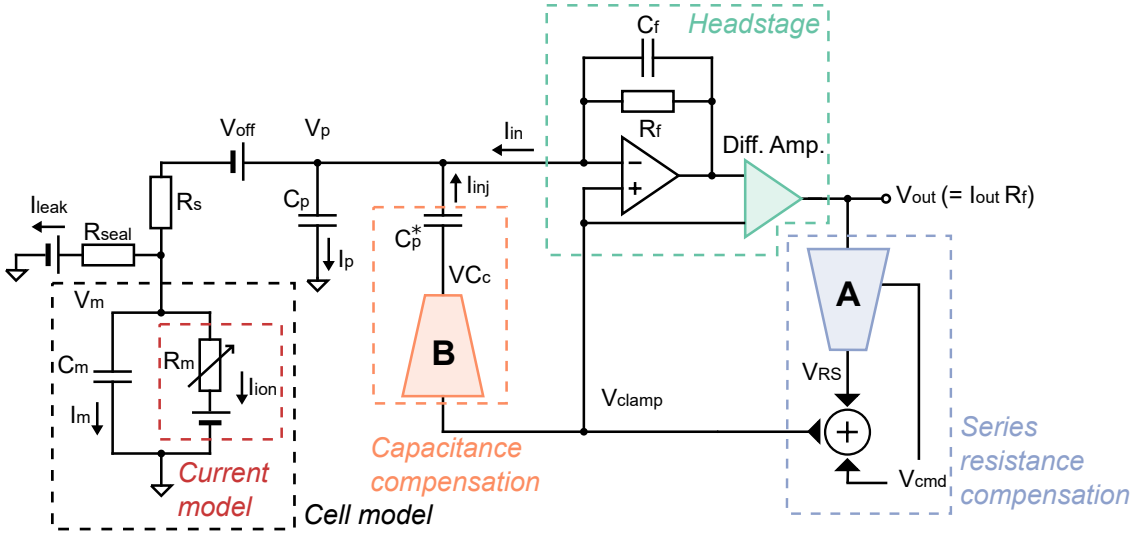

Figure 6.2: A more realistic voltage-clamp experiment equivalent circuit. This includes undesired factors such as voltage offset (V_{off}), series resistance (R_{s}) between the pipette electrode and the cell, cell capacitance (C_{m}), pipette capacitance (C_{p}), and leakage current (I_{leak}), which can introduce artefacts into the recordings. The circuit also includes the components within a typical amplifier that are designed to compensate for the artefacts. The blue **(A)** and orange **(B)** components are two idealised multiplying digital-to-analogue converters that control the amount of compensation. We assume that these, and the transimpedance amplifier and differential amplifier (green), are ideal electrical components. Please refer to Table 6.1 for a description of the symbols.

current is present in the 'Cell Model' in Figure 6.2 (shown with black, dashed box). Between the Cell Model and the Headstage (green, dashed box) is where the pipette (or the well plate in an automatic system) sits, separating the cell membrane and the pipette electrode, which includes many of the undesired artefact components shown in Figure 6.1 (right). There are five main undesired effects in this voltage-clamp set-up: 1. parasitic/pipette capacitance (a capacitance effect induced by the pipette wall); 2. (cell) membrane capacitance; 3. series resistance (a lumped term for all resistances between the pipette electrode and the cell); 4. voltage offset (due to amplifier offsets, electrode offsets, junction potentials, etc.); 5. leak current (a current leak through the pipette-cell seal and any leak through the membrane). Table 6.1 contains a glossary of symbols and parameters used for these quantities throughout this chapter.

To model the dynamics of the current of interest, I_{ion}, the assumptions behind Eqs. (6.1)–(6.2) can be removed to instead model the entire voltage-clamp experiment and amplifier compensations. A derivation of the voltage-clamp experiment model is given below, where each of the undesired effects and how they are typically compensated is modelled based on published circuitry (Moore et al., 1984; Neher, 1992, 1995; Sigworth et al., 1995; Sigworth, 1995a,b; Strickholm, 1995; Sherman et al., 1999; Weerakoon et al., 2009, 2010; HEKA Elektronik GmbH, 2018; Axon Instruments Inc., 1999). Below, in the first half, we consider a voltage-clamp experiment *without* any compensation, in which we derive the equations for the effects of membrane capacitance, series resistance, leak current (seal resistance), pipette capacitance, etc. In the second half, we include typical compensations that are performed in the model.

Symbol	Typical values	Description
General		
t	—	Time variable
Capacitance		
C_f	0.3 pF	Feedback shunt capacitance
C_m	5–20 pF	Membrane capacitance. These are typical values for the CHO cells used in this chapter (see also Chapter 4); 100–400 pF has been measured for individual cardiomyocytes in various species (Satoh et al., 1996) ($\sim$ 190 pF for human Sakakibara et al., 1993); and can be as high as 100 nF for large cells such as *Xenopus* oocytes (Schmitt and Koepsell, 2002).
C_p	3–5 pF	Parasitic capacitance at the pipette/well plate; also known as 'pipette capacitance' in manual patch
Current		
I_in	—	Voltage-clamp current
I_inj	—	Injection current
I_ion	$O(1)$ nA	Whole-cell ion channel current (can reach $O(1)$ µA for *Xenopus* oocytes (Schmitt and Koepsell, 2002))
I_leak	—	Leakage current through imperfect seal
I_m	—	Membrane current
I_out	—	Recorded current
I_p	—	Current drawn by parasitic capacitance of the pipette/well plate
I_post	—	Post-processed (leak subtracted) current
Resistance		
R_f	25 MΩ	Feedback resistance
R_s	5–20 MΩ	Series resistance between the pipette electrode and the cell
R_seal	0.5–10 GΩ	Seal resistance of the pipette tip
Time constant		
τ_a	50–2000 µs	Membrane access time constant, $\tau_\mathrm{a} = R_\mathrm{s}C_\mathrm{m}$
τ_sum	5–70 µs	Response time of the summing amplifier
τ_clamp	0.8 µs	Voltage-clamp time constant
τ_z	7.5 µs	Transconductor time constant, $\tau_\mathrm{z} = R_\mathrm{f}C_\mathrm{f}$
Voltage		
V_cmd	$O(100)$ mV	Command voltage; follows the voltage-clamp protocols
V_clamp	$O(100)$ mV	Clamp voltage
V_est	$O(100)$ mV	Estimated membrane potential
V_m	$O(100)$ mV	Membrane potential
V_off	$O(10)$ mV	Offset voltage, such as amplifier offsets, electrode offsets, junction potentials, etc.
V_out	$O(100)$ mV	Recorded voltage, $V_\mathrm{out} = I_\mathrm{out}R_\mathrm{f}$
V_p	$O(100)$ mV	Pipette potential

Table 6.1: Glossary of symbols and parameters. We also denote a (machine or post-processing) estimate of a parameter X as X^*, and the error in the estimate of the same parameter as $X^\dagger$. The range of typical values are taken from Weerakoon et al. (2009); Neher (1995); HEKA Elektronik GmbH (2018); Axon Instruments Inc. (1999), unless otherwise specified.

Modelling undesired effects in patch clamping

First of all, at the electrode-membrane junction in Figure 6.2, by applying Kirchhoff's current law, we have

$$I_{\mathrm{m}} = I_{\mathrm{in}} - I_{\mathrm{p}} - I_{\mathrm{leak}} - I_{\mathrm{ion}}, \tag{6.3}$$

where

$$C_{\mathrm{p}} \frac{\mathrm{d}V_{\mathrm{p}}}{\mathrm{d}t} = I_{\mathrm{p}}, \tag{6.4}$$

and

$$C_{\mathrm{m}} \frac{\mathrm{d}V_{\mathrm{m}}}{\mathrm{d}t} = I_{\mathrm{m}}. \tag{6.5}$$

Therefore

$$C_{\mathrm{m}} \frac{\mathrm{d}V_{\mathrm{m}}}{\mathrm{d}t} = I_{\mathrm{in}} - C_{\mathrm{p}} \frac{\mathrm{d}V_{\mathrm{p}}}{\mathrm{d}t} - I_{\mathrm{leak}} - I_{\mathrm{ion}}, \tag{6.6}$$

$$I_{\mathrm{in}} = I_{\mathrm{ion}} + I_{\mathrm{leak}} + C_{\mathrm{m}} \frac{\mathrm{d}V_{\mathrm{m}}}{\mathrm{d}t} + C_{\mathrm{p}} \frac{\mathrm{d}V_{\mathrm{p}}}{\mathrm{d}t}. \tag{6.7}$$

This shows that I_{in} is 'contaminated' by a leak current, a C-Slow (C_{m}) term, and a C-Fast (C_{p}) term. Here, I_{in} is observed via V_{out} using the transimpedance amplifier within the Headstage (green box in Fig. 6.2), a feedback system that converts an input current to a voltage output, which is low-pass filtered by the transconductor time constant $\tau_{\mathrm{z}} = R_{\mathrm{f}} C_{\mathrm{f}}$. We then have

$$V_{\mathrm{out}} + \tau_{\mathrm{z}} \frac{\mathrm{d}V_{\mathrm{out}}}{\mathrm{d}t} = I_{\mathrm{in}} R_{\mathrm{f}}, \tag{6.8}$$

and since $V_{\mathrm{out}} = I_{\mathrm{out}} R_{\mathrm{f}}$, we have

$$I_{\mathrm{out}} + \tau_{\mathrm{z}} \frac{\mathrm{d}I_{\mathrm{out}}}{\mathrm{d}t} = I_{\mathrm{in}}. \tag{6.9}$$

Therefore, our final observed current I_{out} is given by

$$\frac{\mathrm{d}I_{\mathrm{out}}}{\mathrm{d}t} = \frac{I_{\mathrm{in}} - I_{\mathrm{out}}}{\tau_{\mathrm{z}}}. \tag{6.10}$$

Furthermore, most of the current measured using voltage-clamp depends on V_{m} which we try to control through the command voltage, V_{cmd}. By analysing the voltage drop across the series resistance, R_{s}, we have

$$(V_{\mathrm{p}} + V_{\mathrm{off}}) - V_{\mathrm{m}} = R_{\mathrm{s}} \left(I_{\mathrm{in}} - I_{\mathrm{p}}\right), \tag{6.11}$$

and together with Eq. (6.6), we get

$$C_{\mathrm{m}} \frac{\mathrm{d}V_{\mathrm{m}}}{\mathrm{d}t} = \frac{V_{\mathrm{p}} + V_{\mathrm{off}} - V_{\mathrm{m}}}{R_{\mathrm{s}}} - I_{\mathrm{ion}} - I_{\mathrm{leak}}. \tag{6.12}$$

This is more usually written as

$$\frac{\mathrm{d}V_{\mathrm{m}}}{\mathrm{d}t} = \frac{1}{\tau_{\mathrm{a}}} \left(V_{\mathrm{p}} + V_{\mathrm{off}} - V_{\mathrm{m}}\right) - \frac{1}{C_{\mathrm{m}}} \left(I_{\mathrm{ion}} + I_{\mathrm{leak}}\right), \tag{6.13}$$

where $\tau_{\mathrm{a}} = R_{\mathrm{s}} C_{\mathrm{m}}$, and V_{off} is the voltage offset. There are two types of effects introduced by R_{s}, one by the ionic current deviating V_{m} from V_{cmd}, and the other by the cell membrane capacitance slowing down V_{m} from approaching V_{cmd}. From Eq. (6.13) we can see that as $R_{\mathrm{s}} \to 0$, $V_{\mathrm{m}} \to V_{\mathrm{p}}$ (with an offset V_{off}) instantly; whilst, as $R_{\mathrm{s}} \to \infty$, V_{m} behaves independently of V_{p} and is determined by the

membrane ion channels as if an isolated cell. The pipette voltage V_p is controlled by the command voltage V_{cmd}, and is delayed by the electrical components,

$$\frac{dV_p}{dt} = \frac{1}{\tau_{clamp}} \left(V_{clamp} - V_p \right). \tag{6.14}$$

When *no* compensation is performed, V_{clamp} is simply the command voltage V_{cmd} in the above equation. In the second half of this derivation, we will see how modern voltage-clamp amplifiers manipulate V_{clamp} to reduce some of the undesired effects described above.

Finally, we model a linear-in-voltage leak current of the form

$$I_{leak} = g_{leak} \left(V_m - E_{leak} \right), \tag{6.15}$$

where g_{leak} and E_{leak} are the conductance and the reversal potential of the leak current. If this is a clean setup with no other leaks apart from a non-selective ion current leak through the pipette-cell seal, the parameters of this current would be $g_{leak} = 1/R_{seal}$ and $E_{leak} = 0$.

Modelling modern patch amplifier compensations

In this second half of the derivation, after analysing all the undesired artefacts, we mathematically model how modern patch amplifiers typically compensate for them (Weerakoon et al., 2009; Axon Instruments Inc., 1999; HEKA Elektronik GmbH, 2018). Firstly, the voltage offset is usually estimated and compensated *prior* to adding the cell to the system, either with an automated correction estimated using *software control* or by applying manually a voltage offset such that it gives zero current when clamped at zero voltage, so the compensation circuit is not shown in our patch clamp equivalent circuits (Neher, 1995; Sigworth et al., 1995). The major source of voltage offset may be the liquid junction potential, a potential difference of $\sim 2 - 12\,\text{mV}$ which develops when the pipette-filling solution is different from the bath solution (Neher, 1992). The adjustment is usually done by adding the theoretically estimated liquid junction potential offset to V^*_{off}. We can write the error in the estimate of the overall voltage offset $V^\dagger_{off}$ as

$$V^\dagger_{off} = V_{off} - V^*_{off}. \tag{6.16}$$

We then simply need to replace all instances of V_{off} in the equations above with $V^\dagger_{off}$ to describe the effect of imperfect voltage offset compensation, and $V^\dagger_{off}$ is assumed to be $O(10)\,\text{mV}$.

Secondly, to compensate the effect of the parasitic capacitance at the electrode, an additional current I_{inj} is injected at the electrode to compensate for the current drawn by the parasitic capacitance. By analysing the capacitance compensation part (orange box in Figure 6.2), we get

$$I_{inj} = C^*_p \frac{dV_{clamp}}{dt}, \tag{6.17}$$

where C^*_p is the amplifier's estimate of the parasitic capacitance C_p. Then Eq. (6.3) becomes

$$I_m = I_{in} + I_{inj} - I_p - I_{leak} - I_{ion}, \tag{6.18}$$

and Eq. (6.7) becomes

$$I_{\text{in}} = I_{\text{ion}} + I_{\text{leak}} + C_{\text{m}}\frac{\mathrm{d}V_{\text{m}}}{\mathrm{d}t} + \left(C_{\text{p}}\frac{\mathrm{d}V_{\text{p}}}{\mathrm{d}t} - C_{\text{p}}^{*}\frac{\mathrm{d}V_{\text{clamp}}}{\mathrm{d}t}\right). \tag{6.19}$$

This is usually known as 'C-Fast' compensation.

Thirdly, we need to consider compensation for the cell membrane capacitance C_{m}. Usually the effect of C_{m} is reduced by a hardware 'C-Slow' compensation, using a similar circuit to the 'C-Fast' compensation discussed above (Sigworth et al., 1995; Sigworth, 1995a). However, since the value of C_{m} can reach 100 pF in some cell types, and capacitor sizes can be limited, the 'C-Slow' compensation is sometimes performed as a post-processing step by the amplifier control software rather than using built-in amplifier hardware (Weerakoon et al., 2010). In either case, the full capacitance compensation can be written as

$$I_{\text{in}} = I_{\text{ion}} + I_{\text{leak}} + \left(C_{\text{m}}\frac{\mathrm{d}V_{\text{m}}}{\mathrm{d}t} - C_{\text{m}}^{*}\frac{\mathrm{d}V_{\text{clamp}}}{\mathrm{d}t}\right) + \left(C_{\text{p}}\frac{\mathrm{d}V_{\text{p}}}{\mathrm{d}t} - C_{\text{p}}^{*}\frac{\mathrm{d}V_{\text{clamp}}}{\mathrm{d}t}\right), \tag{6.20}$$

where C_{m}^{*} is the amplifier (or user's) estimate of the membrane capacitance C_{m}.

Finally, in voltage clamp, we want V_{m} to approach V_{cmd} as quickly as possible. However, in Eq. (6.13), there are two effects introduced by R_{s}, the first one causes V_{m} to deviate from V_{cmd} and the second slows down V_{m}'s approach to V_{cmd}. The first effect is caused by the second term on the right hand side of Eq. (6.13), $\left(I_{\text{ion}} + I_{\text{leak}}\right)$, which can be reduced through a series resistance compensation (Moore et al., 1984; Strickholm, 1995; Sigworth et al., 1995; Sigworth, 1995a; Sherman et al., 1999; Weerakoon et al., 2009). By analysing the series resistance compensation part (blue box in Figure 6.2), instead of clamping to V_{cmd}, it is set to $V_{\text{cmd}} + \alpha R_{\text{s}}^{*} I_{\text{out}}$, where R_{s}^{*} is the machine estimation of the series resistance R_{s}, and α is the requested proportion of series resistance compensation (a machine setting, typically 70–85 %).

The second effect is caused by the product of the series resistance R_{s} and the membrane capacitance C_{m}, i.e. the membrane assess time constant τ_{a}, which can be reduced through a compensation termed "supercharging" (Armstrong and Chow, 1987; Sigworth, 1995b). We set the clamping voltage to have a large overshoot (hence the name "supercharging") proportional to $\alpha R_{\text{s}}^{*} C_{\text{m}}^{*}\,\mathrm{d}V_{\text{est}}/\mathrm{d}t$, where

$$\frac{\mathrm{d}V_{\text{est}}}{\mathrm{d}t} = \frac{1}{R_{\text{s}}^{*}C_{\text{m}}^{*}}\left(V_{\text{cmd}} + \alpha R_{\text{s}}^{*}C_{\text{m}}^{*}\frac{\mathrm{d}V_{\text{est}}}{\mathrm{d}t} - V_{\text{est}}\right) \tag{6.21}$$

$$= \frac{V_{\text{cmd}} - V_{\text{est}}}{(1-\alpha)R_{\text{s}}^{*}C_{\text{m}}^{*}}, \tag{6.22}$$

according to Sigworth (1995b, Figure 18). The effect of the overshooting is to charge the membrane capacitance quickly. Including all the compensations, V_{clamp} becomes

$$\frac{\mathrm{d}V_{\text{clamp}}}{\mathrm{d}t} = \frac{1}{\tau_{\text{sum}}}\left(\left(V_{\text{cmd}} + \alpha R_{\text{s}}^{*}\left(I_{\text{out}} + C_{\text{m}}^{*}\frac{\mathrm{d}V_{\text{est}}}{\mathrm{d}t}\right)\right) - V_{\text{clamp}}\right), \tag{6.23}$$

to counterbalance the two effects caused by the series resistance. Note that the supercharging correction is particularly important when measuring big, very fast currents such as I_{Na} which has a time-to-peak within ~5 ms, however this correction poses almost no issue when analysing smaller, slower currents, for example I_{Kr}.

A summary of the voltage-clamp experiment model equations is as following:

$$I_{\text{ion}} = f(t, V_{\text{m}}), \qquad \text{Ion channel model} \tag{6.24}$$

$$I_{\text{leak}} = g_{\text{leak}} \left(V_{\text{m}} - E_{\text{leak}}\right), \qquad \text{Leak current} \tag{6.25}$$

$$\frac{\mathrm{d}V_{\text{m}}}{\mathrm{d}t} = \frac{1}{R_{\text{s}}C_{\text{m}}}\left(V_{\text{p}} + V_{\text{off}}^{\dagger} - V_{\text{m}}\right) - \frac{1}{C_{\text{m}}}\left(I_{\text{ion}} + I_{\text{leak}}\right), \qquad V_{\text{off}} \text{ compensation} \tag{6.26}$$

$$\frac{\mathrm{d}V_{\text{p}}}{\mathrm{d}t} = \frac{1}{\tau_{\text{clamp}}}\left(V_{\text{clamp}} - V_{\text{p}}\right), \qquad \text{Amplifier delay} \tag{6.27}$$

$$\frac{\mathrm{d}V_{\text{est}}}{\mathrm{d}t} = \frac{V_{\text{cmd}} - V_{\text{est}}}{(1-\alpha)R_{\text{s}}^{*}C_{\text{m}}^{*}}, \qquad \text{Supercharging} \tag{6.28}$$

$$V_{\text{cmd}}' = V_{\text{cmd}} + \alpha R_{\text{s}}^{*}\left(I_{\text{out}} + C_{\text{m}}^{*}\frac{\mathrm{d}V_{\text{est}}}{\mathrm{d}t}\right), \qquad R_{\text{s}} \text{ compensation} \tag{6.29}$$

$$\frac{\mathrm{d}V_{\text{clamp}}}{\mathrm{d}t} = \frac{1}{\tau_{\text{sum}}}\left(V_{\text{cmd}}' - V_{\text{clamp}}\right), \qquad \text{Compensation delay} \tag{6.30}$$

$$I_{\text{in}} = I_{\text{ion}} + I_{\text{leak}} + C_{\text{p}}\frac{\mathrm{d}V_{\text{p}}}{\mathrm{d}t} - C_{\text{p}}^{*}\frac{\mathrm{d}V_{\text{clamp}}}{\mathrm{d}t}, \qquad C_{\text{p}} \text{ compensation} + C_{\text{m}}\frac{\mathrm{d}V_{\text{m}}}{\mathrm{d}t} - C_{\text{m}}^{*}\frac{\mathrm{d}V_{\text{clamp}}}{\mathrm{d}t}, \qquad C_{\text{m}} \text{ compensation} \tag{6.31}$$

$$\frac{\mathrm{d}I_{\text{out}}}{\mathrm{d}t} = \frac{1}{\tau_{\text{z}}}\left(I_{\text{in}} - I_{\text{out}}\right). \qquad \text{Observed current} \tag{6.32}$$

In these equations, α is a user-specified proportion of series resistance compensation, and g_{leak} and E_{leak} are the conductance and the reversal potential of the leak current. The meaning of the remaining symbols is given in Table 6.1.

In the real cell data analysed later, a leak compensation was applied to the data itself, prior to model fitting, as shown in Eqs. (6.33) and (6.34). The parameters in Eq. (6.33) are estimated in post-processing by assuming I_{leak} is the only current active during a 'leak step' between voltages where $I_{\text{ion}} \approx 0$. Estimation and compensation are typically performed automatically by e.g. the HEKA Patchmaster and the Nanion SyncroPatch, although we performed our specially designed leak compensation using the ramp-step in the staircase protocol as discussed in Chapter 4. Finally, I_{out} is then adjusted by subtracting estimated leak

$$I_{\text{leak}}^{*} = g_{\text{leak}}^{*}\left(V_{\text{cmd}} - E_{\text{leak}}^{*}\right), \tag{6.33}$$

$$I_{\text{post}} = I_{\text{out}} - I_{\text{leak}}^{*}. \tag{6.34}$$

to give I_{post} as a better approximation of I_{ion}.

6.3 Validating the mathematical model with electrical model cell experiments

Before applying the voltage-clamp experiment model to currents from a real biological cell, we tested the performance of our mathematical model with *electrical model cells* — circuits made of electrical hardware components to mimic real cells. Some of these model cells are commercially available, e.g. HEKA MC 10, HEKA TESC, Axon or Molecular Devices PATCH-1U, and used to test and calibrate patch-clamp amplifiers.

We are interested in both the current readout of a voltage-clamp experiment and the membrane voltage that the cell experiences. Therefore we designed a circuit that connects the model cell to two amplifiers, one in voltage-clamp mode and one in current-clamp mode, as shown in Figure 6.3. This set-up can simultaneously perform the conventional voltage-clamp procedure on the model cell with one amplifier; whilst using the other in current-clamp mode (clamped to zero) to measure the clamped voltage at the terminal corresponding to the membrane via the current-clamp. Effectively, this set-up allows the membrane voltage V_{m} of the electrical model cell to be recorded with one amplifier whilst performing the conventional voltage-clamp current measurement with the other.

6.3.1 Electrical model cell design

In Figure 6.3 (left and middle) is a circuit which is equivalent to commercially-available model cells (the design was based on the HEKA TESC in 'whole cell' mode). In this chapter, we call this a *Type I Model Cell*. It consists of a capacitor and a resistor in parallel to mimic the membrane capacitance, C_{m}, and membrane resistance, R_{m}. Unlike real ion channels, this simple electrical model cell lacks any time-varying current dynamics in the R_{m} resistor representing ion currents. We therefore developed a new type of model cell, termed a *Type II Model Cell*, which exhibits simple current dynamics when stepping to different voltages.

Figure 6.3 (right) shows the equivalent circuit of our Type II Model Cell. In addition to the usual C_{m} and R_{m} connected in parallel, this model cell has an extra component (R_{k} in series with C_{k}) connected in parallel, to mimic the addition of another ion current with some kinetic properties. The time constant ($\tau_k = R_{\mathrm{k}}C_{\mathrm{k}}$) for this extra component was chosen to be $O(100)$ ms, which is of the same order of magnitude as I_{Kr} dynamics. The dynamics of the Type II Model Cell allow us to test and understand the effects of series resistance, etc., and enable us to validate our mathematical voltage-clamp experiment model experimentally to check we have correctly modelled amplifier compensations.

6.3.2 Validation of the mathematical model

The experimental recordings using the simultaneous voltage clamp and current clamp set-up are shown in Figure 6.4 (solid lines), with Type I (Figures 6.4A, C) and Type II (Figures 6.4B, D) Model Cells. The measurements were performed with a holding potential of 0 mV.

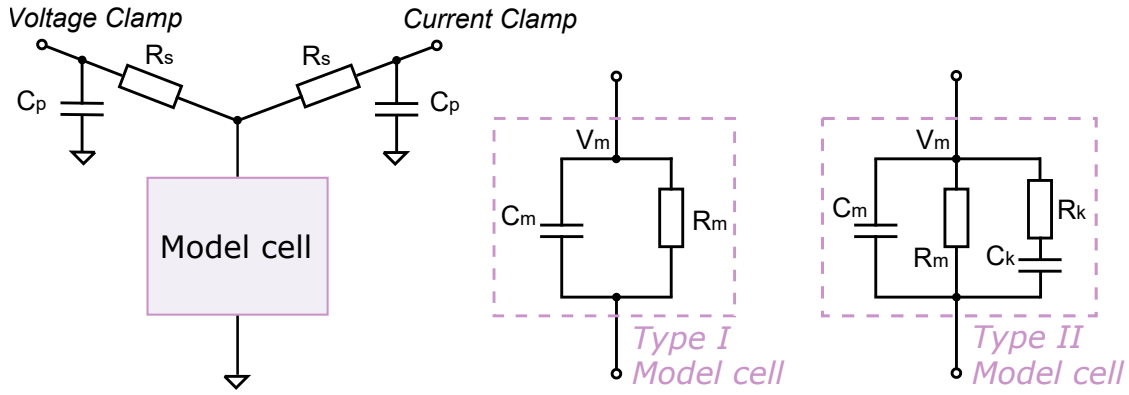

Figure 6.3: Circuit diagrams for electrical model cell experiments. **(Left)** A circuit set-up where a model cell is connected to both a voltage-clamp amplifier and a current-clamp amplifier. The voltage-clamp imposes a command voltage, V_{cmd}, on the model cell and measures the current, I_{out}; while the current-clamp simultaneously measures its 'membrane voltage', V_{m}. **(Middle)** An equivalent circuit of the Type I Model Cell, which is identical to the commercial 'black box' model cells (HEKA TESC) under the 'whole cell' mode. **(Right)** An equivalent circuit for the Type II Model Cell. This model cell is designed to exhibit dynamics when stepping to different voltages, with a time constant similar to ionic currents. The circuits were built with discrete electrical components, with $C_{\text{p}} = 4.7\,\text{pF}$, $R_{\text{s}} = 30\,\text{M}\Omega$, $C_{\text{m}} = 22\,\text{pF}$, $R_{\text{m}} = 500\,\text{M}\Omega$, $C_{\text{k}} = 1000\,\text{pF}$, and $R_{\text{k}} = 100\,\text{M}\Omega$.

We performed two sets of experiments, firstly with no amplifier compensation, and secondly with automatic amplifier compensation using a computer controlled amplifier (HEKA EPC 10 Double Plus) where amplifier settings could be set with high precision. Here, automatic adjustment of the compensation settings, including V_{off}, C_{p}, C_{m}, and R_{s}, was performed using the HEKA Patchmaster software which closely follows the compensation procedure operators perform by hand on many manual patch-clamp amplifiers (pages 80–84 of the HEKA manual (HEKA Elektronik GmbH, 2016)).

For the simulations, parameters were set in Eqs. (6.24)–(6.32) to correspond to each set of experiments: for no amplifier compensation $\{V_{\text{off}}^{\dagger}, C_{p}^{*}, C_{\text{m}}^{*}, R_{\text{s}}^{*}, g_{\text{leak}}\}$ were set to zero; while for the automatic amplifier compensation those parameters were set to the amplifier's estimates. Results are shown in Figure 6.4 for part of the voltage clamp protocol to be used for I_{Kr} measurements later in this chapter.

Our model (dashed lines) is able to capture both the current and the membrane voltage very closely, for all these experiments. Note the differences between the membrane voltage V_{m} (grey) and the command voltage V_{cmd} (orange/red). For example, in the uncompensated case, due to the voltage drop across R_{s} in the Type I Model Cell V_{m} shows a simple offset. But in the Type II Model Cell V_{m} exhibits nonlinear dynamics while V_{cmd} does not. When the amplifier was actively compensating the differences between V_{m} and V_{cmd} were successfully reduced. All of these details are captured by the mathematical model so we are confident that Eqs. (6.24)–(6.32) are a good representation of the model cells, amplifier compensations and artefacts that occur when compensations are disabled or imperfect.

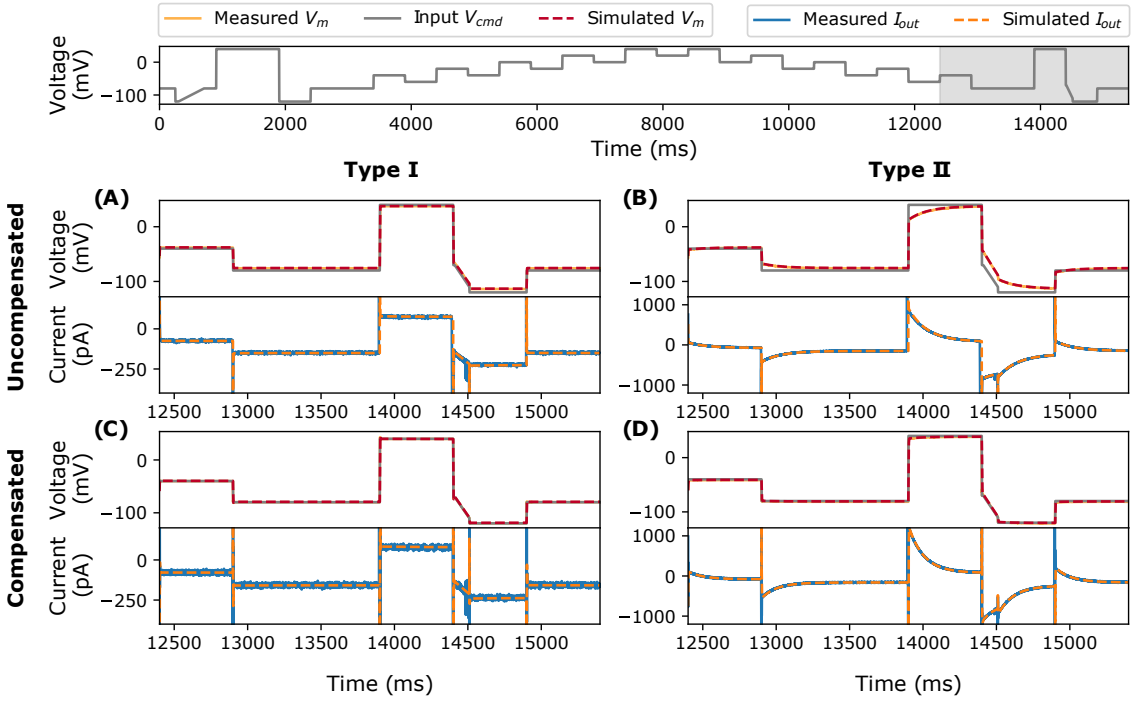

Figure 6.4: Model simulations (dashed lines) using the amplifier settings compared against the simultaneous voltage clamp-current clamp measurements of the model cells (solid lines). Measurements are shown without compensation using **(A)** Type I Model Cell and **(B)** Type II Model Cell; and measurements with automatic amplifier compensation for V_{off}, C_{p}, C_{m}, and R_{s} with $\alpha = 80\%$ using **(C)** Type I Model Cell and **(D)** Type II Model Cell. All command voltages were set to be the staircase voltage protocol developed in Chapter 4 (top panel); here only the last 3 s of the measurement is shown, the whole trace is shown in later figures. In the top panel of each subfigure, the grey lines represent the command voltage V_{cmd}, and the orange/red lines represent the membrane voltage V_{m}; the bottom panel shows the current readout via the voltage-clamp, I_{out}.

6.3.3 Parameter inference without compensations

Next, we attempt to use only the uncompensated, raw voltage-clamp measurements (i.e. only I_{out} in Figure 6.6A, and V_{cmd}) to infer the underlying membrane voltage, V_{m}, and the parameters of the model cells. We then compare the model V_{m} predictions with the current-clamp measurements. To optimise the model parameters root-mean-square error (RMSE) between the simulated and recorded I_{out} was minimised using a global optimisation algorithm Covariance Matrix Adaptation Evolution Strategy (CMA-ES) as described in Chapter 2. Model simulations and optimisation were performed as described in Chapter 2. All codes and data are freely available online, see Data and Software Availability at the end of the chapter.

6.3.3.1 Application to the Type I Model Cell

Figure 6.5A shows the fitted model I_{out} (bottom, orange dashed line) and its prediction of the membrane voltage V_{m} (top, red dashed line), compared with experimental recordings (solid lines). Figure 6.5B further shows that the fitted model is able to predict current measurements under an independent, unseen voltage-clamp command protocol — a series of action potential waveforms (blue lines in the first panel). The series of action potential-like waveforms were concatenated from

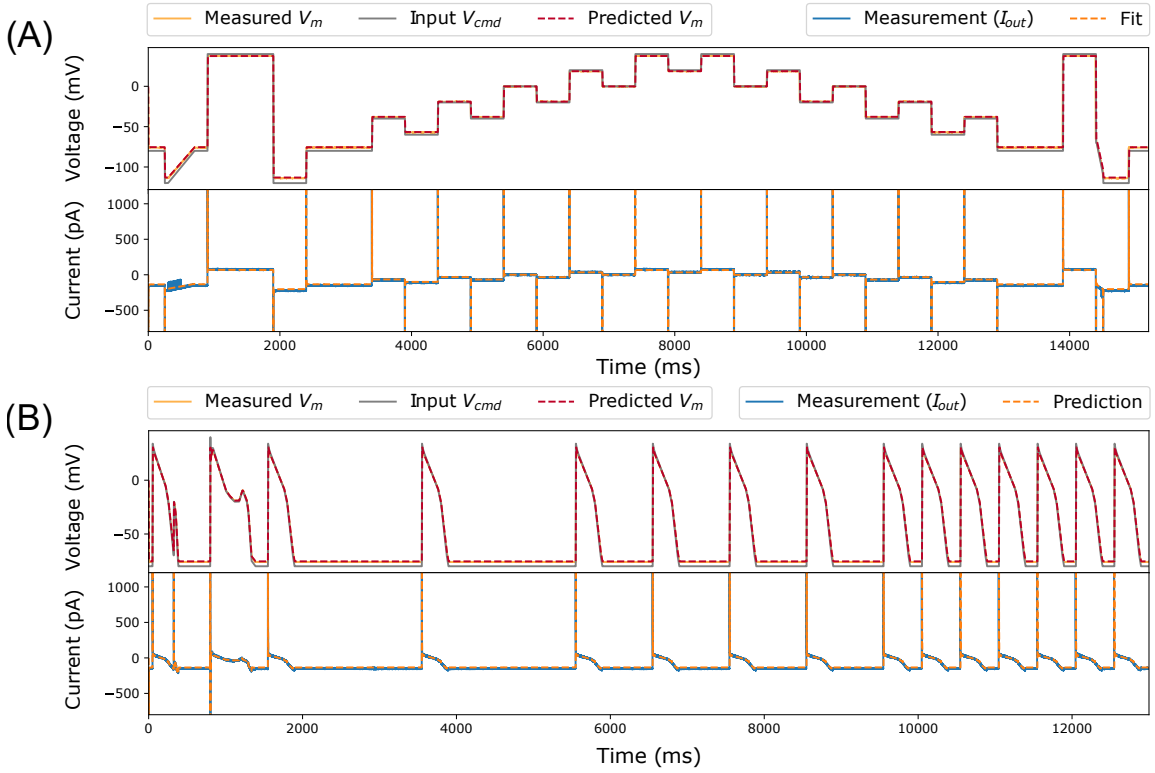

Figure 6.5: Inferred model simulations and predictions (dashed lines) compared to experimental data (solid lines) from a Type I Model Cell. **(A)** Model calibration with the staircase protocol (grey lines in the top panel), where the model was fitted to only the current recording (blue, solid line in the lower panel). The fitted model was able to predict the membrane voltage, V_m (orange, solid line), measured using current-clamp. **(B)** Further model validation using an independent voltage-clamp protocol, a series of action potentials (grey lines in the top panel). Again, predictions from the model fitted to the staircase protocol above (dashed lines) are excellent for both the current and the membrane voltage.

	R_m (MΩ)	C_p (pF)	C_m (pF)	R_s (MΩ)	V_{off} (mV)
Component label	500.00	4.70	22.00	30.00	0.00
Patchmaster estimate	498.00	7.80	32.85	32.60	0.20
Fitted parameters	567.21	23.36	32.51	34.85	-0.12

Table 6.2: Type I Model Cell parameters, comparing the values of hardware component labels in the circuit, the values estimated by the Patchmaster amplifier software using a simple test pulse, and our inferred values from the mathematical model.

those in Chapter 4; they are composed of linear ramps and steps to permit use on high-throughput machines that cannot clamp to arbitrary waveforms. Magnifications of the protocols are shown later in Figure 6.10C–F; they include a delayed afterdepolarization (DAD)-like protocol, an early afterdepolarization (EAD)-like protocol, and a series of action-potential-like protocols with different beating frequencies. Additionally, the agreement between predictions and measurements of V_m (the model is only given the command voltage V_{cmd}) provide assurance the scheme is able to infer the applied V_m as well as predict current.

6.3.3.2 Application to the Type II Model Cell

Next we look at the Type II Model Cell; this should be the more challenging of the two and more similar to a real ionic current. Figure 6.6A shows the fitted model I_{out} (bottom, orange dashed line) and its corresponding prediction of the membrane voltage, V_{m} (top, red dashed line), compared against the experimental recordings (solid lines). Figure 6.6B further shows that the fitted model is able to predict measurements under an independent, unseen voltage-clamp protocol, the series of action potential-like waveforms (grey lines in the first panel). Note the excellent predictions for V_{m} and its deviation from V_{cmd}.

Table 6.3 also shows a comparison of the values of the hardware components (with manufacturing tolerances of ±1 to 2%) in Figure 6.3, the amplifier's estimation using a standard test pulse, and the fitted values using the mathematical model. Our model-inferred values are much closer to the component labels than the amplifier estimates because the Type II Model Cell exhibits nonlinear dynamics (as do real cells); whereas the amplifier uses a simple square-wave test pulse and assumes a simple resistor-capacitor model cell (i.e. a Type-I Model Cell) when estimating the parameters. That is, there is a difference between the electrical model cell we attached and the circuit the amplifier

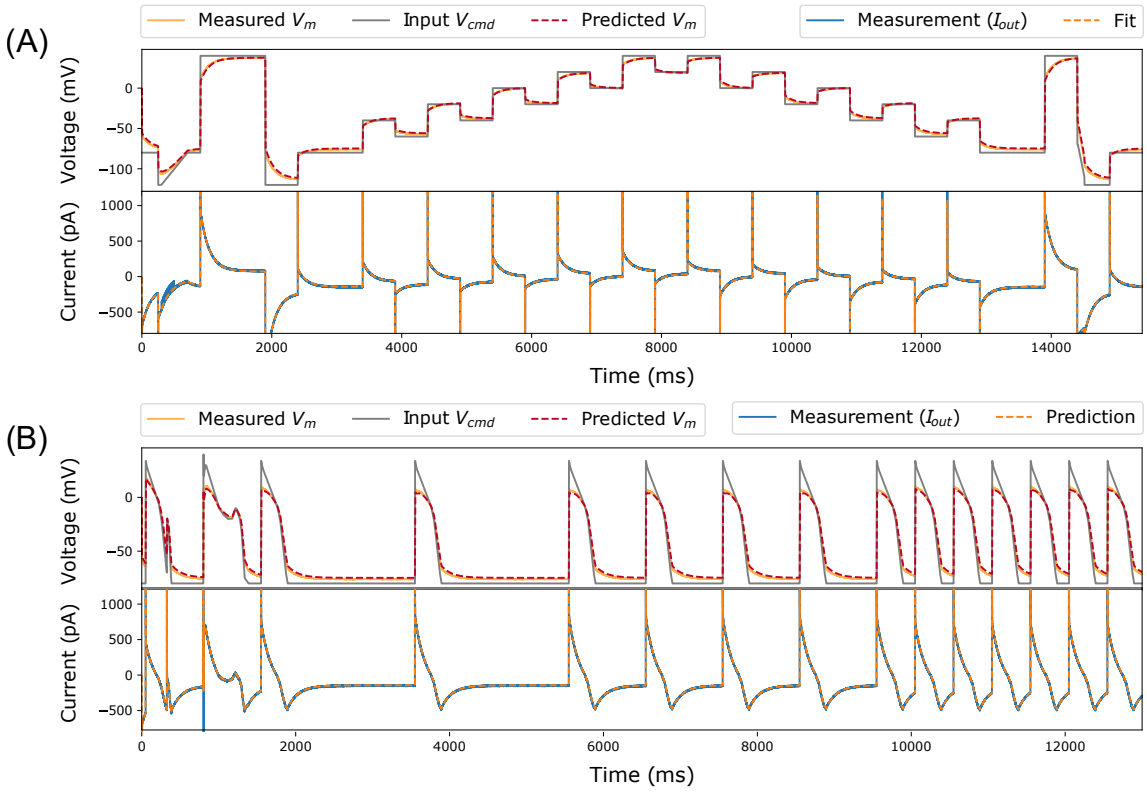

Figure 6.6: Inferred model simulations and predictions (dashed lines) compared to experimental data (solid lines) from a Type II Model Cell. **(A)** Model calibration with the staircase protocol (grey lines in the top panel), where the model was fitted to only the current recording (blue, solid line in the lower panel). The fitted model was able to predict the membrane voltage, V_{m} (orange, solid line), measured using current-clamp. **(B)** Further model validation using an independent voltage-clamp protocol, a series of action potentials (grey lines in the top panel). Again, predictions from the model fitted to the staircase protocol above (dashed lines) are excellent for both the current and the membrane voltage.

	R_k (MΩ)	C_k (pF)	R_m (MΩ)	C_p (pF)	C_m (pF)	R_s (MΩ)	V_{off} (mV)
Component label	100	1000	500	4.7	22	30	0
Patchmaster estimate	—	—	91.30	8.80	41.19	33.60	-1.20
Fitted parameters	94.20	1062.69	520.70	4.85	36.38	34.87	0.20

Table 6.3: Type II Model Cell parameters (for the components shown in Figure 6.3). (Row 1) hardware component labels (V_{off} is zero as there is no battery/voltage-offset component); (Row 2) Patchmaster amplifier software estimates using a simple test pulse; (Row 3) inferred values from the mathematical model. The mathematical model captures the fact that there are kinetics/dynamics in the Type II cell and improves on the amplifier's estimates of the components.

is designed to compensate, thus leading to inaccurate automated estimation of some components. For example, even though we did not apply any voltage offset, V_{off}, in the experiment, the amplifier incorrectly estimated an offset of -1.2 mV. Proceeding with this amplifier-estimated value would lead to a voltage offset artefact of $V_{off}^{\dagger} = -1.2$ mV in all recordings. Using the full model would capture these effects and take them into account when calibrating current kinetic parameters.

Thus far, we considered a realistic voltage-clamp experiment and developed a detailed mathematical model for such a setting, where imperfect compensations made by the amplifier and imperfect leak current subtraction are included. We then validated this mathematical model via electrical model cell experiments, demonstrating that our model captures the main effects of the voltage-clamp artefacts and amplifier compensations. In the next part of the chapter, we apply our mathematical model to the experimental CHO-hERG1a data presented in Chapter 4.

6.4 Application to variability in CHO-hERG1a patch-clamp data

After experimentally validating the mathematical model of the full voltage-clamp experiment with two electrical model cells, it is now applied to experimental data from real cells. Here, the high-throughput dataset from the previous chapter, Chapter 4, is used. The dataset contains 124 voltage-clamp recordings of the potassium current that flows through hERG ($K_V11.1$) channels (I_{Kr}) measured with the staircase protocol and eight other independent protocols. The measurements were performed on CHO cells stably transfected with hERG1a at 25 °C, using the Nanion SyncroPatch 384PE, a 384-well automated patch-clamp platform (see Figure 4.1). All the data were leak-corrected (see Eq. (6.34)), E-4031 subtracted, and passed a semi-automated quality control. The recordings, and parameter values derived from them, showed good agreement with earlier work using manual patch (Beattie et al., 2018), for details of the methods please see Chapter 4.

In Chapter 4, all of the observed variability in the post-processed data was assumed to be due to biological variability in I_{Kr} conductance and kinetics, which we term "Hypothesis 1", and so 124 cell-specific variants/parameterisations of the I_{Kr} model were created. Kinetic parameters fitted to cell-specific data using the staircase calibration protocol enabled very good predictions for eight

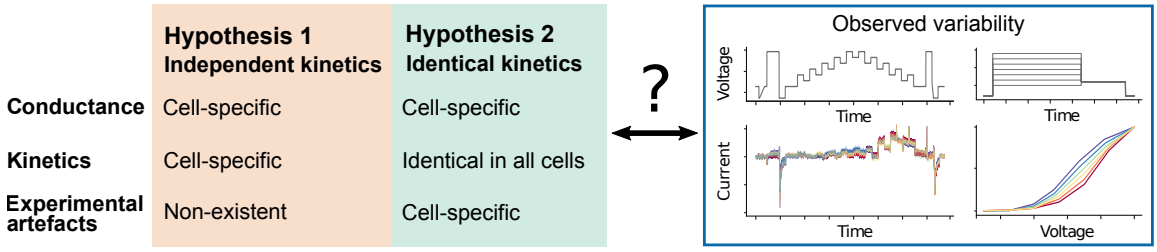

Figure 6.7: A schematic overview of the two hypotheses we explore. Hypothesis 1 assumes the collected data represent a perfect, idealised voltage-clamp experiment where any experimental artefacts have been perfectly compensated by the amplifier and leak subtraction, so all the observed variability is rooted in biological variability (varying conductance and model kinetics in every cell), we term these 'independent kinetics models'. Hypothesis 2 assumes that the observed variability is due to differences in the voltage-clamp experimental artefacts, and that all of the cells share identical ion channel kinetics (although the maximum conductance is allowed to vary across cells), we term these 'identical kinetics models'.

independent validation protocols (see Chapter 4). However, covariance in the inferred parameters across cells led us to speculate about a voltage offset ($V_{\text{off}}^{\dagger}$) being responsible for much of the variability.

So an alternative hypothesis is that all cells have the same I_{Kr} *kinetics* (functional properties of the channel proteins), but different maximal conductances (expression levels of the proteins) and different patch-clamp artefacts from cell-to-cell, so that the observed variability in the current kinetics is due to variability in the voltage-clamp experiment model. We term this set of assumptions "Hypothesis 2". Figure 6.7 shows a schematic overview of the two hypotheses.

For the details of the mathematical model of I_{Kr} please refer to Chapter 4 Section 4.2.1, where we have

$$I_{\text{ion}} = I_{\text{Kr}} = f(t, V_{\text{m}}; g_{\text{Kr}}, \boldsymbol{\theta}) = g_{\text{Kr}} \cdot a \cdot r \cdot (V_{\text{m}} - E_{\text{K}}). \tag{6.35}$$

We now discuss the extent to which patch-clamp artefacts and imperfect compensations can explain the variability in the biological recordings.

6.4.1 Inference with the full voltage-clamp experiment model

Earlier we saw how the full voltage-clamp experiment model (Eqs. (6.24)–(6.32)) had parameters that could be successfully inferred from data for the electrical model cells. We now test how this inference scheme performs when combined with the I_{Kr} model of Eq. (6.35) in a synthetic data study. The idea is to show that with an information-rich current signal measured under such as the staircase protocol developed in Chapter 4, even combined with the voltage-clamp experiment model, theoretically we are able to infer all of the parameters.

We first simulated 10 traces of patch-clamp data by using one set of kinetic parameters $\boldsymbol{\theta}$ (the identical kinetics assumption, with the hierarchical Bayesian mean parameters from Chapter 4, also shown in Table 6.5) together with a set of randomly generated voltage-clamp experiment model parameters. The voltage-clamp experiment model parameters were sampled as follows:

$$V_{\text{off}}^{\dagger} \sim \mathcal{N}(0, 1.5) \ \text{(mV)}, \tag{6.36}$$

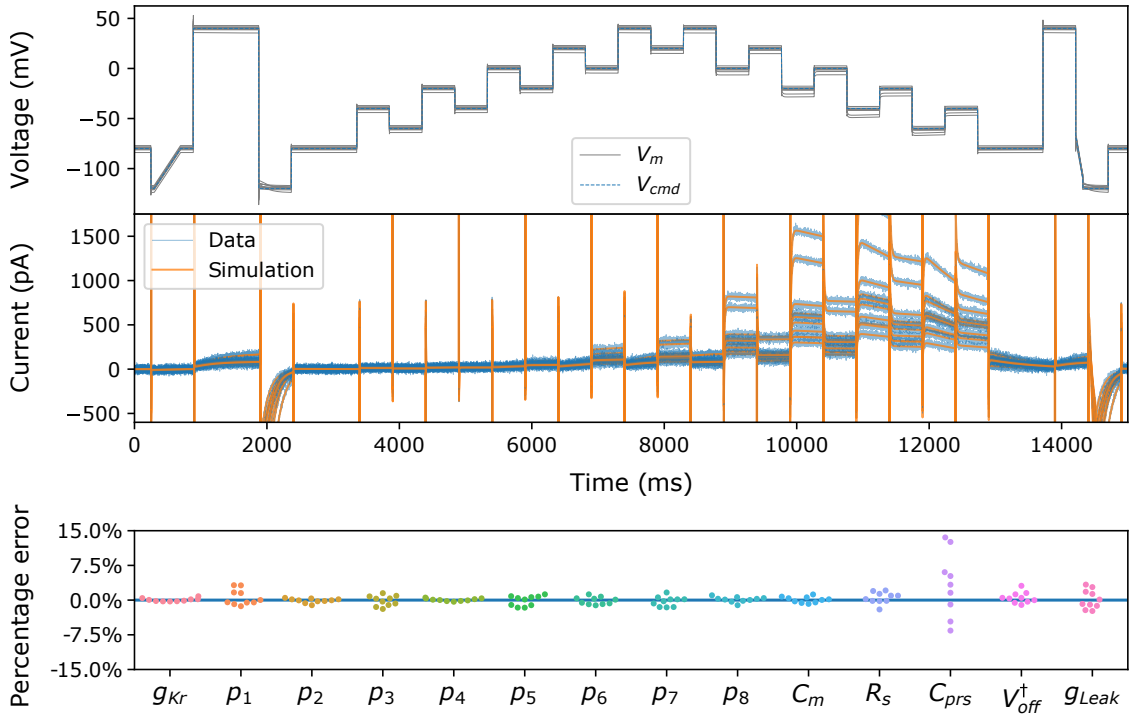

Figure 6.8: Synthetic I_{Kr} data study with 10 traces with identical kinetics and different patch artefacts: membrane capacitance, series resistance, seal resistance, pipette capacitance, and leak. The pipette capacitance is the hardest parameter to infer, with errors of up to 15%. But overall, both kinetic parameters and voltage-clamp experiment model parameters are practically identifiable.

$$R_{\mathrm{s}} \sim \ln \mathcal{N}(12.5, 2) \ \ (\mathrm{M}\Omega), \tag{6.37}$$

$$C_{\mathrm{m}} \sim \ln \mathcal{N}(15, 2.5) \ \ (\mathrm{pF}), \tag{6.38}$$

$$C_{\mathrm{p}} \sim \ln \mathcal{N}(4, 1) \ \ (\mathrm{pF}), \tag{6.39}$$

$$g_{\mathrm{leak}} \sim \mathcal{N}(0.25, 0.1) \ \ (\mathrm{nS}), \tag{6.40}$$

$$g_{\mathrm{Kr}} \sim \ln \mathcal{N}(32.3, 32.3) \ \ (\mathrm{nS}). \tag{6.41}$$

Additionally E_{leak} was set to be $-80\,\mathrm{mV}$. We also assumed that the experiments were done with 80% series resistance compensation ($\alpha = 0.8$), and that the amplifier estimations had normally distributed errors with a standard deviation of 10%, i.e. after a realisation of R_{s} we sampled R^{*}_{s} from $\mathcal{N}(R_{\mathrm{s}}, 0.1R_{\mathrm{s}})$. Then we performed parameter inference for these synthetic data. Since in actual experiments we know the values of the machine estimations, we do not infer them. We attempted to infer the rest: $g_{\mathrm{Kr}}, \boldsymbol{\theta}, C_{\mathrm{m}}, R_{\mathrm{s}}, C_{\mathrm{p}}, V^{\dagger}_{\mathrm{off}}$, and g_{leak}.

Figure 6.8 shows the results of the simulated study with the voltage-clamp experiment model. Figure 6.8 (top, middle) shows the simulated membrane voltage V_{m} (grey lines) traces differ from the command voltage V_{cmd} (blue dashed line). The simulated voltage-clamp data are shown in blue with simulated noise, plotted against the fitted model shown in orange. Figure 6.8 (bottom) shows the relative error of the inferred parameters. It shows that all of the parameters could be identified (model parameters g_{Kr} and $\boldsymbol{\theta}$ together with artefact parameters C_{m}, C_{p}, R_{s}, $V^{\dagger}_{\mathrm{off}}$ and g_{leak}) from a single cell recording.

We then tested this approach with real experimental data. However, values of the series resistance, R_s, were consistently estimated to be at the lower bound we had imposed, which we consider unrealistic; results and code for this analysis can be found in the online repository. This behaviour could be due to imperfections in the representation of I_{Kr} by the model (model discrepancy (Lei et al., 2020c)), as all parameters in the full voltage-clamp experiment model were successfully inferred in the cases of electrical model cells or synthetic I_{Kr} data. We therefore propose a simplification of the voltage-clamp experiment model whilst capturing the principal causes of variability.

6.4.2 A simplified voltage-clamp experiment model

Modelling the entire voltage-clamp machine may not be necessary, because the timescales of the components in the system span multiple orders of magnitude; ranging from the order of 0.1 µs (e.g. τ_{clamp}) to tens of ms (e.g. 'C-slow') or many seconds for ion channel gating (e.g. activation of I_{Kr} at room temperature in Vandenberg et al., 2006). For these I_{Kr} investigations the two fastest processes, τ_{clamp} and τ_z, can be approximated as instantaneous responses. That is, Eqs. (6.27) and (6.32) can be approximated as $V_p \approx V_{clamp}$ and $I_{out} \approx I_{in}$, respectively.

To study the behaviour of the voltage-clamp experiment model further, we performed a simple local sensitivity analysis of the model. We examine the sensitivity of the four parameters, C_m^*, R_s^*, $C_p^\dagger$ and $V_{off}^\dagger$, to the output/observed current. The 'local' values that we used are $C_m^* = 10\,\text{pF}$, $R_s^* = 5\,\text{M}\Omega$, $C_p^\dagger = 0\,\text{pF}$ and $V_{off}^\dagger = 0\,\text{mV}$, respectively. We assume all settings (C_m, R_s, etc.) are estimated perfectly and we use $\alpha = 85\%$ series resistance compensation. For parameters C_m^* and R_s^*, they are swept with a factor from 0.3 to 3; for parameter $C_p^\dagger$, from $-4\,\text{pF}$ to $4\,\text{pF}$; and for parameter $V_{off}^\dagger$, from $-5\,\text{mV}$ to $5\,\text{mV}$. These values were chosen to show the extreme effects of these imperfect compensations (e.g. we might expect C_m^* would be within three times its true value C_m). Although there are no direct measurements for these parameters (these parameters describe machine estimates of true values and error in these), we based this analysis on variability in machine estimates and observed variability in reversal potential in Chapter 4.

Figure 6.9 shows the results of the sensitivity analysis. After analysing the local sensitivity of the voltage-clamp experiment model, we found that in the observed current, the effects of $V_{off}^\dagger$ and imperfect R_s compensation are most apparent (on timescales relevant to I_{Kr}); whereas C_m^* and $C_p^\dagger$ affect only a small portion of the current (the transient current that occurs when the voltage is stepped to a new value). As a result, we further assume that (1) τ_{sum}, part of the fast amplifier processes, is instantaneous; (2) the effects of C_p and C_m are negligible; and (3) $C_m^*, R_s^* \approx C_m, R_s$.

Finally, the data were leak subtracted, where the leak current parameters (g_{leak}^* and E_{leak}^*) were estimated by fitting Eq. (6.25) to current during the -120 to $-80\,\text{mV}$ leak-ramp at the beginning of the measurements, to yield zero current at holding potential (see Chapter 4). We allow this leak subtraction to be imperfect by retaining a small residual leak current with parameters $g_{leak}^\dagger$ and $E_{leak}^\dagger$.

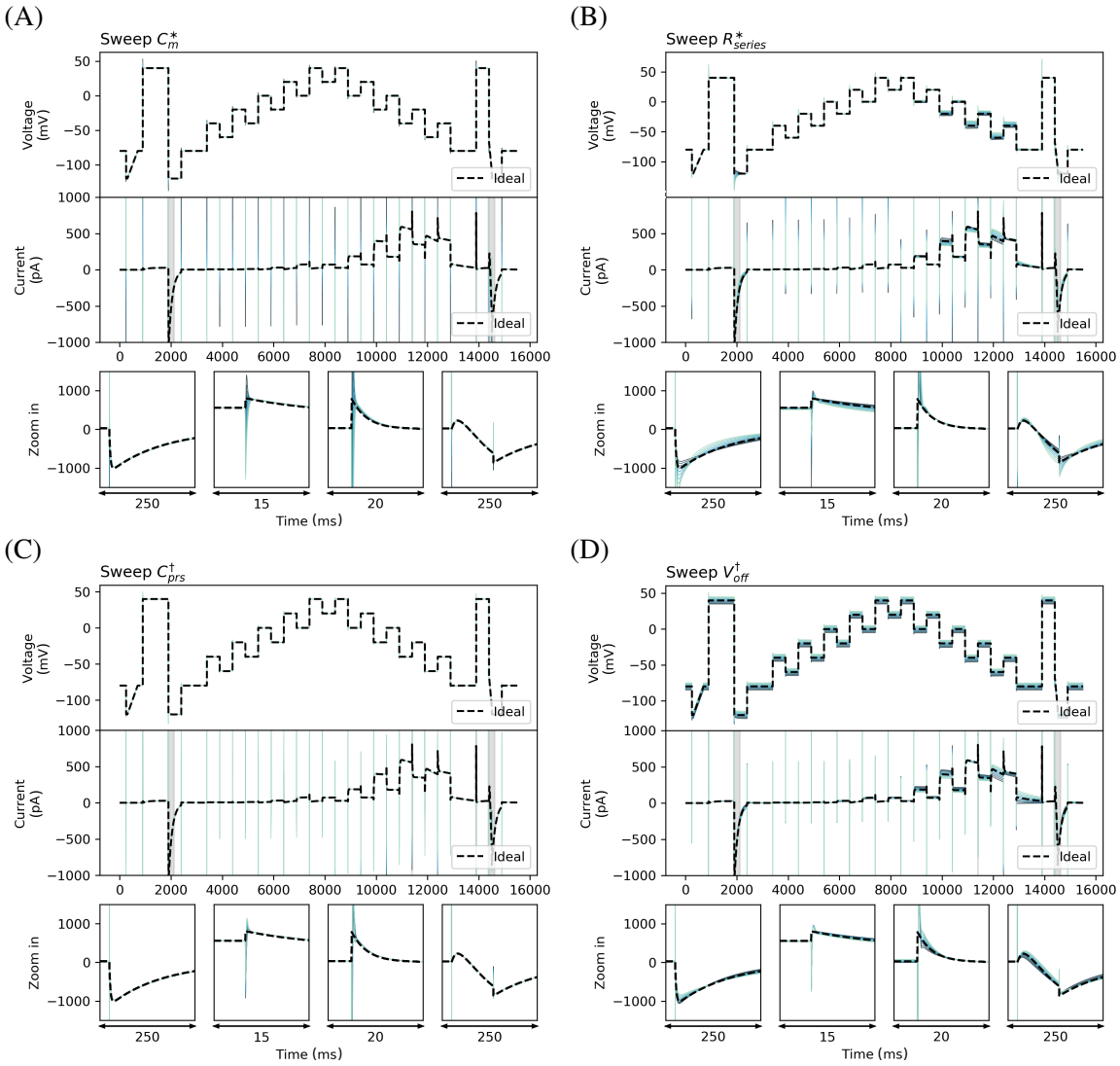

Figure 6.9: A sensitivity analysis of the voltage-clamp experiment model, showing the effects of imperfect compensation in the voltage-clamp amplifier. Dashed black lines indicate the ideal case, that is V_{cmd} and I_{Kr} simulated with V_{cmd}. The voltage traces shown in colour are V_{m} that the cell sees, and current traces shown in colour are I_{out} that we observe. Only effects from V_{off} and R_{s} are predominant while effects from C_{m} and C_{p} have less effect.

With these assumptions, Eqs. (6.24)–(6.32) become

$$I_{\text{ion}} = f(t, V_{\text{m}}; g_{\text{Kr}}, \boldsymbol{\theta}) = I_{\text{Kr}}, \qquad \text{Ion channel model} \tag{6.42}$$

$$I_{\text{leak}} = g_{\text{leak}}^\dagger \left(V_{\text{m}} - E_{\text{leak}}^\dagger\right) + I_{\text{leak}}^*, \qquad \text{Total leak current} \tag{6.43}$$

$$\frac{\mathrm{d}V_{\text{m}}}{\mathrm{d}t} = \frac{1}{R_{\text{s}}^* C_{\text{m}}^*}\left(V_{\text{p}} + V_{\text{off}}^\dagger - V_{\text{m}}\right) - \frac{1}{C_{\text{m}}^*} I_{\text{out}}, \qquad V_{\text{off}} \text{ compensation} \tag{6.44}$$

$$V_{\text{p}} = V_{\text{cmd}} + \alpha R_{\text{s}}^* I_{\text{out}}, \qquad R_{\text{s}} \text{ compensation} \tag{6.45}$$

$$I_{\text{out}} = I_{\text{ion}} + I_{\text{leak}}, \qquad \text{Observed current} \tag{6.46}$$

$$I_{\text{post}} = I_{\text{out}} - I_{\text{leak}}^*. \qquad \text{Post-processed current} \tag{6.47}$$

For all symbols refer to Table 6.1, and I_{leak}^* is given by Eq. (6.33). The effective reversal potential of

the residual leak current, $E^{\dagger}_{\text{leak}}$, is chosen to be the holding potential ($-80\,\text{mV}$) because the primary leak-subtraction (fit of g^{*}_{leak} and E^{*}_{leak}) ensured approximately zero current at holding potential. Therefore, we have only two voltage-clamp model parameters ($V^{\dagger}_{\text{off}}$ and $g^{\dagger}_{\text{leak}}$) to infer along with the ion current parameters (g_{Kr} and $\boldsymbol{\theta}$). Note that the other parameters (α, C^{*}_{m}, and R^{*}_{s}) can be obtained from the amplifier settings without performing any inference.

This simplified voltage-clamp experiment model was successfully applied to the model cell experiments (as shown below) and, like the full model, was able to correct imperfect R_m estimates made by the amplifier.

6.4.2.1 Applying the simplified model to electrical model cell

We assess the performance of the simplified voltage-clamp experiment model (Eqs. (6.42)–(6.47)) by applying it to the electrical model cell experiments. We focus on the Type II Model Cell as it exhibits nonlinear dynamics. The most interesting consequence of this dynamical behaviour is that it misleads the amplifier into incorrect estimation of R_{m} and erroneous compensation for V_{off}. As shown in Table 6.3, with a simple test pulse the amplifier estimated $R^{*}_{\text{m}} \approx 90\,\text{M}\Omega$ (when the component $R_{\text{m}} = 500\,\text{M}\Omega$), and $V^{*}_{\text{off}} \approx -1.2\,\text{mV}$ (in the model cell, $V_{\text{off}} = 0\,\text{mV}$). Note that because the amplifier (erroneously) applied $V^{\dagger}_{\text{off}} \approx -1.2\,\text{mV}$, that is the target $V^{\dagger}_{\text{off}}$ for the parameter fit to return.

	R_{k} (MΩ)	C_{k} (pF)	R_{m} (MΩ)	$V^{\dagger}_{\text{off}}$ (mV)
Effective component values	100	1000	500	-1.20
Fitted parameters	96.02	1044.68	508.34	-1.40

Table 6.4: Inference of Type II Model Cell parameters with active amplifier compensation using the simplified voltage-clamp experiment model. We compare the components' labelled values in the circuit setup (with $V^{\dagger}_{\text{off}} = -1.2\,\text{mV}$ added alongside as an effective component due to active amplifier compensation), and inferred values from the mathematical model.

Since the simplified voltage-clamp experiment model is based on compensated data, we use amplifier compensated data collected from the Type II Model Cell (Figure 6.4D). Table 6.4 shows the parameter inference results using the simplified voltage-clamp experiment model. The simplified model is able to: (i) recover Type II Model Cell parameters R_{k}, C_{k}, R_{m} with acceptable accuracy; and (ii) 're-correct' the amplifier's incorrectly estimated (and thereby artificially introduced) voltage offset. Note that these component estimates are better than the ones from the experiment with no compensation, suggesting a strategy of correcting the amplifier's active compensations may be better than running experiments with no compensation and inferring all these values in post-processing.

6.4.3 Optimisation of model parameters

We now present the parameter optimisation schemes used to test each hypothesis.

6.4.3.1 Hypothesis 1: Cell-specific kinetics with no artefacts

Under Hypothesis 1, any experimental artefacts are perfectly compensated by the amplifier and leak subtraction in post-processing. Any variability in the kinetic parameters obtained in current models fitted to the resulting data would reflect underlying variability in the biological function of the channels. To test this hypothesis, the parameter inference scheme detailed in Chapter 4 was employed. In summary, a Bayesian inference scheme was used which resulted in very narrow posterior distributions. This scheme used some parameter transforms so that the optimisation algorithm (CMA-ES) searches in log-transformed space for certain parameters. Here we look for the most likely parameter set under that scheme, which is identical to that given by a least square-error fit. So the log-likelihood of a given parameter set for cell i is proportional to

$$L_i = -\sum \left(I_i^{\text{model}} - I_i^{\text{data}}\right)^2 . \tag{6.48}$$

Under this hypothesis, I_i^{model} is a function of just conductance g_i and kinetic parameters $\boldsymbol{\theta}_i$, and is given by Eq. (6.35) while assuming $V_{\text{m}} = V_{\text{cmd}}$. So we performed an optimisation to maximise L_i by finding g_i and $\boldsymbol{\theta}_i$ for each cell i independently. The resulting models under this hypothesis are termed *independent kinetics models*.

6.4.3.2 Hypothesis 2: Identical kinetics for all cells, with cell-specific artefacts

Hypothesis 2 (Figure 6.7, right) assumes that the observed variability is due to the imperfect voltage-clamp experiments. Under this assumption, models fitted to the data should have the same kinetic parameters, $\boldsymbol{\theta}^*$, across all cells, that is, $\boldsymbol{\theta}_i = \boldsymbol{\theta}^*$ for any cell i. But there will be a cell-specific I_{Kr} conductance, g_i, and different patch-clamp experiment parameters for each cell too, $\boldsymbol{\phi}_i = \{V_{\text{off},i}^{\dagger}, g_{\text{leak},i}^{\dagger}\}$. These models are termed *identical kinetics models*.

To impose the assumption that all N cells have the same kinetics, and that the observed variability arises only from the experimental artefacts, the log-likelihood becomes

$$\mathcal{L}\left(\boldsymbol{\theta}, \{g_1, \ldots, g_N, \boldsymbol{\phi}_1, \ldots, \boldsymbol{\phi}_N\}\right) = \sum_{i=1}^{N} L_i\left(\boldsymbol{\theta}, g_i, \boldsymbol{\phi}_i\right), \tag{6.49}$$

where L_i, still defined by Eq. (6.48), is the log-likelihood for the i^{th} cell. But under this hypothesis, I_i^{model} is the post-processed current I_{post} in Eq. (6.47) and hence L_i is a function of the artefact parameters $\boldsymbol{\phi}_i$ too.

Optimising $\mathcal{L}$ is a high-dimensional optimisation problem, which is computationally expensive. This burden is reduced with a Gibbs-sampling style scheme; breaking the optimisation problem into two: (i) optimising the common kinetics parameters, $\boldsymbol{\theta}$; and (ii) optimising the cell-specific parameters, $\{g_i, \boldsymbol{\phi}_i\}_{i=1,\ldots,N}$. To evaluate the maximum likelihood of $\boldsymbol{\theta}$, we nest optimisation schemes. That is, for any single estimate of $\boldsymbol{\theta}$, we optimise $\{g_i, \boldsymbol{\phi}_i\}$ for each cell i independently to compute an approximate likelihood for $\boldsymbol{\theta}$. The estimate of $\boldsymbol{\theta}$ is then updated by running a single iteration of the outer optimisation loop, followed again by optimisation to convergence for $\{g_i, \boldsymbol{\phi}_i\}$ in each cell. This overall scheme converges to the full set of optimal parameters: $\boldsymbol{\theta}^*, \{g_i^*, \boldsymbol{\phi}_i^*\}_{i=1,\ldots,N}$.

Algorithm 6.1: Identical kinetic models (Hypothesis 2) parameter inference scheme

Result: Obtain $\boldsymbol{\theta}^*, \left\{g^*_{\mathrm{Kr},i}, \boldsymbol{\phi}^*_i\right\}_i = \mathrm{argmax}_{\boldsymbol{\theta},\{g_{\mathrm{Kr},i},\boldsymbol{\phi}_i\}_i} \mathcal{L}\left(\boldsymbol{\theta}, \{g_{\mathrm{Kr},i}, \boldsymbol{\phi}_i\}_i\right)$
Initialise $\{L_{\mathrm{kinetics},i}\}_i, \{L_{\mathrm{artefacts},i}\}_i$;
Set $\boldsymbol{\theta}^0, \left\{g^0_{\mathrm{Kr},i}, \boldsymbol{\phi}^0_i\right\}_i$;
$L^0 \leftarrow \prod_i L_{\mathrm{kinetics},i}\left(\boldsymbol{\theta}^0 \,\middle|\, g^0_{\mathrm{Kr},i}, \boldsymbol{\phi}^0_i\right)$;
$j \leftarrow 0$;
while *not terminate* **do**
  $\boldsymbol{\theta}^{j+1} \leftarrow$ sample $\boldsymbol{\theta}$ with an optimisation algorithm given L^j;
  foreach i **do**
    $g^{j+1}_{\mathrm{Kr},i}, \boldsymbol{\phi}^{j+1}_i \leftarrow \mathrm{argmax}_{g_{\mathrm{Kr},i},\boldsymbol{\phi}_i} L_{\mathrm{artefacts},i}\left(g_{\mathrm{Kr},i}, \boldsymbol{\phi}_i \,\middle|\, \boldsymbol{\theta}^{j+1}\right)$
  end
  $L^{j+1} \leftarrow \prod_i L_{\mathrm{kinetics},i}\left(\boldsymbol{\theta}^{j+1} \,\middle|\, g^{j+1}_{\mathrm{Kr},i}, \boldsymbol{\phi}^{j+1}_i\right)$;
  $j \leftarrow j+1$;
end
$\boldsymbol{\theta}^*, \left\{g^*_{\mathrm{Kr},i}, \boldsymbol{\phi}^*_i\right\}_i \leftarrow \boldsymbol{\theta}^j, \left\{g^j_{\mathrm{Kr},i}, \boldsymbol{\phi}^j_i\right\}_i$

The parameter inference scheme is shown in Algorithm 6.1, where $L_{\mathrm{kinetics},i}$ is the likelihood of the kinetic parameters $\boldsymbol{\theta}$, and $L_{\mathrm{artefacts},i}$ is the likelihood of $g_{\mathrm{Kr},i}, \boldsymbol{\phi}_i$ for the i^{th} measurement. By optimising $\mathcal{L}(\boldsymbol{\theta})$, we get $\boldsymbol{\theta}^*, \{g^*_{\mathrm{Kr},i}, \boldsymbol{\phi}^*_i\}_i$, where $\{g^*_{\mathrm{Kr},i}, \boldsymbol{\phi}^*_i\}_i$ vary across measurements which explains all the observed variability.

6.4.4 Variability in ion channel kinetics or variability in patch-clamp artefacts?

The performance of the models arising from the two hypotheses is compared next. For Hypothesis 1 the results from Chapter 4 are used, where all the variability was assumed to be the result of kinetic variability (giving 9 parameters $\times$ 124 cells $=$ 1116 parameters in total). For Hypothesis 2 we use the results from optimising $\mathcal{L}(\boldsymbol{\theta})$ in Eq. (6.49).

As in Chapter 4, fits and predictions are quantified using relative root-mean-square error (RRMSE), defined as the root mean square error between the model simulation and the experimental data, divided by the root mean square distance of the data to a zero current trace:

$$\mathrm{RRMSE} = \sqrt{\sum \left(I^{\mathrm{model}} - I^{\mathrm{data}}\right)^2 \Big/ \sum \left(I^{\mathrm{data}}\right)^2}. \tag{6.50}$$

Using this RRMSE quantification, the difference in the absolute size of the current across cells (due to varying conductance) is eliminated such that the scores are comparable between cells.

Figure 6.10 shows the RRMSE histograms for all 124 cells, for all nine different protocols, and for the two sets of models. Markers indicate the best ($*$), median ($\ddagger$) and 90$^{\mathrm{th}}$ percentile (#) RRMSE values for the independent kinetics models (red), and the corresponding raw current traces are shown in the three panels above. The model predictions for the same three cells with the identical kinetics model are shown in green. These protocols were used in Chapter 4 where they were intended to explore physiologically-relevant predictions for I_{Kr} behaviour.

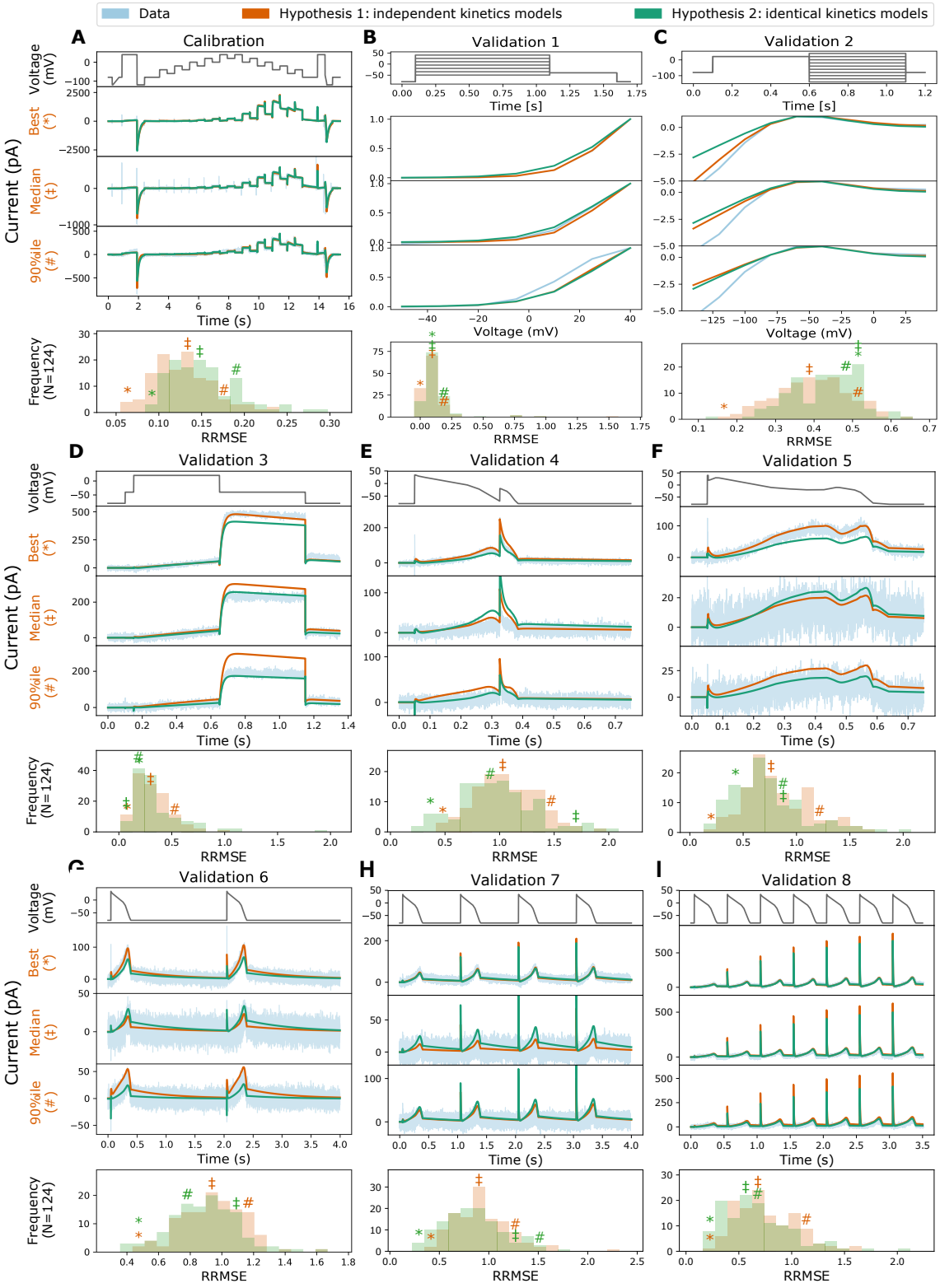

Figure 6.10: The RRMSE histograms for all protocols, comparing the independent kinetics models from Chapter 4 and the identical kinetics models with voltage-clamp artefact. Each histogram represents the same 124 cells with a different protocol and RRMSE each time. Red markers indicate the best (∗), median (‡) and 90$^{\text{th}}$ percentile (#) RRMSE values for the independent kinetics model; green markers are the same cell prediction from the identical kinetics models. For each protocol, the raw traces for the identical kinetics model (green), the independent kinetics model (red), and data (blue) are shown, with the voltage-clamp above. Note that the currents are shown on different scales for each cell, to reveal the details of the traces.

Quantitatively, the two models show a similar RRMSE distribution for each protocol. For the calibration protocol shown in Figure 6.10A, the RRMSE histogram of independent kinetics models (Hypothesis 1, shown in red) clearly shows lower errors on average (and hence better fits) than the identical kinetics models (Hypothesis 2, in green). This is expected, as under the independent kinetics hypothesis 9 parameters can be varied per cell (leading to $9 \times 124 = 1116$ degrees of freedom overall), while under the identical kinetics hypothesis there are only 3 (for $8 + 3 \times 124 = 380$ degrees of freedom). This increased freedom allows Hypothesis 1 to achieve better fits, but could also lead to *overfitting* (Whittaker et al., 2020).

In overfitting, an increased number of degrees-of-freedom leads to improved fits to calibration data, but at the expense of a loss of predictive power on new data sets. Examples in Figure 6.10D, Validation #3, hint that this may be happening. Here, the 'median quality' Hypothesis 1 prediction (with nine cell-specific parameters) over-predicts the peak current under the Validation #3 protocol. In contrast, the Hypothesis 2 prediction (with three cell-specific parameters) is much closer to the data, suggesting that the cell-specific Hypothesis 1 parameter set may have varied kinetic parameters to fit details that are better explained by patch artefacts. To summarise such fits across all 124 recordings we can examine the histograms of RRMSE beneath each protocol in Figure 6.10. Interestingly Hypothesis 1 only shows better predictive performance than Hypothesis 2 for the Validation #2 protocol in Figure 6.10C. We believe this is due to the similarity between Validation #2 and the Calibration protocol — they both step up and down to the same range of voltages in the same duration steps of 500 ms — i.e. this is the validation situation closest to the training protocol which Hypothesis 1 does better at due to having extra parameters to fit. Further evidence that overfitting might be occurring under Hypothesis 1 is shown by Figure 6.10E-I, where the red RRMSE histogram is shifted right, indicating that validation predictions show higher error for Hypothesis 1 than Hypothesis 2. In summary, Hypothesis 2 provides predictions in new situations that overall are at least as good as, or even slightly better than, Hypothesis 1. Coupled with the greatly reduced number of degrees-of-freedom in Hypothesis 2 (736 fewer parameters), this is a strong indication that identical kinetics is the preferred hypothesis for these data.

In the identical kinetics models, all the variability must be explained by the voltage-clamp artefact parameters, $\boldsymbol{\phi}_i$, and the cell conductance, $g_{\mathrm{Kr},i}$, in Eq. (6.49). Figure 6.11 shows the histograms and the pairwise scatter plots of the obtained $\{g^*_{\mathrm{Kr},i}, \boldsymbol{\phi}^*_i\}_{i=1,\ldots,124}$. The artefact parameter values are within reasonable ranges ($\sim \pm 5$ mV for $V^\dagger_{\mathrm{off}}$ and $g^\dagger_{\mathrm{leak}} \ll g_{\mathrm{Kr}}$) and are not strongly correlated, which lends further credibility to the identical kinetics models (Hypothesis 2).

Finally, one might expect that the mean of the kinetic parameters identified under Hypothesis 1 would be similar to the single set of kinetic parameters identified under Hypothesis 2. Table 6.5 shows the inferred parameters of the identical kinetics across all 124 cells under the assumptions of Hypothesis 2 (the mean of Hypothesis 1 from Chapter 4 is also shown for comparison). Kinetic parameters and model predictions from the two hypotheses are very similar, but not exactly the same. Figure 6.12 shows the predictions for voltage dependency of steady-states, open probability and time constants using the inferred parameters in Table 6.5. All of them are calculated directly from inferred parameters using Eqs. (4.3) and (4.4). Grey lines show the predictions from Hypothesis 1 (assuming

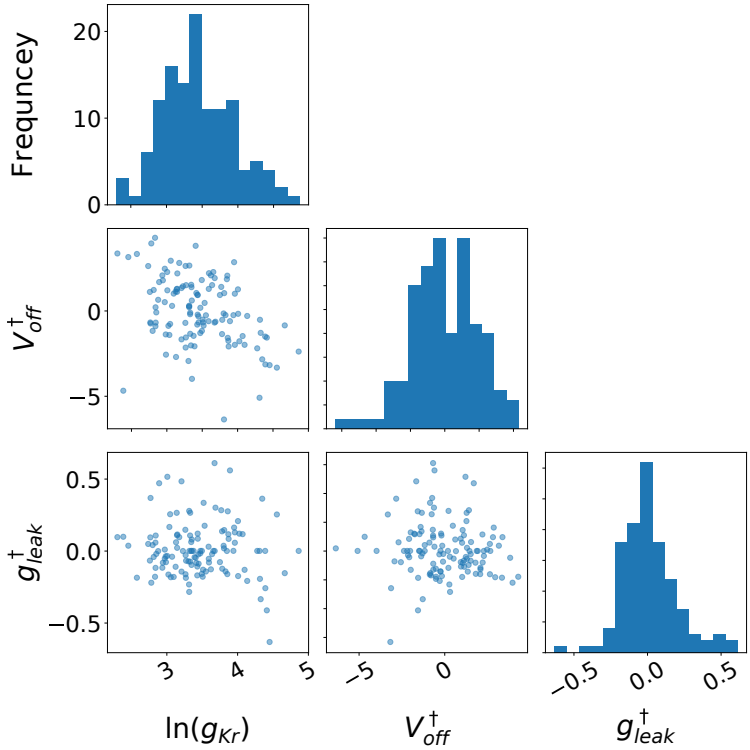

Figure 6.11: The inferred voltage-clamp artefact parameters across experimental wells. Each of the parameters exhibits a Gaussian-like distribution under this choice of transformation. The artefact parameter values are within reasonable ranges: $V^{\dagger}_{\text{off}} \sim \pm 5\,\text{mV}$ and $g^{\dagger}_{\text{leak}} \ll g_{\text{Kr}}$.

a gate	p_1 (ms^{-1})	p_2 (mV^{-1})	p_3 (ms^{-1})	p_4 (mV^{-1})
Hypothesis 1	7.65×10^{-5}	9.05×10^{-2}	2.84×10^{-5}	4.74×10^{-2}
Hypothesis 2	1.13×10^{-4}	7.45×10^{-2}	3.60×10^{-5}	4.49×10^{-2}
r gate	p_5 (ms^{-1})	p_6 (mV^{-1})	p_7 (ms^{-1})	p_8 (mV^{-1})
Hypothesis 1	1.03×10^{-1}	2.13×10^{-2}	8.01×10^{-3}	2.96×10^{-2}
Hypothesis 2	9.61×10^{-2}	2.36×10^{-2}	7.85×10^{-3}	3.06×10^{-2}

Table 6.5: Inferred parameters for the mean of Hypothesis 1 (assuming cell-specific kinetics with no artefacts; from Chapter 4) and Hypothesis 2 (assuming identical kinetics for all cells with cell-specific artefacts).

cell-specific kinetics with no artefacts; from Chapter 4), and red lines show the predictions from the mean of Hypothesis 1. Green lines show the predictions from Hypothesis 2 (assuming identical kinetics for all cells with cell-specific artefacts). There is a noticeable shift of the parameters between Hypothesis 1 (mean) and Hypothesis 2. Finally the predictions using the parameters in Table 6.5 for the staircase protocol is shown in Figure 6.13, showing the differences in terms of current prediction. The difference is due to the unaccounted experimental artefacts in Hypothesis 1 that are included in the (model) kinetic parameters. If Hypothesis 2 is correct, the kinetic parameters derived from it are the more physiologically-relevant.

We also examined a 'Hypothesis 3' where conductance, kinetics and artefacts were all cell-specific. Fits improved slightly (as expected with more parameters) but predictions were of similar quality to

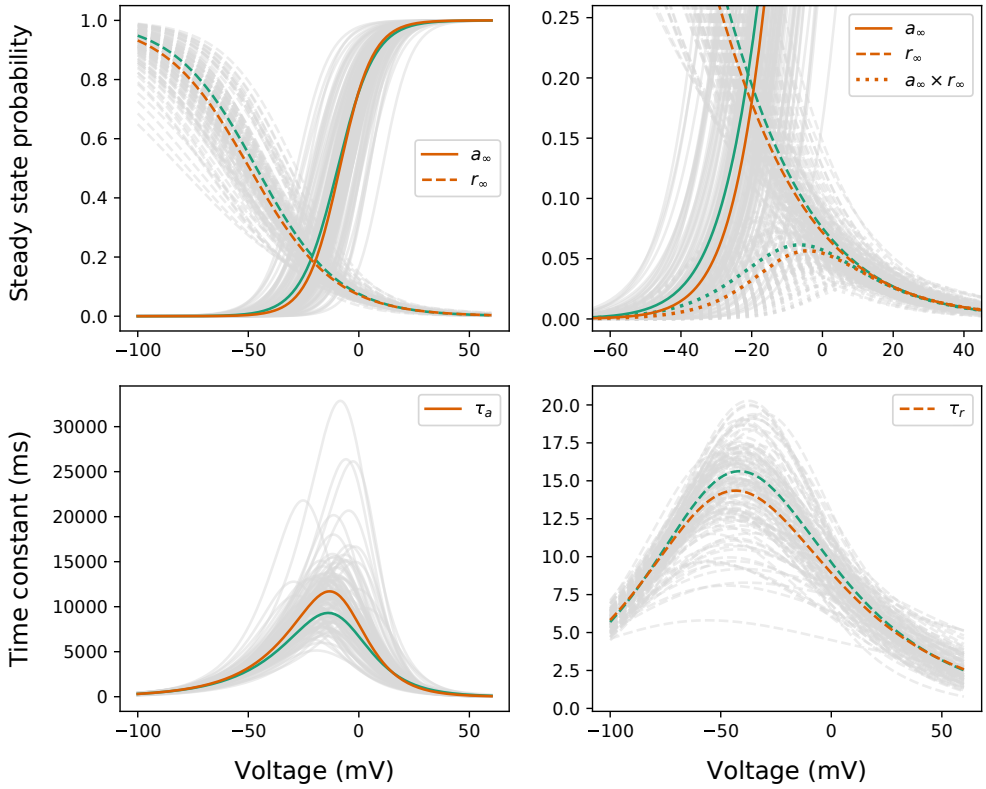

Figure 6.12: Predictions for voltage dependency of steady-states, open probability and time constants of the model. These lines are calculated directly from inferred parameters. Grey lines show the predictions from Hypothesis 1 (assuming cell-specific kinetics with no artefacts; from Chapter 4), and red/orange lines show the predictions from the mean of Hypothesis 1. Green lines show the predictions from Hypothesis 2 (assuming identical kinetics for all cells with cell-specific artefacts).

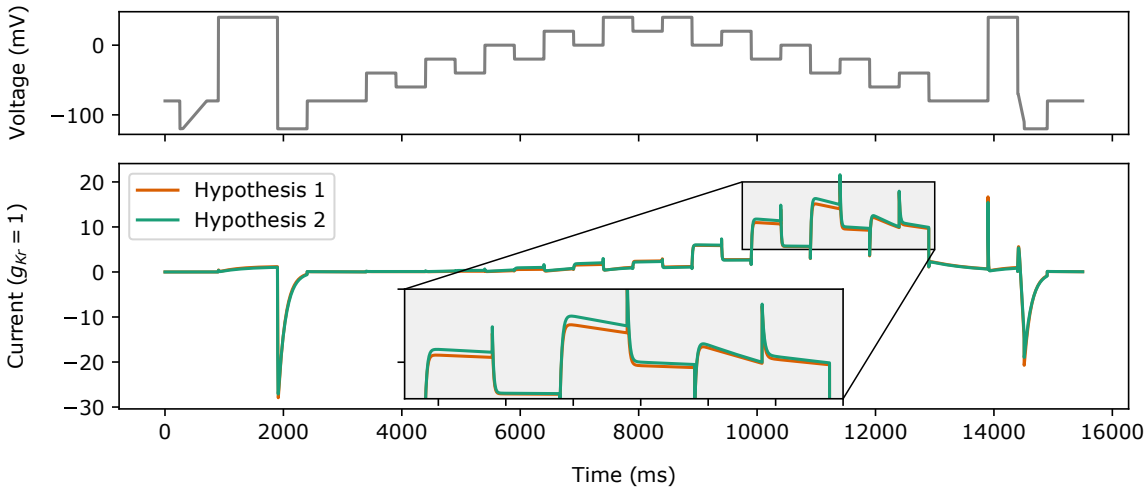

Figure 6.13: Predictions for the staircase protocol using the two sets of mean parameters from the two hypotheses in Table 6.5. The mean of Hypothesis 1, assuming cell-specific kinetics with no artefacts (from Chapter 4), is shown in red/orange. Hypothesis 2, assuming identical kinetics for all cells with cell-specific artefacts, is shown in green.

Hypothesis 1, and not as good as Hypothesis 2. Figures and code for this analysis can be found in the online repository (see Data and Software Availability at the end of the chapter).

6.5 Discussion

In this chapter we have introduced a new mathematical model for voltage-clamp experiments that accounts for experimental artefacts and imperfect compensations of these artefacts, as well as imperfections in leak current subtraction. The model gives insight into the process of how experimental artefacts are introduced and the performance of the compensation procedure. For example, often the largest currents have the highest signal-to-noise ratio and could be interpreted as the 'cleanest' recordings. But in Eq. (6.29), the model shows that the effect of R_s in distorting the applied voltage is proportional to the current size. So, for a given series resistance and a fixed percentage compensation (α), the bigger the current then the larger this artefact; after we published this work (Lei et al., 2020a), Montnach et al. (2020) used a simplified artefact model (accounting for only the series resistance) to study the same effect with I_{Na} and I_{Ks}.

We validated the mathematical model through experiments using two types of electrical model cells, where we showed that our mathematical model is able to rectify imperfect amplifier estimations; then applied it to account for artefacts whilst inferring parameters of an I_{Kr} model from hERG1a CHO cell data. This is, to our knowledge, the first time a detailed voltage-clamp experiment model has been used for parameter optimisation in ion channel modelling.

6.5.1 Origin of variability

Whole-cell patch-clamp data show a high degree of variability (Zhou et al., 1998; Vandenberg et al., 2006; Beattie et al., 2018; Lei et al., 2019a,b), with differences in observed current kinetics between experiments. As recordings measure whole-cell 'macroscopic' current one might expect variation due to stochastic 'microscopic' ion channel opening. But in Chapter 4 we have observed currents to be reproducible within a given cell — that is, the apparent kinetic variability upon protocol repeats in the same cell at different times is much smaller than cell-to-cell variability. We expect the maximum *conductance* of the current to differ between cells, due to varying cell sizes and gene expression levels. Since each CHO cell over-expresses the same channel gene, there is no such obvious reason for the current *kinetics* to vary cell-to-cell, especially if the cells are from the same culture and recorded simultaneously under very similar conditions, as they were in our high-throughput data.

Each voltage-clamp experiment has a different cell membrane capacitance, pipette (or well-plate in automated clamp) capacitance, voltage offset, series resistance, and leak current. This led us to propose two competing hypotheses (as shown in Figure 6.7): Hypothesis 1 is that there are cell-specific kinetics with no artefacts; and Hypothesis 2 is that there are identical kinetics for all cells with cell-specific artefacts. A parameter optimisation technique was developed for Hypothesis 2, so that we were able to optimise all the model parameters at once (cell-specific conductances and measurement artefact parameters, with a single set of kinetic parameters shared by all the cells). One may also

speculate an intermediate hypothesis between the two hypotheses, where conductance, kinetics and artefacts are all cell-specific. We referred this all cell-specific assumption to as Hypothesis 3.

Models based on cell-specific conductances and kinetics (Hypothesis 1) or cell-specific conductances, kinetics and artefacts (Hypothesis 3) included many parameters/degrees-of-freedom. The simpler model of just cell-specific conductances and artefacts (Hypothesis 2) made better predictions, on average, over all 124 cells that were analysed. Considering Occam's razor, this makes the 'identical kinetics' hypothesis, in which fewer assumptions are made, the favourable explanation. So it is more plausible that the observed variability in the current traces arose from patch-clamp experimental artefacts, that is imperfect amplifier compensations and imperfect leak current subtraction, than from varying current kinetics. One might expect this result, since the current is carried by thousands of identical ion channel proteins, especially in our over-expression cell line.

It should be noted that these results and this interpretation are specific to our preparation, and cell-cell biological variability in kinetics in general cannot be ruled out. For instance, in native myocytes one might speculate that differing subunit expression and other signalling-related changes in proteins' states in the membrane (e.g. by PI3K signalling, see Ballou et al., 2015) could also confer real biological variability in kinetics from cell to cell. But the results of this chapter suggests the major factor causing apparent variability in expression system current kinetics will be artefacts introduced by the patch-clamp experimental procedure, and offers an approach to address it.

6.5.2 Implication for whole-cell level modelling

Determining the origin of variability is particularly important for forward propagation of uncertainty in cardiac modelling. If each ion current biologically exhibited a high-degree of variability in kinetics from cell to cell, then a description of this variability for all currents would be necessary to make predictions at the whole-cell level that accounted for it. However, if the majority of the variability is due to experimental artefacts, then a single set of kinetic parameters could accurately describe the physiology of each current type. If our findings also apply to myocytes, the standard approach to building action potential models with a single set of kinetic parameters for each current is appropriate (Ten Tusscher et al., 2004; O'Hara et al., 2011; Groenendaal et al., 2015; Lei et al., 2017a), and the observed cell-cell variability in kinetics data should not be propagated forward in action potential simulations (as some studies have examined, e.g. Pathmanathan et al., 2015). Nevertheless, we still need an approach like the one demonstrated here to determine unbiased ion channel kinetic parameters to build the most physiologically-relevant action potential models; as opposed to taking the mean of biased recordings which could accidentally include some experimental artefacts within the kinetics models (see Figure 6.12).

6.5.3 Implication for cardiac electrophysiology studies

Identifying ion current kinetics and separating out experimental artefacts is crucial for many cardiac electrophysiology studies. For example, ion channel mutation studies often conclude with a statement such as "there is a 5–10 mV shift in the half-activation potential" (a recent example is Ng et al. (2020); see Clerx et al. (2018) for a list of reported shifts in I_{Na}). However, given the variability that we

observe in patch-clamp data, often the cell to cell variability in half-activation potential can be in the range of 10–15 mV. Therefore, it is important to separate out experimental artefacts from real biological effects. The same principle applies to other cardiac electrophysiology studies, such as drug studies and the basic characterisation of ion channel kinetics.

6.5.4 'Ideal' compensation

The findings raise the question of whether a mathematical model of the voltage-clamp experiment could remove the need for amplifier compensations altogether. This approach works well when we have an almost perfect model of the current, as in the electrical model cell cases in Sections 6.3.3.1 and 6.3.3.2 (see e.g. Figure 6.6). But we do not recommend it in general, because unlike the reduced model, the full voltage-clamp experiment model (Eqs. (6.24)–(6.32)) with an I_{Kr} model appeared to produce spurious fits to real cell data. This behaviour is possibly due to I_{Kr} model discrepancy — extra artefact components in the full model may attempt to 'mop up' real I_{Kr} current which the approximations in this simple I_{Kr} model do not explain. We envision that a more detailed I_{Kr} model, or techniques for accounting for discrepancy (Lei et al., 2020c), could allow us to infer parameters for the full patch-clamp model. Yet our simplified voltage-clamp model (Eqs. (6.42)–(6.47)) appears to account for imperfect amplifier compensation even with an inevitably imperfect mathematical model of I_{Kr} kinetics.

We would therefore suggest fitting a simplified voltage-clamp model together with the model of interest for the measured current to the data, such that the voltage-clamp model can account for the experimental artefacts rather than the current model absorbing those non-physiological effects. The assumption of 'identical kinetics' (i.e. whether one should use Hypothesis 2 or Hypothesis 3) should be subject to the specific study; for expression system current kinetics measured in very similar conditions as we have in this chapter, we expect 'identical kinetics' would be a reasonable assumption, whereas for native myocytes further investigation would be needed.

6.6 Conclusion

A mathematical model was derived to describe the entire voltage-clamp experiment including artefacts, imperfect amplifier compensations, and imperfect leak current subtraction. Using this model, variability in a set of experimental observations could be explained either by varying current properties or varying measurement artefacts. After comparing model predictions in each case, the results suggest that most of the observed variability in a set of expression system patch-clamp data measured in high-throughput under the same conditions is caused by experimental artefacts. These varying experimental artefacts can be compensated in post-processing by fitting the mathematical model for the patch-clamp experiment at the same time as fitting ion channel kinetics. This chapter raises questions for the biological significance of any cell-cell variability in macroscopic ion channel kinetics, and provides a new way for better correction of artefacts in patch-clamp data.

After applying the conventional methods for calibrating human induced pluripotent stem cell-derived cardiomyocyte (hiPSC-CM) models in Chapter 3, we suspected better ion channel kinetics models

are needed. We therefore moved on and looked at using experimental designs to improve models of ion channel kinetics. We performed experimental design for hERG kinetics in Chapter 4, we then showed why it is so important and extended applications including temperature dependence of hERG in Chapter 5 and origin of variability in this chapter. In the next chapter, we revisit adult cardiomyocyte and hiPSC-CM action potential models. We look into optimal experimental design techniques in the literature and apply them to the action potential models. We ask how accurate the kinetics models need to be in order to be able to calibrate a cell-specific whole-cell action potential model.

6.7 Data and Software Availability

Data and software (GitHub repository):
https://github.com/CardiacModelling/VoltageClampModel

Chapter 7

Tailoring Action Potential Models: An Optimal Experimental Design Approach and Real-World Problems

A publication I led relating to this chapter: Lei, C. L., Ghosh, S., Whittaker, D. G., Aboelkassem, Y., Beattie, K. A., Cantwell, C. D., Delhaas, T., Houston, C., Novaes, G. M., Panfilov, A. V., Pathmanathan, P., Riabiz, M., dos Santos, R. W., Walmsley, J., Worden, K., Mirams, G. R., and Wilkinson, R. D. (2020c). Considering discrepancy when calibrating a mechanistic electrophysiology model. *Philosophical Transactions of the Royal Society A*, 378:20190349.

Contributions: I assisted in designing the study, and wrote code for and performed all the simulation studies and data analysis.

Overview:

In previous chapters we designed experiments, constructed and validated models for the *human Ether-à-go-go-Related Gene* (hERG) channel. In this chapter, we revisit fitting cell-specific whole-cell action potential models for human induced pluripotent stem cell-derived cardiomyocytes (hiPSC-CMs). We first review a range of optimal experimental design (OED) techniques from the literature, then we apply these techniques to the action potential models. Similarly to Chapter 3, we focus on developing an experimental protocol that allows us to identify cell-specific maximum conductance values for each current type. We consider the potential for errors to be induced by discrepancy in the underlying ion channel kinetics by validating the robustness of the design using multiple existing (adult human cardiomyocyte) ion channel kinetics models. Through synthetic data studies, we show that large errors in conductance estimates can be introduced and there are no simple fixes when there is discrepancy in the model of the kinetics. We then address the question of how discrepant a model can be before whole-cell fitting fails, by replacing an existing hERG model with the one that we developed in Chapter 5, as well as slightly perturbing the kinetics models. Results show that we need to develop ion channel models with good accuracy to infer maximum conductances correctly. Finally we also investigate the effect of the experimental artefacts that we studied in Chapter 6 on whole trace fitting.

7.1 Introduction

In Chapter 3, we used a relatively simple approach to reparameterise the maximum conductance values of a human induced pluripotent stem cell-derived cardiomyocyte (hiPSC-CM) model using experimental data. We assumed that the ion channel kinetics were perfectly described by the model — i.e. there was no discrepancy in the ion channel kinetics models. We used simple conventional step protocols to generate the voltage-clamp data. The results in that chapter revealed the limitations of both the conventional step protocols and the ideal kinetics assumption.

There are two potential routes to continue the tailoring of the action potential model study from Chapter 3. First, we could focus on the kinetics and apply a suitably designed protocol for each current in a hiPSC-CM to fully characterise its ion channel electrophysiology. In Chapter 4 and Chapter 5, we therefore focused on developing a new approach to experimental design to allow rapid characterisation of the channel kinetics for the *human Ether-à-go-go-Related Gene* (hERG). This showed the feasibility of accurately characterising the kinetics of an ion channel with a recording of about 10–20 s; this approach can be extended for other ion currents in the action potential model as a first route. Secondly, assuming the kinetics of each current to be known, we can focus on designing experiments for inferring the maximum conductance values of the hiPSC-CM model, or indeed any action potential model.

The assumption for the second route, i.e. fitting conductances to whole-cell recordings while using ion channel kinetics models taken (or slightly adapted) from the literature, has been commonly used (Whittaker et al., 2020). For example, Groenendaal et al. (2015) have proposed to use (cell-specific) voltage-clamp and current-clamp data with a genetic algorithm to find maximum conductances in an action potential model. Similarly Johnstone et al. (2016b) adapted a Bayesian approach with Markov Chain Monte Carlo (MCMC) to infer maximum conductances using action potential recordings. Many more inference approaches have been adapted, including multivariate regression (Sarkar and Sobie, 2010), history matching (Coveney and Clayton, 2018), "population of models" (Britton et al., 2013; Muszkiewicz et al., 2016), and moment-matching (Tixier et al., 2017), and all of them assumed "out of the box" or slightly modified kinetics models when fitting maximum conductances.

In this chapter, we perform synthetic data studies to explore the feasibility of the second route. First we apply *model-based* optimal experimental design (OED) to optimise the protocol for inferring the maximum conductance values for cardiac action potential models. We assume the ion channel kinetics are known. Along with our comparison of optimised protocols, we also compare against two other voltage-clamp protocols: one from Chapter 3 and one from Groenendaal et al. (2015). Second, we examine whether any of these designs is robust to the discrepancy of kinetics that we expect when fitting the maximum conductance values and handling real data. However, we find that none of these designs is robust to kinetics discrepancy, which is not surprising as OED does not take into account model discrepancy. We then investigate a series of further questions: if our approach in Chapter 4 creates a 'good' kinetics model, are we able to retrieve the correct contribution of each current to whole-cell electrophysiology? If we apply channel-specific blockers and perform current subtraction, a widely used technique thought to isolate each current's contribution, are we able to

find the 'correct' current contributions? Finally, if our experimental measurements suffer from the voltage-clamp artefacts discussed in Chapter 6, can we still reliably infer the maximum conductance values?

7.2 Optimal Experimental Design (OED)

In the design of experiments, the results of OEDs are experimental designs that are optimal with respect to some statistical criteria — *optimal design measures*. Formally, we consider a nonlinear differential equation model of the form

$$\frac{\mathrm{d}\boldsymbol{x}}{\mathrm{d}t} = \boldsymbol{f}(\boldsymbol{x}, \boldsymbol{u}(\boldsymbol{\zeta}), \boldsymbol{\theta}), \tag{7.1}$$

$$\boldsymbol{y} = \boldsymbol{h}(\boldsymbol{x}, \boldsymbol{u}(\boldsymbol{\zeta}), \boldsymbol{\theta}), \tag{7.2}$$

where $\boldsymbol{x}$ is the vector of model states, $\boldsymbol{u}$ is the vector of system inputs, $\boldsymbol{\theta}$ is the vector of model parameters, $\boldsymbol{f}$ and $\boldsymbol{h}$ are the systems of equations, and $\boldsymbol{y}$ is the vector of observable model outputs we compare with data. We assume that the system input $\boldsymbol{u}$ can be parameterised with $\boldsymbol{\zeta}$, i.e. $\boldsymbol{\zeta}$ is the vector of parameters that controls the experimental conditions. For example, if $\boldsymbol{u}$ is an applied voltage-clamp, $\boldsymbol{\zeta}$ could be the voltages and durations of its steps. The optimisation of the experimental design procedure is then defined as

$$\hat{\boldsymbol{\zeta}} = \underset{\boldsymbol{\zeta}}{\operatorname{argmin}}\, \Phi(\boldsymbol{\zeta}), \tag{7.3}$$

where the function Φ represents the optimal design measure to be minimised.

All optimal design measures discussed in this chapter assume the model calibration process described in Chapter 2, such as least-square estimation, maximum likelihood estimation, or posterior estimation; if one considers a different calibration process, such as bounded-error parameter estimation (also known as guaranteed parameter estimation) or Approximate Bayesian Computation (ABC), then a different set of design measures should be used (Gottu Mukkula and Paulen, 2017). All methods discussed in this chapter are implicitly conditional on the chosen set of model equations, i.e. they are only optimal for the models used during the design. This is a general limitation of model-based OED.

In the rest of this section, we discuss several optimal design criteria based on local sensitivity analysis (LSA), global sensitivity analysis (GSA), and Shannon (information) entropy. There is another class of optimal design criteria that stems from Bayesian statistics and decision theory (see e.g. Raiffa and Schlaifer, 1961; Lindley, 1972; Chaloner and Verdinelli, 1995). However, as we will see in Section 7.5, the limitation in 'real-world problems' is the potential model discrepancy rather than the variants of the designs. Therefore, for simplicity, in this chapter we show results for only the criteria discussed in the rest of Section 7.2 below.

7.2.1 Local designs

The sensitivity matrix based on local sensitivity analysis (LSA), $\mathbf{S}_{\mathrm{L}}(\boldsymbol{\zeta} \mid \boldsymbol{\theta} = \hat{\boldsymbol{\theta}})$, is defined as

$$(\mathbf{S}_{\mathrm{L}})_{ij} = \left.\frac{\partial y_i}{\partial \theta_j}\right|_{\boldsymbol{\theta}=\hat{\boldsymbol{\theta}}}. \tag{7.4}$$

Here the subscript i (row) in y_i runs through all model outputs in $\boldsymbol{y}$ and all sampled time points t_k[1], and the subscript j (column) θ_j goes over all model parameters in $\boldsymbol{\theta}$. The *Fisher Information Matrix* (FIM) is given by

$$\mathrm{FIM}(\boldsymbol{\theta}) = \mathbf{S}_\mathrm{L}^T \, \boldsymbol{\Sigma}^{-1} \, \mathbf{S}_\mathrm{L}, \tag{7.5}$$

where $\boldsymbol{\Sigma}$ is the covariance matrix of the measurement data (noise), in this chapter we assume data are a single output (a single current trace) with independent and identically distributed (i.i.d.) Gaussian noise through time such that $\boldsymbol{\Sigma} = \sigma^2 \mathbf{I}$ with σ constant and $\mathbf{I}$ the identity matrix.

Many local design criteria are based on the parameter (co)variance matrix defined as

$$\mathbf{C}_{\boldsymbol{\theta}} = \mathbb{E}\left[(\boldsymbol{\theta} - \mathbb{E}[\boldsymbol{\theta}])(\boldsymbol{\theta} - \mathbb{E}[\boldsymbol{\theta}])^T\right] \geq \mathrm{FIM}(\boldsymbol{\theta})^{-1}, \tag{7.6}$$

where $\mathbb{E}[\cdot]$ denotes the expected value. This describes the covariance of the estimates of a fixed true parameter set[2]. For any unbiased estimator, where the expected value is equal to the true value of the parameter set, a lower bound for the variance is given by the inverse of the FIM (the inequality in Eq. (7.6)), known as the Cramér-Rao bound. Therefore, to evaluate the local design criteria based on the covariance matrix, we use the the Cramér-Rao bound and calculate $\mathrm{FIM}(\boldsymbol{\theta})^{-1}$ instead (Walter and Pronzato, 1997; Schenkendorf et al., 2018). In fact, equality with the Cramér-Rao bound would be achieved as K (number of observations) approaches infinity

$$\lim_{K \to \infty} \mathbf{C}_{\boldsymbol{\theta}} = \mathrm{FIM}(\boldsymbol{\theta})^{-1}. \tag{7.7}$$

For proof of Eq. (7.7) see, for example, Pant (2018). Note, $\mathbf{C}_{\boldsymbol{\theta}}$, FIM, and $\mathbf{S}_\mathrm{L}$ all depend on the choice of the system input $\boldsymbol{\zeta}$.

A common class of the local design criteria is the '*alphabetic family*' of design criteria (Kiefer, 1959; Walter and Pronzato, 1997). These criteria each represent a cost function to be minimised, a subset of them (A-optimal, D-optimal, and E*-optimal designs, Atkinson and Donev, 1992) are shown in Table 7.1, where $\lambda_{\max}(\mathbf{X})$ and $\lambda_{\min}(\mathbf{X})$, respectively, denote the maximum and minimum eigenvalues of a matrix $\mathbf{X}$.

Local design criteria	Cost functions
A-optimal design	$\Phi_\mathrm{A} = \mathrm{trace}([\mathbf{S}_\mathrm{L}^T \, \mathbf{S}_\mathrm{L}]^{-1})$
D-optimal design	$\Phi_\mathrm{D} = \det([\mathbf{S}_\mathrm{L}^T \, \mathbf{S}_\mathrm{L}]^{-1})$
E*-optimal design	$\Phi_{\mathrm{E}^*} = \lambda_{\max}([\mathbf{S}_\mathrm{L}^T \, \mathbf{S}_\mathrm{L}]^{-1}) / \lambda_{\min}([\mathbf{S}_\mathrm{L}^T \, \mathbf{S}_\mathrm{L}]^{-1})$

Table 7.1: Local design criteria for OED. Here we have assumed the parameter covariance matrix $\mathbf{C}_{\boldsymbol{\theta}}$ for some given model parameters $\boldsymbol{\theta}$ can be approximated as $\sigma^{-2}[\mathbf{S}_\mathrm{L}^T \mathbf{S}_\mathrm{L}]^{-1}$, where σ^{-2} is dropped in the design criteria (cost functions) as it is assumed to be constant. E* is the modified E criterion.

The design criteria in Table 7.1 are parameter based criteria (Atkinson and Donev, 1992): these cost functions (as functions of the FIM) can be interpreted as properties (the shape and size) of the

[1] That is, for N_o model outputs and N_t time points, $i = 1, 2, \ldots, N_o, N_o + 1, N_o + 2, \ldots, N_o \times N_t$.

[2] Note that under this framework, the true parameters do not vary, as opposed to the Bayesian framework where the true parameters can be treated as random variables.

confidence hyper-ellipsoid (a generalisation of the confidence interval for multivariate statistics) for the parameters $\boldsymbol{\theta}$ (Vanrolleghem and Dochain, 1998; Banga and Balsa-Canto, 2008). The A-optimal design can be interpreted as minimising the average variance of the confidence ellipsoid; the D-optimal design minimises the volume of the confidence ellipsoid; and the E*-optimal design minimises the ratio of the length of the largest to the smallest axis, making the ellipsoid as spherical as possible. Therefore, by improving these properties of the confidence ellipsoid, the uncertainty of the inferred parameters using the data measured under these optimal design protocol would (in theory) be reduced, as we will see in Section 7.4.2.

One obvious limitation of the local designs is that they are *local*, i.e. they depend on a particular choice of the model parameters ($\boldsymbol{\theta} = \hat{\boldsymbol{\theta}}$ in the equations above). Hence the design is only guaranteed to be optimal for that particular choice of parameters. However, we do not know the true model parameters in the experiments by definition. This issue can be alleviated by replacing the local sensitivity with an averaged sensitivity matrix

$$\mathbb{E}[(\mathbf{S}_\mathrm{L})_{ij}] = \int_\Theta (\mathbf{S}_\mathrm{L})_{ij}\, p(\theta_j)\mathrm{d}\theta_j, \tag{7.8}$$

where $p(\theta_j)$ is the probability density function of the j^{th} parameter, defined over a domain Θ (a subspace of the parameter space). The integral in Eq. (7.8) can be approximated using Monte Carlo simulations. Although this averaged sensitivity matrix has been shown to give a more robust design (Chu and Hahn, 2013), it is does not take the multivariate interaction into account (Schenkendorf et al., 2018), and hence the framework of global sensitivity analysis (GSA) comes into play.

7.2.2 Global designs

Next we explore global design criteria that do not rely on a particular choice of the model parameters $\boldsymbol{\theta}$.

7.2.2.1 Global sensitivity analysis-based design criteria

One of the most straight forward ways of doing GSA-based design is by replacing the $\mathbf{S}_\mathrm{L}$ in Table 7.1 with a sensitivity matrix based on GSA methods (Rodriguez-Fernandez et al., 2007; Kucerová et al., 2016; Schenkendorf et al., 2018). We can use variance-based methods such as the *Sobol method* (also known as the *Sobol indices* Sobol, 2001). The Sobol method decomposes the variance of the model output into fractions, and attributes these variances to parameters or sets of parameters, usually referred to as the *order*. The first-order Sobol index attributes these variances to each parameter θ_j alone; whilst higher order Sobol indices attribute the variances to different combinations of parameters. These variances are calculated using a set of parameters sampled within a domain Θ, a subspace of the parameter space. These parameters can be sampled using various methods, for example Monte Carlo methods, or some low-discrepancy sequences (including Sobol sequences or Latin hypercube sampling); we used the extension of the Sobol sequence by Saltelli (2002) and Saltelli et al. (2010) in this chapter. The first-order Sobol sensitivity index is given by

$$(\mathbf{S}_\mathrm{G})_{ij} = \frac{1}{\mathrm{Var}\,(y_i)} \underset{\theta_j}{\mathrm{Var}}\left(\underset{\boldsymbol{\theta}_{-j}}{\mathbb{E}}\left[y_i \mid \theta_j\right]\right), \tag{7.9}$$

GSA-based design criteria	Cost functions
A-optimal design	$\Phi_{\mathrm{A}}^{\mathrm{GSA}} = \mathrm{trace}([\mathbf{S}_{\mathrm{G}}^T \mathbf{S}_{\mathrm{G}}]^{-1})$
D-optimal design	$\Phi_{\mathrm{D}}^{\mathrm{GSA}} = \det([\mathbf{S}_{\mathrm{G}}^T \mathbf{S}_{\mathrm{G}}]^{-1})$
E*-optimal design	$\Phi_{\mathrm{E}^*}^{\mathrm{GSA}} = \lambda_{\max}([\mathbf{S}_{\mathrm{G}}^T \mathbf{S}_{\mathrm{G}}]^{-1}) / \lambda_{\min}([\mathbf{S}_{\mathrm{G}}^T \mathbf{S}_{\mathrm{G}}]^{-1})$

Table 7.2: Global design criteria for OED based on a generalisation of the local design criteria in Table 7.1 using a GSA method.

where $\mathrm{Var}\,(y_i)$ is the total variance of the model output y_i, $\mathrm{Var}_{\theta_j}(X) = \mathbb{E}_{\theta_j}(X^2) - (\mathbb{E}_{\theta_j}(X))^2$ denotes the conditional variance only over parameter θ_j, and $\mathbb{E}_{\boldsymbol{\theta}_{-j}}[\cdot]$ indicates the expected value taken over all parameters $\boldsymbol{\theta}$ except parameter θ_j. Criteria using $\mathbf{S}_{\mathrm{G}}$ are given in Table 7.2. As a side note, one may further include higher order Sobol indices for analysing multivariate parameter interactions and dependencies (Kucerová et al., 2016), but we do not investigate these here for simplicity.

However, there are some limitations for GSA-based design criteria in Table 7.2:

1. the normalisation term in Eq. (7.9) may pose a problem, as minimising the inverse of Eq. (7.9) may lead to a reduction of the total variance $\mathrm{Var}\,(y_i)$ (i.e. worsen the sensitivity/estimates for all model parameters) to improve some of the designs (Schenkendorf et al., 2018); and
2. GSA-based measures may not necessarily simplify to local measures for linear problems, which may lead to sub-optimal designs and counter-intuitive outcomes (Chu and Hahn, 2013; Schenkendorf et al., 2018).

7.2.2.2 Shannon entropy-based design criteria

The Shannon entropy (Lindley, 1956) can be used to avoid some of the issues from GSA-based design criteria. A GSA-based Shannon entropy has been used as a design criterion in fields outside cardiac modelling (Auder and Iooss, 2008; Li et al., 2017a; Schenkendorf et al., 2018). The criteria (cost functions to be minimised) in Table 7.3 emphasise different features of an OED (Schenkendorf et al., 2018): (a) The criterion $\Phi_{\mathrm{SE}}^{\mathrm{all}}$ tries to ensure a balanced sensitivity of all model parameters (i.e. giving an equally distributed values of the first-order Sobol indices) over the whole time series; (b) $\Phi_{\mathrm{SE}}^{\mathrm{seg}}$ limits the number of parameters contributing at a given time point or time segment (e.g. over a voltage-step), i.e. minimising any nonlinear correlation effects; (c) Φ_{OU} aims to get a high overall output variance, and hence a high parameter sensitivity.

Global design criteria	Cost functions
Shannon entropy (SE) (over entire time horizon)	$\Phi_{\mathrm{SE}}^{\mathrm{all}} = -1 / \sum_j \left(\sum_i (\mathbf{S}_{\mathrm{G}})_{ij} \ln \sum_i (\mathbf{S}_{\mathrm{G}})_{ij} \right)$
Shannon entropy (SE) (at time segment s: T_s^1 to T_s^2)	$\Phi_{\mathrm{SE}}^{\mathrm{seg}} = -\sum_s \sum_j \left(\sum_{i=T_s^1}^{T_s^2} (\mathbf{S}_{\mathrm{G}})_{ij} \ln \sum_{i=T_s^1}^{T_s^2} (\mathbf{S}_{\mathrm{G}})_{ij} \right)$
Overall output uncertainty (OU)	$\Phi_{\mathrm{OU}} = 1 / \sum_i \mathrm{Var}\,(y_i)$

Table 7.3: Global design criteria for OED based on a GSA method and Shannon entropy*; adapted from Schenkendorf et al. (2018). Subscripts i (row) run through all model outputs in $\boldsymbol{y}$ and all measured time points t_k, subscripts j (column) run through all model parameters $\boldsymbol{\theta}$. For $\Phi_{\mathrm{SE}}^{\mathrm{seg}}$, we split all measured time points t_k into multiple segments s that run from $t_k = T_s^1$ to $t_k = T_s^2$.

Following Schenkendorf et al. (2018), one may use a multi-objective design to incorporate all the desired features listed in Table 7.3 by optimising

$$\Phi_{\text{SE}} = \boldsymbol{w} \cdot \left(\Phi_{\text{SE}}^{\text{all}} \;\; \Phi_{\text{SE}}^{\text{seg}} \;\; \Phi_{\text{OU}}\right)^T, \tag{7.10}$$

where w is a weighting vector. Although Φ_{SE} is powerful and intuitive, a drawback is that there is no general guidance for choosing the weighting vector w; a poor weighting can lead to a sub-optimal design that is just as bad as using a local design, see Schenkendorf et al. (2018, Figure 9). In this chapter, we use the weighting vector $\boldsymbol{w} = (10 \;\; 0.1 \;\; 1)$ as discussed in Schenkendorf et al. (2018).

7.3 Formulating Models and Experiments for OEDs

In this section we discuss the formulation of the models as well as the experiments for the OED in this chapter.

7.3.1 Action potential models for OEDs

Designing experiments with a single model

We consider an electrophysiology action potential model under an ideal (no artefacts) voltage-clamp experiment, and we aim to optimise the voltage-clamp protocol for conductance identification. We use the Paci et al. (2013) model as a 'proposed model', the same as Chapter 3; in practise, we may design the experiments and perform the fitting to data with this proposed model which would be our current best representation of reality. The observed current I_{obs} can be expressed as

$$I_{\text{obs}}(t) = \sum_j g_j \cdot x_j(V,t), \tag{7.11}$$

where g_j is the maximum conductance and $x_j(V)$ is some nonlinear function of the voltage V for the current of type j, and we consider the same set of major currents as in Chapter 3. These nonlinear functions $x_j(V)$ are the product of the 'kinetics' (describing the voltage-dependent opening and closing of ion channels in response to changes in membrane voltage, denoted as f_j in Eqs. (2.11) and (2.15)) and the 'driving term' of the currents (either the Ohmic $V - E_S$ term or the GHK flux equation described in Chapter 2). We *assume* that these kinetics terms are known (and correct), and we later explore the results of discrepancy in these kinetic models. We are interested in finding all g_j, which determine the magnitude of the currents when the channels are fully open, therefore we have

$$\boldsymbol{\theta} = \{g_{\text{Na}}, g_{\text{CaL}}, g_{\text{Kr}}, g_{\text{Ks}}, g_{\text{to}}, g_{\text{NaCa}}, g_{\text{K1}}, g_{\text{NaK}}\} \tag{7.12}$$

to be inferred.

In this case, the observed current I_{obs} is the output defined in Eq. (7.2). The vector of system inputs $\boldsymbol{u}$ describes the applied voltage-clamp protocol $V(t)$, see Section 7.3.2 for the parameterisation of the protocol.

Designing experiments with an averaged model

Each OED is optimal for the model used to perform the design. However, we may want to get a design that is optimal for a range of biological assumptions instead of focusing on one particular model, so that the same data can be used to study multiple similar models. We also consider using averaged model kinetics terms for x_j; instead of using only one model to optimise the experiment while the true data generating process could potentially be more similar to another model. Therefore, instead of using Eq. (7.11) from a single model, if we have $M_1, \dots M_{N_m}$ models, we use the output from

$$I_{\text{obs}} = \sum_{l=1}^{N_m} w^{M_l} I_{\text{obs}}^{M_l}, \tag{7.13}$$

to design the experiments, where w^{M_l} is the weighting term.

Here we use four models to represent an averaged model with a uniform weight $w^{M_l} = 1/4$ for each model: the Ten Tusscher et al. (2004) model, the Fink et al. (2008) model, the O'Hara et al. (2011) model, and the Paci et al. (2013) model. Next we consider averaging the cost functions for each model, instead of the cost function of the averaged model. And below, we take this idea a step further — we consider randomly generated models with current kinetics randomly sampled (with replacement) from the set of models to calculate the average cost function, which we termed the "bootstrapped kinetics models", instead of using the original models directly.

Designing experiments with bootstrapped kinetics models

Another approach to considering different model kinetics is to use samples for different *combinations* of the model kinetics, instead of using an 'averaged' model. That is we generate many samples of I_{obs} by randomly swapping in current kinetics x_j from different models M_l. The idea is to evaluate an optimal design measure for each of the samples, and optimise on the average of these measures.

Suppose we have N_m models and each model consists of N_j currents, we define a set of random integer variables $\{X_1, X_2, \dots, X_{N_j}\}$ where each element is a realisation, drawn from the set $\{1, 2, \dots, N_m\}$. Then each sample s of $I_{\text{obs},s}$ is constructed as

$$I_{\text{obs},s} = \sum_j g_j \cdot x_j(V, t \mid M_{X_j}). \tag{7.14}$$

In this way, we would not be limited to the fixed combinations of the current kinetics used in the original models M_l. Each sample s of $I_{\text{obs},s}$ is used to calculate an optimal design measure Φ_s, and we find the voltage-clamp protocol parameters for an optimal experimental design by minimising

$$\hat{\zeta} = \underset{\zeta}{\text{argmin}} \, \mathbb{E}_s \left(\Phi_s(\zeta) \right). \tag{7.15}$$

And we use the same set of models as for the averaged model.

The differences between this method and the one proposed in the above sections are that first, here we treat each current's x_j as an individual component from a model, and combinations of these currents give samples of $I_{\text{obs},s}$; we use a subset of all the (4^8) permutations, where we randomly sampled 100 of $I_{\text{obs},s}$. Second, we optimise the average of the optimal design measures instead of computing an optimal design measure using an averaged model.

7.3.2 Experiments to be optimised

We design the experiment by varying the system input $\boldsymbol{u}(\boldsymbol{\zeta})$, the voltage-clamp protocol V, and we choose it to be a piecewise function defined as

$$\boldsymbol{u}(\boldsymbol{\zeta}) = V(t) = \begin{cases} V_1, & 0 \leq t < T_1 \\ V_2, & T_1 \leq t < T_2 \\ \vdots & \vdots \\ V_N, & T_{N-1} \leq t < T_N. \end{cases} \tag{7.16}$$

Where the vector of parameters that defines the voltage-clamp protocol is

$$\boldsymbol{\zeta} = \{V_1, T_1, V_2, T_2, \ldots, V_N, T_N\} \tag{7.17}$$

for a N-step protocol; equivalently we can define $\Delta T_i = T_i - T_{i-1}$ with $T_0 = 0$, then we obtain

$$\boldsymbol{\zeta} = \{V_1, \Delta T_1, V_2, \Delta T_2, \ldots, V_N, \Delta T_N\}. \tag{7.18}$$

In order to ensure the resulting voltage-clamp protocol V is feasible to be run experimentally, we constrain the protocol to have $V_i \in [-120, 60]$ mV and $\Delta T_i \in [50, 2000]$ ms for all i, which defines the protocol parameter space. We choose N to be 20 in this chapter; a simple extension would be to try using different values of N.

In theory, the voltage-clamp protocol can be replaced with any arbitrary function, e.g. a sum of sinusoidal functions, as long as it can be parameterised with some vector of parameters $\boldsymbol{\zeta}$. However, the benefit of choosing this piecewise step function is that it can be directly applied in any patch-clamp system, including some of the high-throughput automated patch-clamp systems such as the SyncroPatch from Nanion Technologies used in the previous chapters of this thesis.

7.3.3 Optimisation of the protocols

To perform the optimisation of the voltage-clamp protocol as defined by Eq. (7.3), we optimise the design measures discussed in Section 7.2 by varying the protocol parameters $\boldsymbol{\zeta}$ in Eq. (7.18). The protocol was initialised with parameters $\boldsymbol{\zeta} = \boldsymbol{\zeta}_0$ randomly sampled uniformly within the defined boundaries (the protocol parameter space). Optimisations were performed using the Covariance Matrix Adaptation Evolution Strategy (CMA-ES) algorithm as described in Chapter 2. This was repeated 10 times with different initial protocol parameters, and the best result out of all repeats was used and presented in the next section.

To compute the Sobol indices, we define a hypercube for the model parameter space Θ, where each conductance value g_j in Eq. (7.12) can be scaled from $e^{-2} \approx 0.14$ to $e^2 \approx 7.39$ times its original value. We use the Saltelli et al. (2010) extension of a Sobol sequence to generate 100 parameter samples within this parameter space Θ for computing the Sobol indices. The score calculated with 100 samples versus 500 samples at the optimum of the A-criterion were 3.2 and 2.4, respectively, when the optimisation was initialised from a score of 3.3×10^4. Since we would like to find only a representative protocol based on these scores for comparison, we believe the uncertainty in the score

is acceptable, but we would increase the number of samples if using GSA-based scores for a final selected experimental design.

To numerically calculate the local sensitivity matrix $\mathbf{S}_{\mathrm{L}}$, we use the first-order central difference to approximate the local derivatives with a step-size of 0.1% of the parameter values. It may be worth noting that although LSA-based criteria require local derivatives, we are not truly interested in (local) infinitesimal changes when designing the protocols, hence a reasonable approximation of the derivatives is typically enough.

7.4 Results of the OED Methods

As discussed in the previous sections, we have seven design criteria (the LSA A-, D-, E*-designs, the GSA A-, D-, E*-designs, and the Shannon entropy design) and three types of model (the Paci et al. (2013) model, averaged model, and bootstrapped kinetics models), giving us in total 21 optimal designs. The resulting optimised protocols using different optimal designs are shown in Figure 7.1 with the corresponding I_{obs} simulated using the Paci et al. (2013) model . Each of the protocols appears to elicit rich and varied dynamics of the model current, as expected from the optimal designs which maximise the information for inference.

In this section, we explore different ways to evaluate the 'quality' of these optimised protocols. We evaluate the protocols by assessing some of the properties that we would like or expect them to have. First, we might expect a good 'all-round' protocol from this set (that is by definition optimal under a given design criterion) not to be the worst under another criterion, and on average to be good under all criteria. This comparison is somewhat theoretical, as it still relies on the design criteria that we defined. Second, taking a practical approach, we generate synthetic data under these optimised protocols, then ask: can we identify the parameters correctly using these synthetic data? And how does the error, if any, and uncertainty in the parameters vary between these optimised protocols?

As a benchmark, in addition to the comparison between the optimised protocols, we include two further voltage-clamp protocols: the one from Chapter 3 and one from Groenendaal et al. (2015). Both protocols were used for the same cell-specific conductance fitting as our optimised protocols in this chapter. The protocol from Groenendaal et al. (2015) in particular was designed, manually with expertise, to elicit the distinct kinetics of the different currents; whilst the one from Chapter 3 is a more conventional voltage-clamp protocol that is simpler and probably more familiar to electrophysiologists.

7.4.1 Cross-measure evaluations

In this subsection we evaluate the 21 optimised protocols by comparing their performance across all the design measures; a design measure is defined by the choice of the model and a design criterion. We define a cross-measure matrix M for each optimised protocol, such that each entry $M_{i,j}$ is the criterion j score for this protocol with currents generated by model i, with $1 < j < N_{\mathrm{measure}}$ and $1 < i < N_{\mathrm{model}}$. The models indexed by i are the Ten Tusscher et al. (2004) model, the Fink et al. (2008) model, the O'Hara et al. (2011) model, the Paci et al. (2013) model, the averaged model, and

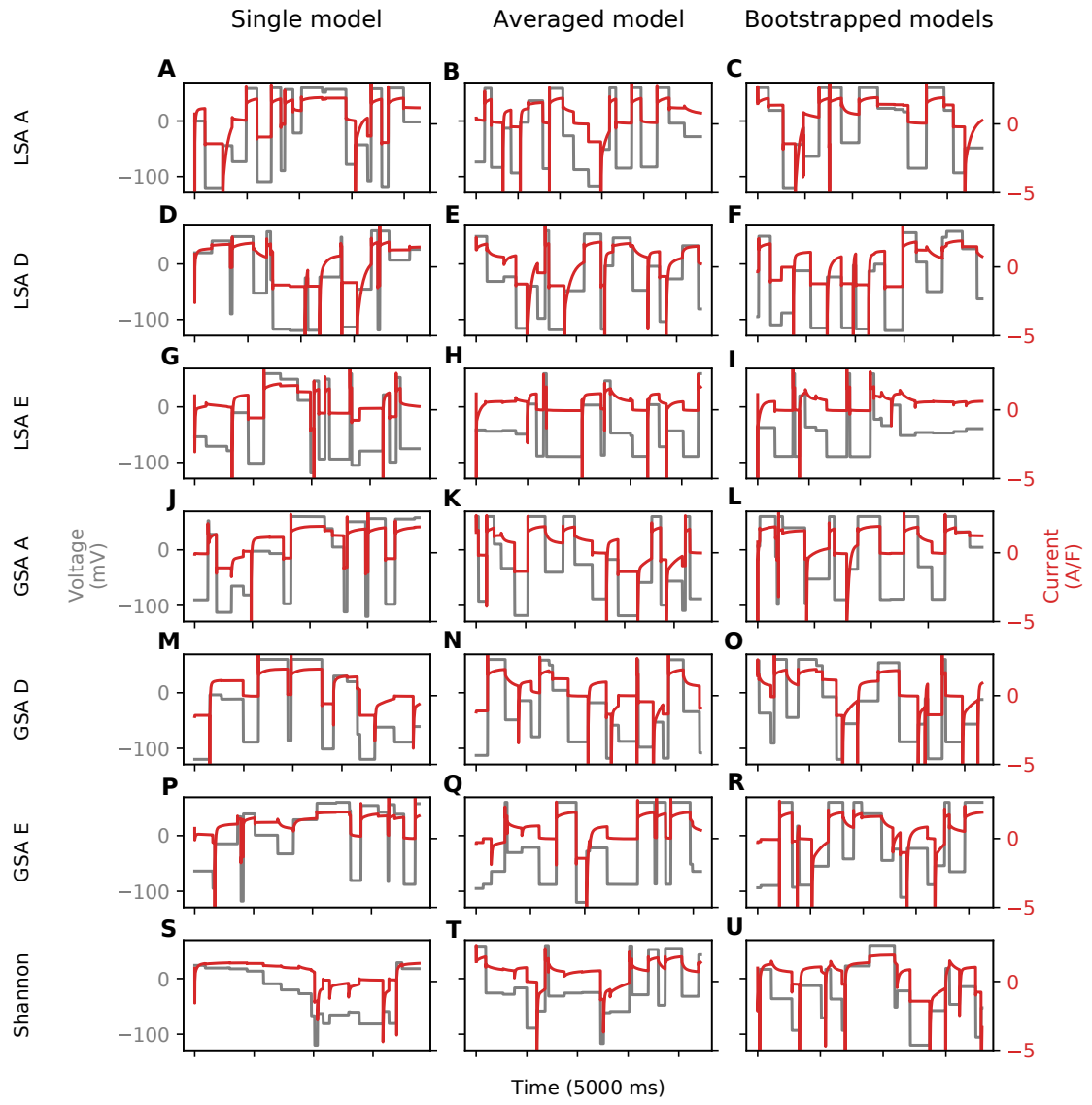

Figure 7.1: The optimised protocols (shown in grey, values on left axis) using different criteria and the corresponding I_{obs} (shown in red, values on right axis) simulated using the Paci et al. (2013) model. Rows are protocols optimised with different optimal design criteria: the LSA A-, D-, E*-designs, the GSA A-, D-, E*-designs, and the Shannon entropy design. Columns are protocols optimised based on different types of models: the single model, averaged model, and bootstrapped kinetics models.

the bootstrapped kinetics models; the last three were used to optimise the protocols, and the first three are now also included to assess how these optimised protocols perform for currents from different models. The criteria indexed by j were the LSA A-, D-, E*-designs, the GSA A-, D-, E*-designs, and the Shannon entropy design, respectively.

The numerical values for different cost functions are not directly comparable, so we normalise the values. Normalisation should be better than using a simple ranking as it should highlight outliers better. Outliers concern us here, because we expect the best protocols to be robust to the model (possible current kinetics in reality) and to perform well under all measures. Ideally we would like to have a protocol that is good under all criteria and all possible models of kinetics. The normalisation

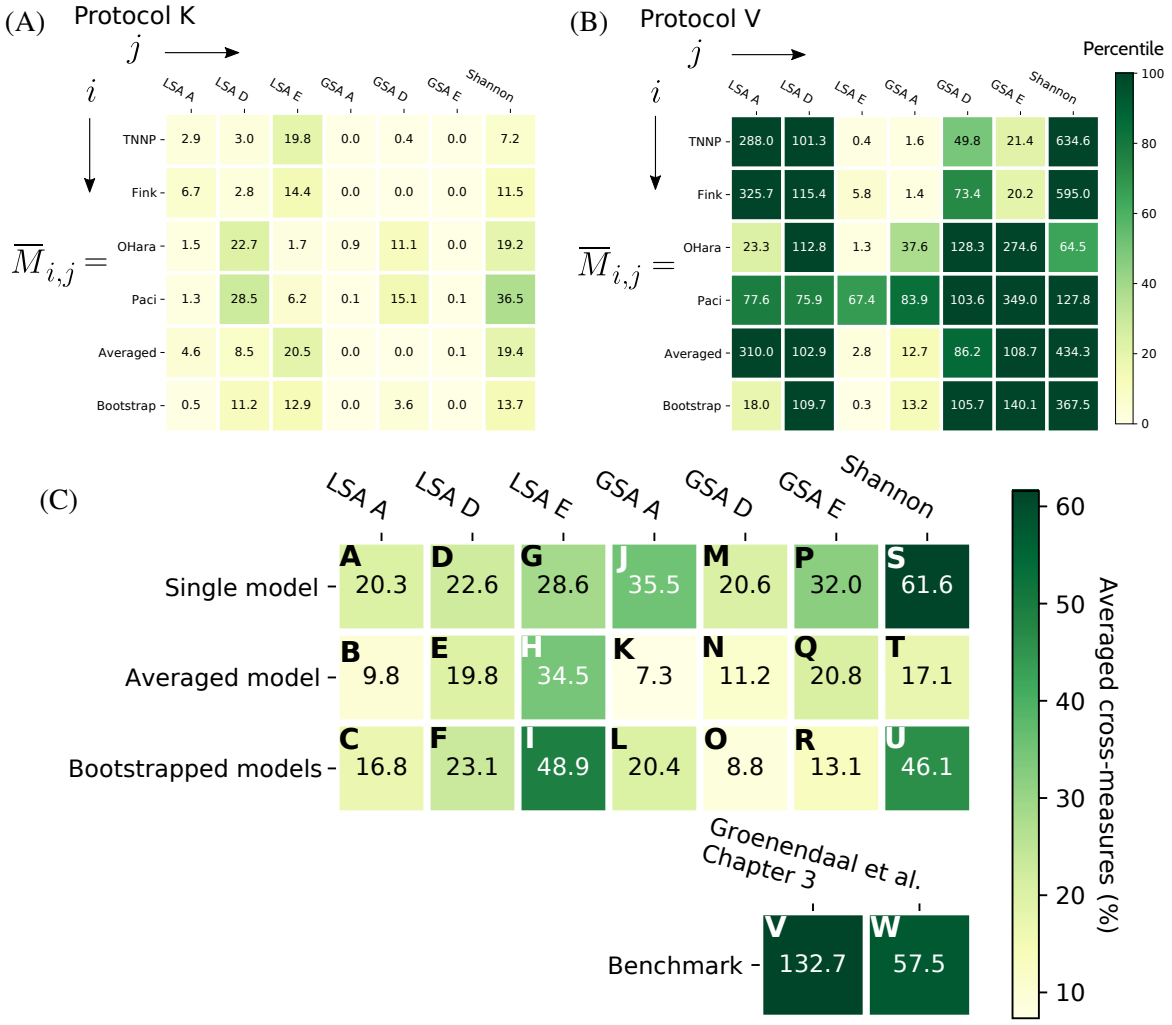

Figure 7.2: Cross-measure evaluations for the optimised protocols, compared against the benchmark protocols. **(A)** The normalised cross-measure matrix $\overline{M}$ for the best protocol, Protocol K, optimised using the GSA A-criterion and the averaged model. **(B)** The matrix for the worst protocol, Protocol V, adapted from Chapter 3. **(C)** The mean of the normalised cross-measure evaluations for all of the optimised protocols, as well as the benchmark protocols.

for each entry is calculated using $\overline{M}_{i,j} = (M_{i,j} - a_{i,j}) / (b_{i,j} - a_{i,j}) \times 100\%$, where $a_{i,j}$ and $b_{i,j}$ are the minimum (best) and maximum (worst) scores seen across all the Protocols A–U[3] at the entry i, j (i.e. with this criterion and current model).

Two examples of $\overline{M}_{i,j}$ are shown in Figure 7.2A and B. Figure 7.2A shows our best protocol design, the OED for averaged model under GSA A-criterion (Protocol K), which performs well under all measures and model currents. The worst protocol, the benchmark protocol adapted from Chapter 3 (Protocol V) shown in Figure 7.2B, performs badly for most of the design measures, which may be expected as it is not designed using any of these measures. 'Best' and 'worst' protocols in this subsection were decided based simply on the mean of all entries in $\overline{M}$. This averaged score for each optimised protocol k, together with the benchmark protocols, is shown in Figure 7.2C. The

[3]Note the normalisation (percentile) was calculated with only the optimised protocols, i.e. without the benchmark protocols, for clarity. Therefore the percentiles shown in Figure 7.2B are not necessary to be within 100%.

Groenendaal et al. (2015) protocol beats one of our Shannon designs which is impressive given its manual design.

Figure 7.2C shows that the protocols based on multiple models (middle and bottom rows) are consistently better than those based on only the Paci et al. (2013) model (top row), apart from the LSA E criterion. This may be expected as the protocols based on only one model may perform relatively badly under other models. We also noticed that the protocols based on the LSA E criterion are worse than the other LSA criteria. Finally, the protocols based on the GSA criteria are better than (or similar to) their LSA counterparts, apart from the A-design using the Paci et al. (2013) model.

We consider these cross-measure evaluations are theoretical as they rely on the design criteria that we defined. Next, we move on to assessing the optimised protocols through a practical evaluation.

7.4.2 Practical evaluations

In this subsection we evaluate the optimised protocols from a practical point of view. Similarly to the approach taken in the previous chapters, we generate synthetic data under these protocols with synthetic noise, and we ask whether we can identify the parameters in Eq. (7.12) correctly if we know the ground truth model.

We start by generating synthetic data using the Paci et al. (2013) model. The same type of synthetic noise as in Chapter 3 is used $\sim \mathcal{N}(0, \sigma^2)$ with $\sigma = 0.15$ A/F. Then the same model is used to fit the synthetic data, to test the ideal case where we know the ground truth kinetics. Similarly to Chapter 3, we reparameterise the models with a scaling factor s_j for the maximum conductance g_j, where $s_j = 1$ is the original literature value. The posterior distribution of the parameters are defined in the same way as described in Section 2.6 in Chapter 2. Uniform priors are used $\mathcal{U}(0.04, 25)$ for the scaling of the conductance values, which is wider than the subspace we used for computing the GSA to test its robustness for parameters outside the design parameter space.

The posterior distributions of the parameters were estimated using a Monte-Carlo based sampling scheme — a population MCMC (Jasra et al., 2007) algorithm with adaptive Metropolis (see Chapter 2) as the base sampler. We ran three chains for the population MCMC, each with 4×10^4 samples, and discarded the first 10^4 samples as warm-up period. The final chains had $\widehat{R} < 1.1$ for all parameters, implying the chains were converged (see e.g. Gelman et al., 2013). The resulting posterior estimation (using all three chains) is shown and analysed in Figure 7.3.

For models without discrepancy in ion current kinetics, the two most successful optimal designs were the LSA A-design for the single model (Protocol A) and the averaged model (Protocol B), in terms of reducing the uncertainty in the inferred parameters, as shown in Figure 7.3A; whilst the benchmark protocols resulted in considerably wider posterior distributions than most of the optimised protocols. Each chain returned a posterior distribution over the parameters, since all chains converge and they are all very similar to each other, we use all three chains to compute the marginal parameter distributions (per parameter). The mean (over all the parameters) standard deviation of these distributions is shown in Figure 7.3B for all of the protocols. Often the number of data samples (or data points) in the i.i.d. Gaussian likelihood that we use is a major factor determining the width

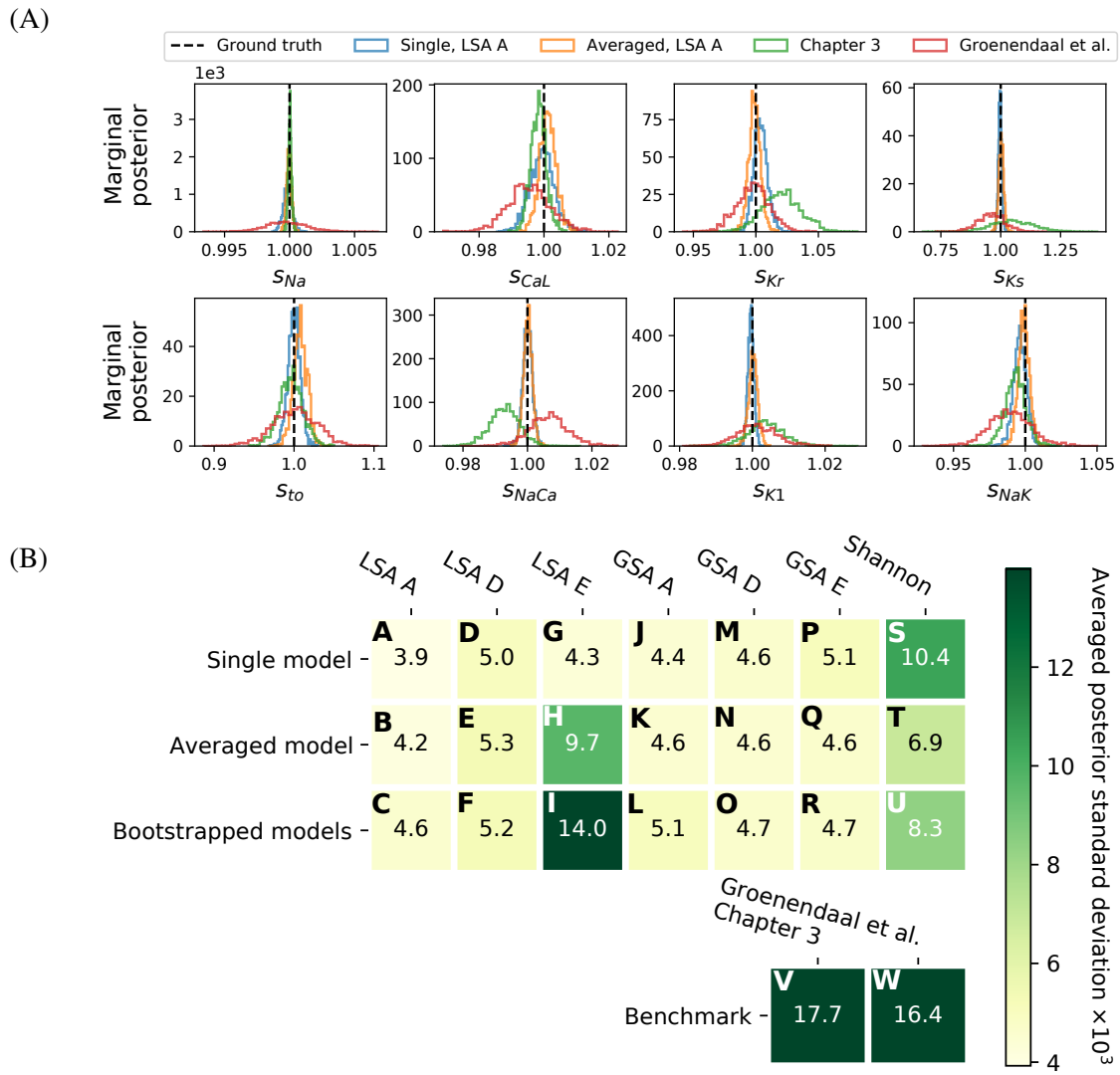

Figure 7.3: The posterior distribution of the parameters for the synthetic study, generated with the Paci et al. (2013) model and fitted with the same model. **(A)** The marginal posterior for the best two protocols: LSA A-design for the single model (Protocol A) and the averaged model (Protocol B), and for the worst two protocols: the two benchmark protocols (Protocols V and W), according to the mean standard deviation of the marginal posterior. **(B)** The mean standard deviation of the marginal posterior for all of the optimised protocols, as well as the benchmark protocols.

of the posterior. Here even for the protocol from Chapter 3 (Protocol V) which is much longer in duration (hence more data samples) than any of the optimised protocols, the width of its posterior is still bigger than other protocols. This shows that the OED methods were successful in bringing down the parameter uncertainty.

Interestingly, even though the protocol by Groenendaal et al. (2015) (Protocol W) was designed specifically to tease out different dynamics of the ionic currents, the width of the posterior is similar to that of the protocol from Chapter 3. Also, although the optimised protocols from the Shannon entropy measure are better than the benchmark ones, they are consistently worse than the other optimised protocols. This could be due to the choice of the weighting vector w, as discussed by Schenkendorf et al. (2018). However, we will not investigate further, because this involves tuning

hyperparameters (optimising the optimal design), also the other designs have achieved the same objective.

7.5 Influence of Discrepancy in Model Kinetics

In the above section, OED showed improvements in reducing the parameter uncertainty when the 'correct' model was used (the same as the model generating the synthetic data). However, in reality, we expect discrepancy between our models of ion channel kinetics and the true kinetics, as discussed in Chapter 3. In this section, we test the effects of the common assumption that the kinetics are represented well enough to fit conductances to whole-cell measurements. We ask, how would discrepancy in the ion current model affect estimates of the maximum conductances (Eq. (7.12)) in an action potential model? How wrong can the current model be before we fail to identify the current contributions to whole-cell electrophysiology? We also ask whether using channel-specific blockers and performing current subtraction help? The subtraction approach is widely used and thought to isolate each current's contribution, but does it allow us to fit 'correct' current contributions when there is discrepancy present?

7.5.1 Issues with discrepant kinetics models

To test what would happen to the inferred current contribution using discrepant kinetics models, we generated synthetic data with the Fink et al. (2008) model to represent the ground truth (in the same way as described in Section 7.4.2) and fitted the Paci et al. (2013) model (to that synthetic data) to represent a proposed mathematical model we might fit. There are many variants of cardiac action potential models in the literature, as discussed in Chapter 2, and they vary hugely, see for example Beattie et al. (2018) for a comparison between the existing I_{Kr} models. Each of these models attempted to describe the very same physiological system, and there is no obvious reason that a particular model is closer to reality than it is to other models. We then use the difference between literature models to mimic the difference between model and reality, to illustrate the community's uncertainty in the kinetics of the ionic currents. Therefore the use of different models to represent the size of the discrepancy between reality and models is not unrealistic.

We repeated the fitting of discrepant kinetics models with all the 21 (in Figure 7.1) plus two benchmark protocols, and compared their performance. Due to the model discrepancy in the kinetics, directly comparing the maximum conductance values may overstate the error. For example, if the current kinetics in the fitted (potentially discrepant) model result in an open probability twice as large as the true process that generated the data, then we would expect to infer a maximum conductance value that was only half that used to generate the data, but the current could still be very close to the truth. Therefore, instead, the goodness of fit was ranked using the mean of the root-mean-square error (RMSE) for each individual current under the action potential clamp (black lines) shown in the top panels of the following figures.

Figure 7.4A shows the maximum a posteriori (MAP) estimate for one of the optimised protocols (Protocol H). Synthetic data were generated with the Fink et al. (2008) model and shown in grey.

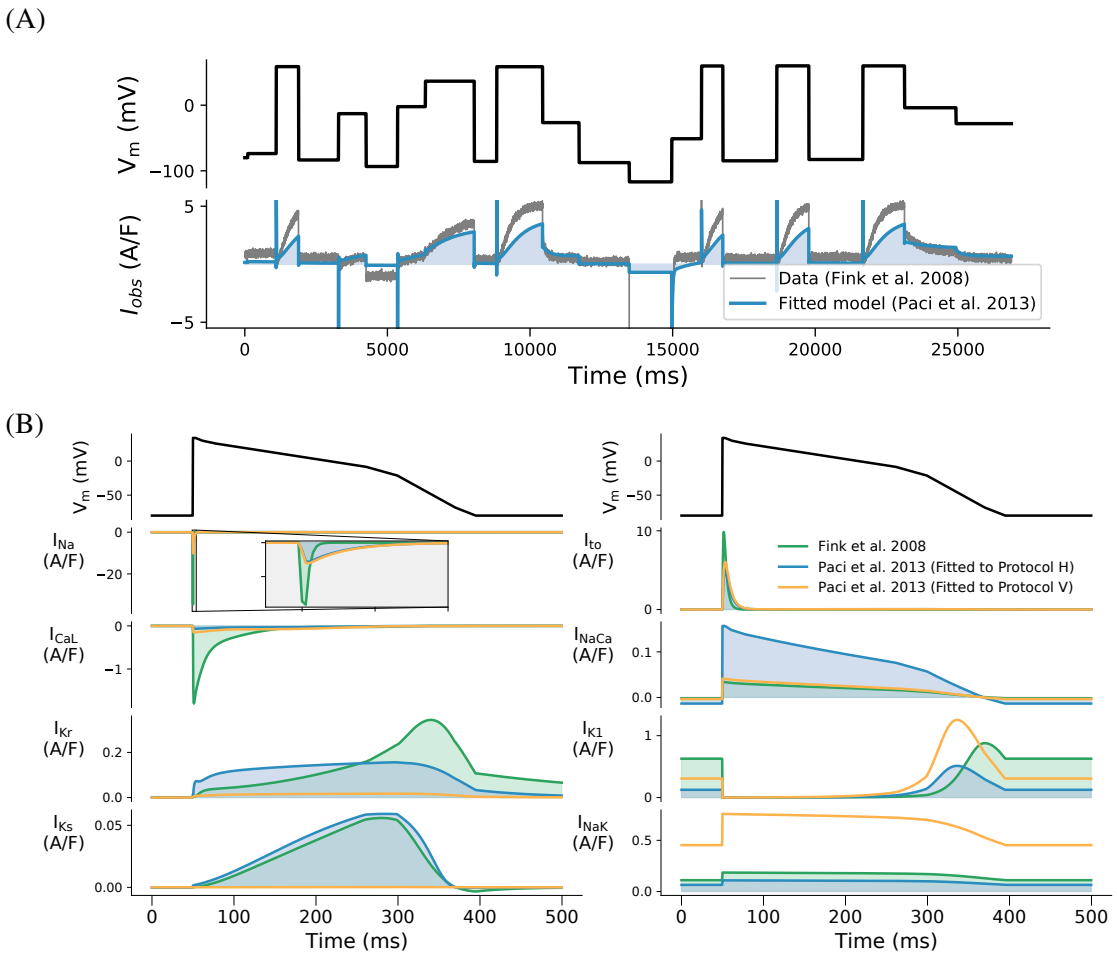

Figure 7.4: Model fitting and prediction results for a discrepant model. **(A)** The Paci et al. (2013) model (blue) fitted to the synthetic data (generated from the Fink et al. (2008) model, grey) using Protocol H (the protocol is shown in the top panel). **(B)** The model simulation for each current under an action potential clamp (top panels, black lines) for the ground truth model and the fitted models using two different protocols. The true model is shown in green. The fitted model using Protocol H plotted in blue, gave the lowest averaged RMSE for each individual current shown here; the fitted model using Chapter 3's Protocol V shown in orange for comparison, which is better in some situations (e.g. I_{NaCa}) but worse in others (I_{Kr}, I_{Ks}, and I_{NaK}).

The fitted Paci et al. (2013) model (blue) does not give a perfect match to the data due to model discrepancy. However, the agreement between the calibrated model output and the synthetic data would often be considered acceptable if these were real experimental data, see for example Chapter 3 and Groenendaal et al. (2015). Therefore, it may be tempting to conclude that this model is calibrated well, and that the model discrepancy is not critical. But the prediction results of the MAP estimate for the best RMSE (Protocol H, blue) and the worst (Chapter 3, orange) for an action potential clamp are shown in Figure 7.4B. Even for the protocol with the best RMSE, the fit (blue) was far from ideal. Some major currents such as I_{Na} and I_{CaL} are not able to match the ground truth at all, and would make very bad predictions in certain situations, e.g. drug block of these currents. These results raise serious concerns about discrepancy in current kinetics when fitting maximum conductance values to experimental data.

7.5.2 Fitting with slightly discrepant kinetics

One of the most obvious solutions to the issue posed in the previous subsection is to get the kinetics 'right', at least to such a degree that the maximum conductance values can be identified acceptably. This is in fact the approach that we have been working towards in the previous three chapters for the hERG channel.

In Chapter 5, Figure 5.12 showed that the difference between predictions from our 37 °C hERG model and the I_{Kr} Markov model by Fink et al. (2008) is similar in magnitude to the difference between our model's predictions and the experimental data. In this subsection, we use the differences between the I_{Kr} model from Fink et al. (2008) and our 37 °C hERG model from Chapter 5 as a guide for the extent of the discrepancy we might encounter in practice; the RMSE between the two models under the action potential clamp was $\sim 0.22\,\text{A/F}$. To generate a model with slightly discrepant kinetics, we randomly perturbed the *kinetic* parameters of the Fink et al. (2008) model for each current; each original kinetic parameter was multiplied by $(1+\delta)$, where δ is a random variable that follows $\mathcal{N}\left(0, \sigma_\delta^2\right)$. The standard deviation σ_δ was chosen such that the RMSE between the current from the original model and the perturbed model is about $0.22\,\text{A/F}$. Here we consider the original Fink et al. (2008) model as the ground truth (to generate synthetic data), and the slightly perturbed model as a proposed mathematical model (for fitting).

We repeated the fitting of the slightly discrepant kinetics models with all the 21 (in Figure 7.1) plus two benchmark protocols, and compared their performance. The goodness of fit was again ranked using the mean of the RMSE for each individual current under the action potential clamp (black lines) shown in top panels of Figure 7.5. The results of the MAP estimate for the best RMSE (Protocol E, blue) and the worst (Chapter 3's Protocol V, orange) are shown in Figure 7.5. For Protocol E, the fit (blue) was able to infer all current contributions quite well, and much better than those shown in Figure 7.4B; none of the currents have more than 29% (mean ± standard deviation: 18 ± 8%) RMSE percentage error in the action potential clamp predictions. For Protocol V from Chapter 3 (orange), although most of the currents were inferred correctly, it still missed (when comparing the area under the curve, the amount of charge carried by the current) I_{Kr} by almost a factor of two, as well as the two small currents I_{NaCa} and I_{NaK}.

Comparing Figure 7.4B to Figure 7.5 shows that the level of discrepancy in the kinetics can appreciably affect the fitting of the maximum conductance values. Such maximum conductance values fitting methods have started being widely-used in the cellular cardiac electrophysiology community (Whittaker et al., 2020). But to use these methods safely we need low discrepancy in kinetics. Applying the approach developed in the previous three chapters to develop accurate models of as many individual ion channel kinetics as possible is one way to reduce discrepancy, so that we can be confident with the accuracy of the kinetics models. The aim would be to improve the accuracy of kinetics models so that our individual current contributions could be fitted as well as Figure 7.5 rather than Figure 7.4B.

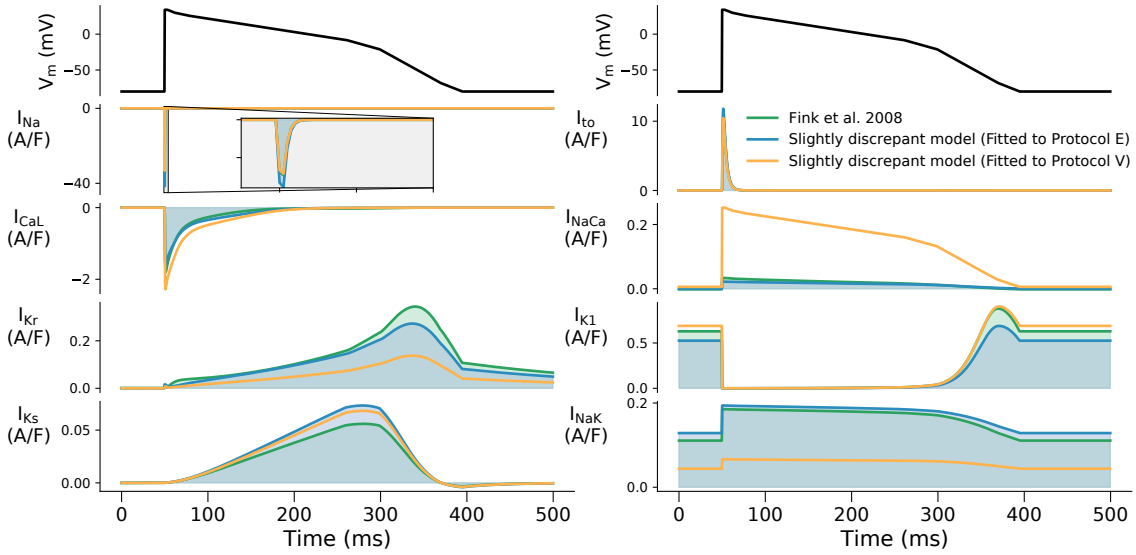

Figure 7.5: The model simulation for each current under an action potential clamp (top panels, black lines) for the ground truth model (Fink et al., 2008) and the two fitting results using a slightly discrepant kinetics model. In the slightly discrepant model, each current's kinetics were perturbed to give an RMSE of about 0.22 A/F between the slightly discrepant model and the ground truth model. The true model is shown in green. The model fitted using Protocol E plotted in blue, gave the lowest averaged RMSE for each individual current trace shown here; the model fitted using Chapter 3's Protocol V is shown in orange for comparison.

7.5.3 Sequential dissection using current-specific blockers

As an alternative to getting kinetics models that are good enough to fit simultaneously to a single current trace, a temporary solution that one might think of is to use selective ion channel blocking molecules. By applying a channel-specific blocker one can almost completely shutdown a given type of current I_x. If we then remeasure the leftover current, the difference between the two recordings should be mainly the blocked current I_x. We can then fit the conductance of the blocked current directly to this subtracted current, and the rest of the conductances using the leftover current. This procedure can be repeated with various current-specific blockers to to get isolated currents from a single cell. This approach was used by Banyasz et al. (2011) who used a total of four blockers in the study and termed it a "sequential dissection" experiment.

In this subsection, we simulate such a sequential block experiment, whilst assuming the original model discrepancy issue from Section 7.5.1. Without considering the experimental feasibility, we assume that we could apply eight[4] current-specific blockers and perfectly isolate all current types. Figure 7.6 shows the simulations and the predictions of (panel A) the calibration protocol (Protocol B) and (panel B) an action potential clamp using the fits to isolated currents (dashed purple), compared against the fitting without applying specific blockers (blue). Some of the currents show an improved fit and prediction, for example I_{NaCa} and I_{NaK}, but some are even worse, such as I_{Ks}.

The cause of a poor prediction even with isolated currents from specific blockers is twofold. Firstly, some of the kinetics simply do not match well through a simple scaling, see for example I_{Kr} in

[4]The eighth blocker is needed to make sure we isolate the last current from some other small currents and leak current.

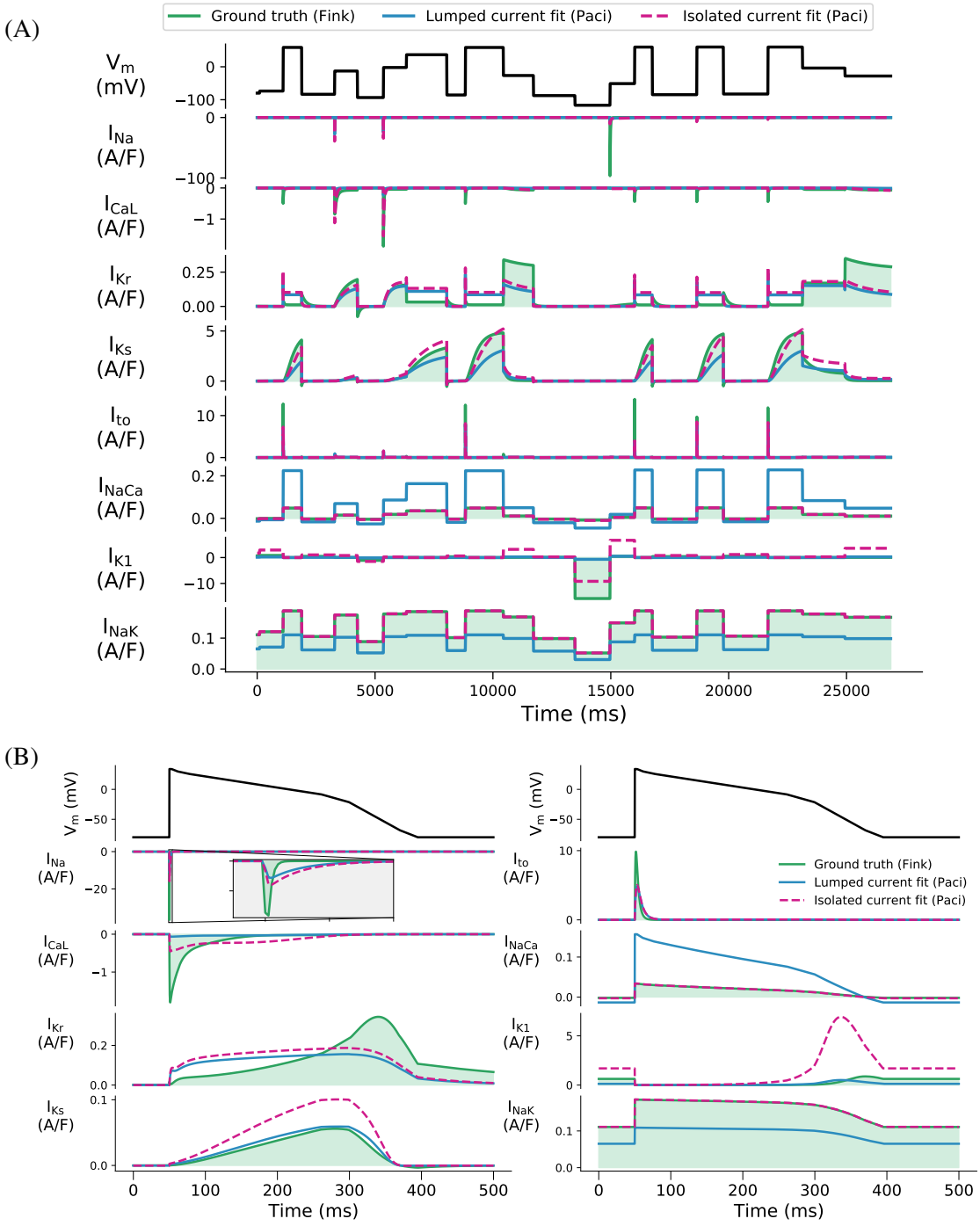

Figure 7.6: A comparison between the fits to isolated currents (dashed purple) and the results in Figure 7.4B (blue) using the Paci et al. (2013) model and synthetic data generated with the Fink et al. (2008) model (green). **(A)** Model simulation of each current under calibration Protocol B. By definition here, each isolated current is scaled to give a least-squares fit to the synthetic data. **(B)** Model prediction for each current under an action potential clamp (top panels, black lines).

Figure 7.6. Secondly, even if the kinetics match during the calibration, the prediction can still be incorrect when the current undergoes different dynamics in a new situation, as demonstrated by I_{Ks} in Figure 7.6. The top panel (A) shows the fitted traces of I_{Ks} under Protocol B, and that the fitting

with isolated current (dashed purple) is better than the one without (blue). However, in the action potential clamp prediction in the panel below (B), the isolated current (dashed purple) was inferior. To understand this second issue, imagine we try to fit a straight line (e.g. $y = x + 1$) to an exponential curve ($y = e^x$) around zero ($x \approx 0$) by scaling the straight line, we can find a best fit for it around zero (in this case the scaling is simply unity) but the prediction for any value far away from zero would still be wrong. Even if we try to repeat this example with a different region of data (say x around 10), the resulting fit will still give an incorrect prediction for values outside the calibration data.

This subsection has demonstrated that even if we had a perfect specific blocker for each current, simply fitting conductance values will not work with the level of discrepancy shown in Figure 7.4. We showed this issue by fitting one literature model to another, one may suspect it was because we compared an hiPSC-CM model to an adult cardiomyocyte model, but the differences between literature models of the same cell type can easily be larger than we have used in this section (see for example Beattie et al., 2018; Lei et al., 2020c). It is therefore particularly important to first get a 'good enough' kinetics model before fitting conductances using the approach shown in this chapter.

7.6 Effects of Ignoring Experimental Artefacts

Finally, we examine the effect of ignoring experimental artefacts during conductance inference, by generating synthetic data with the full voltage-clamp experiment model in Chapter 6 whilst assuming an ideal voltage-clamp when fitting to data (as in previous sections and most, if not all, literature examples). We use Eqs. (6.24)–(6.32) to simulate voltage-clamp experiments, where I_{ion} in this case is the lumped currents in the Paci et al. (2013) model. When generating the synthetic data, we perform the typical compensations as in real patch-clamp experiments, including voltage-offset correction, membrane (slow) and pipette (fast) capacitance compensations, supercharging, and series resistance compensation (see Chapter 6). In the synthetic data, we also perform a leak correction using Eqs. (6.33) and (6.34), and filter the capacitance spikes by removing the first 2 ms after each voltage step, to emulate the post-processing for real experiments.

Similar to the previous chapter (see also the notation), we randomly generate artefacts using the following distributions

$$V_{\text{off}}^{\dagger} \sim \mathcal{N}(0, 1.5) \ \text{(mV)}, \tag{7.19}$$

$$R_{\text{s}} \sim \ln \mathcal{N}(12.5, 2) \ \text{(M}\Omega\text{)}, \tag{7.20}$$

$$C_{\text{m}} \sim \ln \mathcal{N}(98.7, 5) \ \text{(pF)}, \tag{7.21}$$

$$C_{\text{p}} \sim \ln \mathcal{N}(4, 1) \ \text{(pF)}, \tag{7.22}$$

$$g_{\text{leak}} \sim \mathcal{N}(1, 0.1) \ \text{(nS)}. \tag{7.23}$$

E_{leak} was set to be -80 mV. We assume that the measurements are performed on an automated patch-clamp system for hiPSC-CMs; the values are taken from the measurements in Chapter 4 and Chapter 6, and C_{m} was taken from Paci et al. (2013). We also assume 80% series resistance compensation, and that the amplifier estimations have normally distributed errors with a standard

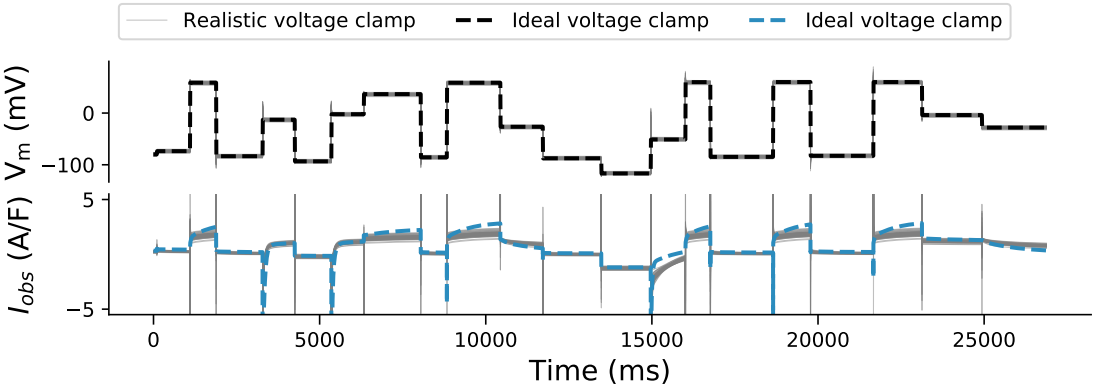

Figure 7.7: Simulations of the membrane voltage and observed current under Protocol B, using 50 samples of artefact parameters of a realistic voltage-clamp model (shown in grey). The cardiomyocyte model is the Paci et al. (2013) model, and its simulation using the ideal voltage clamp assumption is shown in dashed lines.

deviation of 5%, i.e. after a realisation of R_s we sample R_s^* from $\mathcal{N}(R_s, 0.05 \times R_s)$; similarly for the other compensations and machine estimated values (i.e. those denoted with '*' in the equations).

Figure 7.7 shows 50 realisations of the realistic voltage-clamp synthetic measurements using the above distributions, under Protocol B (averaged model LSA A-design). The membrane voltage in the realistic voltage-clamp model (grey) deviates from the ideal membrane voltage or the command voltage (dashed black line) due to the imperfect compensations described in Chapter 6. Similarly, the observed current in the realistic voltage-clamp model (grey) is 'contaminated' and differs from the Paci et al. (2013) model simulated with the ideal voltage clamp assumption.

To investigate the effect of ignoring experimental artefacts during the parameter inference, we generate 500 samples of artefact parameters (using the above distributions) under Protocol B. We then fit the same cardiomyocyte model, the Paci et al. (2013) model (simulated with an ideal voltage-clamp experiment) to each synthetic whole-cell current trace. Figure 7.8A shows an example of the fitted trace (dashed purple) compared to the model trace generated with the realistic voltage-clamp (green). The fitted trace shown is the result of one of the 500 inferred parameters, and it is chosen with the parameters that are closest to the mean of the 500 inferred parameters (blue histograms in Figure 7.8B).

Figure 7.8B shows the histograms of the inferred parameters for the 500 full voltage-clamp experiments. The resulting parameters inferred in the presence of experimental artefacts generated with the above distributions are shown in blue. First of all, compared to *uncertainty in the parameters* where the same protocol and cardiomyocyte model were used (Figure 7.3), the possible *error in the parameters* due to experimental artefacts is much larger. Furthermore, not only a random error (the width of the histograms in Figure 7.8B) but also a systematic error (a shift of the whole histograms) is introduced to some of the inferred parameters as the histograms move away from the ground truth (dashed lines). For example, the inferred conductance values for I_{Na} are consistently smaller than the true value, because the effect of series resistance can shift the current-voltage (I-V) relationships of the measured I_{Na} (Marty and Neher, 1995; Sherman et al., 1999; Montnach et al., 2020). Also, the

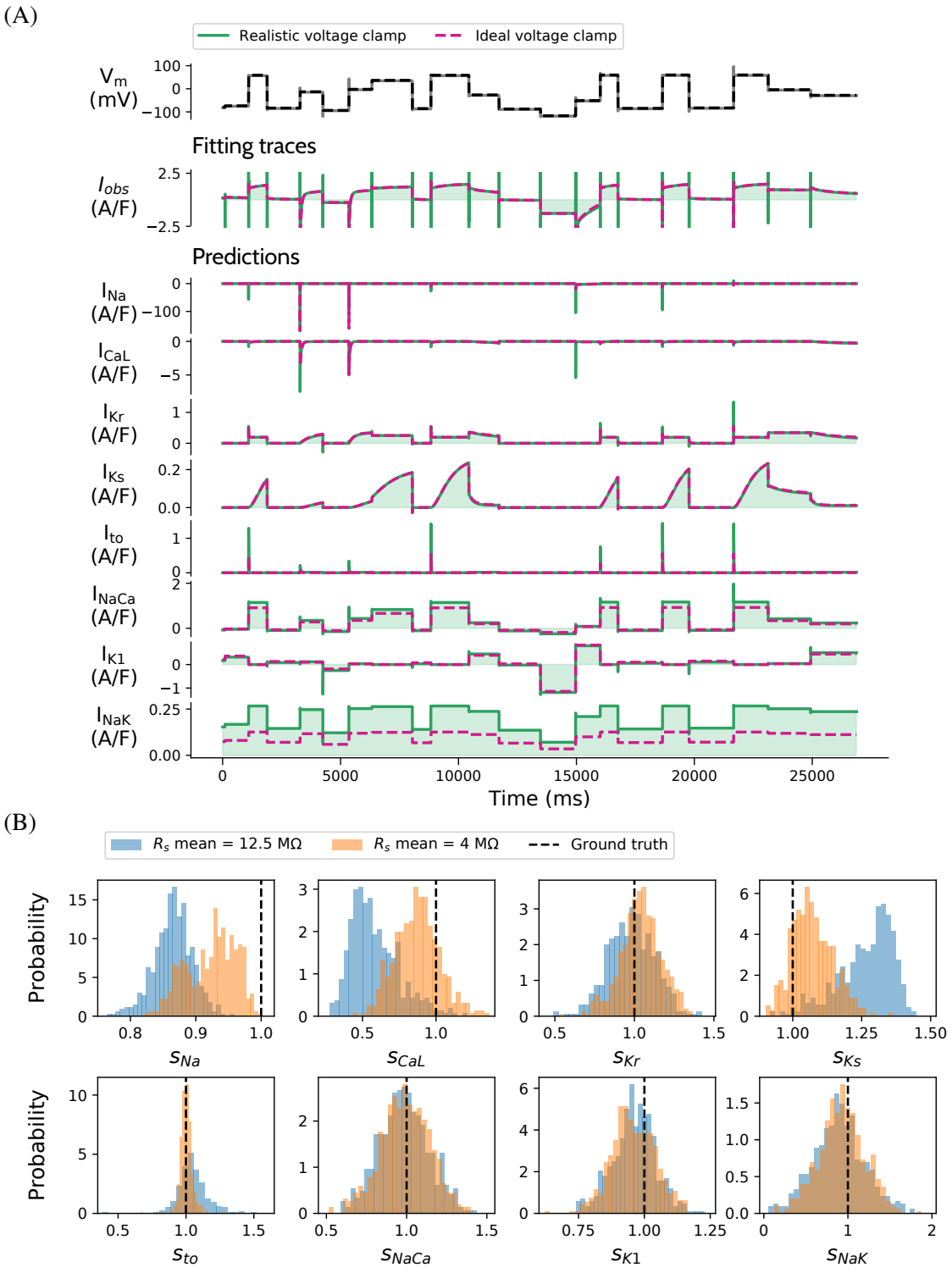

Figure 7.8: Fitting results of the Paci et al. (2013) model when ignoring experimental artefacts generated using a realistic voltage-clamp model developed in Chapter 6. The fits was performed using the averaged model LSA A-design. **(A)** Shows an example of fitted trace (dashed purple) and the realistic voltage-clamp model (green) with 12.5 MΩ mean series resistance. The parameters of this example are chosen as the closest to the mean of the blue histograms in the bottom panel. **(B)** Histograms of 500 inferred parameters. The inferred parameter affected by the experimental artefacts with 12.5 MΩ mean series resistance is shown in blue (approximating automated patch); while the mean series resistance of 4 MΩ is shown in orange (approximating manual patch). Both are plotted with transparency to show the overlap.

conductance of I_{CaL} is almost halved whilst I_{Ks} is consistently larger, potentially because they are 'compensating' each other. The scaling of I_{NaK} permeability ranges from zero to almost two. Such an unidentifiability issue can be due to the effect of imperfect leak compensation, as the dynamics of I_{NaK} and the leftover I_{leak} are very similar (when the ionic concentration is clamped), hence I_{NaK} 'mops up' the leftover I_{leak} in the data.

The parameters listed above were taken from an automated patch-clamp system, but most of the parameters are similar to many of the manual patch experiments except the series resistance. Although automated systems have a much higher throughput compared to manual patch-clamp systems, they tend to have a higher series resistance. The series resistance for automated systems is about 12.5 MΩ in Chapter 4; whilst some high quality manual measurements present series resistance less than 5 MΩ (e.g. Ma et al., 2011). To compare the effect of the series resistance, we also generate another set of synthetic data with $R_{\text{s}} \sim \ln \mathcal{N}(4, 1)$ MΩ to represent a manual patch-clamp experiment, the results are shown in orange in Figure 7.8B. Similar to the mean $R_{\text{s}} = 12.5$ MΩ (blue) case, the inferred parameters are affected by both random and systematic errors, but to a lesser extent. For example, the inferred conductance values of I_{Na} are now closer to the ground truth (dashed line). The inferred conductance values for both I_{CaL} and I_{Ks} cover the true values. The inferred I_{NaK} permeability is not affected by reducing R_{s}, reflecting the random error is not due to the series resistance.

The results shown above have opened the question of whether we should always take these experimental artefacts into account, such as having the voltage-clamp model as part of the data generating process during inference, as we did in Chapter 6. An alternative would be to average the data before performing model inference. However, such an approach may reduce only the random error induced by the artefacts, i.e. reducing the width of the histograms in Figure 7.8B, and it does not alleviate the systematic error, hence the bias remains in the inferred parameters.

7.7 Discussion and Conclusions

This chapter combines lessons that we have learned from the previous chapters. We have first applied optimal experimental design (OED) to various action potential models to design voltage-clamp protocols for fitting maximum conductances while assuming kinetics are known. This is, to our knowledge, the first time such an approach has been taken in cardiac cellular electrophysiology. The optimised protocols successfully reduced the uncertainty in the inferred parameters, compared to the conventional protocol that we used in Chapter 3. We then consider problems that are likely to occur in the real-world. Firstly we expect discrepancy in our models of ion channel kinetics. We showed that with the level of discrepancy similar to the differences between models in the literature, none of the protocols were able to infer the maximum conductance values accurately. This issue can be rectified by a 'good' kinetics model. However applying channel-specific blockers and performing current subtraction will not completely fix the issue of discrepancy in current kinetics. Finally, artefacts in experimental measurements such as those shown in Chapter 6 will also introduce both random and systematic errors into the inferred conductance values.

We explored various designs adapted from the OED literature. Most of them were able to improve the uncertainty in the inferred parameters compared to the benchmark protocols. We tried to seek for the best protocol amongst the OED generated protocols. However, we were not able to identify the best one, as each of them perform slightly differently under different situations. For example Protocol K was the best in the cross-measures comparison, Protocols A and B were better in reducing parameter uncertainty, but Protocol H was slightly more robust against discrepancy that we tested. We found that the protocols based on averaged model were consistently (slightly) better than the others, which may be a better model for designing voltage-clamp protocols.

Next, we considered issues that we may encounter when applying the 'perfect kinetics' assumption to real data; we questioned how discrepant a model of current kinetics can be before whole-cell conductance fitting fails. This assumption has been commonly used as fitting conductances to whole-cell (mostly voltage-clamp and/or action potential, sometimes also calcium transient) recordings while using ion channel kinetics models taken or slightly adapted from the literature has recently become popular (Whittaker et al., 2020). For example, Groenendaal et al. (2015) have proposed to use (cell-specific) voltage-clamp and current-clamp data to fit the maximum conductances of several currents in an action potential model. Similarly, various inference approaches have been developed or adapted, including genetic algorithms (Groenendaal et al., 2015), multivariate regression (Sarkar and Sobie, 2010), MCMC (Johnstone et al., 2016b), history matching (Coveney and Clayton, 2018), "population of models" (Britton et al., 2013; Muszkiewicz et al., 2016), and moment-matching (Tixier et al., 2017), but all of them assumed "out of the box" or slightly modified kinetics models when fitting maximum conductances.

We assessed the susceptibility to kinetics discrepancy when fitting conductances to only whole-cell voltage-clamp experiments; we concluded that the approach (or assumption) is indeed susceptible to kinetics discrepancy. However this issue is not only applied to voltage-clamp experiments but also action potential recordings (such as current-clamp or optical mapping for membrane voltage). In Lei et al. (2020c), a publication that I led, we demonstrated that fitting conductances to action potential recordings with discrepant kinetics models can lead to spurious results and predictions, very similar to what we showed in Section 7.5.1. Therefore fitting conductances can suffer from discrepancy in the current kinetics regardless of using voltage-clamp or action potential data.

The results shown Section 7.6 and Section 7.5 are, perhaps, 'best case scenarios'. In reality, we expect model discrepancy and experimental artefacts to be a joint-problem. That is, we might not be able to isolate these two issues easily, and hence the errors that we observed in these two sections are potentially only part of the error to be induced in reality. We believe once methods for solving model discrepancy and experimental artefacts become more mature, we would need to consider and solve them together.

As we described earlier in the chapter, we believe there are two possible routes to continue from the work presented in the previous chapters. One route would be to apply an approach similar to Chapters 4–6 for as many current types as possible, such that we could construct a cell-specific model from the channel-level (kinetics) to cell-level (conductance). Another route would be to design protocols for fitting conductances while assuming the kinetics of each current to be known. This

chapter assessed the feasibility of the second route. We showed that the second route is possible only for the perfect kinetics case and for the slightly discrepant kinetics case. The perfect kinetics case is most probably impossible when applied to real data. To achieve the slightly discrepant kinetics case, we believe approaches such as those developed in Chapter 4 will help. Therefore, we can take the second route only if we have confidence that the kinetics models are as accurate as those shown in Section 7.5.2.

We anticipate that developing methods to quantify the sensitivity of parameters to the 'level of discrepancy between model and data' would be tremendously useful for assessing the credibility of a model calibration process (and its resulting models). If an inference process relies heavily on the perfectness of the model equations, e.g. the 'distance' between the posterior and the true parameter is sensitive to the level of discrepancy, then caution should be taken when applying such approach to real data as we usually expect uncertainty in the model equations. We also note that one may first need to define 'level of discrepancy', which might not be trivial. As we see in Section 7.5, the performance of the inference process depends on how discrepant the current kinetics are. Although we were not able to directly quantify when the inference process will fail, we were able to learn qualitatively that small discrepancy was acceptable; whilst if the difference between model and reality is about the same size as the difference between literature models, it would lead to erroneous results. A potentially useful approach to extend our investigation would be to analyse the distance between the posterior and the true parameter (or simply the RMSE of the fitted currents in our case) as a function of the model error term δ introduced in Section 7.5.2 (or as a function of the RMSE between the model to fit and the ground truth).

To conclude, this chapter showed that applying optimal experimental design (OED) to voltage-clamp protocols can improve fitting maximum conductances while assuming kinetics are known, compared to the conventional protocol that we used in Chapter 3. We then considered problems that are likely to occur in reality. We assessed the assumption of perfect current kinetics, and considered the potential for errors to be induced by discrepancy. We also looked at the errors introduced by the voltage-clamp artefacts described in Chapter 6. In the next chapter, we will discuss how each chapter contributes to the field of cardiac cellular electrophysiology, and finish with suggestions for future research.

Chapter 8

Discussion

The goal of systems biology is to provide a quantitative understanding of complex biological systems using mathematical and computational models. Mathematical modelling and computational simulation have been a crucial tool for basic research in cardiac electrophysiology for decades, and has provided remarkable insights into many of the physiological mechanisms (Noble, 2008, 2011; Fink et al., 2011). More recently these quantitative cardiac models have begun to be used predictively and are transitioning into clinical and pharmaceutical applications (Mirams et al., 2012; Li et al., 2019). The use of mathematical modelling for prediction in these safety-critical applications requires a high level of confidence as well as accurate quantification of the uncertainty in the model predictions.

Chapters 3–7 of this thesis address different aspects of cardiac electrophysiology modelling that are essential to making credible models and quantifying their uncertainty (see Figure 1.1). In Chapter 3, we tailored the maximal conductance parameters in human induced pluripotent stem cell-derived cardiomyocyte (hiPSC-CM) cell-line specific models using a method based on conventional voltage-clamp protocols. During this exercise we assumed the current kinetics were known perfectly — we identified this as a strong limitation that was likely to be our main source of error. We then designed experiments for rapid characterisation of the kinetics of the *human Ether-à-go-go-Related Gene* (hERG) channel in Chapter 4, and studied their temperature dependence in Chapter 5. Chapter 6 then investigated the origin of the variability observed in the previous chapters by deriving a mathematical model for the artefacts in patch-clamp experiments. Finally, in Chapter 7 we applied optimal experimental design (OED) to voltage-clamp protocol design for action potential models and discussed issues that we expect to encounter when using these methods in real experiments. We concluded that we will need more accurate models of many ion currents to do cell-specific cardiomyocyte modelling.

In this chapter, I summarise and discuss the main contributions of this thesis to the field of cardiac cellular electrophysiology. I then discuss the potential future studies that extend the presented work.

8.1 Main Contributions

Chapter 3 reparameterised an existing hiPSC-CM mathematical model from the literature to a new set of experimental data collected in an automated high-throughput system, creating a set of cell-specific hiPSC-CM models. This chapter is primarily exploratory, providing motivation for the rest of this thesis, but it also has valuable implications for drug testing. There has been a significant increase in the popularity of hiPSC-CMs as an *in vitro* model for drug screening and, as a pillar of the Comprehensive *in vitro* Proarrhythmia Assay (CiPA) strategy, the use of hiPSC-CMs is anticipated to become a routine part of the cardiac safety testing pipeline. It is therefore critical to understand how to interpret hiPSC-CM data (including intra- and inter-cell line variability) and to translate findings in hiPSC-CMs to the adult human situation. This chapter demonstrates that mathematical models are a promising tool to integrate data, gain mechanistic insights and perform this translation.

We showed that differences between hiPSC-CM cell lines can be analysed and understood using tailored computational models. Furthermore, even models based on relatively simple methods (e.g., scaling maximum conductances) and a limited set of measurements (two inward current and one outward current experiments) can lead to improved predictions of action potential duration (APD) under baseline and drug-applied conditions. Tailoring cell line-specific hiPSC-CM models would also benefit precision and personalised medicine. However, we noticed that the obtained fits and predictions of the ion current profiles could not be recreated as well as we would have liked, and we hypothesised this was because the kinetics of ion currents were not captured accurately enough by the existing models. We therefore anticipated that better characterisation of ion current kinetics may be needed when tailoring these models.

In Chapter 4, I presented a novel design of experiments for high-throughput characterisation of hERG potassium channel kinetics. We developed inference methods that work well with this novel design and tested them thoroughly using synthetic data. We then fitted a mathematical model of hERG to results of over 100 experimental single-cell voltage-clamp measurements collected simultaneously on an automated patch-clamp platform. The short duration of the new protocol also allowed collection of extensive data for validation of the models and enabled us to study experimental variability and its origins in Chapter 6.

We demonstrated the feasibility of automated and rapid development of mathematical models from quick and high-throughput experiments. The short duration experiments on high-throughput systems can produce a large number of successful recordings, and are still able to collect cell-specific information for parameterising ion channel models fully. This approach avoids issues with averaging, allows variability studies, and could therefore have benefits for personalised medicine. Given the variability that we see in the data, low N numbers may not be appropriate to draw rigorous conclusions, e.g. if we randomly select 10 cells from the full dataset, the error in estimated statistics can be large compared to the full dataset.

The novel short protocol approach also enables us to study the ion channel kinetics under different conditions rapidly with large numbers of recordings to enable uncertainty quantification (UQ). We applied this method to study the temperature dependence of hERG in Chapter 5; we could also apply

this approach to study other conditions such as mutations, and it could be adapted to study many other voltage-dependent ionic currents.

The work described in this chapter increases the utility of automated high-throughput systems. For example, our method can potentially be adapted and used to investigate not only how much the hERG channel is blocked by a drug, but also how that drug influences channel kinetics. Our model parameterisation based on a single experiment can potentially show which parameters are affected by a drug, thus shedding light on the drug-binding mechanism. This might be useful for the CiPA initiative, as both automated high-throughput systems and *in silico* modelling constitute the core of the initiative (Fermini et al., 2016; Chang et al., 2017). Our approach may give us a better understanding of the pharmacological properties of drugs in the screening process and hence a better pharmaceutical safety assessment. The method also provides robust tools for the UQ that is an essential component of an *in silico* assay. With such large numbers of repeats, we can also incorporate an accurate description of the cell-to-cell (or rather experiment-to-experiment as shown in Chapter 6) variability in the *in silico* modelling as part of the UQ for safety-critical predictions (Mirams et al., 2016).

In Chapter 5, we investigated the temperature dependence of hERG kinetics. Ion channel currents are highly sensitive to temperature changes. Yet, because many experiments are performed more easily at room temperature, it is common to extrapolate findings to physiological temperatures using Q_{10} coefficients or Eyring rate theory. We applied the short, information-rich protocol developed in Chapter 4 and identified how kinetic parameters change as a function temperature. We found that the commonly used Q_{10} and Eyring formulations are incapable of describing the parameters' temperature dependence. A more generalised Eyring relationship fits the data better, but still does not match the patterns seen when refitting a parameters at a range of temperatures.

The findings in this chapter have implications for the accuracy of Q_{10} coefficients in electrophysiology, and show that care is needed to avoid misleading extrapolations in the many scientific and industrial pharmaceutical applications of Q_{10} coefficients. First, extrapolating temperature effects in ion channel kinetics is commonly used in action potential modelling. For example, many cardiac action potential models (Greenstein and Winslow, 2002; Iyer et al., 2004; Tanskanen et al., 2005; Sampson et al., 2010) adapted the Mazhari et al. (2001) hERG model which used Q_{10} values from Zhou et al. (1998) to extrapolate room temperature recordings to physiological temperature. Within action potential models, many other ion current models (such as I_{Na}, I_{CaL}, etc.) are also based on experiments performed at different temperatures (Niederer et al., 2009), most of which are then corrected via Q_{10} extrapolations (Courtemanche et al., 1998; Ten Tusscher et al., 2004; O'Hara et al., 2011; Paci et al., 2013). Our results therefore raise concerns about the accuracy of many of the existing current models within action potential models in the literature, and in Chapter 7 we saw that discrepancy in current kinetics (e.g. introduced by an inaccurate temperature extrapolation) can lead to further complications when inferring maximum conductances to build accurate action potential models.

Second, since many of the drug screening platforms work only at ambient temperature, measurements at different temperatures not only give rise to a large source of (deterministic) variation (Kirsch et al., 2004; Yao et al., 2005) but also introduce the problem of translation to physiological temperatures.

This translation can be particularly problematic when an imperfect temperature model is used, such as the commonly used Q_{10} coefficient. Given that we have shown that Q_{10} coefficients cannot capture the full temperature dependence of the parameters in our model of hERG kinetics (as shown in Figure 5.8), and given that different drugs target different kinetics, then a previous finding that there are no common sets of Q_{10} coefficients to describe the kinetics of drug block (Windley et al., 2018), is consistent with our results. The work raises a similar question as to whether the temperature dependence of drug binding kinetics follows the (Generalised) Eyring relationship? Our results show that extreme caution should be taken when using temperature-extrapolated *in vitro* drug screening data in *in silico* models for risk prediction.

We observed a high degree of experiment-to-experiment variability in hERG *kinetics* measurements in both Chapter 4 and Chapter 5. In Chapter 4, we also compared the experimentally estimated reversal potential with the theoretical Nernst potential, showing the difference was distributed close to zero with a standard deviation of 1.36 mV. Since all of the measurements were performed at the same time with the same temperature and extra- and intra-cellular solutions, we would expect the variability in reversal potential to be much smaller than this observed variability. A difference between the membrane voltage (what the cell experienced, V_{m}) and the command voltage (what we applied, V_{cmd}) could cause the apparent shift in the reversal potential, and this led us to inspect the hypothesis that artefacts could cause such an offset.

In Chapter 6, we developed a mathematical model for patch-clamp experiments to investigate the possible effects of experimental artefacts. The artefact components of the model include series resistance, membrane and pipette capacitances, voltage offsets, imperfect compensations made by the amplifier for these phenomena, and leak current. The model gives insight into how experimental artefacts are introduced and into the performance of the hardware compensation procedures; for example, the model shows that the effect of series resistance in distorting the applied voltage is proportional to the current size, so for a given series resistance and a fixed percentage compensation, then the bigger the current the larger this artefact.

We investigated three possible scenarios where variability in the observations can be explained by either varying current kinetics, measurement artefacts, or both. Remarkably, by assuming that variability arises exclusively from measurement artefacts, the model is able to predict (on average) the observed variability better than assuming cell-specific ion current kinetics (either with or without measurement artefacts). The assumption that variability arises from measurement artefacts also leads to a smaller number of model parameters, and hence is a more favourable explanation.

The work described in Chapter 6 demonstrated that a voltage-clamp experiment model can unify the kinetics of I_{Kr} measured across many cells. This result has strong implications for verification, validation, and uncertainty quantification (VVUQ) in the field, because perhaps *apparent* variability in kinetics of ion currents can be explained by experimental artefacts. This finding would make modular building of action potential models simpler, as one would not need to propagate all the observed variability in e.g. Chapter 4 for each current when predicting action potentials. Instead, we can use the voltage-clamp model to filter out the non-physiological uncertainty and keep only a

single set of physiologically-relevant kinetics model parameters, and propagate forward uncertainty in these into action potential models.

Our model represents the voltage-clamp experimental set-up and could be applied to any voltage-clamp data gathered with a standard patch-clamp amplifier. Our full model of the voltage-clamp experiment could be particularly useful for currents like the fast sodium current (I_{Na}) where the time constants are similar to those in the capacitance artefacts, and imperfect compensations for the series resistance and supercharging can strongly affect measurements of its kinetics (see for example Montnach et al., 2020).

The observation and the approach taken in this chapter also apply to other fields in computational or mathematical biology. One does not only have to handle the parameter uncertainty in the model caused by the data, but also needs to consider how the experiments were performed. We should not blindly assume the experimental data are ideal, and we should examine whether there are uncertainties, biases and artefacts in the data used to fit and test the model. If these factors are not properly handled, the models that we fit to these data can absorb all these effects and lead to incorrect interpretations or predictions.

The work presented in Chapters 4–6 is not limited to hERG, but can be applied to many other voltage-gated ion channels in the human heart (see also Section 8.2) or elsewhere in the body (such as neurons, skeletal muscle cells, etc.). We also anticipate that these methods can be extended to voltage-clamp experiments for ion channels in plants and other animals.

Finally, in Chapter 7, we revisited parameterisation of the maximum conductances in cardiac action potential models. We applied a set of optimal experimental design (OED) methods to these problems and found that they all improved the inferred parameter uncertainty as intended under the (commonly used) assumption of perfectly-known kinetics. Through synthetic data studies, we then considered potential real-world problems that we expect to encounter when applying these methods. We found that if we assume that the differences between existing current kinetics models in the literature (for human cardiomyocyte action potentials) can represent the differences between a model and reality, then the inferred maximum conductance values can be erroneous. Fitting maximum conductance values when there is discrepancy in the current kinetics can suffer from this 'practical unidentifiability due to discrepancy' issue whether using voltage-clamp or action potential (such as current-clamp or optical mapping for membrane voltage) data (Lei et al., 2020c). These examples show that caution is needed for the field as a whole, as such approaches have recently become popular (Whittaker et al., 2020).

This perfect kinetics assumption has been widely used, due to the complexity of the problem and a large identifiability issue if we try to infer both kinetics and conductance parameters (Dokos and Lovell, 2004; Fink and Noble, 2009). Our synthetic data studies have implications for VVUQ in the field and address one of the sources of uncertainty — structural uncertainty (or model uncertainty). By evaluating the model uncertainty of the current kinetics, we assess the validity of the commonly used assumption. Since fitting conductances is strongly influenced by the accuracy of the models of current kinetics, quantifying model uncertainty is crucial to the quantification of the overall

uncertainty in this calibration process. However, a calibration process may not always be such susceptible to structural uncertainty. For example, in Chapter 5, we showed that even though our hERG model is not the same as the Markov model used by Fink et al. (2008), the two models were able to predict currents under action potential clamps very closely. Therefore it is very important to study, understand, and quantify the effects of structural uncertainty, which perhaps does not only apply to cardiac electrophysiology modelling but is also relevant to mathematical and computational modelling more generally.

We then examined the case where we are able to get a 'good but not perfect' model for current kinetics, using methods that we developed in the previous chapters as examples. We showed that the difference between our 37 °C hERG model and the I_{Kr} Markov model by Fink et al. (2008) is similar to the difference between our hERG model predictions and the experimental data in Chapter 5. We used this difference as a guide to the level of model discrepancy in a 'good' model, and showed that we are able to infer the correct current contributions at this level.

We also tried simulating a sequence of current-selective blockers to infer the maximum conductances, a method suggested in the literature, while again assuming discrepant kinetics using two literature models. The striking result was that even if we had a perfect specific blocker for each current (which we do not have) and every current were to be perfectly isolated and subtracted, it would still not be good enough to get the right current contributions if the kinetics are too discrepant. According to the above synthetic data studies, it is therefore important to create a set of predictive and accurate kinetics models, before fitting maximum conductances to construct whole action potential models.

One might think using the sequential selective blocker experiments as demonstrated in Banyasz et al. (2011) with an action potential clamp would allow us to fit both the maximum conductance and get a 'reasonable' kinetics during an action potential. Indeed, that would allow us to get a good response of the kinetics to an action potential, however, the dynamics of an action potential clamp are not rich enough to identify all the model parameters. Therefore if we were able to perform sequential blocker experiments, instead of using an action potential clamp, it would be more beneficial to run variants of the staircase or optimised protocols for each current, such that we can infer both the maximum conductance and kinetics in a truly cell-specific way.

Lastly, we considered introducing the experimental artefacts that we studied in Chapter 6 to the synthetic data studies, while assuming an ideal voltage clamp during fitting. The inferred parameters suffered from both random and systematic errors, which may be expected as we saw the same problem when considering hERG kinetics parameters in Chapter 6. For example, there was a systematic underestimation of the I_{Na} contribution. Therefore the effects of experimental artefacts in typical patch data cannot be neglected (by post-processing or by the model), and we have to understand their influence on the experiment that was performed and the data that were recorded. It is important for us to handle the experimental artefacts during parameter inference in a similar way to Chapter 6, rather than leaving the action potential models to absorb any non-physiological artefacts.

8.2 Future Work

This thesis presented a first attempt at applying (model-driven) experimental design to high-throughput experiments in cardiac electrophysiology, leading to better characterisation and validation for the models. There are areas that can be improved upon, but the work presented in this thesis demonstrates the feasibility and usefulness of such an approach in this field, as well as opening up several research directions to follow up on.

The first extension of Chapter 4 would be to apply the developed high-throughput rapid characterisation approach to study other conditions such as mutations. As briefly discussed in Chapter 4, it is possible to apply the approach to study other conditions, and we have extended that study to consider the temperature dependence of the hERG kinetics in Chapter 5. High-throughput patch clamp has been used to study hERG mutants (Ng et al., 2020); similarly to the temperature dependence study, the staircase protocol could be applied to characterise these hERG mutants. The resulting models could be used for improved assessment of clinical phenotypes arising from patients carrying hERG mutations, such as Long QT Syndrome Type 2 (LQT2) which can result in the potentially fatal arrhythmia, Torsade de Pointes (TdP).

A further extension of this work would be to adapt the staircase protocol to different ion channel currents. Although this extension is not trivial, one can first adapt the voltage values to relevant voltages that would open and bring the current of interest to different gating states, and change the duration of the steps to reflect the time constants of the current. Another potential avenue to improve the staircase protocol would be to apply the OED techniques to the hERG kinetics and perhaps set the initial protocol as the staircase protocol. In this way, OED could be used to improve the staircase protocol to reduce the inferred parameter uncertainty. This optimisation is not needed for the hERG model that we used in Chapter 4, as we were able to identify the parameters reliably, but this would be particularly useful for more complex Markov models where the staircase protocol fails to identify the parameters, see for example Fink and Noble (2009).

It would also be useful to extend the approach developed in Chapter 4 to study pharmaceutical compounds. For example, one may design protocols to allow high-throughput systems to be used to investigate not only how much the hERG channel is blocked by a drug, but also the kinetics of drug binding and whether the drug influences underlying channel kinetics. This may provide a better quantitative characterisation of drug action than simply the concentration at which hERG channel activity is reduced by 50% (the IC_{50} value) under a certain protocol.

A possible extension of the study in Chapter 5 would be to investigate whether it was the temperature dependence model (e.g. the Typical Eyring formulation) or the hERG model structure being 'incorrect' which leads to an inaccurate temperature inter- or extrapolation. One way to address this question would be to assume the opposite of what we did in Chapter 5, i.e. one could assume the Eyring formulation is true for any transition of ion channel from one conformational state to another, and repeat the work in the chapter with different hERG models; a similar idea was suggested by Tsien and Noble (1969), using Q_{10} coefficients to study rate-limiting processes, i.e. the model structure.

This could be a potential way to perform model selection[1], namely, pick the hERG model that gives the correct temperature inter- or extrapolation using the Typical Eyring formulation. However, it is worth noting that this approach implicitly assumes the channel conformational states do *not* change with temperature, as we use the same model structure with different temperatures.

It would be useful to generalise the voltage-clamp experiment model in Chapter 6 to current-clamp experiments. This generalisation should be possible by introducing an extra feedback circuit to the full voltage-clamp model for standard patch-clamp amplifiers. However, note that some microelectrode amplifiers, such as the Axoclamp and the Axoprobe, have a different headstage design, hence a re-analysis of their circuits would be needed to build a similar model for these amplifiers.

An interesting question is raised after seeing that the optimised voltage-clamp protocols are not very robust against the experimental artefacts in Chapter 7. Is it possible to design optimal experiments that also take experimental artefacts into account, such that they are robust to these artefacts? One way of addressing this is to maximise the information needed for parameter inference at the same time minimise the sensitivity to the experimental artefacts. In this way, cardiac modellers may not need to worry about the experimental artefacts in Chapter 6 introducing systematic biases to their physiological models. Alternatively, we could aim to make artefacts easy to parameterise too (as the reversal ramp aimed to do in Chapter 4).

8.3 Concluding Remarks

In this thesis, I have shown how experimental designs using mathematical and computational models can be applied to aid uncertainty quantification (UQ) for high-throughput cardiac cellular electrophysiology experiments. These designs can save a lot of time when performing experiments and make examining various experimental conditions much quicker. When combined with appropriate statistical methods, short information-rich protocols allow us to quantify uncertainty when fitting parameters to data. Automated high-throughput experiments also allow us to quantify the variability between experiments, and hence are a first step in allowing us to determine the source of the observed experimental variability.

It is crucial to understand what the experimental data mean and whether it is appropriate to use a physiological model to study the observations. By developing mathematical models and statistical techniques, we can track down not only the uncertainty in physiological model parameters but also the uncertainty caused by experimental artefacts, to examine the consequences of these different sources of uncertainty on model predictions. A better understanding of uncertainty in the experiments will yield a better quantification and higher confidence in the physiological model and its predictions.

I have also begun to explore the effects of model discrepancy in the context of model fitting and predictions. When fitting (conductance) parameters of a cardiac action potential model to data, discrepancy in the model (kinetics) can give to misleading UQ results and predictions, raising interesting questions about the importance of the model accuracy for further exploration. Overall,

[1] Picking the most appropriate or the best model in a (given) set of models.

experimental design and UQ techniques applied to cardiac cellular electrophysiology modelling will greatly improve the development of models and will provide deeper physiological understanding of variability. These methods will be valuable for all cardiac electrophysiology modelling predictions, including clinical and pharmaceutical applications.

Appendix A

Abbreviations

APD	action potential duration
CHO	Chinese Hamster Ovary
CiPA	Comprehensive *in vitro* Proarrhythmia Assay
CMA-ES	Covariance Matrix Adaptation Evolution Strategy
DAD	delayed afterdepolarization
EAD	early afterdepolarization
FDA	Food and Drug Administration
GSA	global sensitivity analysis
hERG	*human Ether-à-go-go-Related Gene*
hESC-CM	human embryonic stem cell-derived cardiomyocyte
hiPSC-CM	human induced pluripotent stem cell-derived cardiomyocyte
I-V	current-voltage
i.i.d.	independent and identically distributed
ICH	International Conference on Harmonisation

LSA local sensitivity analysis

MAP maximum a posteriori

MCMC Markov Chain Monte Carlo

MwG Metropolis within Gibbs

OED optimal experimental design

pseudo-MwG pseudo-Metropolis within Gibbs

RMSD root-mean-square distance

RMSE root-mean-square error

RMSPE root-mean-square percentage error

RRMSE relative root-mean-square error

SNR signal-to-noise ratio

TdP Torsade de Pointes

UQ uncertainty quantification

VVUQ verification, validation, and uncertainty quantification

References

Akimoto, Y., Nagata, Y., Ono, I., and Kobayashi, S. (2010). Bidirectional relation between CMA evolution strategies and natural evolution strategies. In *Parallel Problem Solving from Nature, PPSN XI*, volume 6238 LNCS, pages 154–163, Heidelberg. Springer.

Akimoto, Y., Nagata, Y., Ono, I., and Kobayashi, S. (2012). Theoretical foundation for CMA-ES from information geometry perspective. *Algorithmica*, 64(4):698–716.

Altomare, C., Bartolucci, C., Sala, L., Bernardi, J., Mostacciuolo, G., Rocchetti, M., Severi, S., and Zaza, A. (2015). IKr impact on repolarization and its variability assessed by dynamic clamp. *Circulation: Arrhythmia and Electrophysiology*, 8(5):1265–1275.

Ando, H., Yoshinaga, T., Yamamoto, W., Asakura, K., Uda, T., Taniguchi, T., Ojima, A., Shinkyo, R., Kikuchi, K., Osada, T., Hayashi, S., Kasai, C., Miyamoto, N., Tashibu, H., Yamazaki, D., Sugiyama, A., Kanda, Y., Sawada, K., and Sekino, Y. (2017). A new paradigm for drug-induced torsadogenic risk assessment using human iPS cell-derived cardiomyocytes. *Journal of Pharmacological and Toxicological Methods*, 84:111–127.

Andreasson, N., Evgrafov, A., and Patriksson, M. (2020). *An Introduction to Continuous Optimization: Foundations and Fundamental Algorithms*. Dover Publications, Mineola, NY, 3rd edition.

Annecchino, L. A. and Schultz, S. R. (2018). Progress in automating patch clamp cellular physiology. *Brain and Neuroscience Advances*, 2:2398212818776561.

Armstrong, C. M. and Chow, R. H. (1987). Supercharging: a method for improving patch-clamp performance. *Biophysical Journal*, 52(1):133–136.

Atkinson, A. C. and Donev, A. N. (1992). *Optimum Experimental Designs*. Oxford University Press, Oxford.

Auder, B. and Iooss, B. (2008). Global sensitivity analysis based on entropy. In Martorell, S., Guedes Soares, C., and Barnett, J., editors, *In Safety, Reliability and Risk Analysis - Proceedings of the ESREL 2008 Conference*, pages 2107–2115, London. CRC Press.

Avior, Y., Sagi, I., and Benvenisty, N. (2016). Pluripotent stem cells in disease modelling and drug discovery. *Nature Reviews Molecular Cell Biology*, 17(3):170–182.

Axon Instruments Inc. (1999). Axopatch 200B patch clamp theory and operation. https://www.autom8.com/wp-content/uploads/2016/07/Axopatch-200B.pdf.

Ballou, L. M., Lin, R. Z., and Cohen, I. S. (2015). Control of cardiac repolarization by phosphoinositide 3-kinase signaling to ion channels. *Circulation Research*, 116(1):127–137.

Banga, J. R. and Balsa-Canto, E. (2008). Parameter estimation and optimal experimental design. *Essays in Biochemistry*, 45:195–209.

Banyasz, T., Horvath, B., Jian, Z., Izu, L. T., and Chen-Izu, Y. (2011). Sequential dissection of multiple ionic currents in single cardiac myocytes under action potential-clamp. *Journal of Molecular and Cellular Cardiology*, 50(3):578–581.

Beattie, K. A., Hill, A. P., Bardenet, R., Cui, Y., Vandenberg, J. I., Gavaghan, D. J., de Boer, T. P., and Mirams, G. R. (2018). Sinusoidal voltage protocols for rapid characterisation of ion channel kinetics. *The Journal of Physiology*, 596(10):1813–1828.

Bedada, F. B., Wheelwright, M., and Metzger, J. M. (2016). Maturation status of sarcomere structure and function in human iPSC-derived cardiac myocytes. *Biochimica et Biophysica Acta*, 1863(7, Part B):1829–1838.

Běhrádek, J. (1930). Temperature coefficients in biology. *Biological Reviews*, 5(1):30–58.

Bekkers, J. M., Richerson, G. B., and Stevens, C. F. (1990). Origin of variability in quantal size in cultured hippocampal neurons and hippocampal slices. *Proceedings of the National Academy of Sciences*, 87(14):5359–5362.

Bellman, R. and Åström, K. (1970). On structural identifiability. *Mathematical Biosciences*, 7(3-4):329–339.

Bendahhou, S., Cummins, T. R., Tawil, R., Waxman, S. G., and Ptácek, L. J. (1999). Activation and inactivation of the voltage-gated sodium channel: role of segment S5 revealed by a novel hyperkalaemic periodic paralysis mutation. *Journal of Neuroscience*, 19(12):4762–71.

Bers, D. M. (2002). Cardiac excitation-contraction coupling. *Nature*, 415(6868):198–205.

Bers, D. M., Barry, W. H., and Despa, S. (2003). Intracellular Na+ regulation in cardiac myocytes. *Cardiovascular Research*, 57(4):897–912.

Bett, G. C., Kaplan, A. D., Lis, A., Cimato, T. R., Tzanakakis, E. S., Zhou, Q., Morales, M. J., and Rasmusson, R. L. (2013). Electronic "expression" of the inward rectifier in cardiocytes derived from human-induced pluripotent stem cells. *Heart Rhythm*, 10(12):1903–1910.

Bhattacharyya, G. K. and Soejoeti, Z. (1981). Asymptotic normality and efficiency of modified least squares estimators in some accelerated life test models. *Sankhya: The Indian Journal of Statistics, Series B*, 43(1):18–39.

Billet, A., Froux, L., Hanrahan, J. W., and Becq, F. (2017). Development of automated patch clamp technique to investigate CFTR chloride channel function. *Frontiers in Pharmacology*, 8:195.

Blazeski, A., Zhu, R., Hunter, D. W., Weinberg, S. H., Zambidis, E. T., and Tung, L. (2012). Cardiomyocytes derived from human induced pluripotent stem cells as models for normal and diseased cardiac electrophysiology and contractility. *Progress in Biophysics and Molecular Biology*, 110(2-3):166–177.

Blinova, K., Stohlman, J., Vicente, J., Chan, D., Johannesen, L., Hortigon-Vinagre, M. P., Zamora, V., Smith, G., Crumb, W. J., Pang, L., Lyn-Cook, B., Ross, J., Brock, M., Chvatal, S., Millard, D., Galeotti, L., Stockbridge, N., and Strauss, D. G. (2017). Comprehensive translational assessment of human-induced pluripotent stem cell derived cardiomyocytes for evaluating drug-induced arrhythmias. *Toxicological Sciences*, 155(1):234–247.

Bosman, A., Sartiani, L., Spinelli, V., Del Lungo, M., Stillitano, F., Nosi, D., Mugelli, A., Cerbai, E., and Jaconi, M. (2013). Molecular and functional evidence of HCN4 and caveolin-3 interaction during cardiomyocyte differentiation from human embryonic stem cells. *Stem Cells and Development*, 22(11):1717–1727.

Bowler, L. A., Gavaghan, D. J., Mirams, G. R., and Whiteley, J. P. (2019). Representation of multiple cellular phenotypes within tissue-level simulations of cardiac electrophysiology. *Bulletin of Mathematical Biology*, 81(1):7–38.

Boyd, S. and Vandenberghe, L. (2004). *Convex Optimization*. Cambridge University Press, Cambridge, 1st edition.

Brezinski, C. and Wuytack, L. (2012). *Numerical Analysis: Historical Developments in the 20th Century*. Elsevier Science.

Britton, O. J., Bueno-Orovio, A., Van Ammel, K., Lu, H. R., Towart, R., Gallacher, D. J., and Rodriguez, B. (2013). Experimentally calibrated population of models predicts and explains intersubject variability in cardiac cellular electrophysiology. *Proceedings of the National Academy of Sciences*, 110(23):E2098–E2105.

Burridge, P. W., Matsa, E., Shukla, P., Lin, Z. C., Churko, J. M., Ebert, A. D., Lan, F., Diecke, S., Huber, B., Mordwinkin, N. M., Plews, J. R., Abilez, O. J., Cui, B., Gold, J. D., and Wu, J. C. (2014). Chemically defined generation of human cardiomyocytes. *Nature Methods*, 11(8):855–860.

Burridge, P. W., Thompson, S., Millrod, M. A., Weinberg, S., Yuan, X., Peters, A., Mahairaki, V., Koliatsos, V. E., Tung, L., and Zambidis, E. T. (2011). A universal system for highly efficient cardiac differentiation of human induced pluripotent stem cells that eliminates interline variability. *PLOS One*, 6(4):e18293.

Cahan, P. and Daley, G. Q. (2013). Origins and implications of pluripotent stem cell variability and heterogeneity. *Nature Reviews Molecular Cell Biology*, 14(6):357–68.

Carcamo-Orive, I., Hoffman, G. E., Cundiff, P., Beckmann, N. D., D'Souza, S. L., Knowles, J. W., Patel, A., Papatsenko, D., Abbasi, F., Reaven, G. M., Whalen, S., Lee, P., Shahbazi, M., Henrion, M. Y., Zhu, K., Wang, S., Roussos, P., Schadt, E. E., Pandey, G., Chang, R., Quertermous, T., and Lemischka, I. (2017). Analysis of transcriptional variability in a large human iPSC library reveals genetic and non-genetic determinants of heterogeneity. *Cell Stem Cell*, 20(4):518–532.e9.

Cauchy, A.-L. (1847). Méthode générale pour la résolution des systemes d'équations simultanées. *Comptes rendus de l'Académie des Sciences*, pages 536–538.

Chaloner, K. and Verdinelli, I. (1995). Bayesian experimental design: a review. *Statistical Science*, pages 273–304.

Chang, K. C., Dutta, S., Mirams, G. R., Beattie, K. A., Sheng, J., Tran, P. N., Wu, M., Wu, W. W., Colatsky, T., Strauss, D. G., and Li, Z. (2017). Uncertainty quantification reveals the importance of data variability and experimental design considerations for in silico proarrhythmia risk assessment. *Frontiers in Physiology*, 8:917.

Choi, J., Lee, S., Mallard, W., Clement, K., Tagliazucchi, G. M., Lim, H., Choi, I. Y., Ferrari, F., Tsankov, A. M., Pop, R., Lee, G., Rinn, J. L., Meissner, A., Park, P. J., and Hochedlinger, K. (2015). A comparison of genetically matched cell lines reveals the equivalence of human iPSCs and ESCs. *Nature Biotechnology*, 33(11):1173–1181.

Christé, G., Thériault, O., Chahine, M., Millat, G., Rodriguez-Lafrasse, C., Rousson, R., Deschênes, I., Ficker, E., and Chevalier, P. (2008). A new C-terminal hERG mutation A915fs+ 47X associated with symptomatic LQT2 and auditory-trigger syncope. *Heart Rhythm*, 5(11):1577–1586.

Chu, Y. and Hahn, J. (2013). Necessary condition for applying experimental design criteria to global sensitivity analysis results. *Computers and Chemical Engineering*, 48:280–292.

Clerx, M. (2018). Personalisation of cellular electrophysiology models: utopia? *Computing in Cardiology*, 45.

Clerx, M., Beattie, K. A., Gavaghan, D. J., and Mirams, G. R. (2019a). Four ways to fit an ion channel model. *Biophysical Journal*, 117(12):2420–2437.

Clerx, M. and Collins, P. (2014). Reducing run-times of excitable cell models by replacing computationally expensive functions with splines. In *21st International Symposium on Mathematical Theory of Networks and Systems*, pages 84–89, Groningen.

Clerx, M., Collins, P., de Lange, E., and Volders, P. G. (2016). Myokit: a simple interface to cardiac cellular electrophysiology. *Progress in Biophysics and Molecular Biology*, 120(1-3):100–114.

Clerx, M., Heijman, J., Collins, P., and Volders, P. G. A. (2018). Predicting changes to INa from missense mutations in human SCN5A. *Scientific Reports*, 8(1):12797.

Clerx, M., Robinson, M., Lambert, B., Lei, C. L., Ghosh, S., Mirams, G. R., and Gavaghan, D. J. (2019b). Probabilistic Inference on Noisy Time Series (PINTS). *Journal of Open Research Software*, 7(1):23.

Cole, K. S. (1968). *Membranes, Ions, and Impulses: A Chapter of Classical Biophysics*. University of California Press.

Collins, C. A. and Rojas, E. (1982). Temperature dependence of the sodium channel gating kinetics in the node of Ranvier. *Quarterly Journal of Experimental Physiology*, 67(1):41–55.

Colquhoun, D., Dowsland, K. A., Beato, M., and Plested, A. J. (2004). How to impose microscopic reversibility in complex reaction mechanisms. *Biophysical Journal*, 86(6):3510–3518.

Cooper, J., Scharm, M., and Mirams, G. R. (2016). The cardiac electrophysiology web lab. *Biophysical Journal*, 110(2):292–300.

Cooper, J., Spiteri, R. J., and Mirams, G. R. (2015). Cellular cardiac electrophysiology modeling with Chaste and CellML. *Frontiers in Physiology*, 5:511.

Courtemanche, M., Ramirez, R. J., and Nattel, S. (1998). Ionic mechanisms underlying human atrial action potential properties: insights from a mathematical model. *American Journal of Physiology - Heart and Circulatory Physiology*, 275(1):H301–H321.

Coveney, S. and Clayton, R. H. (2018). Fitting two human atrial cell models to experimental data using Bayesian history matching. *Progress in Biophysics and Molecular Biology*, 139:43–58.

Creswell, R., Lambert, B., Lei, C. L., Robinson, M., and Gavaghan, D. (2020). Using flexible noise models to avoid noise model misspecification in inference of differential equation time series models. *arXiv*, 2011.04854.

Curran, M. E., Splawski, I., Timothy, K. W., Vincent, G. M., Green, E. D., and Keating, M. T. (1995). A molecular basis for cardiac arrhythmia: hERG mutations cause long QT syndrome. *Cell*, 80(5):795–803.

Daly, A. C., Clerx, M., Beattie, K. A., Cooper, J., Gavaghan, D. J., and Mirams, G. R. (2018). Reproducible model development in the cardiac electrophysiology Web Lab. *Progress in Biophysics and Molecular Biology*, 139:3–14.

Deb, K. (2000). An efficient constraint handling method for genetic algorithms. *Computer Methods in Applied Mechanics and Engineering*, 186(2-4):311–338.

DeBoever, C., Li, H., Jakubosky, D., Benaglio, P., Reyna, J., Olson, K. M., Huang, H., Biggs, W., Sandoval, E., D'Antonio, M., Jepsen, K., Matsui, H., Arias, A., Ren, B., Nariai, N., Smith, E. N., D'Antonio-Chronowska, A., Farley, E. K., and Frazer, K. A. (2017). Large-scale profiling reveals the influence of genetic variation on gene expression in human induced pluripotent stem cells. *Cell Stem Cell*, 20(4):533–546.e7.

Denbigh, K. G. (1981). *The Principles of Chemical Equilibrium*. Cambridge University Press, Cambridge.

Dhaka, A., Viswanath, V., and Patapoutian, A. (2006). Trp ion channels and temperature sensation. *Annual Review of Neuroscience*, 29:135–161.

Di Veroli, G. Y., Davies, M. R., Zhang, H., Abi-Gerges, N., and Boyett, M. R. (2013). High-throughput screening of drug-binding dynamics to HERG improves early drug safety assessment. *American Journal of Physiology - Heart and Circulatory Physiology*, 304(1):H104–H117.

DiFrancesco, D. (1993). Pacemaker mechanisms in cardiac tissue. *Annual Review of Physiology*, 55(1):455–472.

Dokos, S. and Lovell, N. H. (2004). Parameter estimation in cardiac ionic models. *Progress in Biophysics and Molecular Biology*, 85(2-3):407–431.

Doss, M. X., Di Diego, J. M., Goodrow, R. J., Wu, Y., Cordeiro, J. M., Nesterenko, V. V., Barajas-Martínez, H., Hu, D., Urrutia, J., Desai, M., Treat, J. A., Sachinidis, A., and Antzelevitch, C. (2012). Maximum diastolic potential of human induced pluripotent stem cell-derived cardiomyocytes depends critically on IKr. *PLOS One*, 7(7):e40288.

Du, D. T., Hellen, N., Kane, C., and Terracciano, C. M. (2015). Action potential morphology of human induced pluripotent stem cell-derived cardiomyocytes does not predict cardiac chamber specificity and is dependent on cell density. *Biophysical Journal*, 108(1):1–4.

Ebert, A. D., Liang, P., and Wu, J. C. (2012). Induced pluripotent stem cells as a disease modeling and drug screening platform. *Journal of Cardiovascular Pharmacology*, 60(4):408–416.

Egashira, T., Yuasa, S., Suzuki, T., Aizawa, Y., Yamakawa, H., Matsuhashi, T., Ohno, Y., Tohyama, S., Okata, S., Seki, T., Kuroda, Y., Yae, K., Hashimoto, H., Tanaka, T., Hattori, F., Sato, T., Miyoshi, S., Takatsuki, S., Murata, M., Kurokawa, J., Furukawa, T., Makita, N., Aiba, T., Shimizu, W., Horie, M., Kamiya, K., Kodama, I., Ogawa, S., and Fukuda, K. (2012). Disease characterization using LQTS-specific induced pluripotent stem cells. *Cardiovascular Research*, 95(4):419–429.

Elkins, R. C., Davies, M. R., Brough, S. J., Gavaghan, D. J., Cui, Y., Abi-Gerges, N., and Mirams, G. R. (2013). Variability in high-throughput ion-channel screening data and consequences for cardiac safety assessment. *Journal of Pharmacological and Toxicological Methods*, 68(1):112–122.

Elliott, D. A., Braam, S. R., Koutsis, K., Ng, E. S., Jenny, R., Lagerqvist, E. L., Biben, C., Hatzistavrou, T., Hirst, C. E., Yu, Q. C., Skelton, R. J. P., Ward-van Oostwaard, D., Lim, S. M., Khammy, O., Li, X., Hawes, S. M., Davis, R. P., Goulburn, A. L., Passier, R., Prall, O. W. J., Haynes, J. M., Pouton, C. W., Kaye, D. M., Mummery, C. L., Elefanty, A. G., and Stanley, E. G. (2011). NKX2-5(eGFP/w) hESCs for isolation of human cardiac progenitors and cardiomyocytes. *Nature Methods*, 8(12):1037–1040.

Escobar, L. A. and Meeker, W. Q. (2006). A review of accelerated test models. *Statistical Science*, 21(4):552–577.

Eyring, H. (1935). The activated complex in chemical reactions. *The Journal of Chemical Physics*, 3(2):107–115.

Fatima, A., Xu, G., Shao, K., Papadopoulos, S., Lehmann, M., Arnáiz-Cot, J. J., Rosa, A. O., Nguemo, F., Matzkies, M., Dittmann, S., Stone, S. L., Linke, M., Zechner, U., Beyer, V., Hennies, H. C., Rosenkranz, S., Klauke, B., Parwani, A. S., Haverkamp, W., Pfitzer, G., Farr, M., Cleemann, L., Morad, M., Milting, H., Hescheler, J., and Saric, T. (2011). In vitro modeling of ryanodine receptor 2 dysfunction using human induced pluripotent stem cells. *Cellular Physiology and Biochemistry*, 28(4):579–592.

Feigenspan, A., Dedek, K., Schlich, K., Weiler, R., and Thanos, S. (2010). Expression and biophysical characterization of voltage-gated sodium channels in axons and growth cones of the regenerating optic nerve. *Investigative Ophthalmology and Visual Science*, 51(3):1789–1799.

Fermini, B. and Fossa, A. A. (2003). The impact of drug-induced QT interval prolongation on drug discovery and development. *Nature Reviews Drug Discovery*, 2(6):439–447.

Fermini, B., Hancox, J. C., Abi-Gerges, N., Bridgland-Taylor, M., Chaudhary, K. W., Colatsky, T., Correll, K., Crumb, W., Damiano, B., Erdemli, G., Gintant, G., Imredy, J., Koerner, J., Kramer, J., Levesque, P., Li, Z., Lindqvist, A., Obejero-Paz, C. A., Rampe, D., Sawada, K., Strauss, D. G., and Vandenberg, J. I. (2016). A new perspective in the field of cardiac safety testing through the comprehensive in vitro proarrhythmia assay paradigm. *Journal of Biomolecular Screening*, 21(1):1–11.

Fine, M., Lu, F.-M., Lin, M.-J., Moe, O., Wang, H.-R., and Hilgemann, D. W. (2013). Human-induced pluripotent stem cell-derived cardiomyocytes for studies of cardiac ion transporters. *American Journal of Physiology-Cell Physiology*, 305(5):C481–C491.

Fink, M., Niederer, S. A., Cherry, E. M., Fenton, F. H., Koivumäki, J. T., Seemann, G., Thul, R., Zhang, H., Sachse, F. B., Beard, D., Crampin, E. J., and Smith, N. P. (2011). Cardiac cell modelling: observations from the heart of the cardiac physiome project. *Progress in Biophysics and Molecular Biology*, 104(1-3):2–21.

Fink, M. and Noble, D. (2009). Markov models for ion channels: versatility versus identifiability and speed. *Philosophical Transactions of the Royal Society A*, 367(1896):2161–2179.

Fink, M., Noble, D., Virag, L., Varro, A., and Giles, W. R. (2008). Contributions of HERG K+ current to repolarization of the human ventricular action potential. *Progress in Biophysics and Molecular Biology*, 96(1-3):357–376.

Finkel, A., Wittel, A., Yang, N., Handran, S., Hughes, J., and Costantin, J. (2006). Population patch clamp improves data consistency and success rates in the measurement of ionic currents. *Journal of Biomolecular Screening*, 11(5):488–496.

Foster, T., Lei, C. L., Robinson, M., Gavaghan, D., and Lambert, B. (2020). Model evidence with fast tree based quadrature. *arXiv*, 2005.11300.

Friedrichs, G. S., Patmore, L., and Bass, A. (2005). Non-clinical evaluation of ventricular repolarization (ICH S7B): results of an interim survey of international pharmaceutical companies. *Journal of Pharmacological and Toxicological Methods*, 52(1):6–11.

Garny, A., Nickerson, D. P., Cooper, J., dos Santos, R. W., Miller, A. K., McKeever, S., Nielsen, P. M. F., and Hunter, P. J. (2008). CellML and associated tools and techniques. *Philosophical Transactions of the Royal Society A*, 366(1878):3017–3043.

Gelman, A., Carlin, J. B., Stern, H. S., Dunson, D. B., Vehtari, A., and Rubin, D. B. (2013). *Bayesian Data Analysis*. Texts in Statistical Science. Chapman and Hall/CRC, Boca Raton, FL, 3rd edition.

Geneser, S. E., Kirby, R. M., Xiu, D., and Sachse, F. B. (2007). Stochastic Markovian modeling of electrophysiology of ion channels: reconstruction of standard deviations in macroscopic currents. *Journal of Theoretical Biology*, 245(4):627–637.

Gertler, T. S., Thompson, C. H., Vanoye, C. G., Millichap, J. J., and George, A. L. (2019). Functional consequences of a KCNT1 variant associated with status dystonicus and early-onset infantile encephalopathy. *Annals of Clinical and Translational Neurology*, 6(9):1606–1615.

Gherghiceanu, M., Barad, L., Novak, A., Reiter, I., Itskovitz-Eldor, J., Binah, O., and Popescu, L. (2011). Cardiomyocytes derived from human embryonic and induced pluripotent stem cells: comparative ultrastructure. *Journal of Cellular and Molecular Medicine*, 15(11):2539–2551.

Gilks, W. R., Best, N. G., and Tan, K. K. C. (1995). Adaptive rejection Metropolis sampling within Gibbs sampling. *Applied Statistics*, 44(4):455.

Gillespie, D. T. (1976). A general method for numerically simulating the stochastic time evolution of coupled chemical reactions. *Journal of Computational Physics*, 22(4):403–434.

Gintant, G., Sager, P. T., and Stockbridge, N. (2016). Evolution of strategies to improve preclinical cardiac safety testing. *Nature Reviews Drug Discovery*, 15(7):457–471.

Giorgi, M. A., Bolaños, R., Gonzalez, C. D., and Di Girolamo, G. (2010). QT interval prolongation: preclinical and clinical testing arrhythmogenesis in drugs and regulatory implications. *Current Drug Safety*, 5(1):54–57.

Goldman, D. E. (1943). Potential, impedance, and rectification in membranes. *The Journal of General Physiology*, 27(1):37–60.

Golowasch, J. (2014). Ionic current variability and functional stability in the nervous system. *Bioscience*, 64(7):570–580.

Goodrow, R. J., Desai, S., Treat, J. A., Panama, B. K., Desai, M., Nesterenko, V. V., and Cordeiro, J. M. (2018). Biophysical comparison of sodium currents in native cardiac myocytes and human induced pluripotent stem cell-derived cardiomyocytes. *Journal of Pharmacological and Toxicological Methods*, 90:19–30.

Gottu Mukkula, A. R. and Paulen, R. (2017). Model-based design of optimal experiments for nonlinear systems in the context of guaranteed parameter estimation. *Computers and Chemical Engineering*, 99:198–213.

Grandi, E., Pasqualini, F. S., and Bers, D. M. (2010). A novel computational model of the human ventricular action potential and Ca transient. *Journal of Molecular and Cellular Cardiology*, 48(1):112–121.

Grandi, E., Pasqualini, F. S., Pes, C., Corsi, C., Zaza, A., and Severi, S. (2009). Theoretical investigation of action potential duration dependence on extracellular Ca2+ in human cardiomyocytes. *Journal of Molecular and Cellular Cardiology*, 46(3):332–342.

Grant, A. O. (2009). Cardiac ion channels. *Circulation: Arrhythmia and Electrophysiology*, 2(2):185–194.

Greenstein, J. L. and Winslow, R. L. (2002). An integrative model of the cardiac ventricular myocyte incorporating local control of Ca2+ release. *Biophysical Journal*, 83(6):2918–2945.

Groenendaal, W., Ortega, F. A., Kherlopian, A. R., Zygmunt, A. C., Krogh-Madsen, T., and Christini, D. J. (2015). Cell-specific cardiac electrophysiology models. *PLOS Computational Biology*, 11(4):e1004242.

Haario, H., Saksman, E., and Tamminen, J. (2001). An adaptive Metropolis algorithm. *Bernoulli*, 7(2):223.

Han, D., Tan, H., Sun, C., and Li, G. (2018). Dysfunctional Nav1.5 channels due to SCN5A mutations. *Experimental Biology and Medicine*, 243(10):852–863.

Hansen, N. (2006). The CMA Evolution Strategy: a comparing review. In Lozano, J. A., Larrañaga, P., Inza, I., and Bengoetxea, E., editors, *Towards a New Evolutionary Computation: Advances in the Estimation of Distribution Algorithms*, pages 75–102. Springer-Verlag, Heidelberg.

HEKA Elektronik GmbH (2016). Patchmaster multi-channel data acquisition software reference manual. https://www.heka.com/downloads/software/manual/m_patchmaster.pdf.

HEKA Elektronik GmbH (2018). EPC 10 USB hardware manual version 2.8. http://www.heka.com/downloads/hardware/manual/m_epc10.pdf.

Hill, A. V. (1910). The possible effects of the aggregation of the molecules of haemoglobin on its dissociation curves. *The Journal of Physiology*, 40:4–7.

Hille, B. (2001). *Ion Channels of Excitable Membranes*, volume 507. Sinauer Associates, Sunderland, MA.

Hindmarsh, A. C., Brown, P. N., Grant, K. E., Lee, S. L., Serban, R., Shumaker, D. E., and Woodward, C. S. (2005). SUNDIALS: suite of nonlinear and differential/algebraic equation solvers. *ACM Transactions on Mathematical Software*, 31(3):363–396.

Hobbs, K. H. and Hooper, S. L. (2008). Using complicated, wide dynamic range driving to develop models of single neurons in single recording sessions. *Journal of Neurophysiology*, 99(4):1871–1883.

Hodgkin, A. L. (1950). Conduction of the nervous impulse: some recent experiments. *British Medical Bulletin*, 6(4):322–325.

Hodgkin, A. L. and Huxley, A. F. (1952a). A quantitative description of membrane current and its application to conduction and excitation in nerve. *The Journal of Physiology*, 117(4):500–544.

Hodgkin, A. L. and Huxley, A. F. (1952b). Currents carried by sodium and potassium ions through the membrane of the giant axon of Loligo. *The Journal of Physiology*, 116(4):449–472.

Hodgkin, A. L. and Huxley, A. F. (1952c). The components of membrane conductance in the giant axon of Loligo. *The Journal of Physiology*, 116(4):473–496.

Hodgkin, A. L. and Huxley, A. F. (1952d). The dual effect of membrane potential on sodium conductance in the giant axon of Loligo. *The Journal of Physiology*, 116(4):497–506.

Hodgkin, A. L., Huxley, A. F., and Katz, B. (1952). Measurement of current-voltage relations in the membrane of the giant axon of Loligo. *The Journal of Physiology*, 116(4):424–448.

Holm, S. (2008). Time to reconsider stem cell ethics–the importance of induced pluripotent cells. *Journal of Medical Ethics*, 34(2):63–64.

Honda, M., Kiyokawa, J., Tabo, M., and Inoue, T. (2011). Electrophysiological characterization of cardiomyocytes derived from human induced pluripotent stem cells. *Journal of Pharmacological Sciences*, 117(3):149–159.

Hume, J. R. and Grant, A. O. (2015). Agents used in cardiac arrhythmias. In Katzung, B. G. and Trevor, A. J., editors, *Basic & Clinical Pharmacology*. McGraw-Hill Education / Medical, New York, NY, 13 edition.

Hutter, O. F. and Noble, D. (1960). Rectifying properties of heart muscle. *Nature*, 188(4749):495.

Huxley, A. (2002). From overshoot to voltage clamp. *Trends in Neurosciences*, 25(11):553–558.

Hwang, H. S., Kryshtal, D. O., Feaster, T., Sánchez-Freire, V., Zhang, J., Kamp, T. J., Hong, C. C., Wu, J. C., and Knollmann, B. C. (2015). Comparable calcium handling of human iPSC-derived cardiomyocytes generated by multiple laboratories. *Journal of Molecular and Cellular Cardiology*, 85:79–88.

ICH (2001). S7A Safety pharmacology studies for human pharmaceuticals. https://www.ema.europa.eu/en/ich-s7a-safety-pharmacology-studies-human-pharmaceuticals.

ICH (2005a). E14 Clinical evaluation of QT/QTc interval prolongation and proarrhythmic potential for non-antiarrhythmic drugs. https://www.ema.europa.eu/en/ich-e14-clinical-evaluation-qtqtc-interval-prolongation-proarrhythmic-potential-non-antiarrhythmic.

ICH (2005b). S7B Non-clinical evaluation of the potential for delayed ventricular repolarization (QT interval prolongation) by human pharmaceuticals. https://www.ema.europa.eu/en/ich-s7b-non-clinical-evaluation-potential-delayed-ventricular-repolarization-qt-interval.

Irvine, L. A., Jafri, M. S., and Winslow, R. L. (1999). Cardiac sodium channel Markov model with temperature dependence and recovery from inactivation. *Biophysical Journal*, 76(4):1868–1885.

Ishii, K., Nagai, M., Takahashi, M., and Endoh, M. (2003). Dissociation of E-4031 from the HERG channel caused by mutations of an amino acid results in greater block at high stimulation frequency. *Cardiovascular Research*, 57(3):651–659.

Ito, E., Ikemoto, Y., and Yoshioka, T. (2015). Thermodynamic implications of high Q10 of thermo-TRP channels in living cells. *Biophysics*, 11:33–38.

Itzhaki, I., Maizels, L., Huber, I., Gepstein, A., Arbel, G., Caspi, O., Miller, L., Belhassen, B., Nof, E., Glikson, M., and Gepstein, L. (2012). Modeling of catecholaminergic polymorphic ventricular tachycardia with patient-specific human-induced pluripotent stem cells. *Journal of the American College of Cardiology*, 60(11):990–1000.

Itzhaki, I., Maizels, L., Huber, I., Zwi-Dantsis, L., Caspi, O., Winterstern, A., Feldman, O., Gepstein, A., Arbel, G., Hammerman, H., Boulos, M., and Gepstein, L. (2011a). Modelling the long QT syndrome with induced pluripotent stem cells. *Nature*, 471(7337):225–229.

Itzhaki, I., Rapoport, S., Huber, I., Mizrahi, I., Zwi-Dantsis, L., Arbel, G., Schiller, J., and Gepstein, L. (2011b). Calcium handling in human induced pluripotent stem cell derived cardiomyocytes. *PLOS One*, 6(4):e18037.

Iyer, V., Mazhari, R., and Winslow, R. L. (2004). A computational model of the human left-ventricular epicardial myocyte. *Biophysical Journal*, 87(3):1507–1525.

Jæger, K. H., Charwat, V., Charrez, B., Finsberg, H., Maleckar, M. M., Wall, S., Healy, K. E., and Tveito, A. (2020). Improved computational identification of drug response using optical measurements of human stem cell derived cardiomyocytes in microphysiological systems. *Frontiers in Pharmacology*, 10:1648.

Jasra, A., Stephens, D. A., Holmes, C. C., Jasra, A., Stephens, D. A., and Holmes, C. C. (2007). On population-based simulation for static inference. *Statistics and Computing*, 17(3):263–279.

Jiang, P., Rushing, S. N., Kong, C.-w., Fu, J., Lieu, D. K.-T., Chan, C. W., Deng, W., and Li, R. A. (2010). Electrophysiological properties of human induced pluripotent stem cells. *American Journal of Physiology-Cell Physiology*, 298(3):C486–C495.

Johnstone, R. H. (2018). *Uncertainty characterisation in action potential modelling for cardiac drug safety*. PhD thesis, University of Oxford, Oxford.

Johnstone, R. H., Bardenet, R., Gavaghan, D. J., and Mirams, G. R. (2017). Hierarchical Bayesian inference for ion channel screening dose-response data. *Wellcome Open Research*, 1(6).

Johnstone, R. H., Bardenet, R., Gavaghan, D. J., Polonchuk, L., Davies, M. R. D., and Mirams, G. R. (2016a). Hierarchical Bayesian modelling of variability and uncertainty in synthetic action potential traces. In *Computing in Cardiology Conference*, volume 43, pages 1089–1092.

Johnstone, R. H., Chang, E. T. Y., Bardenet, R., De Boer, T. P., Gavaghan, D. J., Pathmanathan, P., Clayton, R. H., and Mirams, G. R. (2016b). Uncertainty and variability in models of the cardiac action potential: can we build trustworthy models? *Journal of Molecular and Cellular Cardiology*, 96:49–62.

Jones, E., Oliphant, T., and Peterson, P. (2001). SciPy: open source scientific tools for Python.

Jonsson, M. K., Vos, M. A., Mirams, G. R., Duker, G., Sartipy, P., De Boer, T. P., and Van Veen, T. A. (2012). Application of human stem cell-derived cardiomyocytes in safety pharmacology requires caution beyond hERG. *Journal of Molecular and Cellular Cardiology*, 52(5):998–1008.

Jost, N., Virág, L., Bitay, M., Takács, J., Lengyel, C., Biliczki, P., Nagy, Z., Bogáts, G., Lathrop, D. A., Papp, J. G., and Varró, A. (2005). Restricting excessive cardiac action potential and QT prolongation. *Circulation*, 112(10):1392–1399.

Jung, C. B., Moretti, A., y Schnitzler, M., Iop, L., Storch, U., Bellin, M., Dorn, T., Ruppenthal, S., Pfeiffer, S., Goedel, A., Dirschinger, R. J., Seyfarth, M., Lam, J. T., Sinnecker, D., Gudermann, T., Lipp, P., and Laugwitz, K. L. (2012). Dantrolene rescues arrhythmogenic RYR2 defect in a patient-specific stem cell model of catecholaminergic polymorphic ventricular tachycardia. *EMBO Molecular Medicine*, 4(3):180–191.

Jurkiewicz, N. K. and Sanguinetti, M. C. (1993). Rate-dependent prolongation of cardiac action potentials by a methanesulfonanilide class III antiarrhythmic agent. Specific block of rapidly activating delayed rectifier K+ current by dofetilide. *Circulation Research*, 72(1):75–83.

Kang, S. K., Vanoye, C. G., Misra, S. N., Echevarria, D. M., Calhoun, J. D., O'Connor, J. B., Fabre, K. L., McKnight, D., Demmer, L., Goldenberg, P., Grote, L. E., Thiffault, I., Saunders, C., Strauss, K. A., Torkamani, A., van der Smagt, J., van Gassen, K., Carson, R. P., Diaz, J., Leon, E., Jacher, J. E., Hannibal, M. C., Litwin, J., Friedman, N. R., Schreiber, A., Lynch, B., Poduri, A., Marsh, E. D., Goldberg, E. M., Millichap, J. J., George, A. L., and Kearney, J. A. (2019). Spectrum of KV2.1 dysfunction in KCNB1-associated neurodevelopmental disorders. *Annals of Neurology*, 86(6):899–912.

Kapplinger, J. D., Tester, D. J., Alders, M., Benito, B., Berthet, M., Brugada, J., Brugada, P., Fressart, V., Guerchicoff, A., Harris-Kerr, C., Kamakura, S., Kyndt, F., Koopmann, T. T., Miyamoto, Y., Pfeiffer, R., Pollevick, G. D., Probst, V., Zumhagen, S., Vatta, M., Towbin, J. A., Shimizu, W., Schulze-Bahr, E., Antzelevitch, C., Salisbury, B. A., Guicheney, P., Wilde, A. A. M., Brugada, R., Schott, J.-J., and Ackerman, M. J. (2010). An international compendium of mutations in the SCN5A-encoded cardiac sodium channel in patients referred for Brugada syndrome genetic testing. *Heart Rhythm*, 7(1):33–46.

Karakikes, I., Senyei, G. D., Hansen, J., Kong, C.-W., Azeloglu, E. U., Stillitano, F., Lieu, D. K., Wang, J., Ren, L., Hulot, J.-S., Iyengar, R., Li, R. A., and Hajjar, R. J. (2014). Small molecule-mediated directed differentiation of human embryonic stem cells toward ventricular cardiomyocytes. *STEM CELLS Translational Medicine*, 3(1):18–31.

Kattman, S. J., Witty, A. D., Gagliardi, M., Dubois, N. C., Niapour, M., Hotta, A., Ellis, J., and Keller, G. (2011). Stage-specific optimization of activin/nodal and BMP signaling promotes cardiac differentiation of mouse and human pluripotent stem cell lines. *Cell Stem Cell*, 8(2):228–240.

Kehat, I., Kenyagin-Karsenti, D., Snir, M., Segev, H., Amit, M., Gepstein, A., Livne, E., Binah, O., Itskovitz-Eldor, J., and Gepstein, L. (2001). Human embryonic stem cells can differentiate into myocytes with structural and functional properties of cardiomyocytes. *Journal of Clinical Investigation*, 108(3):407–414.

Kelley, C. T. (1999). *Iterative Methods for Optimization*. Society for Industrial and Applied Mathematics, Philadelphia, PA.

Kennedy, J. and Eberhart, R. (1995). Particle swarm optimization. In *International Conference on Neural Networks*, volume 4, pages 1942–1948, Perth, WA. IEEE.

Kernik, D. C., Morotti, S., Wu, H., Garg, P., Duff, H. J., Kurokawa, J., Jalife, J., Wu, J. C., Grandi, E., and Clancy, C. E. (2019). A computational model of induced pluripotent stem-cell derived cardiomyocytes incorporating experimental variability from multiple data sources. *The Journal of Physiology*, 597(17):4533–4564.

Kiefer, J. (1959). Optimum experimental designs. *Journal of the Royal Statistical Society: Series B*, 21(2):272–304.

Kiehn, J., Lacerda, A. E., Wible, B., and Brown, A. M. (1996). Molecular physiology and pharmacology of hERG: single-channel currents and block by dofetilide. *Circulation*, 94(10):2572–2579.

Kim, J. J., Yang, L., Lin, B., Zhu, X., Sun, B., Kaplan, A. D., Bett, G. C., Rasmusson, R. L., London, B., and Salama, G. (2015). Mechanism of automaticity in cardiomyocytes derived from human induced pluripotent stem cells. *Journal of Molecular and Cellular Cardiology*, 81:81–93.

Kirsch, G. E., Trepakova, E. S., Brimecombe, J. C., Sidach, S. S., Erickson, H. D., Kochan, M. C., Shyjka, L. M., Lacerda, A. E., and Brown, A. M. (2004). Variability in the measurement of hERG potassium channel inhibition: effects of temperature and stimulus pattern. *Journal of Pharmacological and Toxicological Methods*, 50(2):93–101.

Koivumäki, J. T., Naumenko, N., Tuomainen, T., Takalo, J., Oksanen, M., Puttonen, K. A., Lehtonen, Š., Kuusisto, J., Laakso, M., Koistinaho, J., and Tavi, P. (2018). Structural immaturity of human iPSC-derived cardiomyocytes: in silico investigation of effects on function and disease modeling. *Frontiers in Physiology*, 9:80.

Kostyuk, P. G., Krishtal, O. A., and Pidoplichko, V. I. (1975). Effect of internal fluoride and phosphate on membrane currents during intracellular dialysis of nerve cells. *Nature*, 257(5528):691–693.

Kozek, K. A., Glazer, A. M., Ng, C.-A., Blackwell, D., Egly, C. L., Vanags, L. R., Blair, M., Mitchell, D., Matreyek, K. A., Fowler, D. M., Knollmann, B. C., Vandenberg, J. I., Roden, D. M., and Kroncke, B. M. (2020). High-throughput discovery of trafficking-deficient variants in the cardiac potassium channel KV11.1. *Heart Rhythm*, in press.

Kramer, J., Himmel, H. M., Lindqvist, A., Stoelzle-Feix, S., Chaudhary, K. W., Li, D., Bohme, G. A., Bridgland-Taylor, M., Hebeisen, S., Fan, J., Renganathan, M., Imredy, J., Humphries, E. S., Brinkwirth, N., Strassmaier, T., Ohtsuki, A., Danker, T., Vanoye, C., Polonchuk, L., Fermini, B., Pierson, J. B., and Gintant, G. (2020). Cross-site and cross-platform variability of automated patch clamp assessments of drug effects on human cardiac currents in recombinant cells. *Scientific Reports*, 10(1):5627.

Kramer, J., Obejero-Paz, C. A., Myatt, G., Kuryshev, Y. A., Bruening-Wright, A., Verducci, J. S., and Brown, A. M. (2013). MICE models: superior to the HERG model in predicting Torsade de Pointes. *Scientific Reports*, 3:2100.

Kucerová, A., Sykora, J., Janouchová, E., Jarušková, D., and Chleboun, J. (2016). Acceleration of robust experiment design using Sobol indices and polynomial chaos expansion. In *Proceedings of the 7th International Workshop on Reliable Engineering Computing (REC), Bochum, Germany*, pages 15–17.

Kujala, K., Paavola, J., Lahti, A., Larsson, K., Pekkanen-Mattila, M., Viitasalo, M., Lahtinen, A. M., Toivonen, L., Kontula, K., Swan, H., Laine, M., Silvennoinen, O., and Aalto-Setälä, K. (2012). Cell model of catecholaminergic polymorphic ventricular tachycardia reveals early and delayed afterdepolarizations. *PLOS One*, 7(9):e44660.

Lambert, B. (2018). *A Student's Guide to Bayesian Statistics*. Sage Publications, London, 1st edition.

Läuger, P. (1985). Ionic channels with conformational substates. *Biophysical Journal*, 47(5):581–590.

Läuger, P., Stephan, W., and Frehland, E. (1980). Fluctuations of barrier structure in ionic channels. *Biochimica et Biophysica Acta - Biomembranes*, 602(1):167–180.

Laverty, H., Benson, C., Cartwright, E., Cross, M., Garland, C., Hammond, T., Holloway, C., McMahon, N., Milligan, J., Park, B., Pirmohamed, M., Pollard, C., Radford, J., Roome, N., Sager, P., Singh, S., Suter, T., Suter, W., Trafford, A., Volders, P., Wallis, R., Weaver, R., York, M., and Valentin, J. (2011). How can we improve our understanding of cardiovascular safety liabilities to develop safer medicines? *British Journal of Pharmacology*, 163(4):675–693.

Lei, C. L., Clerx, M., Beattie, K. A., Melgari, D., Hancox, J. C., Gavaghan, D. J., Polonchuk, L., Wang, K., and Mirams, G. R. (2019a). Rapid characterization of hERG channel kinetics II: temperature dependence. *Biophysical Journal*, 117(12):2455–2470.

Lei, C. L., Clerx, M., Gavaghan, D. J., Polonchuk, L., Mirams, G. R., and Wang, K. (2019b). Rapid characterization of hERG channel kinetics I: using an automated high-throughput system. *Biophysical Journal*, 117(12):2438–2454.

Lei, C. L., Clerx, M., Whittaker, D. G., Gavaghan, D. J., de Boer, T. P., and Mirams, G. R. (2020a). Accounting for variability in ion current recordings using a mathematical model of artefacts in voltage-clamp experiments. *Philosophical Transactions of the Royal Society A*, 378:20190348.

Lei, C. L., Fabbri, A., Whittaker, D. G., Clerx, M., Windley, M. J., Hill, A. P., Mirams, G. R., and de Boer, T. P. (2020b). A nonlinear and time-dependent leak current in the presence of calcium fluoride patch-clamp seal enhancer. *Wellcome Open Research*, 5:152.

Lei, C. L., Ghosh, S., Whittaker, D. G., Aboelkassem, Y., Beattie, K. A., Cantwell, C. D., Delhaas, T., Houston, C., Novaes, G. M., Panfilov, A. V., Pathmanathan, P., Riabiz, M., dos Santos, R. W., Walmsley, J., Worden, K., Mirams, G. R., and Wilkinson, R. D. (2020c). Considering discrepancy when calibrating a mechanistic electrophysiology model. *Philosophical Transactions of the Royal Society A*, 378:20190349.

Lei, C. L., Wang, K., Clerx, M., Johnstone, R. H., Hortigon-Vinagre, M. P., Zamora, V., Allan, A., Smith, G. L., Gavaghan, D. J., Mirams, G. R., and Polonchuk, L. (2017a). Tailoring mathematical models to stem-cell derived cardiomyocyte lines can improve predictions of drug-induced changes to their electrophysiology. *Frontiers in Physiology*, 8:986.

Lei, C. L., Wang, K., Gissinger, E., Flint, N., Chabria, M., Badi, L., Hoflack, J. C., Schuler, F., Lave, T., Singer, T., Clerx, M., Gavaghan, D., Mirams, G., and Polonchuk, L. (2017b). Tailoring an in-silico model to the electrophysiology of individual iPSC-derived caradiomyocyte lines: one size fits all? In *Annual Meeting of the Safety Pharmacology Society*, Berlin.

Levine, I. N. (1978). *Physical Chemistry*. McGraw-Hill, New York, NY, USA.

Li, S., Tao, T., Wang, J., Yang, B., Law, C. K., and Qi, F. (2017a). Using sensitivity entropy in experimental design for uncertainty minimization of combustion kinetic models. *Proceedings of the Combustion Institute*, 36(1):709–716.

Li, T., Lu, G., Chiang, E. Y., Chernov-Rogan, T., Grogan, J. L., and Chen, J. (2017b). High-throughput electrophysiological assays for voltage gated ion channels using SyncroPatch 768PE. *PLOS One*, 12(7).

Li, Z., Dutta, S., Sheng, J., Tran, P. N., Wu, W., and Colatsky, T. (2016). A temperature-dependent in silico model of the human ether-a-go-go-related (hERG) gene channel. *Journal of Pharmacological and Toxicological Methods*, 81:233–239.

Li, Z., Mirams, G. R., Yoshinaga, T., Ridder, B. J., Han, X., Chen, J. E., Stockbridge, N. L., Wisialowski, T. A., Damiano, B., Severi, S., Morissette, P., Kowey, P. R., Holbrook, M., Smith, G., Rasmusson, R. L., Liu, M., Song, Z., Qu, Z., Leishman, D. J., Steidl-Nichols, J., Rodriguez, B., Bueno-Orovio, A., Zhou, X., Passini, E., Edwards, A. G., Morotti, S., Ni, H., Grandi, E., Clancy, C. E., Vandenberg, J., Hill, A., Nakamura, M., Singer, T., Polonchuk, L., Greiter-Wilke, A., Wang, K., Nave, S., Fullerton, A., Sobie, E. A., Paci, M., Musuamba Tshinanu, F., and Strauss, D. G. (2020). General principles for the validation of proarrhythmia risk prediction models: an extension of the CiPA in silico strategy. *Clinical Pharmacology and Therapeutics*, 107(1):102–111.

Li, Z., Ridder, B. J., Han, X., Wu, W. W., Sheng, J., Tran, P. N., Wu, M., Randolph, A., Johnstone, R. H., Mirams, G. R., Kuryshev, Y., Kramer, J., Wu, C., Crumb, W. J., and Strauss, D. G. (2019). Assessment of an in silico mechanistic model for proarrhythmia risk prediction under the CiPA initiative. *Clinical Pharmacology & Therapeutics*, 105(2):466–475.

Lian, X., Zhang, J., Azarin, S. M., Zhu, K., Hazeltine, L. B., Bao, X., Hsiao, C., Kamp, T. J., and Palecek, S. P. (2013). Directed cardiomyocyte differentiation from human pluripotent stem cells by modulating Wnt/β-catenin signaling under fully defined conditions. *Nature Protocols*, 8(1):162–175.

Lieu, D. K., Fu, J.-D., Chiamvimonvat, N., Tung, K. C., McNerney, G. P., Huser, T., Keller, G., Kong, C.-W., and Li, R. A. (2013). Mechanism-based facilitated maturation of human pluripotent stem cell-derived cardiomyocytes. *Circulation: Arrhythmia and Electrophysiology*, 6(1):191–201.

Lieu, D. K., Liu, J., Siu, C.-W., McNerney, G. P., Tse, H.-F., Abu-Khalil, A., Huser, T., and Li, R. A. (2009). Absence of transverse tubules contributes to non-uniform Ca2+ wavefronts in mouse and human embryonic stem cell-derived cardiomyocytes. *Stem Cells and Development*, 18(10):1493–1500.

Lindgren, S., Bass, A. S., Briscoe, R., Bruse, K., Friedrichs, G. S., Kallman, M. J., Markgraf, C., Patmore, L., and Pugsley, M. K. (2008). Benchmarking safety pharmacology regulatory packages and best practice. *Journal of Pharmacological and Toxicological Methods*, 58(2):99–109.

Lindley, D. V. (1956). On a measure of the information provided by an experiment. *The Annals of Mathematical Statistics*, 27(4):986–1005.

Lindley, D. V. (1972). *Bayesian Statistics: A Review*, volume 2. SIAM.

Liu, G. X., Zhou, J., Nattel, S., and Koren, G. (2004). Single-channel recordings of a rapid delayed rectifier current in adult mouse ventricular myocytes: basic properties and effects of divalent cations. *Journal of Physiology*, 556(2):401–413.

López-Redondo, F., Kurokawa, J., Nomura, F., Kaneko, T., Hamada, T., Furukawa, T., and Yasuda, K. (2016). A distribution analysis of action potential parameters obtained from patch-clamped human stem cell-derived cardiomyocytes. *Journal of Pharmacological Sciences*, 131(2):141–145.

Lundy, S. D., Zhu, W.-Z., Regnier, M., and Laflamme, M. A. (2013). Structural and functional maturation of cardiomyocytes derived from human pluripotent stem cells. *Stem Cells and Development*, 22(14):1991–2002.

Ma, D., Wei, H., Lu, J., Ho, S., Zhang, G., Sun, X., Oh, Y., Tan, S. H., Ng, M. L., Shim, W., Wong, P., and Liew, R. (2013). Generation of patient-specific induced pluripotent stem cell-derived cardiomyocytes as a cellular model of arrhythmogenic right ventricular cardiomyopathy. *European Heart Journal*, 34(15):1122–1133.

Ma, J., Guo, L., Fiene, S. J., Anson, B. D., Thomson, J. A., Kamp, T. J., Kolaja, K. L., Swanson, B. J., and January, C. T. (2011). High purity human-induced pluripotent stem cell-derived cardiomyocytes: electrophysiological properties of action potentials and ionic currents. *American Journal of Physiology - Heart and Circulatory Physiology*, 301(5):H2006–H2017.

Machiraju, P. and Greenway, S. C. (2019). Current methods for the maturation of induced pluripotent stem cell-derived cardiomyocytes. *World Journal of Stem Cells*, 11(1):33–43.

Malik, M. and Camm, A. J. (2001). Evaluation of drug-induced QT interval prolongation. *Drug Safety*, 24(5):323–351.

Marty, A. and Neher, E. (1995). Tight-seal whole-cell recording. In Sakmann, B. and Neher, E., editors, *Single-Channel Recording*, chapter 2, pages 31–52. Springer, Boston, MA, 2nd edition.

Massenet, A. (2019). *An Overview of Evolution Strategy Optimizers*. PhD thesis, Oxford University.

Mathur, A., Loskill, P., Shao, K., Huebsch, N., Hong, S., Marcus, S. G., Marks, N., Mandegar, M., Conklin, B. R., Lee, L. P., and Healy, K. E. (2015). Human iPSC-based cardiac microphysiological system for drug screening applications. *Scientific Reports*, 5:8883.

Mauerhöfer, M. and Bauer, C. K. (2016). Effects of temperature on heteromeric Kv11.1a/1b and Kv11.3 channels. *Biophysical Journal*, 111(3):504–523.

Mazhari, R., Greenstein, J. L., Winslow, R. L., Marbán, E., and Nuss, H. B. (2001). Molecular interactions between two long-QT syndrome gene products, HERG and KCNE2, rationalized by in vitro and in silico analysis. *Circulation Research*, 89(1):33–38.

Mirams, G. R., Cui, Y., Sher, A., Fink, M., Cooper, J., Heath, B. M., McMahon, N. C., Gavaghan, D. J., and Noble, D. (2011). Simulation of multiple ion channel block provides improved early prediction of compounds' clinical torsadogenic risk. *Cardiovascular Research*, 91(1):53–61.

Mirams, G. R., Davies, M. R., Brough, S. J., Bridgland-Taylor, M. H., Cui, Y., Gavaghan, D. J., and Abi-Gerges, N. (2014). Prediction of Thorough QT study results using action potential simulations based on ion channel screens. *Journal of Pharmacological and Toxicological Methods*, 70(3):246–254.

Mirams, G. R., Davies, M. R., Cui, Y., Kohl, P., and Noble, D. (2012). Application of cardiac electrophysiology simulations to pro-arrhythmic safety testing. *British Journal of Pharmacology*, 167(5):932–945.

Mirams, G. R., Pathmanathan, P., Gray, R. A., Challenor, P., and Clayton, R. H. (2016). White paper: uncertainty and variability in computational and mathematical models of cardiac physiology. *The Journal of Physiology*, 594(23):6833–6847.

Molleman, A. (2003). *Patch Clamping: An Introductory Guide to Patch Clamp Electrophysiology*. John Wiley & Sons.

Montnach, J., Lorenzini, M., Lesage, A., Simon, I., and Nicolas, S. (2020). Computer modeling of whole-cell voltage-clamp analyses to delineate guidelines for good practice of manual and automated patch-clamp. bioRxiv:10.1101/2020.04.27.062182.

Moore, J. W., Hines, M., and Harris, E. M. (1984). Compensation for resistance in series with excitable membranes. *Biophysical Journal*, 46(4):507–514.

Moran, A. E., Forouzanfar, M. H., Roth, G. A., Mensah, G. A., Ezzati, M., Murray, C. J., and Naghavi, M. (2014). Temporal trends in ischemic heart disease mortality in 21 world regions, 1980 to 2010: the Global Burden of Disease 2010 study. *Circulation*, 129(14):1483–1492.

Moreau, A., Mercier, A., Thériault, O., Boutjdir, M., Burger, B., Keller, D. I., and Chahine, M. (2017). Biophysical, molecular, and pharmacological characterization of voltage-dependent sodium channels from induced pluripotent stem cell-derived cardiomyocytes. *Canadian Journal of Cardiology*, 33(2):269–278.

Moretti, A., Bellin, M., Welling, A., Jung, C. B., Lam, J. T., Bott-Flügel, L., Dorn, T., Goedel, A., Höhnke, C., Hofmann, F., Seyfarth, M., Sinnecker, D., Schömig, A., and Laugwitz, K. L. (2010). Patient-specific induced pluripotent stem-cell models for long-QT syndrome. *The New England Journal of Medicine*, 363(15):1397–1409.

Moss, A. J. (1993). Measurement of the QT interval and the risk associated with QTc interval prolongation: a review. *The American Journal of Cardiology*, 72(6):23B–25B.

Muench, J. L., Paul, F., Schmauder, R., and Benndorf, K. (2020). Bayesian Hidden Markov modeling and model selection by Kalman filtering applied to multi-dimensional data of ion channels. bioRxiv:10.1101/2020.04.27.029207.

Mummery, C. L., Zhang, J., Ng, E. S., Elliott, D. A., Elefanty, A. G., and Kamp, T. J. (2012). Differentiation of human embryonic stem cells and induced pluripotent stem cells to cardiomyocytes: a methods overview. *Circulation Research*, 111(3):344–358.

Muszkiewicz, A., Britton, O. J., Gemmell, P., Passini, E., Sánchez, C., Zhou, X., Carusi, A., Quinn, T. A., Burrage, K., Bueno-Orovio, A., and Rodriguez, B. (2016). Variability in cardiac electrophysiology: using experimentally-calibrated populations of models to move beyond the single virtual physiological human paradigm. *Progress in Biophysics and Molecular Biology*, 120(1-3):115–127.

Nagy, I. and Tóth, J. (2012). Microscopic reversibility or detailed balance in ion channel models. *Journal of Mathematical Chemistry*, 50(5):1179–1199.

National Research Council (2012). *Assessing the Reliability of Complex Models: Mathematical and Statistical Foundations of Verification, Validation, and Uncertainty Quantification*. National Academies Press, Washington, D.C.

Nattel, S. and Carlsson, L. (2006). Innovative approaches to anti-arrhythmic drug therapy. *Nature Reviews Drug Discovery*, 5(12):1034–1049.

Neher, E. (1992). Correction for liquid junction potentials in patch clamp experiments. In *Methods in Enzymology*, volume 207 of *Ion Channels*, chapter 6, pages 123–131. Academic Press, Cambridge, MA.

Neher, E. (1995). Voltage offsets in patch-clamp experiments. In Sakmann, B. and Neher, E., editors, *Single-Channel Recording*, chapter 6, pages 147–153. Springer, Boston, MA, 2nd edition.

Neher, E. and Sakmann, B. (1976). Single-channel currents recorded from membrane of denervated frog muscle fibres. *Nature*, 260(5554):799–802.

Nerbonne, J. M. and Kass, R. S. (2005). Molecular physiology of cardiac repolarization. *Physiological Reviews*, 85(4):1205–1253.

Ng, C.-A., Perry, M. D., Liang, W., Smith, N. J., Foo, B., Shrier, A., Lukacs, G. L., Hill, A. P., and Vandenberg, J. I. (2020). High-throughput phenotyping of heteromeric human Ether-à-go-go-Related Gene potassium channel variants can discriminate pathogenic from rare benign variants. *Heart Rhythm*, 17(3):492–500.

Niederer, S. A., Fink, M., Noble, D., and Smith, N. P. (2009). A meta-analysis of cardiac electrophysiology computational models. *Experimental Physiology*, 94(5):486–495.

Noble, D. (1960). Cardiac action and pacemaker potentials based on the Hodgkin-Huxley equations. *Nature*, 188(4749):495–497.

Noble, D. (2008). Computational models of the heart and their use in assessing the actions of drugs. *Journal of Pharmacological Sciences*, 107(2):107–117.

Noble, D. (2011). Successes and failures in modeling heart cell electrophysiology. *Heart Rhythm*, 8(11):1798–1803.

Obejero-Paz, C. A., Bruening-Wright, A., Kramer, J., Hawryluk, P., Tatalovic, M., Dittrich, H. C., and Brown, A. M. (2015). Quantitative profiling of the effects of vanoxerine on human cardiac ion channels and its application to cardiac risk. *Scientific Reports*, 5:17623.

Oberkampf, W. L. and Roy, C. J. (2010). *Verification and Validation in Scientific Computing*. Cambridge University Press, Cambridge.

Oberkampf, W. L., Trucano, T. G., and Hirsch, C. (2004). Verification, validation, and predictive capability in computational engineering and physics. *Applied Mechanics Reviews*, 57(5):345.

Ogden, D. and Stanfield, P. (1994). Patch clamp techniques for single channel and whole-cell recording. In *Microelectrode Techniques: The Plymouth Workshop Handbook*, book section 4, pages 53–78. The Company of Biologists, Cambridge, 2nd edition.

O'Hara, T., Virág, L., Varró, A., and Rudy, Y. (2011). Simulation of the undiseased human cardiac ventricular action potential: model formulation and experimental validation. *PLOS Computational Biology*, 7(5):e1002061.

Ohler, A., Weisser-Thomas, J., Piacentino, V., Houser, S. R., Tomaselli, G. F., O'Rourke, B., and O'Rourke, B. (2009). Two-photon laser scanning microscopy of the transverse-axial tubule system in ventricular cardiomyocytes from failing and non-failing human hearts. *Cardiology Research and Practice*, 2009:802373.

Okano, H., Nakamura, M., Yoshida, K., Okada, Y., Tsuji, O., Nori, S., Ikeda, E., Yamanaka, S., and Miura, K. (2013). Steps toward safe cell therapy using induced pluripotent stem cells. *Circulation Research*, 112(3):523–533.

Olivetti, G., Giordano, G., Corradi, D., Melissari, M., Lagrasta, C., Gambert, S. R., and Anversa, P. (1995). Gender differences and aging: effects on the human heart. *Journal of the American College of Cardiology*, 26(4):1068–1079.

Ollivier, Y., Arnold, L., Auger, A., and Hansen, N. (2017). Information-Geometric Optimization algorithms: a unifying picture via invariance principles. *The Journal of Machine Learning Research*, 18(1):1–65.

Ortmann, D. and Vallier, L. (2017). Variability of human pluripotent stem cell lines. *Current Opinion in Genetics & Development*, 46:179–185.

Paci, M., Hyttinen, J., Aalto-Setälä, K., and Severi, S. (2013). Computational models of ventricular- and atrial-like human induced pluripotent stem cell derived cardiomyocytes. *Annals of Biomedical Engineering*, 41(11):2334–2348.

Paci, M., Hyttinen, J., Rodriguez, B., and Severi, S. (2015). Human induced pluripotent stem cell-derived versus adult cardiomyocytes: an in silico electrophysiological study on effects of ionic current block. *British Journal of Pharmacology*, 172(21):5147–5160.

Paci, M., Passini, E., Klimas, A., Severi, S., Hyttinen, J., Rodriguez, B., and Entcheva, E. (2020). All-optical electrophysiology refines populations of in silico human iPS-CMs for drug evaluation. *Biophysical Journal*, 118(10):2596–2611.

Paci, M., Pölönen, R.-P., Cori, D., Penttinen, K., Aalto-Setälä, K., Severi, S., and Hyttinen, J. (2018). Automatic optimization of an in silico model of human iPSC derived cardiomyocytes recapitulating calcium handling abnormalities. *Frontiers in Physiology*, 9:709.

Paci, M., Sartiani, L., Del Lungo, M., Jaconi, M., Mugelli, A., Cerbai, E., and Severi, S. (2012). Mathematical modelling of the action potential of human embryonic stem cell derived cardiomyocytes. *BioMedical Engineering OnLine*, 11:61.

Pant, S. (2018). Information sensitivity functions to assess parameter information gain and identifiability of dynamical systems. *Journal of The Royal Society Interface*, 15(142):20170871.

Pathmanathan, P. and Gray, R. A. (2013). Ensuring reliability of safety-critical clinical applications of computational cardiac models. *Frontiers in Physiology*, 4:358.

Pathmanathan, P. and Gray, R. A. (2014). Verification of computational models of cardiac electro-physiology. *International Journal for Numerical Methods in Biomedical Engineering*, 30(5):525–544.

Pathmanathan, P., Shotwell, M. S., Gavaghan, D. J., Cordeiro, J. M., and Gray, R. A. (2015). Uncertainty quantification of fast sodium current steady-state inactivation for multi-scale models of cardiac electrophysiology. *Progress in Biophysics and Molecular Biology*, 117(1):4–18.

Pekkanen-Mattila, M., Chapman, H., Kerkelä, E., Suuronen, R., Skottman, H., Koivisto, A.-P., and Aalto-Setälä, K. (2010). Human embryonic stem cell-derived cardiomyocytes: demonstration of a portion of cardiac cells with fairly mature electrical phenotype. *Experimental Biology and Medicine*, 235(4):522–530.

Po, S. S., Wang, D. W., Yang, I. C.-H., Johnson Jr, J. P., Nie, L., and Bennett, P. B. (1999). Modulation of HERG potassium channels by extracellular Magnesium and Quinidine. *Journal of Cardiovascular Pharmacology*, 33(2):181–185.

Polak, S. and Fijorek, K. (2012). Inter-individual variability in the pre-clinical drug cardiotoxic safety assessment–analysis of the age-cardiomyocytes electric capacitance dependence. *Journal of Cardiovascular Translational Research*, 5(3):321–332.

Priori, S. G., Napolitano, C., Di Pasquale, E., and Condorelli, G. (2013). Induced pluripotent stem cell-derived cardiomyocytes in studies of inherited arrhythmias. *Journal of Clinical Investigation*, 123(1):84–91.

Pugsley, M. K. (2005). Methodology used in safety pharmacology: appraisal of the state-of-the-art, the regulatory issues and new directions. *Journal of Pharmacological and Toxicological Methods*, 52(1):1–5.

Pullan, A. J., Cheng, L. K., and Buist, M. L. (2005). *Mathematically Modeling the Electrical Activity of the Heart: From Cell to Body Surface and Back Again*. World Scientific.

Raiffa, H. and Schlaifer, R. (1961). *Applied Statistical Decision Theory*. Wiley Cambridge.

Ranjan, R., Khazen, G., Gambazzi, L., Ramaswamy, S., Hill, S. L., Schürmann, F., and Markram, H. (2011). Channelpedia: an integrative and interactive database for ion channels. *Frontiers in Neuroinformatics*, 5:36.

Raue, A., Kreutz, C., Maiwald, T., Bachmann, J., Schilling, M., Klingmüller, U., and Timmer, J. (2009). Structural and practical identifiability analysis of partially observed dynamical models by exploiting the profile likelihood. *Bioinformatics*, 25(15):1923–1929.

Redondo-Iglesias, E., Venet, P., and Pelissier, S. (2017). Eyring acceleration model for predicting calendar ageing of lithium-ion batteries. *Journal of Energy Storage*, 13:176–183.

Redondo-Iglesias, E., Venet, P., and Pelissier, S. (2018). Global model for self-discharge and capacity fade in lithium-ion batteries based on the generalized eyring relationship. *IEEE Transactions on Vehicular Technology*, 67(1):104–113.

Ren, Y., Lee, M. Y., Schliffke, S., Paavola, J., Amos, P. J., Ge, X., Ye, M., Zhu, S., Senyei, G., Lum, L., Ehrlich, B. E., and Qyang, Y. (2011). Small molecule Wnt inhibitors enhance the efficiency of BMP-4-directed cardiac differentiation of human pluripotent stem cells. *Journal of Molecular and Cellular Cardiology*, 51(3):280–287.

Riedel, M., Jou, C. J., Lai, S., Lux, R. L., Moreno, A. P., Spitzer, K. W., Christians, E., Tristani-Firouzi, M., and Benjamin, I. J. (2014). Functional and pharmacological analysis of cardiomyocytes differentiated from human peripheral blood mononuclear-derived pluripotent stem cells. *Stem Cell Reports*, 3(1):131–41.

Robert, C. P. and Casella, G. (2004). *Monte Carlo Statistical Methods*. Springer-Verlag, New York, NY.

Robertson, C., Tran, D. D., and George, S. C. (2013). Concise review: maturation phases of human pluripotent stem cell-derived cardiomyocytes. *Stem Cells*, 31(5):829–37.

Robinton, D. A. and Daley, G. Q. (2012). The promise of induced pluripotent stem cells in research and therapy. *Nature*, 481(7381):295–305.

Roden, D. M., Lazzara, R., Rosen, M., Schwartz, P. J., Towbin, J., and Vincent, G. M. (1996). Multiple mechanisms in the long-QT syndrome. Current knowledge, gaps, and future directions. *Circulation*, 94(8):1996–2012.

Rodriguez, M. L., Graham, B. T., Pabon, L. M., Han, S. J., Murry, C. E., and Sniadecki, N. J. (2014). Measuring the contractile forces of human induced pluripotent stem cell-derived cardiomyocytes with arrays of microposts. *Journal of Biomechanical Engineering*, 136(5):51005.

Rodriguez-Fernandez, M., Kucherenko, S., Pantelides, C., and Shah, N. (2007). Optimal experimental design based on global sensitivity analysis. *Computer Aided Chemical Engineering*, 24:63–68.

Rothberg, B. S. and Magleby, K. L. (2001). Testing for detailed balance (microscopic reversibility) in ion channel gating. *Biophysical Journal*, 80(6):3025–3026.

Rouhani, F., Kumasaka, N., de Brito, M. C., Bradley, A., Vallier, L., and Gaffney, D. (2014). Genetic background drives transcriptional variation in human induced pluripotent stem cells. *PLOS Genetics*, 10(6):e1004432.

Sager, P. T., Gintant, G., Turner, J. R., Pettit, S., and Stockbridge, N. (2014). Rechanneling the cardiac proarrhythmia safety paradigm: a meeting report from the Cardiac Safety Research Consortium. *American Heart Journal*, 167(3):292–300.

Sakakibara, Y., Furukawa, T., Singer, D. H., Jia, H., Backer, C. L., Arentzen, C. E., and Wasserstrom, J. A. (1993). Sodium current in isolated human ventricular myocytes. *American Journal of Physiology - Heart and Circulatory Physiology*, 265(4):H1301–H1309.

Saltelli, A. (2002). Making best use of model evaluations to compute sensitivity indices. *Computer Physics Communications*, 145(2):280–297.

Saltelli, A., Annoni, P., Azzini, I., Campolongo, F., Ratto, M., and Tarantola, S. (2010). Variance based sensitivity analysis of model output. Design and estimator for the total sensitivity index. *Computer Physics Communications*, 181(2):259–270.

Sampson, K. J., Iyer, V., Marks, A. R., and Kass, R. S. (2010). A computational model of Purkinje fibre single cell electrophysiology: implications for the long QT syndrome. *The Journal of Physiology*, 588(14):2643–2655.

Sanguinetti, M. C., Jiang, C., Curran, M. E., and Keating, M. T. (1995). A mechanistic link between an inherited and an acquird cardiac arrthytmia: hERG encodes the IKr potassium channel. *Cell*, 81(2):299–307.

Santillo, S., Moriello, A. S., and Di Maio, V. (2014). Electrophysiological variability in the SH-SY5Y cellular line. *General Physiology and Biophysics*, 33:121–129.

Sarkar, A. X. and Sobie, E. A. (2010). Regression analysis for constraining free parameters in electrophysiological models of cardiac cells. *PLOS Computational Biology*, 6(9):e1000914.

Sartiani, L., Bettiol, E., Stillitano, F., Mugelli, A., Cerbai, E., and Jaconi, M. E. (2007). Developmental changes in cardiomyocytes differentiated from human embryonic stem cells: a molecular and electrophysiological approach. *Stem Cells*, 25(5):1136–1144.

Satoh, H., Delbridge, L. M., Blatter, L. A., and Bers, D. M. (1996). Surface: volume relationship in cardiac myocytes studied with confocal microscopy and membrane capacitance measurements: species-dependence and developmental effects. *Biophysical Journal*, 70(3):1494–1504.

Schenkendorf, R., Xie, X., Rehbein, M., Scholl, S., and Krewer, U. (2018). The impact of global sensitivities and design measures in model-based optimal experimental design. *Processes*, 6(4):27.

Schmitt, B. M. and Koepsell, H. (2002). An improved method for real-time monitoring of membrane capacitance in Xenopus laevis oocytes. *Biophysical Journal*, 82(3):1345–1357.

Schuetze, S. M. (1983). The discovery of the action potential. *Trends in Neurosciences*, 6:164–168.

Schulz, D. J., Goaillard, J.-M., and Marder, E. (2006). Variable channel expression in identified single and electrically coupled neurons in different animals. *Nature Neuroscience*, 9(3):356–362.

Sedan, O. and Binah, O. (2011). Excitation-contraction coupling, functional properties, and autonomic and hormonal regulation in human embryonic stem cell derived cardiomyocytes. In *Regenerating the Heart*, pages 37–52. Humana Press, Totowa, NJ.

Shah, R. R. (2005). Drugs, QT interval prolongation and ICH E14: the need to get it right. *Drug safety*, 28(2):115–25.

Sherman, A. J., Shrier, A., and Cooper, E. (1999). Series resistance compensation for whole-cell patch-clamp studies using a membrane state estimator. *Biophysical Journal*, 77(5):2590–2601.

Shi, Y., Inoue, H., Wu, J. C., and Yamanaka, S. (2017). Induced pluripotent stem cell technology: a decade of progress. *Nature Reviews Drug Discovery*, 16(2):115–130.

Shimizu, W. and Antzelevitch, C. (1998). Cellular basis for the ECG features of the LQT1 form of the long-QT syndrome: effects of beta-adrenergic agonists and antagonists and sodium channel blockers on transmural dispersion of repolarization and torsade de pointes. *Circulation*, 98(21):2314–2322.

Sigworth, F. (1995a). Design of the EPC-9, a computer-controlled patch-clamp amplifier. 1. Hardware. *Journal of Neuroscience Methods*, 56(2):195–202.

Sigworth, F., Affolter, H., and Neher, E. (1995). Design of the EPC-9, a computer-controlled patch-clamp amplifier. 2. Software. *Journal of Neuroscience Methods*, 56(2):203–215.

Sigworth, F. J. (1995b). Electronic design of the patch clamp. In Sakmann, B. and Neher, E., editors, *Single-Channel Recording*, chapter 6, pages 95–127. Springer, Boston, MA, 2nd edition.

Silva, J. and Rudy, Y. (2005). Subunit interaction determines IKs participation in cardiac repolarization and repolarization reserve. *Circulation*, 112(10):1384–1391.

Sobol, I. M. (2001). Global sensitivity indices for nonlinear mathematical models and their Monte Carlo estimates. *Mathematics and Computers in Simulation*, 55(1-3):271–280.

Stevens, C. F. (1978). Interactions between intrinsic membrane protein and electric field. An approach to studying nerve excitability. *Biophysical Journal*, 22(2):295–306.

Strickholm, A. (1995). A single electrode voltage, current-and patch-clamp amplifier with complete stable series resistance compensation. *Journal of Neuroscience Methods*, 61(1-2):53–66.

Synnergren, J., Améen, C., Jansson, A., and Sartipy, P. (2012). Global transcriptional profiling reveals similarities and differences between human stem cell-derived cardiomyocyte clusters and heart tissue. *Physiological Genomics*, 44(4):245–258.

Takahashi, K., Tanabe, K., Ohnuki, M., Narita, M., Ichisaka, T., Tomoda, K., and Yamanaka, S. (2007). Induction of pluripotent stem cells from adult human fibroblasts by defined factors. *Cell*, 131(5):861–872.

Tanskanen, A. J., Greenstein, J. L., O'Rourke, B., and Winslow, R. L. (2005). The role of stochastic and modal gating of cardiac L-type Ca2+ channels on early after-depolarizations. *Biophysical Journal*, 88(1):85–95.

Tasaki, I. and Takenaka, T. (1964). Effects of various potassium salts and proteases upon excitability of intracellularly perfused squid giant axons. *Proceedings of the National Academy of Sciences*, 52(3):804–810.

Ten Tusscher, K., Noble, D., Noble, P.-J., and Panfilov, A. V. (2004). A model for human ventricular tissue. *American Journal of Physiology - Heart and Circulatory Physiology*, 286(4):H1573–H1589.

Terrenoire, C., Wang, K., Tung, K. W., Chung, W. K., Pass, R. H., Lu, J. T., Jean, J. C., Omari, A., Sampson, K. J., Kotton, D. N., Keller, G., and Kass, R. S. (2013). Induced pluripotent stem cells used to reveal drug actions in a long QT syndrome family with complex genetics. *The Journal of General Physiology*, 141(1):61–72.

Thomson, J. A., Itskovitz-Eldor, J., Shapiro, S. S., Waknitz, M. A., Swiergiel, J. J., Marshall, V. S., and Jones, J. M. (1998). Embryonic stem cell lines derived from human blastocysts. *Science*, 282(5391):1145–1147.

Tixier, E., Lombardi, D., Rodriguez, B., and Gerbeau, J. F. (2017). Modelling variability in cardiac electrophysiology: a moment-matching approach. *Journal of the Royal Society Interface*, 14(133):20170238.

Toh, M. F., Brooks, J. M., Strassmaier, T., Haedo, R. J., Puryear, C. B., Roth, B. L., Ouk, K., and Pin, S. S. (2020). Application of high-throughput automated patch-clamp electrophysiology to study voltage-gated ion channel function in primary cortical cultures. *SLAS Discovery*, 25(5):447–457.

Trayanova, N. A., O'Hara, T., Bayer, J. D., Boyle, P. M., McDowell, K. S., Constantino, J., Arevalo, H. J., Hu, Y., and Vadakkumpadan, F. (2012). Computational cardiology: how computer simulations could be used to develop new therapies and advance existing ones. *EP Europace Journal*, 14(5):v82–v89.

Tsien, R. W. and Noble, D. (1969). A transition state theory approach to the kinetics of conductance changes in excitable membranes. *The Journal of Membrane Biology*, 1(1):248–273.

Vaidyanathan, R., Markandeya, Y. S., Kamp, T. J., Makielski, J. C., January, C. T., and Eckhardt, L. L. (2016). IK1-enhanced human-induced pluripotent stem cell-derived cardiomyocytes: an improved cardiomyocyte model to investigate inherited arrhythmia syndromes. *American Journal of Physiology - Heart and Circulatory Physiology*, 310(11):H1611–H1621.

van den Heuvel, N. H., van Veen, T. A., Lim, B., and Jonsson, M. K. (2014). Lessons from the heart: mirroring electrophysiological characteristics during cardiac development to in vitro differentiation of stem cell derived cardiomyocytes. *Journal of Molecular and Cellular Cardiology*, 67:12–25.

Vandenberg, J. I., Varghese, A., Lu, Y., Bursill, J. A., Mahaut-Smith, M. P., and L-H Huang, C. (2006). Temperature dependence of human Ether-à-go-go-Related Gene K+ currents. *American Journal of Physiology-Cell Physiology*, 291:C167–C175.

Vanoye, C. G., Desai, R. R., Fabre, K. L., Gallagher, S. L., Potet, F., DeKeyser, J.-M., Macaya, D., Meiler, J., Sanders, C. R., and George, A. L. (2018). High-throughput functional evaluation of KCNQ1 decrypts variants of unknown significance. *Circulation: Genomic and Precision Medicine*, 11(11):e002345.

Vanrolleghem, P. A. and Dochain, D. (1998). Bioprocess model identification. In Van Impe J.F.M., Vanrolleghem P.A., and Iserentant D.M., editors, *Advanced Instrumentation, Data Interpretation, and Control of Biotechnological Processes*, chapter 10, pages 251–318. Springer, Dordrecht.

Veldkamp, M. W., Van Ginneken, A. C., Opthof, T., and Bouman, L. N. (1995). Delayed rectifier channels in human ventricular myocytes. *Circulation*, 92(12):3497–3504.

Verkerk, A. O., Veerman, C. C., Zegers, J. G., Mengarelli, I., Bezzina, C. R., and Wilders, R. (2017). Patch-clamp recording from human induced pluripotent stem cell-derived cardiomyocytes: improving action potential characteristics through dynamic clamp. *International Journal of Molecular Sciences*, 18(9):1873.

Verkhratsky, A., Krishtal, O. A., and Petersen, O. H. (2006). From Galvani to patch clamp: the development of electrophysiology. *Pflügers Archiv*, 453(3):233–247.

Vernon, I., Goldstein, M., and Bower, R. G. (2010). Galaxy formation: a Bayesian uncertainty analysis. *Bayesian Analysis*, 5(4):619–669.

Villaverde, A. F., Barreiro, A., and Papachristodoulou, A. (2016). Structural identifiability of dynamic systems biology models. *PLOS Computational Biology*, 12(10):e1005153.

Walter, E. and Pronzato, L. (1997). *Identification of Parametric Models: From Experimental Data*. Communications and Control Engineering. Springer, London.

Wang, D., Tan, D., and Liu, L. (2018). Particle swarm optimization algorithm: an overview. *Soft Computing*, 22(2):387–408.

Wang, J., Schwinger, R. H., Frank, K., Müller-Ehmsen, J., Martin-Vasallo, P., Pressley, T. A., Xiang, A., Erdmann, E., and McDonough, A. A. (1996). Regional expression of sodium pump subunits isoforms and Na+-Ca++ exchanger in the human heart. *Journal of Clinical Investigation*, 98(7):1650–1658.

Wang, K., Lee, P., Mirams, G. R., Sarathchandra, P., Borg, T. K., Gavaghan, D. J., Kohl, P., and Bollensdorff, C. (2015). Cardiac tissue slices: preparation, handling, and successful optical mapping. *American Journal of Physiology - Heart and Circulatory Physiology*, 308(9):H1112–H1125.

Weerakoon, P., Culurciello, E., Klemic, K. G., and Sigworth, F. J. (2009). An integrated patch-clamp potentiostat with electrode compensation. *IEEE Transactions on Biomedical Circuits and Systems*, 3(2):117–125.

Weerakoon, P., Culurciello, E., Yang, Y., Santos-Sacchi, J., Kindlmann, P. J., and Sigworth, F. J. (2010). Patch-clamp amplifiers on a chip. *Journal of Neuroscience Methods*, 192(2):187–192.

Weiss, J. N. (1997). The Hill equation revisited: uses and misuses. *The FASEB Journal*, 11(11):835–841.

Whittaker, D. G., Clerx, M., Lei, C. L., Christini, D. J., and Mirams, G. R. (2020). Calibration of ionic and cellular cardiac electrophysiology models. *Wiley Interdisciplinary Reviews: Systems Biology and Medicine*, 12(4):e1482.

Wierstra, D., Schaul, T., Glasmachers, T., Sun, Y., Peters, J., and Schmidhuber, J. (2014). Natural Evolution Strategies. *Journal of Machine Learning Research*, 15(27):949–980.

Windley, M. J., Lee, W., Vandenberg, J. I., and Hill, A. P. (2018). The temperature dependence of kinetics associated with drug block of hERG channels is compound-specific and an important factor for proarrhythmic risk prediction. *Molecular Pharmacology*, 94(1):760–769.

Yang, F. and Zheng, J. (2014). High temperature sensitivity is intrinsic to voltage-gated potassium channels. *eLife*, 3:1–15.

Yao, J.-A., Du, X., Lu, D., Baker, R. L., Daharsh, E., and Atterson, P. (2005). Estimation of potency of HERG channel blockers: impact of voltage protocol and temperature. *Journal of Pharmacological and Toxicological Methods*, 52(1):146–153.

Yap, Y. G. and Camm, A. J. (2003). Drug induced QT prolongation and torsades de pointes. *Heart*, 89(11):1363–1372.

Yazawa, M., Hsueh, B., Jia, X., Pasca, A. M., Bernstein, J. A., Hallmayer, J., and Dolmetsch, R. E. (2011). Using induced pluripotent stem cells to investigate cardiac phenotypes in Timothy syndrome. *Nature*, 471(7337):230–234.

Zeng, J., Laurita, K. R., Rosenbaum, D. S., and Rudy, Y. (1995). Two components of the delayed rectifier K+ current in ventricular myocytes of the guinea pig type. Theoretical formulation and their role in repolarization. *Circulation Research*, 77(1):140–152.

Zhang, J., Wilson, G. F., Soerens, A. G., Koonce, C. H., Yu, J., Palecek, S. P., Thomson, J. A., and Kamp, T. J. (2009). Functional cardiomyocytes derived from human induced pluripotent stem cells. *Circulation Research*, 104(4):e30–41.

Zhou, Z., Gong, Q., Ye, B., Fan, Z., Makielski, J. C., Robertson, G. A., and January, C. T. (1998). Properties of HERG channels stably expressed in HEK 293 cells studied at physiological temperature. *Biophysical Journal*, 74(1):230–41.

Zipes, D. P. and Jalife, J. (2009). *Cardiac Electrophysiology: From Cell to Bedside*. Saunders/Elsevier, Philadelphia, Penn, 5th edition.